Numerical and Experimental Study of Heat Pipes Used in Solar Applications

Kods Grissa

THÈSE

Pour l'obtention du Grade de

DOCTEUR DE L'ÉCOLE NATIONALE SUPÉRIEURE DE MÉCANIQUE ET D'AÉROTECHNIQUE
en partenariat international avec
L'ECOLE NATIONALE D'INGENIEURS DE MONASTIR

(Diplôme National – Arrêté du 25 mai 2016)

École Doctorale :

SCIENCES ET INGENIERIE EN MATERIAUX, MECANIQUE, ENERGETIQUE ET AERONAUTIQUE

Secteur de Recherche : Énergétique, thermique et combustion

Présentée par :

Kods GRISSA

Numerical and experimental study of heat pipes used in solar applications

---

Directeurs de thèse : **Yves BERTIN** et **Abdelmajid JEMNI**

Co-Encadrant : **Adel M. BENSELAMA**

****

Soutenue le mardi 18 Décembre 2018

devant la Commission d'Examen

****

JURY

Rapporteurs :
M. Abdulmajeed A. **MOHAMAD**, Professeur, Université de Calgary, Canada
M. Mohamed Chaker **ZAGHDOUDI**, Professeur à l'INSAT, Université de Carthage, Tunisie

Membres du jury :
Mme. Souad **HARMAND**, Professeur à l'Université de Valenciennes et du Hainaut-Cambrésis, France
M. Ezeddine **SEDIKI**, Professeur à la FST, Université Tunis El Manar, Tunisie
M. Abdelmajid **JEMNI**, Professeur à l'ENIM, Université de Monastir, Tunisie
M. Yves **BERTIN**, Professeur à l'ISAE-ENSMA, France
M. Adel M. **BENSELAMA**, Maitre de Conférences à l'ISAE-ENSMA, France

Acknowledgements

Firstly, I would like to thank God for immensely blessing and providing me with everything needed to achieve all that I have accomplished. I am grateful to work in two highly qualified laboratory of research (Laboratoire d'Etude des Systémes thermiques et Energétique (LESTE) and Institut Pprime). Under the direction of Pr. Abdelmajid Jemni and Pr. Yves Bertin, I have learned much through their experience. A special thanks goes to my supervisor Dr. Adel M. Benselama for invaluable assistance, guidance and support during my thesis at Institut Pprime. He was my source of encouragement and motivation especially in the bad moments. Through your exemplary working method and technical knowledge, he has been always a source of inspiration.
I would like to express my special thanks to Dr. Raoudha Chaabane and Dr. Zied Lataoui for their precious comments on my work, their motivation and support during my thesis in LESTE. Another sincere acknowledgement is for Dr. Cyril Romestant, a research engineer at the Prime Institut. His guidance, support and previous experiences in thermal engineering were a constant source of reliable knowledge. Also, he allowed for the experimental portion of this thesis to be relative. Special thanks goes to Dr. Vincent Ayel and Dr. Nicolas Chauris for their time and support. A special thanks goes to Mr. Hérvé Arlaub and Mr. André Piteau for their continuous help and assistance during the experimental setup. Without their knowledge and skills the experimental setup would have been more time consuming and less successful then it was.

I would like to thank all the COST members especially Fillipo for his help supporting me while doing my experiments. Also, I would like to thank all the LESTE members especially Abir Yahia. Their tireless efforts are sincerely appreciated. Working for both teams has been a privilege and a pleasure throughout the years.

Profuse thanks go equally to Pr. Abdulmajeed Mohamad and Pr. Mohamed Zaghdoudi for accepting reporting my thesis. Also, I would like to thank Pr. Souad Harmand and Pr. Ezeddine Sediki for being part of the jury board of my PhD.

Last but not least I would like to thank Eiffel Scholarship, which made this PhD thesis possible through their financial support under the following number 870763D.
I would like to thank my parents, Mohamed and Emna, for their encouragement and support for me during my challenges. I would also like to thank my sisters Najla and Hajer and my brothers Saif, Tarek and Zied for their words of encouragement and understanding during my studies.
Most importantly, I would like to thank my husband Abdou for his perfect grace and sacrifice, for giving me the talent, resources and strength to continue for my accomplishments. I praise him for the joy he gives me and the passion he has given me for life. Finally, I dedicate this thesis to my future baby.

Table of contents

List of figures xi

List of tables xix

Nomenclature xxi

Introduction 1

1 Context . . . 2

2 Motivation and objectives . . . 4

3 Manuscript overview/outline . . . 5

Chapter 1 Generalities and state of the art 7

1.1 Historical development and background of heat pipes . . . 8

1.2 Heat pipe working principal . . . 10

1.3 Heat pipe construction . . . 11

1.3.1 Container materials . . . 11

1.3.2 Working fluids . . . 11

1.3.3 Wick structure . . . 13

1.3.4 Charge filling . . . 15

1.4 The physics of heat pipes . . . 15

1.4.1 Fluid phases bulk flow . . . 15

1.4.2 Liquid/vapor interface . . . 16

1.5 Heat pipe applications . . . 18

1.5.1 Terrestrial applications . . . 18

1.5.2 Space applications . . . 19
1.6 Types of heat pipes . . . 19
1.6.1 Thermosyphon (gravity-driven heat pipes) . . . 19
1.6.2 Pulsating heat pipes (PHP) . . . 20
1.6.3 Loop heat pipes (LHP) . . . 21
1.6.4 Capillary Pumped Loop (CPL) . . . 22
1.6.5 Miniature and micro heat pipes (MHP) . . . 23
1.6.6 Vapor chamber . . . 23
1.7 Heat pipe cycle and operating limits . . . 24
1.7.1 Temperature and operating range . . . 25
1.7.2 Capillary limit . . . 25
1.7.3 Viscous limit . . . 27
1.7.4 Boiling limit . . . 28
1.7.5 Sonic limit . . . 29
1.7.6 Entrainment limit . . . 30
1.8 A focus on heat pipe application in solar thermal collectors . . . 30
1.8.1 Main solar collectors design and their performance . . . 30
1.8.2 Heat pipe evacuated tube solar collectors . . . 31
1.8.3 Development of collectors . . . 36
1.8.4 Challenges when using HPETSCs . . . 45
1.9 Conclusions . . . 46

Chapter 2 Lattice Boltzmann Method **47**

2.1 Background and basics of Lattice Boltzmann method . . . 48
2.2 Advantages of Lattice Boltzmann Method . . . 49
2.3 The different approaches . . . 49
2.3.1 Grad's representation approach . . . 50
2.3.2 Chapman-Enskog expansion approach . . . 50
2.3.3 Systematic approach . . . 50

2.4 Formulation . . . 50
2.4.1 Boltzmann equation . . . 50
2.4.2 Collision term . . . 52
2.4.3 From the Boltzmann equation to the lattice Boltzmann equation . . . 53
2.4.4 H-theorem . . . 54
2.4.5 Equilibrium distribution function . . . 56
2.4.6 The forcing schemes . . . 57
2.5 Initial and boundary conditions . . . 57
2.5.1 Initial conditions . . . 57
2.5.2 Boundary conditions . . . 58
2.6 Lattice Models and isotropy . . . 65
2.6.1 Lattice structure . . . 66
2.6.2 One-dimensional arrangements . . . 67
2.6.3 Two-dimensional arrangements . . . 67
2.6.4 Three-dimensional arrangements . . . 68
2.7 Unit conversion . . . 69
2.7.1 Direct conversion . . . 69
2.7.2 Dimensionless formulation . . . 70
2.8 Lattice Boltzmann algorithm . . . 71
2.8.1 Discretization of the physical domain and making dimensionless the related parameters . . . 71
2.8.2 Choice of simulation parameters . . . 71
2.8.3 Domain initialization . . . 73
2.8.4 Collision step . . . 73
2.8.5 Streaming step . . . 74
2.8.6 Implementation of boundary conditions . . . 74
2.8.7 Calculation of the macroscopic parameters . . . 74
2.8.8 Checking the convergence . . . 74
2.9 Conclusion . . . 75

Chapter 3 Axisymmetric Lattice Boltzmann model for fluid flow through porous media **77**

3.1 Axisymmetric models . . . 78

3.1.1 Literature review . . . 78

3.1.2 Governing equations . . . 80

3.2 Axisymmetric lattice Boltzmann equation for fluid flow through porous media 82

3.2.1 Lattice Boltzmann equation for the velocity field . . . 82

3.2.2 Lattice Boltzmann equation for the temperature field . . . 84

3.3 Lattice Boltzmann boundary conditions . . . 85

3.4 From lattice Boltzmann equation to balances for axisymmetric fluid flow through porous media . . . 86

3.4.1 Derivation of mass and momentum equations . . . 86

3.4.2 Derivation of the energy equation . . . 90

3.5 Model validation . . . 91

3.5.1 The incompressible isothermal fluid flow in a clear pipe driven by a constant force . . . 92

3.5.2 The incompressible isothermal fluid flow in a porous pipe driven by a constant force . . . 93

3.5.3 The incompressible isothermal fluid flow in a porous pipe driven by a constant velocity on the pipe wall . . . 96

3.5.4 The incompressible heated fluid flow in a porous pipe partly filled with porous medium . . . 98

3.6 Enhanced axisymmetric model . . . 100

3.6.1 Compressibility problem statement . . . 100

3.6.2 Lattice Boltzmann equation for the velocity field . . . 101

3.6.3 From lattice Boltzmann equation to mass and momentum equations for axisymmetric fluid flow through porous media . . . 102

3.6.4 Performance of the enhanced model . . . 105

3.7 Conclusion . . . 106

Chapter 4 Numerical analysis of the heat pipe **107**

4.1 Heat pipe modeling using Lattice Boltzmann method . . . 108

4.1.1 Assumptions . . . 108

4.1.2 Governing equations . . . 108
4.1.3 Boundary conditions . . . 109
4.1.4 LB implementation . . . 110
4.1.5 Validations . . . 113
4.2 Numerical analysis of a wicked heat pipe . . . 117
4.2.1 Analysis of working fluid potential . . . 119
4.2.2 Effect of working fluid . . . 121
4.2.3 Effect of wick structure . . . 122
4.3 Numerical study of heat pipe performance used in solar applications . . . 124
4.3.1 Heat input effect . . . 127
4.3.2 Porosity and permeability effect . . . 128
4.3.3 Wick thickness effect . . . 131
4.3.4 Evaporator length effect . . . 131
4.3.5 Inclination effect . . . 132
4.3.6 Working fluid effect . . . 133
4.4 HPETSC thermal analysis . . . 134
4.4.1 HPETSC configurations . . . 134
4.4.2 Single pipe thermal analysis . . . 135
4.5 Energy and exergy analysis . . . 137
4.5.1 Effect of solar radiation intensity . . . 137
4.5.2 Effect of the number of tubes . . . 139
4.6 Conclusion . . . 140

Chapter 5 Experimental analysis of heat pipe **143**

5.1 Heat pipe design . . . 144
5.2 Instrumentation . . . 144
5.2.1 Condenser . . . 145
5.2.2 Evaporator . . . 146
5.2.3 Temperature measurement . . . 146
5.2.4 Leak test and envelop degassing . . . 148

5.2.5 Inclination . . . 148
5.2.6 Calibration . . . 149
5.2.7 Thermal insulation . . . 151
5.3 Data acquisition and control devices . . . 152
5.3.1 Labview software . . . 153
5.3.2 Temperature measurement . . . 153
5.3.3 Power control and measurement . . . 153
5.4 Measurement uncertainty . . . 153
5.4.1 Uncertainties on the measured temperature . . . 153
5.4.2 Uncertainties on power measurement and applied power . . . 155
5.4.3 Uncertainties on the thermal resistance . . . 155
5.5 Heat pipe filling . . . 156
5.6 Test cases . . . 157
5.6.1 Case A . . . 157
5.6.2 Case B . . . 157
5.6.3 Case C . . . 158
5.6.4 HP limits . . . 158
5.7 Latin Hypercube Sampling method applied to experimental design . . . 159
5.7.1 Latin Hypercube Sampling methodology . . . 159
5.7.2 The reliability of the LHS method . . . 161
5.8 Results and discussions . . . 162
5.8.1 Case A . . . 163
5.8.2 Cases A and B . . . 181
5.8.3 Cases A and C . . . 183
5.9 The optimum solution in solar collector situations . . . 184
5.10 Conclusion . . . 186

6 Conclusions **187**

6.1 Summary . . . 188
6.2 Notable Findings . . . 190

6.3 Future Directions 190

Appendices **193**

Appendix A Derivation of the formula of the velocity field **195**

Appendix B Heat pipe temperature and velocity profiles **197**

Appendix C Heat pipe plan by Atherm **201**

Appendix D Heat pipe components **203**

Appendix E Uncertainty calculation **209**

E.1 Calculation of variance and standard uncertainties 209

E.1.1 Uncertainty type A 209

E.1.2 Uncertainty type B 210

E.2 Expanded uncertainty 210

E.3 Compound uncertainties 210

Appendix F Comparison between the two technical implementations **213**

Appendix 193

Bibliography **215**

List of figures

1 Energy consumption of heating networks in million tonnes of oil equivalent (mtoe) by source [152]. . . . 2

2 The primary production of renewable energies in mtoe by sector in 2015 [152]. 3

3 The residential energy consumption in mtoe per type of energy in France [152]. 3

4 The rate of installed surface in m^2 per year for each solar collector technology [152]. . . . 4

5 The installed surface in m^2 per year for each collector technology [152]. . . 4

1.1 Drawing of Perkin's boiler [229]. . . . 8

1.2 Heat pipe schematic description. . . . 10

1.3 Different wick structures used in heat pipes [229]. . . . 14

1.4 Thermosyphon. . . . 20

1.5 Schematics of a pulsating heat pipe [229]. . . . 21

1.6 Schematics of loop heat pipes [229]. . . . 22

1.7 Heat pipe limits [229]. . . . 24

1.8 One tube HPETSC schematic description. . . . 32

1.9 Heat pipe evacuated tube solar collector. . . . 32

1.10 HPETSC with bad contact between the finner and the inner tube [1]. . . . 37

1.11 Cross section of the evacuated tube heat pipe in case of inserting (a) finned surface (b) finned surface and oil and (c) foamed copper and oil. Courtesy of [1] (adapted). . . . 38

1.12 Heat transfer process in LHTES tank. (a) solar heat absorption, (b) PCM charging and (c) PCM discharging and water supply heating. Courtesy of [192] (adapted). 38

1.13 Schematic of HPETSC filled with PCM. Courtesy of [208] (adapted). . . . 39

1.14 HPSC-LHS system [193] (adapted). 40

1.15 Solar intensity for a black body at 5800K and a heat pipe at 310K. 40

1.16 Aluminum finned HP proposed by the authors: (a) outer view of the HP's fragment and (b) cross-sectional profile of the HP: 1-absorber and 2-grooved HP. [228]. 43

1.17 Photography of manifold header prototype from different phase of manufacturing (A)-illustration of inner arrangement, (B)-front view of partially assembled manifold, (C)-comparison of standard manifold (top) and prototype of manifold header (bottom), where is clearly visible similar dimensions [242]. 44

2.1 Scheme of D2Q9 lattice. 54

2.2 Boundary distribution functions [186]. 58

2.3 Half way bounce back. 59

2.4 Symmetry boundary condition. 62

2.5 Scheme of the implimented boundary condition. 63

2.6 Periodic boundary condition [186]. 65

2.7 D1Q5 lattice. 67

2.8 D2Q9 lattice (recall of figure 2.1). 68

2.9 D3Q19 lattice. 69

2.10 LBM algorithm synoptic. 72

2.11 pre-streaming step (a) and post-streaming step (b). Note the propagation of the information. 75

3.1 Symmetry axis boundary; dashed-dotted line: symmetry axis; and dashed line: ghost boundary along symmetry axis. 86

3.2 Illustration of the first (clear pipe) and second (porous pipe) test cases. . . 92

3.3 A comparison of the axial velocity profiles for different external forces of the first test as obtained from the present LBE model simulation (solid lines) versus the closed-form solution (symbols) for the first test case. . . . 93

3.4 A comparison of the axial velocity profiles for different permeabilities as obtained from the present LBE model simulation (solid lines) and the closed-form solution (symbols) for the second test case with Forchheimer term. . . 95

3.5 A comparison of the axial velocity profiles for different permeabilities as obtained from the present LBE model simulation (solid lines) and the numerical solution by Rong *et al.* [238] (symbols) for the second test case without Forchheimer term. 95

3.6 Illustration of the third case test. 96

3.7 A comparison of the axial velocity profiles for different permeability as obtained from the present LBE model simulation (solid lines) without Forchheimer term versus the closed-form solution (symbols) for the third test. 97

3.8 A comparison of the axial velocity profiles for different permeability of the third test case as obtained from the present LBE model simulation (solid lines) with Forchheimer term versus numerical solution by Rong *et al.* [238] (symbols). 97

3.9 Schematic diagram of the fourth case test. 98

3.10 A comparison of the 3.10a axial velocity and 3.10b temperature profiles of the fourth test case as obtained from the present LBE model simulation (solid lines) versus the results of Rong *et al.* [241] (symbols). 99

3.11 L_2-norm errors with respect to mesh resolution for the different test case for the proposed LBE model ($\triangleright$ symbols) and its enhanced version ($\circ$ symbols). 106

4.1 Heat pipe schematic description. (Lengths are not to scale.) 108

4.2 Half lattice division for the solid/fluid interface processing; dashed line: solid/fluid interface; A: one lattice on the liquid; B: one lattice on the solid. 111

4.3 Artificial seperation of the domain into two parts at the solid/fluid interface; solid red line: solid/fluid interface. 111

4.4 Vapor-liquid interface. 112

4.5 LBM algorithm synoptics applied to HP. 114

4.6 Comparison between velocity profiles obtained from the present LBE model simulation (solid line) and from the results of Brahim *et al.* (symbols) [20]. (a) the axial velocity along the vapor core center, (b) the radial velocity along the liquid-vapor interface. 115

4.7 A comparison of the present LBE model simulation (solid line) with the analytical results of Zhu *et al.* [319] (▷ symbols) and the experimental results of Huang *et al.* [159] (○ symbols). 118

4.8 L_2-norm errors versus the grid spacing. 118

4.9 Resistance circuit equivalent to the heat pipe. 120

4.10 Profiles for different working fluid. 123

4.11 Profiles in the liquid/wick region for different wick structures. 125

4.12 Heat pipe coupled to heat exchanger. (All sizes are given in mm.) 126

4.13 Variations of thermal resistance versus heat input density for different working fluids. 128

4.14 Variations of thermal resistance versus the porosity for different working fluids and permeability equal to $1.17 \times 10^{-11}\mathrm{m}^{-2}$. 129

4.15 Variations of thermal resistance versus the permeability for different working fluids and porosity set to 0.4. 129

4.16 Variations of thermal resistance versus the wick thickness for different working fluids. 131

4.17 Variations of the ratio of thermal resistance versus the evaporator length for different working fluids. 132

4.18 Variations of thermal resistance versus the sine of inclination angle for different working fluids. 133

4.19 Cross section of heat pipe evacuated tube solar collector. 134

4.20 General description of heat pipe evacuated tube solar collector. 135

4.21 Heat pipe evacuated tube solar collector. 135

4.22 The evolution of (4.22a) outlet temperature, (4.22b) energy efficiency and (4.22c) exergy efficiency for different solar radiations. 139

4.23 The evolution of (4.23a) outlet temperature, (4.23b) energy efficiency and (4.23c) exergy efficiency for different tubes numbers. 140

5.1 Schematic of the heat pipe experimental system. . . . 145
5.2 Condenser bundles. . . . 145
5.3 Evaporator block. . . . 146
5.4 Thermocouple implementation. . . . 147
5.5 Details of thermocouple locations in test bench in cm. . . . 148
5.6 Leak test . . . 148
5.7 Temperature measurement technique. . . . 150
5.8 Calibration bench test. . . . 151
5.9 Ertalon support. . . . 151
5.10 Isolated heat pipe. . . . 152
5.11 Filling system. . . . 156
5.12 Schematic of case A. . . . 157
5.13 Schematic of case B. . . . 158
5.14 Schematic of case C. . . . 158
5.15 The distributions of the 18 points given in table 5.5 and represented by a circle. . . . 160
5.16 Generated points using the LHS for water. . . . 161
5.17 Comparison between the LHS and the experimental results. . . . 162
5.18 Resistance circuit equivalent to the heat pipe. . . . 163
5.19 Illustration of solar incident radiation. . . . 163
5.20 Schematic of the symmetric and asymmetric heating configurations. . . . 164
5.21 Variations of the thermal resistance versus the heat input for different fluids and filling ratios using symmetric and asymmetric configurations under condenser temperature, 37°C, and inclination angle, 63°. . . . 165
5.22 Variations of the thermal resistance versus the heat input for different filling ratios under condenser temperature, 37°C, and inclination angle, 63°. . . . 167

5.23 Variations of the thermal resistance versus the heat input for different working fluids under condenser temperature, 37°C, and inclination angle, 63°. 168

5.24 Variations of the thermal resistance versus heat input density for different working fluids for a HP with 1.76m of length (1.4m evaporator, 0.06m adiabatic and 0.3 condenser length), $\varepsilon = 0.4$, $K = 1.17 \times 10^{-10} m^{-2}$, convective heat transfer coefficient of $1400 W.m^{-2}.K^{-1}$ and inlet temperature of 22°C. 168

5.25 Gravity-assisted and gravity-opposed orientations. 169

5.26 Variations of the thermal resistance versus the inclination angle under condenser temperature, 55°C, and heat input, 47.75W. 170

5.27 Variations of thermal resistance versus the sine of inclination angle for different working fluids for a HP with 1.76m of length (1.4m evaporator, 0.06m adiabatic and 0.3 condenser length), $\varepsilon = 0.4$, $K = 1.17 \times 10^{-10} m^{-2}$, convective heat transfer coefficient of $1400 W.m^{-2}.K^{-1}$ and inlet temperature of 22°C. 171

5.28 Variations of the thermal resistance versus the condenser temperature under inclination angle, 63°, and heat input, 38.75W. 172

5.29 Variations of the wall temperature versus the heat pipe length using water as working fluid by referring to experimental and numerical results for gravity-assisted and gravity-opposed orientations under condenser temperature, 10°C, and heat input, 5W. 173

5.30 Variations of the wall temperature versus the heat pipe length using methanol as working fluid by referring to experimental and numerical results for gravity-assisted and gravity-opposed orientations under condenser temperature, 10°C, and heat input, 5W. 174

5.31 Variations of the maximum heat input versus the operation temperature for (5.31a) water and (5.31b) methanol. 175

5.32 Temperature iso-contours in °C in the wall/liquid-wick region using water as working fluid by referring to numerical results for gravity-assisted and gravity-opposed orientations under condenser temperature, 10°C, and heat input, 5W. 176

5.33 Temperature iso-contours in °C in the wall/liquid-wick region using methanol as working fluid by referring to numerical results for gravity-assisted and gravity-opposed orientations under condenser temperature, 10°C, and heat input, 5W. 176

5.34 Axial liquid-wick velocity iso-contours in $\times 10^{-1}$m/s using water as working fluid by referring to numerical results for gravity-assisted and gravity-opposed orientations under condenser temperature, 10°C, and heat input, 5W. 177

5.35 Axial liquid-wick velocity iso-contours in $\times 10^{-1}$m/s using methanol as working fluid by referring to numerical results for gravity-assisted and gravity-opposed orientations under condenser temperature, 10°C, and heat input, 5W. 178

5.36 Axial vapor velocity iso-contours in m/s using water as working fluid by referring to numerical results for gravity-assisted and gravity-opposed orientations under condenser temperature, 10°C, and heat input, 5W. 179

5.37 Axial vapor velocity iso-contours in m/s using methanol as working fluid by referring to numerical results for gravity-assisted and gravity-opposed orientations under condenser temperature, 10°C, and heat input, 5W. . . . 179

5.38 A comparison of the error between the experimental and numerical results for the tested points (1 to 5 given in table 5.5) by varying the condenser temperature, the inclination angle and the heat input power. 181

5.39 Variations of the thermal resistance versus the heat input for different fluids and filling ratios configurations with and without the adiabatic region under condenser temperature, 37°C, and inclination angle, 63°. 182

5.40 Variations of the thermal resistance versus the heat input for water with 150% filling ratios using symmetric and asymmetric configurations under condenser temperature, 37°C, and inclination angle, 63°. 183

5.41 The optimum heat input versus the inclination angle. 186

B.1 Temperature field in the porous medium expressed in °C for different working fluids using sintered steel (case I). 198

B.2 Temperature field in the porous medium expressed in °C for different working fluids using copper screen (case II). 198

B.3 Temperature field in the porous medium expressed in °C for different working fluids using sintered copper (case III). 199

B.4 Axial velocity field expressed in the vapor core in m/s for different working fluids using sintered steel in the vapor region (case I). 199

B.5 Axial velocity field expressed in the vapor core in m/s for different working fluids using copper screen in the vapor region (case II). 200

B.6 Axial velocity field expressed in the vapor core in m/s for different working fluids using sintered copper in the vapor region (case III). 200

C.1 Heat pipe sizes. 201

D.1 Evaporator design first version. 204

D.2 Evaporator design second version. 205

D.3 Condenser design first version. 206

D.4 Condenser design first second version. 207

D.5 Bench test. 208

F.1 Schematic of the initial heat pipe experimental system. 213

List of tables

1.1 Heat pipe main working fluids [229]. 12

1.2 Working fluids and their compatibility with heat pipe wick material. 13

1.3 Classification of heat transfer fluids temperature range [237]. 25

4.1 Heat pipe validation parameters [20]. 116

4.2 Heat pipe validation parameters [319]. 117

4.3 Thermophysical properties of the working fluids at standard conditions. . . 120

4.4 Heat pipe parameters. 122

4.5 Thermal resistance, R_{th}, for different working fluids. 122

4.6 Proprieties of the different wick structure. 124

4.7 Thermal resistance, R_{th}, for different wick structure. 124

4.8 Heat pipe parameters. 126

4.9 Thermal resistance (Rth($K.W^{-1}$)) of each case for different working fluids and different wick structures. 130

4.10 HPETSC parameters. 138

5.1 Heat pipe characteristics parameters. 144

5.2 Uncertainty of temperature measurement. 154

5.3 Heat pipe functionality limits for water at 35°C. 158

5.4 Heat pipe functionality limits for methanol at 35°C. 158

5.5 The experimental measurement points. 160

5.6 Comparison between the numerical and experimental resistances for different experimental tested points using water as working fluid. 180

5.7 Comparison between the numerical and experimental resistances for different experimental tested points using methanol as working fluid. 180

F.1 Thermal resistance at 30°C under heat input of 5W for case A. 213

F.2 Thermal resistance at 60°C under heat input of 5W for case A. 214

Nomenclature

Greek letters

α	Thermal diffusion coefficient ($m^2.s^{-1}$)
β	Thermal expansion coefficient (K^{-1})
Δt	Time step (s)
Δx	Space step in the x direction (m)
$\delta_{i,j}$	Kronecker symbol
γ	Ratio of the vapor specific heat capacity (c_p/c_v)
λ	Thermal conductivity ($W.m^{-1}.K^{-1}$)
$(\tau\alpha)_e$	Collector effective transmittance-absorptance product
μ	Dynamic viscosity ($kg.m^{-1}.s^{-1}$)
ν	Kinetic viscosity ($m^2.s^{-1}$)
Ω	Collision operator
ρ	Density ($kg.m^{-3}$)
$\sigma_{'}$	liquid-vapor surface tension ($N.m^{-1}$)
$\sigma^{'}$	Ratio between the heat capacities of the porous medium solid and liquid phases
τ	Relaxation time (s)
Θ	Forcing term in the mass equation
θ	Tilt angle (°)
ε	Porosity of the porous medium
$\widetilde{\sigma}$	Accommodation coefficient

Latin letters

$\dot{m}$	Mass flow rate ($kg.s^{-1}$)
$\mathbf{a}$	Acceleration ($m.s^{-2}$)
$\mathbf{c}$	Lattice velocity vector
$\mathbf{G}$	Body force (N)
$\mathbf{g}$	Gravitational acceleration ($m.s^{-2}$)
$\mathbf{I}$	Identity matrix
$\mathbf{u}$	Velocity vector ($m.s^{-1}$)
$\mathbf{x}$	Position (m)
A_c	Collector aperture area (m^2)
c_s	Speed of sound
c_p	Thermal capacity at constant pressure ($J.kg^{-1}.K^{-1}$)
c_v	Thermal capacity at constant volume ($J.kg^{-1}.K^{-1}$)
D	Dimension of the problem
d_p	Pores mean diameter (m)
f	Velocity distribution function
$F^{'}$	Removal factor
F_α	Forcing term in the momentum equation
F_ε	Geometric function
F_p	Source term due to the presence of porous medium
g	Temperature distribution function
h_{lv}	Latent heat of vaporization ($J.kg^{-1}$)

I	Solar radiation intensity (W.m^{-2})
i	Position in the z-direction
j	Position in the r-direction
K	Permeability (m^{-2})
L	Length (m)
M	Molar mass (g.mol^{-1})
m	Number of cells in the r-direction
M_e	Merit number
n	Number of cells in the z-direction
p	Pressure (Pa)
Q	Heat input (W)
q	Heat flux density (W.m^{-2})
R	Dimensionless radial coordinate
r	Radial coordinate (m)
R_g	Ideal gas constant (8.314 J.mol^{-1}K^{-1})
S	Surface (m^2)
T	Temperature (K)
t	Time (s)
u	Axial velocity (m.s^{-1})
U_L	Heat loss coefficient (W.m^{-2}.K^{-1})
V	Volume (m^3)
v	Radial velocity (m.s^{-1})
w	Weight
Z	Dimensionless axial coordinate
z	Axial coordinate (m)

Dimensionless numbers

Bi	Biot number($= H\,R/\lambda$)
Da	Darcy number ($= K/L^2$)
Ma	Mach number ($= V/c_0$)
Pr	Prandtl number($= \nu/\alpha$)
Ra	Rayleigh number ($= g\beta(T - T_0)R^3/\nu\alpha$)
Re	Reynolds number ($= U\,R/\nu$)

Superscripts

$'$	Symmetry component
eq	Equilibrium
neq	Non-equilibrium

Subscripts

0	Reference
$adia$	Adiabatic
b	Boiling
$cond$	Condenser
$crit$	Critical
e	Effective
ent	Entertainment
$envi$	Environmental
$evap$	Evaporator
f	Fluid
g	Gas
g	Meniscus
in	Inlet
k	Lattice direction
l	Liquid

lb	Lattice Boltzmann units
out	Outlet
p	Porous wick
phy	Physical units
PT	Contact line
r	Radial
s	Solid
sat	Saturation
sol	Solar
son	Sonic
tot	Total
v	Vapor
vis	Viscous
w	Wall
z	Axial

Introduction

1 Context

As in the last century the world's population quadrupled, from two to eight billion people, and its corollary the world's economy growing, the demand for energy is also severely increasing at a substantial rate. Currently, this high energy demand mainly depends on non-renewable energy sources such as oil, gas and fossil fuel resources. As some of these energy sources previously mentioned have reached, or are close to reaching, their peak supply, we are expected toward a major energy crisis if no applicable substitutions are found. Besides, the difficulty of meeting the high energy demand, the issue of environment and sustainability has led to a critical concern on power generation and utilization. Fossil fuels are sources of emissions which contribute to the global warming and are unsustainable due to their dwindling reserves, price rise and geographic origin not evenly distributed in the world. Geopolitical instability in resource areas is also a major concern. Due to this energy and environmental issues of non-renewable sources, more attention is being given to renewable energy sources which are environmentally friendly and sustainable. Renewable energy sources such as solar energy are the long term options to substitute conventional energies. It reduces electric/auxiliary energy usage with free solar energy and CO_X, NO_X, SO_X emissions. Recently, France used significantly less fossil resources and significantly more renewable power (see figure 1). There was also a decline in natural gas for domestic heat use, which remains the main source, and increases in renewable power, which represents the third primary energy consumption, according to "Key figures of energy, 2016 Edition".

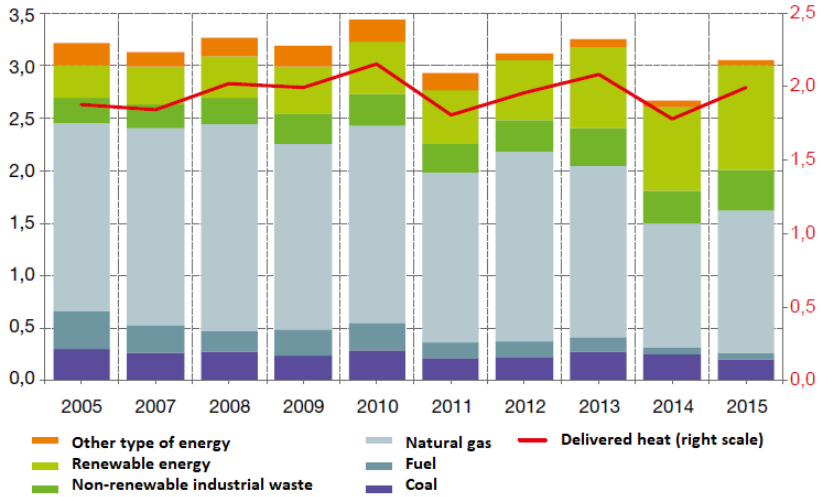

FIGURE 1 – Energy consumption of heating networks in million tonnes of oil equivalent (mtoe) by source [152].

In the recent years solar energy has been strongly promoted as a reliable energy source. One of the most straight forward applications of this energy is converting solar radiation into heat, for example in hot water supply. In 2015, we can see, in figure 2, the primary

production of renewable energies amounted to $23Mtoe$ in a typical french city where the thermal solar and photovoltaic contribution is about 0.7% only the scope for progress is tremendous.

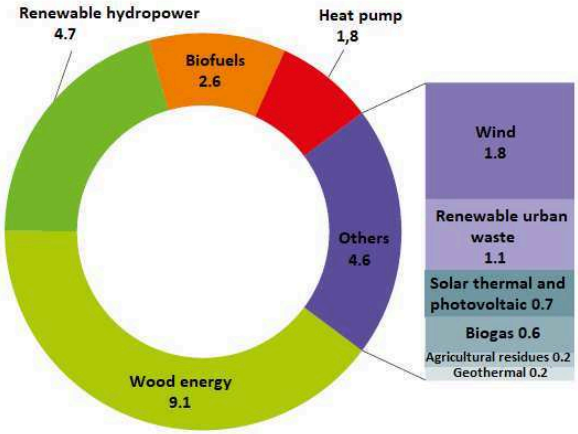

FIGURE 2 – The primary production of renewable energies in mtoe by sector in 2015 [152].

However, the solar water heating technology has greatly improved during the past three decades. Today there are more than 30 million square meters of solar collectors installed around the planet. These technologies are usually at either the industrial or residential scale. At the residential scale, home owners can produce their own hot water from the sun to offset the fluctuations and inflation of gas and electric energy costs. A residential solar water heating system normally consists of the solar collector, the tank used to store the generated hot water, and other components that might be used for auxiliary energy or automated control. In 2015, the energy consumption in the residential-commercial sector amounted to $67.0Mtoe$. Compared to 2014, this value is increased by 0.3% (see figure 3). Since 1980, the consumption of petroleum products has declined steadily in favor of gas and electricity. While, for renewable energies, their consumption has increased every year by 4% on average since 2006.

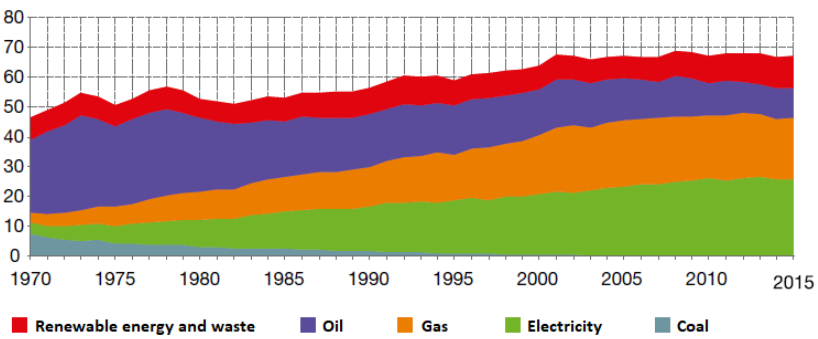

FIGURE 3 – The residential energy consumption in mtoe per type of energy in France [152].

For domestic usage, solar collectors are till now mostly for individual hot water distribution but collective distribution is gaining ground gradually in France (figure 4). The relative slow down of the rate of installation from 2012 may be inferred to the recent fiscal policy less encouraging direct investment in renewable energy than in the past decade. In such a competitive context, a need has developed to predict, as accurate as possible, the performance of solar thermal devices. With that prediction, the best collector can be chosen at most economic way.

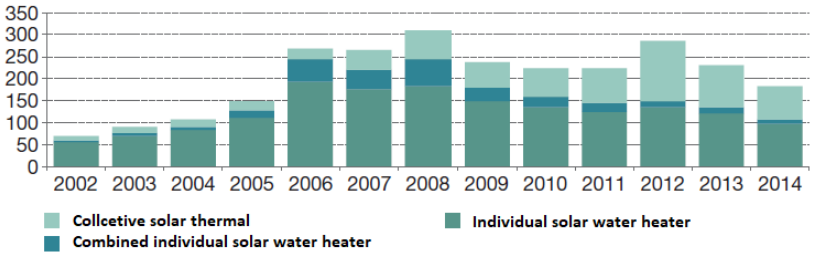

FIGURE 4 – The rate of installed surface in m^2 per year for each solar collector technology [152].

These solar thermal devices may contain either evacuated tubes or flat-plate collectors. Still the use of evacuated tube solar collectors remains modest compared with glass collectors. This due to its recent development of the former technology where research is in perpetual dynamics (figure 5).

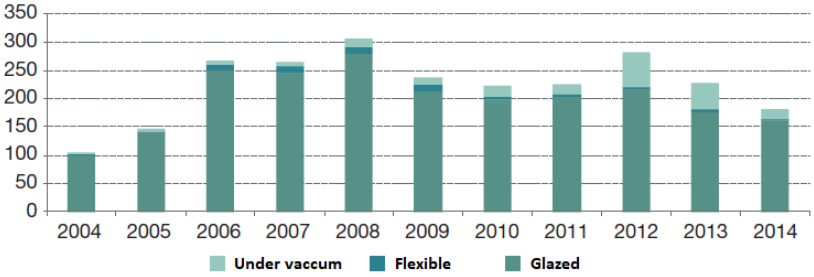

FIGURE 5 – The installed surface in m^2 per year for each collector technology [152].

2 Motivation and objectives

Despite the ubiquity of heat pipes and the large database that helps describing scientifically the phenomena occurring therein, there are still many areas in specific application

and manufacturing considerations which require further attention to get a deeper understanding of the involved phenomena and their impact on their functioning. The following work presents novel and additional effort to the common knowledge of screen mesh wick heat pipes used in solar collectors. The main purposes of the research are:
1. To model and simulate capillary wicked heat pipe using Lattice Boltzmann Method.
2. To compare the performance of heat pipes under different working conditions in order to sketch the device of best performance.
3. To study the performance of heat pipe used in solar collectors numerically, optimize computationally, and experimentally for different working conditions and configurations.

3 Manuscript overview/outline

The thesis manuscript is organized as follows:
- Chapter one presents an introduction of heat pipes: working principal, construction, types, operating limits and their application. Focusing on heat pipes in solar collectors, a detailed literature review is presented and discussed.
- Chapter two outlines the theory behind the lattice Boltzmann method: background, different approaches for Navier-stockes equation derivation, Boltzmann equation and boundary conditions implementation.
- Chapter three presents the detailed derivation of the axisymmetric lattice Boltzmann model and its validation. An enhanced derived model is then proposed.
- Chapter four describes the developed numerical model used to solve the proposed heat pipe configuration along with validations. Different test cases are studied to analyze the effect of various parameters (working fluid, porous medium, etc.).
- Chapter five presents the experimental setup built in this study, the design and construction of the heat pipe used, including a detailed description of the setup and the protocol followed. Then, the experimental results are analyzed and discussed where different heat pipe configurations used in solar collectors are compared under different working conditions.
- Chapter six concludes the manuscript and recall its main findings, ties the result of the study to theory and practice, and suggestions for improvement in future work.

Chapter 1

Generalities and state of the art

Abstract

This chapter presents a track of state of arts related to heat pipes: its working principal, types, limits and applications. A particular attention is given for heat pipes used in solar energy applications: their interest, design and applications. Finally, a literature review on heat pipes and their applications in solar collectors that would guide us throughout this thesis is discussed.

Résumé

Ce chapitre présente une généralité sur l'état de l'art lié aux caloducs: leur principe de fonctionnement, types, limites et applications. Nous mettons l'accent sur les caloducs utilisés dans les applications solaires: leur intérêt, conceptions et applications. Enfin, nous développons avec minutie une revue de la littérature sur les caloducs et leur application dans les collecteurs solaires qui nous guiderait le long de ces travaux de thèse.

1.1 Historical development and background of heat pipes

The development of heat pipes traces back to Jacob Perkins in 1836, who was the first to publish a patent on the concept of the Perkins tube [214]. This tube is basically a form of wickless gravity-assisted thermosyphon. The design, as shown in figure 1.1, was a closed tube containing a small quantity of water operating in either a single or two-phase cycle to transfer heat from a furnace to a boiler. A heat source placed at the bottom of the tube coil causes boiling of water in the closed loop. The resulting vapor generated in the tube moves upward due to buoyancy. When coming in contact with cooler walls, the vapor condenses, and the liquid falls down the coil of the pipe back to the furnace, where it evaporates again. Because there is no wick structure in the system, it can operate only when the boiler is placed above the furnace. The thermosyphon concept remained unchanged for about 50 years. Therefore, the Perkins tube became an essential part of the history of the heat pipe. Through trial and error, Perkins found that the ideal volume of water in the tube was 32%. Any more than that resulted in the tube being completely filled with water and blocking the vapor flow. Any less than that resulted in complete vaporization, dry out, and overheating. In the development of the Perkins tube, the most interesting improvements were made by L. P. Perkins and W. E. Buck [69]. Their work focused on the study of the fluid inventory. While water was the only specific working fluid, they tested the use of anti-freeze type fluids, and fluids having higher boiling temperature at atmospheric pressure than water.

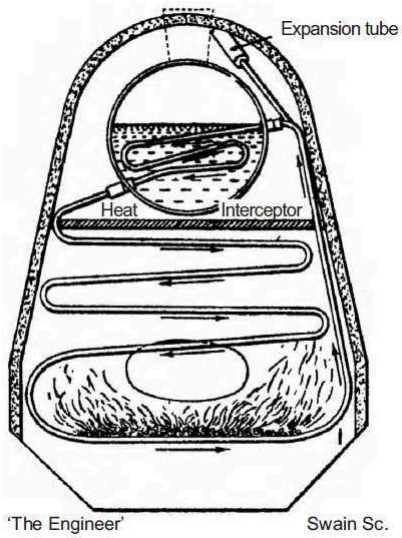

FIGURE 1.1 – Drawing of Perkin's boiler [229].

It was in 1944 when the concept of the capillary-based heat pipes was first put forward was suggested by R. S. Gaugler, who was working on refrigeration problems at that

time, in General Motors. He patented a lightweight, heat transfer instrument which was supposedly applied to a refrigeration system [74]. His device consisted of a closed tube in which the liquid receives heat at one location causing the liquid to evaporate. The vapor travels down the length of the tube where it condenses and releases its latent heat. The liquid phase travels back up the tube by capillary pressure to start the process over. In order to move the liquid back up to a higher point, Gaugler suggested using a capillary structure consisting of a sintered iron wick to make the inner fluid return back to the evaporator, instead of gravity. However, it was not developed beyond the patent stage, as other technologies currently available at that time were applied to solve the particular thermal problem at General Motors Corporation. But throughout that period there was no great need for such a device, so the development made no serious impact for about twenty years. The 1960's brought noticeable heat pipe developments. It was reinvented during 1963 when G. M. Grover and his co-workers, from Los Alamos Scientific Laboratory, designed a device and coined the name "heat pipe" (HP). In the words of Grover [86] "a heat pipe is a synergistic engineering structure which is equivalent to a material having thermal conductivity greatly exceeding that of any known metal". In other words, a heat pipe is a passive two-phase heat transfer device able to transferring large quantities of heat with minimum temperature drop. He is often referred to as the inventor of a heat pipe. Later, he [85] built several prototypes of heat pipe, the first of which used water as working fluid and was soon followed by a sodium heat pipe which operated at higher temperature (1100 K) using wire mesh wick structures. Since that time, interest in the heat pipe concept developed rapidly both for space and terrestrial applications. In 1964, RCA was the first commercial organization to perform heat pipe research RCA® [127]. Work was carried out on many working fluids including metals, water, cesium, sodium, lithium, and bismuth using glass, copper, nickel, stainless steel, molybdenum and TZM molybdenum as heat pipe wall materials. At the same time the theory of the heat pipe became better understood; the most important contribution to this theoretical understanding was due to Cotter in 1965 [48]. Throughout 1969, NASA, which played an important role in heat pipe development in the 1960s particularly regarding applications and reliability in space flight, showed interest in using heat pipes to control spacecraft components temperature. Since heat pipes can operate in micro-gravitational fields due to capillary action without any external force field or pumping, most early efforts were directed toward space applications. The early development of terrestrial applications of heat pipes proceeded at a slow pace. However, due to the high cost of energy, especially in Japan and Europe, the industrial community began to appreciate the significance of heat pipes and thermosyphons in energy savings as well as design improvements in various applications. Through time, heat pipes progressed and modern applications of this technology range today from miniature heat pipes for cooling processors inside laptop computers, to groups of one centimeter diameter and two meters long pipes used in NASA spacecraft and pipes of five centimeter diameters (or more) which are used to cool injection molds used in plastic forming. The lengths of the pipes can vary from some centimeters to eight meters or even more.

1.2 Heat pipe working principal

A heat pipe is a very simple device that transfers heat from one location to another, using the latent heat of vaporization. Heat pipes are referred to as the "superconductors" of heat owing to their important transfer capability with minimal heat loss over large distances with minimal temperature drops, exceptional flexibility, simple construction and easy control all without a need for external pumping power. Such a device consists of a closed container, a wick structure lined on the inner surface and a small amount of working fluid in equilibrium with its own vapor.

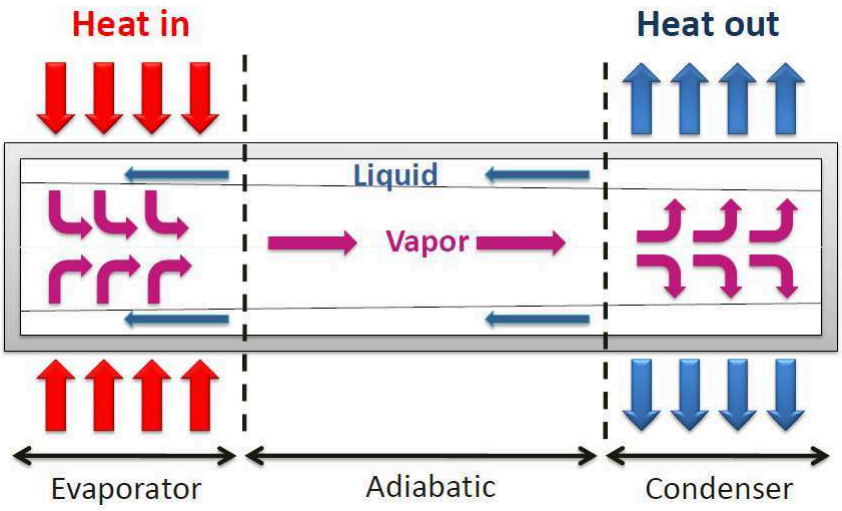

FIGURE 1.2 – Heat pipe schematic description.

It has three main sections as shown in figure 1.2; the evaporator, the adiabatic and the condenser sections. When heat is applied at the evaporator section of the heat pipe, the liquid temperature locally raises leading to the evaporation of the working fluid. Because of the saturation conditions this temperature difference results in a difference in vapor pressure, drives the vapor through the adiabatic section to the condenser, where the vapor condenses, releasing its latent heat of vaporization to the provided heat sink. The rate of vaporization is proportional to the heat absorbed in its latent form. The resulting condensate is pumped back to the evaporator of the container thanks to the capillary forces occurring along the menisci contained in the wick lining inside the pipe. The pumping can also be done by gravitation, in gravity-assisted heat pipes (thermosyphon). This process will continue as long as there is a sufficient capillary pressure to drive the condensate back to the evaporator. Therefore, as long as liquid is driven back to the evaporator, the heat pipe can continuously transport heat from the evaporator to the condenser section. Situations for which a heat pipe can no longer fulfill this transport are explained in section 1.7.

1.3 Heat pipe construction

In its conventional design, a heat pipe consists of a sealed tube that is partially filled with a working fluid. A wick, saturated with a working fluid, lines the inner side of the tube. In general, the performance of a heat pipe depends on several factors, such as its geometry, working fluid, capillary structure material, operating temperature, and applied heat flux and heat flux density. In the selection of a suitable combination of the above, inevitably a number of conflicting factors may arise. The chief bases for selection are discussed below.

1.3.1 Container materials

The issue of material compatibility and the results of life tests on heat pipes and thermosyphons remain critical aspects of heat pipe design and manufacturing. In particular, the generation of non-condensable gases that adversely affect the performance of heat pipes in either short or long term must be taken particularly seriously into account in the emerging technology of micro heat pipes and arrays of such devices. In fact, the heat pipe material must be chemically inert with the working fluid. Any chemical reaction will result in a by-product of non-condensible gas. A non-condensible gas is a gas, different from the working fluid vapor, that is not easily condensed by cooling. It consists mostly of nitrogen, light hydrocarbons, carbon dioxide, or other gaseous materials. So, the gases will collect in the condenser end of the heat pipe, swept thereby the following vapor, and obstruct a portion of the available heat dissipation area.

1.3.2 Working fluids

Since heat pipes utilize the phase change of the working fluid to transport heat, the selection of the working fluid is of paramount importance for enhancing their thermal performance.
A first consideration in the identification of a suitable working fluid is the operating vapor temperature range where a selection of fluids is shown in table 1.1. Within the approximate temperature range several possible working fluids may exist, and a variety of characteristics must be examined in order to determine the most acceptable among them for the considered application. Before starting heat pipe manufacturing, it is important to verify firstly if the desired working fluid is compatible or not with the suggested wick materials. Here we present some typical heat pipe working fluids and their compatibility with the wick material found in literature [229].

Hence, the prime requirements are: compatibility with wick and wall materials as many of the problems associated with long-life heat pipe operation are a direct consequence of material incompatibility; good thermal stability: the possibility of thermal degradation

Working fluid	Boiling point at atmospheric pressure (°C)	Operation range (°C)
Helium	-261	-271 to -269
Nitrogen	-196	-203 to -160
Ammonia	-33	-60 to 100
Pentane	28	-20 to 120
Acetone	57	0 to 120
Methanol	64	10 to 130
Ethanol	78	0 to 130
Water	100	30 to 200
Mercury	361	250 to 650
Potassium	774	500 to 1000
Sodium	1154	600 to 1200
Lithium	1340	1000 to 1800
Silver	2212	1800 to 2300

TABLE 1.1 – Heat pipe main working fluids [229].

with certain organic fluids the fluid breaking down into different compounds; high thermal conductivity; low liquid and vapor viscosity; high surface tension: which enable the heat pipe to operate against gravity and to generate a high capillary driving force; wettability of wick and wall materials: the contact angle must be zero or very small with an acceptable freezing point [229]. All of the above criteria could be resumed through the figure of merit, Me, which is used as the thermal performance index of a certain working fluid for heat pipes. It is defined as:

$$Me = \frac{\rho_l h_{lv} \sigma}{\mu_l} \tag{1.1}$$

The selection of the working fluid must also be based on thermodynamic considerations which are concerned with the various limitations to heat flow occurring within the heat pipe. These will be discussed in section 1.7.
The above mentioned requirements are not the only criteria for the selection of the working fluid. Other factors may, in a particular situation, be of greater importance. At slightly lower temperatures, 270-350 K, ammonia is a desirable fluid, although it requires careful handling to retain high purity. Acetone and alcohols are alternatives solutions having lower vapor pressures. These fluids are commonly used in heat pipes for space applications. Water and methanol, both being compatible with copper, are often used in cooling electronic equipment.

The working fluids used in heat pipes have remained essentially the same, with the exception of the addition of nanoparticles. A great deal of research has been conducted on the use of nanofluids in wide range of heat pipe applications. Recently, Do *et al.* [54] mentioned that the formation of thin coating at the screen mesh wick of the evaporator is the principal reason for the enhancement of thermal performance of the heat pipes using nanofluids and it is not, as thought before, due to their equivalent thermophysical properties. Moreover, Yang *et al.* [304] and Kim *et al.* [142] indicated that the coating layer formed by nanoparticles improves the surface wettability by reducing the contact

Working fluid	Recommended	Not recommended
Ammonia	Aluminum Carbon steel Nickel Stainless steel	Copper
Acetone	Copper Silica Aluminum Stainless steel	
Methanol	Copper Silica Stainless steel	Aluminum
Water	Copper Monel 347 Stainless steel	Aluminum Silica Stainless steel Nickel Carbon steel
Potassium, Sodium	Stainless steel Inconel	Titanium

TABLE 1.2 – Working fluids and their compatibility with heat pipe wick material.

angle and increasing the surface roughness, which in turn acts to increase the critical heat flux. Also, the coating layer induces liquid suction due to capillary wicking, which enhances the maximum heat flux [272]. Nevertheless, when life tests have to be higher than 10 years, some working fluids seem to lose their attractiveness. This may be dictated by health and safety considerations or by environmental pressures (for example in some countries in Europe the use of hydrofluorocarbons is being phased out in favor of fluids that contribute less to global warming).

1.3.3 Wick structure

As a first approach, the thermal performance of a heat pipe can be characterized by both its overall thermal resistance and its maximum power in horizontal and vertical positions. These characteristics depend mainly on the capillary structure, which is usually made of grooves, meshes, sintered powder or a combination of them as shown in figure 1.3.

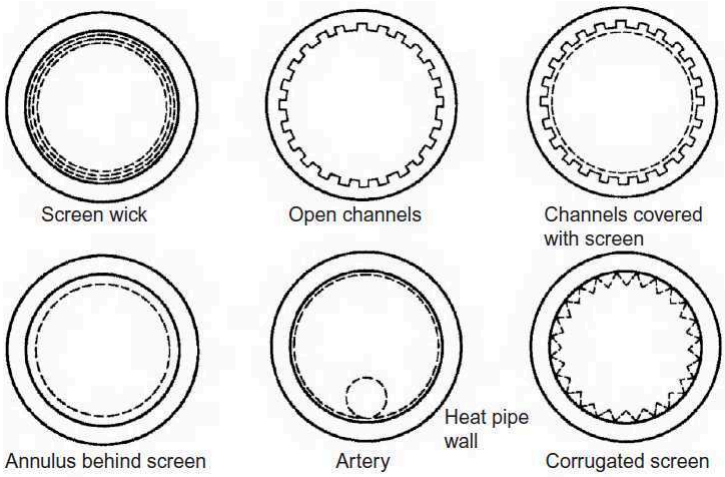

FIGURE 1.3 – Different wick structures used in heat pipes [229].

The wick structure inside the heat pipe works as a capillary pump, moving the liquid from the condenser to the evaporator through the adiabatic section. Besides the working fluid, the heat pipe geometry and material, it is one of the most important elements determining the performance of the heat pipe. To work effectively and efficiently, the wick structure must fulfill two requirements: sufficient capillary pressure and sufficient permeability. These two factors need special attention because the small pore structure creates large capillary pressure, whereas permeability requires large pores [53]. The capillary flow inside the wick structure is also determined by the contact angle between the liquid and the wick structure, known as the wettability, as stated by Shirazy *et al.* [258], where capillarity occurs due to the attractive force between liquid molecules and solid molecules, forcing the liquid to flow through the porous media. The material of the wick structure may be metalic, composite, ceramic, etc. But it is difficult to obtain both high capillarity and high permeability from a single type wick structure with single pore properties (pore size or shape). Thus, it is necessary to investigate a "mixed" wick structure. Good compromise between high capillary pressure and high permeability is found in some special wicks. One example is the biporous structure, which has two separate and distinct pore sizes in it. It includes two types of wicks: the first is made of large rough particles with small pores on the surface, and the second, which is called bidisperse wick structure, is made of clusters of small particles. A biomaterial such as coral is a material with a porous structure made of calcium carbonate deposits produced by stony corals from the animal realm. There are many types of coral, including branching, massive and tabulate corals. This biomaterial has relatively homogeneous pores, which are small in diameter. As a result of these small homogeneous pores, biomaterials have good capillarity. Biomaterials are also non-metallic with a tendency to oxidation significantly reduced.

It is worth to mention that the wick structure must be compatible with the chosen working fluid. More details are given in Appendix 1.2.

1.3.4 Charge filling

In the case of capillary pumped heat pipes, the liquid is supposed to fill in exactly the capillary structure. But, the volume of the liquid varies as a function of the average operating temperature. A capillary structure saturated with liquid, without any liquid out of structure, is therefore not possible for all transferable powers with a given operating temperature. The consequences of this phenomenon are different depending on the operating conditions. For a heat pipe in horizontal position, it is possible to provide an optimum filling for the lowest operating temperature. Indeed, when the temperature increase, the fluid expands and an excess of liquid appears at the end of the condenser. This excess can only appear at the condenser since the porous medium is the only element liquid mixture outside the condensation zone. So the only consequence is a slight plug of liquid at the end of the condenser causing a very small decrease in performance. This can be compensated simply by a slight oversize of the length of the condenser. When the heat pipe is subjected to volume forces, the zone of accumulation of the liquid excess is a function of these volume forces. However, it can be noted that the effects are weak if the heat pipe capillary pumping forces are greater than the volumetric forces. Indeed, in this case the local differences in liquid filling of the capillary structure are small. Volume forces can also lead to angular dissymmetry in exchange coefficients when a radial component exists and is not completely balanced by the capillary forces. As a result, tests of heat pipes in terrestrial environment should be analyzed with particular attention.

1.4 The physics of heat pipes

At specific pressure conditions, two mechanisms occur. The first mechanism is that, at a certain specific temperature, the liquid vaporizes. The resulted vapor can only be condensed when the temperature reaches the saturation conditions. The second mechanism is that the amount of absorbed heat at the evaporator section is equal to the amount of heat rejected at the section of the condenser in steady state.

1.4.1 Fluid phases bulk flow

Since heat pipes need to work with the circulation of a fluid in a closed loop, knowing the main characteristics of the flows in the vapor and liquid phases represent a key element to understand their global behavior. Detailed studies have been carried out in order to define the most important parameters governing such flows. Due to its complexity, the details of mass and momentum equations are needed not only for vapor but also for the liquid in the porous medium. In addition, the equations of energy conservation with the phase change must be solved too. No analytical solution is available in general, numerical resolution remains the last resort although often being out of reach even for the present computers performance. Accordingly, the issue is to simplify as much as possible while

keeping good model approximation of the actual mechanisms. The problem as a whole is usually addressed by artificially uncoupling the vapor and liquid domains.
Experimental validation is very difficult because the measurements inside the heat pipes are extremely complex. The majority of the studies carried out are numerical and are subjected to quite restrictive conditions [110, 235, 319].

Vapor flow

The flow in the vapor phase can be separated into three distinct zones corresponding to the evaporator, the adiabatic and the condenser zone. On the evaporator, the vapor mass flow rate increases along the evaporator axis due to the introduction of vapor resulting from liquid vaporization while the opposite phenomenon occurs at the condenser. The adiabatic region is, ideally, only the location of pressure drops due to flow circulation. Vapor pressure variations are the result of two distinct mechanisms. Firstly, the friction causes pressure drop in the overall flow. Secondly, in the evaporation zone at the interface, the vapor has a mean velocity almost orthogonal to the axial flow. The longitudinal motion of the fluid flow must therefore be achieved by a pressure variation.

Liquid flow

Whether the flow in the liquid phase is subjected to the same stresses as the vapor phase along their common interface, the consequences are very different. The large ratio of the liquid-vapor densities results in a reversal of the relative importance of the variations in inertial pressure and the effect of the volume forces. Indeed, since the velocity of the liquid flow is very low, the inertial pressure variations are totally negligible, whereas the effect of the forces of volume becomes dominant. Friction plays an important role in the fluid circulation, in particular, for heat pipes with capillary pumping.

1.4.2 Liquid/vapor interface

Description of the liquid/vapor interface

While the structure of solids surfaces and insoluble films is fairly well established [45], the structure of liquid surfaces in contact with its own saturated vapor remains somewhat obscure until now due to the complexity of the phenomena involved [156]. During the last decades, many research works were focused on the understanding of the transfer processes occurring in liquid/vapor interface [21, 222, 295]. The microscopic theories provide a description based on the first principle. They are dealing, however, with complicated mathematical formalisms and it is not possible until now to translate their exact results into useful macroscopic language [295]. In contrast, the methods of nonequilibrium ther-

modynamics and hydrodynamics are easier to handle and seem to be more appropriate to describe the problem [18]. The Gibbs theory of surface tension assumes uniform proprieties of the liquid up to the vapor phase on the other hand the theory of van der Waals involves the assumption of a continuous transition from liquid to vapor. Neither of the theories allows for an evaluation of the thickness of the transitional region except by the introduction of an arbitrary potential function. The conflict between the theory of van der Waals, which maintains the presence of a non-uniform capillary layer, and the experimental evidence may be more apparent than real.

The capillarity and surface tension

Molecules in a liquid appeal each other. A molecule in a liquid is attracted by the surrounding molecules and, on average, a molecule in the bulk of the fluid experiences no net force. In the case of a molecule at or near the surface of a liquid, the forces of attraction will no longer balance out and the molecule will experience a resultant inward force. Because of this effect the liquid will tend to take up a shape having minimum surface area; in the case of a free falling drop in a vacuum this would be a sphere. Due to this spontaneous tendency to contract, the liquid surface behaves rather like a rubber membrane under tension. In order to increase the surface area work must be done on the liquid. The energy associated with this work is known as the free surface energy, and the corresponding free surface energy per unit surface area is called surface tension and is given the symbol σ_l. Hence, the Laplace-Young equation could be introduced by:

$$\Delta p = \frac{\sigma}{R} \tag{1.2}$$

where Δp is the Laplace pressure and R is the principal radius of curvature.
The surface tension is numerically equal to the surface energy per unit area measured in any consistent set of units, e.g. N/m. Since latent heat of vaporisation, L, is a measure of the forces of attraction between the molecules of a liquid, we might expect surface energy or surface tension σ_l to be related to L. This is found to be the case. Solids also will have a free surface energy, which magnitude is found to be similar to the value for the same material in the molten state. When a liquid is in contact with a solid surface, molecules in the liquid adjacent to the solid will experience forces from the molecules of the solid in addition to the forces from other liquid molecules. Depending on whether these solid/liquid forces are attractive or repulsive the liquid-solid surface will curve inward or outward. The two best-known examples of attractive and repulsive forces are water and mercury, respectively on copper. Where the forces are attractive the liquid is said to 'wet' the solid. The angle of contact made by the liquid surface with the solid is known as the contact angle, θ. For wetting liquids, θ lies between 0° and 90° and for non-wetting liquids, $\theta > 90°$. The condition for wetting to occur is that the total surface energy is reduced by wetting:

$$\sigma_{sl} + \sigma_{lv} < \sigma_{sv} \tag{1.3}$$

where the subscripts, s, l and v refer to solid, liquid and vapor phases, respectively. Wetting will not occur if $\sigma_{sl} + \sigma_{lv} > \sigma_{sv}$ while the intermediate condition of partial

wetting is $\sigma_{sl} + \sigma_{lv} = \sigma_{sv}$.

1.5 Heat pipe applications

Since the first basic heat pipe concept was proposed by Gaugler (1944), heat pipes have been widely applied to a variety of both simple and complex designs for space and terrestrial applications.

1.5.1 Terrestrial applications

Currently the greatest use of heat pipes is in the cooling of computers and electronic components [183]. The utilization of heat pipes and vapor chamber to spread and transfer heat was a key factor for extending the air cooling limit capability for high performance computers. The main thermal solutions based on heat pipes are the vapor chamber, miniature and micro heat pipes with micro axial grooves, remote heat exchangers and hybrid systems. Because of its small dimensions, some difficulties, in manufacturing, degassing and charging, are expected.

Recently, researches have been reported where developments of high interest in heat pipe technology for heat recovery were made [181, 257]. Studies have analyzed the application of heat pipes on the thermal performance of heat recovery systems. In air-air conditioning facilities consisting of two CHPs and indirect evaporative systems, applying the mixed-energy recovery system makes possible a recovery form the return airflow. This improves significantly the energy efficiency and reduces the environmental impact [59, 173, 202, 305].

The demand for using heat pipes in renewable energy systems along with building heat recovery, highlighting novel concepts and requirements, is increasing. Several terrestrial applications make use of heat pipes in heat exchangers for higher heat transfer rates. Consequently, heat pipes have been expansively used in various energy storage systems due to their passive operation and suitability for heat delivery [31]. The unique method of operation of heat pipes including phase-change materials (PCMs) provide a better efficiency pattern over conventional heat exchangers in major operation conditions including temperature stratification in hot water storage tanks. However, in the case where the working fluid passes through the PCM storage tank, extending the piping length inside the tank causes a large pressure drop of the working fluid and a large decrease in the effective PCM storage volume for conventional latent heat thermal energy storage. Integrating HPs into the system can overcome this problem. Other widespread commercial use of heat pipes is integrating them into solar collectors in order to transfer both the direct and diffuse solar radiation to the water stream. One of the most common uses for heat pipes associated with storage is to absorb solar energy and transfer it to water, either

static or forced flowing.

More recently, researches have been undertaken using thermosyphons to remove heat from solar photovoltaic cells. As well as cooling the cells, the recovered heat may be used for domestic water heating, for example.

1.5.2 Space applications

Heat pipes have been widely used for various space applications, e.g. satellites [266], space stations [301], space probes, etc. The objects operating in space have to work in very harsh thermal environment. So, satellites and other objects working in space encounter many thermal problems for which HPs offer solutions. Autonomous operation without mechanical moving body makes it easy to reach the required reliability specifications. In addition, spacecraft systems require heat rejection systems which remove quantities of heat in the order of 10 to 100 times as much as present single-phase systems do. Another special type of heat pipes has been proposed and extensively tested for this purpose: CPL, PHP, LHP [170, 294]. Low weight penalty, no maintenance and reliability have made heat pipes very attractive components in the area of spacecraft cooling and temperature stabilization. Structural isothermalization is an important issue as regards orbiting astronomy experiments due to the possible warping from solar heating. Heat pipes are also being used to dissipate heat generated by electronic components in satellites.

1.6 Types of heat pipes

All heat pipes have an evaporator and condenser sections where the working fluid evaporates and condenses, respectively. Many heat pipes also have a transport or adiabatic section, which separates the evaporator and condenser sections by an appropriate distance in order to satisfy the heat pipe limitations and/or the design constraints of the application. A given heat pipe may have multiple evaporators, condensers, and adiabatic sections. The working fluid is usually circulated by capillary forces in a wick. However, gravitational, centrifugal, electrostatic, and osmotic forces can also be used to return the liquid from the condenser to the evaporator. Besides the capillary heat pipes, there are many heat pipe configurations that have been built for different applications as discussed earlier in section 1.5. These are presented in the following sections.

1.6.1 Thermosyphon (gravity-driven heat pipes)

The two-phase thermosyphon is thermodynamically similar to the wicked heat pipe but relies on gravity to ensure liquid return from the condenser to the evaporator. The sonic and vapor pressure limits (which discussion is postponed) are constraints to the operation

of the thermosyphon, as with capillary-driven heat pipes. The entrainment limit is more critical in thermosyphons than in capillary-driven heat pipes due to the totally free liquid-vapor interface. A wick or wicks may be incorporated in at least parts of the unit to reduce entrainment and improve liquid distribution within the evaporator. The capillary limit is generally of no concern in the operation of the thermosyphon due to the fact that gravity is the major driving force for condensate return. The counterpart of the entrainment limit in thermosyphons is called flooding, which is the most severe limitation in the operation of these systems. A sudden oscillating wall temperature and vapor pressure rise will occur at the flooding limit. The boiling limit in thermosyphons is due to film boiling, rather than nucleate boiling as in capillary-driven heat pipes. It occurs when a vapor film forms between the pipe wall and the liquid in the evaporator section of the heat pipe. For small liquid fill volumes, the dry-out limit may be reached, where all of the working fluid is held in the liquid film above the evaporator, and no liquid pool exists. In that case, any further increase in the input heat will cause a severe temperature increase at the bottom of the evaporator section. The operation of the thermosyphon is sensitive to the working fluid fill volume, the viscous limit and the Geyser boiling phenomena

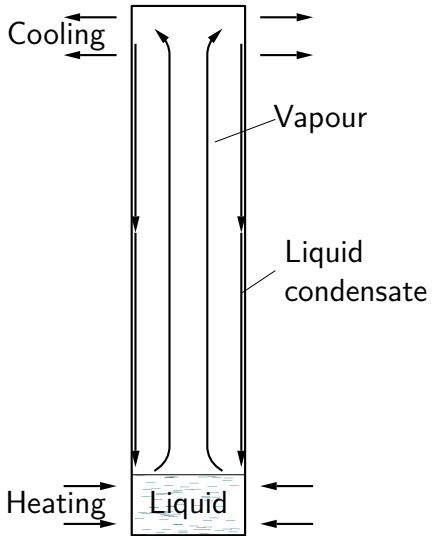

FIGURE 1.4 – Thermosyphon.

1.6.2 Pulsating heat pipes (PHP)

The PHP, as shown in figure 1.5, is made by a long capillary tube bent into many turns, with the evaporator and condenser sections located at these turns. There are two main types of PHPs: looped and unlooped, which are classified according to whether the two ends of the PHP connect. A PHP is usually partially charged with a working fluid,

with a filling ratio between 40% and 60%. Since the diameter of a PHP is small compared to the capillary length (less than 5 mm typically), vapor plugs and liquid slugs are formed as a result of capillarity dominance. Heat input either causes evaporation or boiling, which increases the pressure of the vapor plug in the heating section. Simultaneously, the pressure in the cooling section decreases due to condensation. This pressure difference pushes the liquid slug and vapor plug into the cooling section. The liquid slug and vapor plug in the cooling section are then pushed into the next heating section, which will push the liquid slug and vapor plug back to the cooling section. This process enables the self-excited oscillatory motion of liquid slugs and vapor plugs. Heat is transported from the heating section to the cooling section *via* the pulsation of the working fluid in the axial direction of the tube.

The unique feature of PHPs, compared to conventional heat pipes, is that there is no

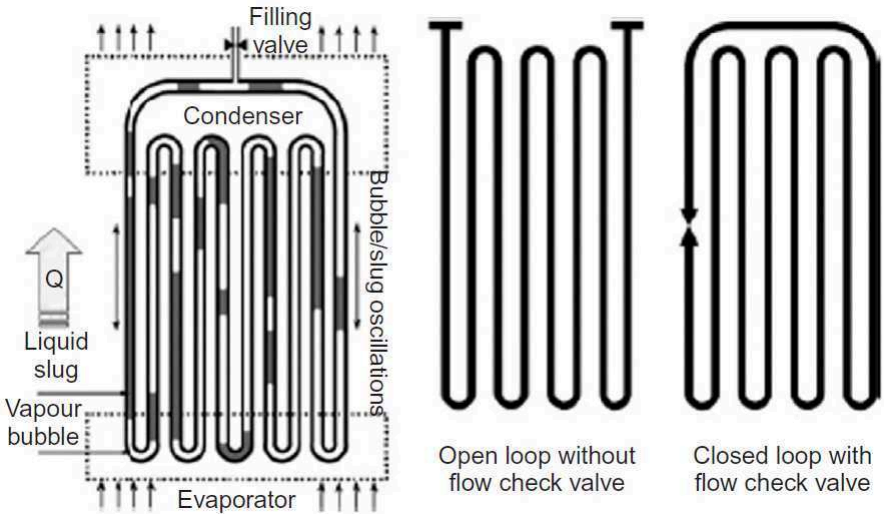

FIGURE 1.5 – Schematics of a pulsating heat pipe [229].

wick structure returning the condensate to the heating section. There is therefore no countercurrent flow between the liquid and vapor. The entrainment limit in the conventional heat pipe does not have any effect on the capacity of heat transport by a PHP. With this simple structure, the PHP weighs less than a conventional heat pipe, making it an ideal candidate for space applications. Since the diameter of the PHP is very small, surface tension plays a greater role in the dynamics of the PHP than gravitational force does, enabling successful operation in both terrestrial and microgravity environments. Other applications of PHPs include thermal control of electrical and electronic devices and components, as well as thyristors, diodes, and ceramic resistors.

1.6.3 Loop heat pipes (LHP)

The LHP was invented in Russia (formally USSR) in 1971 by Maydanik *et al.* [167] and is based on the same physical processes as those of conventional heat pipes. It consists

of a capillary pump (or evaporator), a compensation chamber (or reservoir), a condenser, and liquid and vapor lines. The wick structure is present only in the evaporator and compensation chamber. The high capillary force is created in the evaporator due to fine-pored wicks (primary wicks), such as sintered nickel, titanium, and copper powder with an effective pore radius of 0.7-15 μm and a porosity of 55-75%. The compensation chamber is an important component in the LHP and is often integrated to the evaporator. The purpose of the compensation chamber is to accommodate excess liquid in an LHP during normal operation. A secondary wick (usually made of larger pores) physically connects the evaporator to the compensation chamber in order to supply the primary wick with liquid, particularly when the compensation chamber is below the evaporator, or when the LHP is operating in microgravity conditions. The vapor motion and liquid flow in the primary wick proceed mainly in a radial direction. The evaporator menisci are inverted down toward the wall being heated.

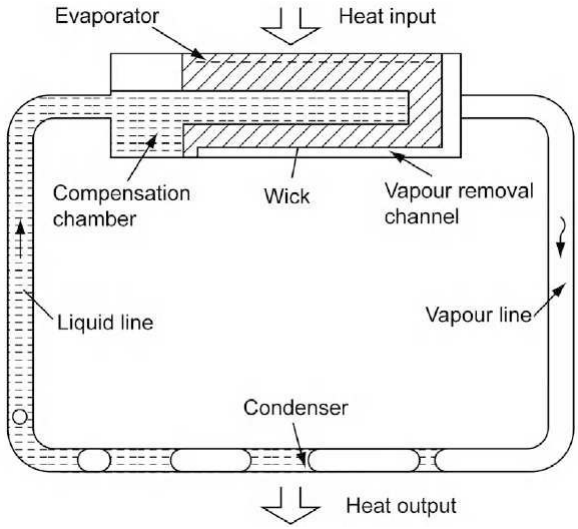

FIGURE 1.6 – Schematics of loop heat pipes [229].

1.6.4 Capillary Pumped Loop (CPL)

The CPL was first proposed by Stenger [270] at NASA Lewis Research Center. Heat is applied to the evaporator component, which consists of a hollow rod of wick material capped at one end and force fitted into an internally axially grooved pipe. The heat applied to the outer surface of the evaporator vaporizes the liquid phase of the working fluid. The vapor thus generated travels then down the length of the axially grooved vapor channel into the vapor header. The vapor travels up to the condenser, where it condenses: first as a liquid film on the inner wall of the pipe, and then as a liquid slug flow. Before reaching the evaporator, the liquid passes through a subcooler to collapse any remaining vapor bubbles and to provide additional subcooling if necessary. The capillary pressure

generated in the wick structure continuously pumps the working fluid through the cycle. A two-phase reservoir is provided to control both the working fluid filling ratio through the cycle and the working temperature of the system. This process is similar to the one found in the variable conductance heat pipe. For multiple-evaporator systems, isolators are provided to prevent any evaporator from depriving the other evaporators. Despite the wide use of the CPL and LHP in space technology, fundamental confusion still exists regarding their similarities and distinctions in operation, as well as their limitations as mentioned by Ku *et al.* [167].

1.6.5 Miniature and micro heat pipes (MHP)

The fisrt MHP was proposed by Cotter [50] designed for the cooling of electronic devices. The micro heat pipe was defined as a heat pipe in which the mean curvature of the liquid-vapor interface is comparable in magnitude to the reciprocal of the hydraulic radius of the total flow channel. Typically, micro heat pipes have convex but cusped cross sections, with a hydraulic diameter in range of $10 - 500$ μm, while a miniature heat pipe is defined as a heat pipe with a hydraulic diameter in the range of 0.5 to 5 mm. It is also worth noting the other structural differences between micro and miniature heat pipes in addition to the size ranges given above. A *true* micro heat pipe, for both metallic and silicon applications, has a single noncircular channel for both liquid and vapor phases, where the liquid returns from the condenser to the evaporator by capillarity occuring in the sharp corner of the channel. These types of micro heat pipes are generally placed in an array of parallel micro heat pipes on the substrate surface in order to increase the overall heat transfer area. Miniature heat pipes can be designed based on micro axially grooved structure (one-dimensional capillary structure), meshes or cross grooves (two-dimensional capillary structure).

1.6.6 Vapor chamber

The vapor chamber is a capillary driven planar design (flat-plate heat pipe in a rectangular or disk-shaped) with a small aspect ratio. Additional wick blocks between the evaporator and the condenser help the condensate flowing back, especially when the condenser is below the evaporator in terrestrial applications. If the condenser is above the evaporator, there is no need to consider a wick in the condenser section, since the condensate on the upper plate will flows back to the evaporator naturally in this case. A wick is needed over the evaporator section, however, in order to uniformly distribute the liquid over the entire surface so to prevent dryout. Vapor chambers are preferred over CHPs for electronic cooling with heat fluxes higher than 50 W.cm^{-2} since heat flow is two or three-dimensional. Furthermore, vapor chambers can be placed in direct contact with CPUs using thermal interface materials, thereby reducing the overall thermal resistance of the heat sinks.

1.7 Heat pipe cycle and operating limits

The operating limits for a wicked heat pipe, first described in Ref. [48], are illustrated in figure 1.7. Each of these limits may be considered a side. In order to operate, the maximum capillary pumping pressure, $\Delta P_{c,max}$ must be greater than the total pressure drop in the pipe. This pressure drop is made up of three components:

— The viscous pressure drop, ΔP_l, generated when the liquid is driven from the condenser to the evaporator;
— The viscous pressure drop, ΔP_v, generated when the vapor flows from the evaporator back to the condenser;
— The pressure due to the gravitational head, ΔP_g which may be zero, positive or negative, depending on the inclination of the heat pipe.

For correct operation, the following necessary condition must be met:

$$\Delta P_{c,max} \geq \Delta P_l + \Delta P_v + \Delta P_g \tag{1.4}$$

In the above relation, the pressure drop due to the liquid-vapor interfacial friction was neglected. If not, the wick will dry out in the evaporator region and the heat pipe will not operate. The maximum allowable heat flux for which inequality (1.4) holds is referred to as the capillary limit.

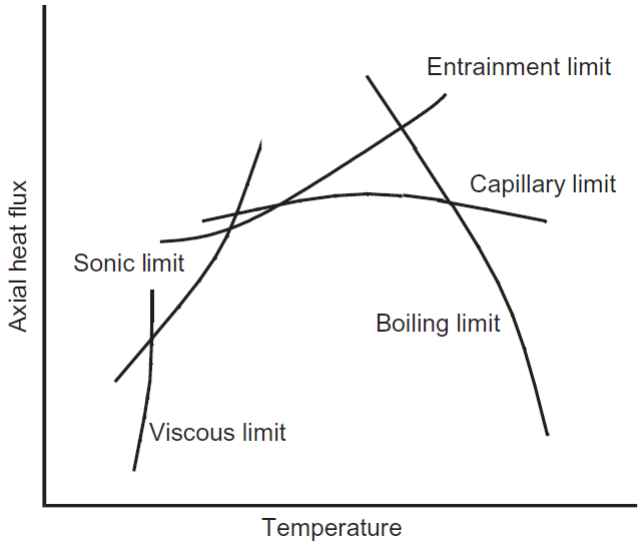

FIGURE 1.7 – Heat pipe limits [229].

The position of the curves and shape of the operating envelop shown in figure 1.7 depend upon the wick material, working fluid and geometry of the heat pipe. This graph presents the maximum power in terms of the operating temperature. Usually, the so-called operating temperature is defined as the mean temperature of the vapor in the adiabatic region. For heat pipes without adiabatic zone, the operating temperature is usually taken in the section separating the evaporator and the condenser regions. It represents a

	Temperature range (K)	Working fluids
Cryogenic temperatures	0 to 200	Hydrogen, nitrogen
Low temperatures	200 to 550	Ammonia, methanol, water
Intermediate temperatures	550 to 700	Mercury
High temperatures	750 to 2600	Silver, sodium

TABLE 1.3 – Classification of heat transfer fluids temperature range [237].

combination of different functions related to the different limits. The definition of each is postponed.

The operating limits are closely related to the thermophysical properties of the working fluid. That is why it appears that for closer temperature of the extreme points (triple point and critical point) the performances are very poor because of the fluid proprieties degradation. At low temperatures, the saturating vapor pressure and the vapor density are low which results in a high vapor velocity for a given flow. In such case, limits linked exclusively to the flow of the vapor phase may be defined such as viscous and sonic limits. For higher temperatures, counter-current flows of liquid and vapor causes the entrainment limit. Depending on the type of heat pipe, the importance of this limit varies greatly.

Thus, the first design element of a heat pipe depends on to the maximum transferable flow and can be figured out from the operating limit curve in figure 1.7. For a given heat pipe under fixed conditions (Evaporator and condenser lengths, working fluids, etc.), this curve depends essentially on the operating temperature.

1.7.1 Temperature and operating range

The two temperatures, which contribute to defining the operating limits of a heat pipe, are as indicated previously the temperatures of triple and critical points. Indeed, below the temperature of the triple point the vapor condenses into a solid phase, and above the critical point there is only one phase whose high density varies continuously as a function of pressure and temperature.

Owing to this usable temperature range, the heat transfer fluids are commonly classified into four broad categories defining temperature ranges as shown in table 1.3.

1.7.2 Capillary limit

The capillary limit concerns heat pipes for which the driving pressure, allowing the condensate to return from the condenser to the evaporator, is mainly linked with capillary forces developed in the wick structure. Since the vapor flow from the evaporator to the

condenser is accompanied by a slight pressure drop. Similarly, the return of the liquid from it to the evaporator through the capillary structure is accompanied by a liquid pressure drop, too. So as longer as these pressure drops are compensated (see equation (1.4)) by the motive capillary pressure, the heat pipe can operate properly. Thus, the capillary limit is reached when the pumping effect of the capillary structure cannot overcome the pressure drops for a given working fluid, wick structure and heat input. This causes the heat pipe evaporator to dry out and shuts down the transfer of heat from the evaporator to the condenser with a sudden evaporator temperature increase. Thus, in order to keep up the operation of such a device, this limit is essential to be taken into account especially for heat pipes with capillary structure.

Because of the condensation process, the pressure jump between the liquid and the vapor phases is very weak at the condenser [143]. Hence, the interface curvature can be considered as infinity. As a result, the maximum capillary driven pressure is calculated by evaluating the maximum curvature of the liquid-vapor interface in the evaporation zone. Its expression depends on the type of capillary structure. Nevertheless, it is possible to express it simply by referring to the Laplace-Young equation:

$$\Delta P_{c,max} = \frac{2\sigma}{r_{eff}} \tag{1.5}$$

where σ is the surface tension and r_{eff} is the effective radius.
- Vapor pressure drop:
The vapor pressure drop corresponds mainly to the drops due to viscous friction. In order to express this pressure drop, we can consider the case of one-dimensional Poiseille flow as the capillary heat pipes involve laminar fluid flows, usually. Thus, we have [237]:

$$\Delta P_{v,vis} = \frac{8\mu_v Q L_{eff}}{\pi \rho_v R_v^4 h_{lv}} \tag{1.6}$$

where L_{eff} is the effective length defined as:

$$L_{eff} = L_a + \frac{1}{2}\left(L_e + L_c\right) \tag{1.7}$$

and L_e, L_a and L_c are the evaporator, adiabatic and condenser lengths, respectively. R_v is the vapor core radius, h_{lv} is the heat latent of vaporization, μ_v is the vapor kinematic viscosity and ρ_v is the vapor density.

In addition, the inertial pressure drops must be considered. Although the energy supplied to the vapor in order to accelerate in the evaporation zone should be returned to the condenser region, many studies have shown that the inertial recovery rate is about 50% only. As there is not, to our best knowledge, detailed study to solve the problem, we will adopt the result of Gourdache [79] and Faghri [66]. Inertial pressure losses are therefore expressed by:

$$\Delta P_{v,iner} = \left(1 - \frac{4}{\pi^2}\right) \frac{Q^2}{8\rho_v R_v^4 h_{lv}^2} \tag{1.8}$$

Thus, the total pressure drop in the vapor region is equal to:

$$\Delta P_v = \Delta P_{v,vis} + \Delta P_{v,iner} \tag{1.9}$$

- Fluid pressure drop:
The fluid pressure drop corresponds mainly to the drops due to viscous friction which can be defined using Darcy low. Thus, we have:

$$\Delta P_{l,vis} = \frac{\mu_l Q L_{eff}}{\rho_l S_p K h_{lv}} \tag{1.10}$$

where S_p is the wick section area, Q is the heat input which is equal to $Q = \dot{m}_l h_{lv}$, μ_l is the liquid kinematic viscosity, K is the permeability of the wick structure, ρ_l is the liquid density and $\dot{m}_l$ the mass flow rate.
-Gravitational pressure:
By taking into account the effect of gravity, we have:

$$\Delta P_g = \rho_l \sin\theta L_{tot} \tag{1.11}$$

where θ is the tilt angle with respect to the horizontal.
-Maximum heat flow:

Using the above expressions, and by neglecting the inertial effect (terms of Q^2 order), the maximum heat flux transmitted by a cylindrical heat pipe is given by [6, 34, 88, 237]:

$$Q_{c,max} = \frac{\frac{2\sigma}{r_{eff}} + \rho_l sin(\theta) L_{tot}}{\frac{\mu_l L_{eff}}{\rho_l S_p K h_{lv}} + \frac{8\mu_v L_{eff}}{\pi \rho_v R_v^4 h_{lv}}} \tag{1.12}$$

So, the capillary limit determines the maximum heat flux over much of the operating range; however, the designer must check that a heat pipe is not required to work outside the range defined by the other operating limits, either at design conditions or at start-up.

1.7.3 Viscous limit

The viscous or vapor pressure limit is generally most relevant at start-up. At low operating temperature, the vapor pressure of the fluid in the evaporator is very low. Since the condenser pressure cannot be less than zero, the difference in vapor pressure is insufficient to overcome viscous and gravitational forces. In this case, the pressure gradients will not be sufficient to generate vapor flow and the vapor will stagnate, thus preventing normal HP operation.
The viscous limit is calculated by considering an isothermal incompressible laminar flow of Poiseuille type. Reporting Bussel's work [23], under the assumption of isothermal flow, the viscous limit is expressed by:

$$Q_{vis} = \frac{\pi r_v^4 h_{lv}}{16 \mu_v L_{eff}} \left(1 - \left(\frac{P_L}{P_{v,0}}\right)^2\right) \rho_{v,0} P_{v,0} \tag{1.13}$$

where 0 refers to the position (z=0).
The expression can be written, when $\frac{P_L}{P_{v,0}} \to 0$, as:

$$Q_{vis} = \frac{\pi r_v^4 h_{lv}}{16 \mu_v L_{eff}} \rho_{v,0} P_{v,0} \tag{1.14}$$

Yet, this expression does not refer to the adiabatic temperature as it refers only to the conditions at both ends of the heat pipe ($z = 0$ and $z = L = L_{tot}$). In order to keep a coherence with the other limits, Romestant [237] redefined an equivalent expression of this limit by taking the conditions between the middle of the adiabatic zone ($z_1 = L_e + L_a/2$) and the end of the condenser ($z = L = L_{tot}$) in terms of thermodynamic conditions at reference and triple point T_{PT}. Under these conditions, the viscous limit can be expressed as::

$$Q_{vis} = \frac{\pi r_v^4 h_{lv,a}}{16 \mu_{v,TP} L_{eff}^{'}} \left(1 - \left(\frac{P_{TP}}{P_{v,a}}\right)^2\right) \rho_{v,a} P_{v,a} \tag{1.15}$$

where TP refers to the triple point, a refers to the adiabatic zone and $L_{eff}^{'}$ is equal to $L_{eff}^{'} = L_c + \frac{L_a}{2}$, when flow is homogeneous.

1.7.4 Boiling limit

The boiling limit, also called heat flux limit, is characterized by two separate phenomena: (1) bubble formation and (2) growth or collapse of bubbles in the evaporator liquid region. The bubble formation is governed by the size and number of nucleation sites on the solid surface and the difference between heat pipe wall temperature and working fluid temperature. The growth or collapse of bubbles formed on plane flat surface depends on liquid temperature and the pressure difference across the liquid-vapor interface caused by the vapor pressure and surface tension of the fluid. In the case of high radial heat flux in the evaporator section, causing excessively high temperature difference, the first stage of boiling is commonly called nucleate boiling and corresponds to the formation of very small diameter bubbles which may occur in the wick structure. This causes vapor to become trapped in the wick. As a consequence, liquid returning is prevented and results in evaporator dry-out. Opposite to the other limits, which depends on the axial heat flux or total thermal power transported by the heat pipe limitations, this phenomenon depends on the radial or circumferential heat flux applied to the evaporator region. In order to guarantee a normal heat pipe operation, one should avoid nucleate boiling phenomena at all costs. For circular heat pipes, the boiling limit is calculated based on Clausius-Clapeyron and Young-Laplace relations, and is given by the following expression [76, 237]:

$$Q_b = \frac{2\pi L_e \lambda_{eff} \Delta T_{crit}}{ln \frac{r_i}{rv}} \tag{1.16}$$

where

$$\Delta T_{crit} = T_b - T_v = \frac{2\sigma T_v}{h_{lv} \rho_v} \left(\frac{1}{R_b} - \frac{1}{R_{men}}\right) \tag{1.17}$$

and T_b and T_v are the heat pipe wall and vapor saturation temperatures at the evaporator section, L_e is the length of the evaporator section, λ_{eff} is the effective thermal conductivity of the wick, r_i and r_v are the inner radius of the pipe wall and the vapor space radius, R_b is the effective radius of the bubble and R_{men} is the radius of the liquid-vapor meniscus.

1.7.5 Sonic limit

During start-up of liquid-metal heat pipes or at low operation temperature, due to the very low vapor densities associated to this condition, the vapor velocity may reach sonic or supersonic values at a given condenser temperature which called choked condition. The sonic velocity sets a limit on the heat pipe performance.

For most heat pipes operating at room temperature or cryogenic temperatures, the sonic limit is typically not an issue, except in the case of very small vapor channel diameters. With the increased vapor velocities, inertial, or dynamic, pressure effects must be included. It is important to note that in cases where the inertial effects of the vapor flow are significant, the heat pipe may no longer operate in a nearly isothermal case, resulting in a significantly increased temperature gradient along the heat pipe. In cases of heat pipe operation where the inertial effects of the vapor flow must be included, an analogy between heat pipe operation and compressible flow in a converging-diverging nozzle can be made. In a converging-diverging nozzle, the mass flow rate is constant and the vapor velocity varies due to the varying cross-sectional area. However, in heat pipes, the area is typically constant and the vapor velocity varies due to mass excess (evaporation) and mass lack (condensation) along the heat pipe. As in nozzle flow, decreased outlet (back) pressure, or in the case of heat pipes, condenser temperatures, results in a decrease in the evaporator temperature until the sonic limit is reached. Any further increase in the heat rejection rate does not reduce the evaporator temperature or the maximum heat transfer capability but only reduces the condenser temperature due to the existence of choked flow. The sonic limitation actually serves as an upper bound to the axial heat transport capacity and does not necessarily result in dry-out of the evaporator wick or total heat pipe failure. Attempts to exceed the sonic limit result in increasing both the evaporator temperature and the axial temperature gradient along the heat pipe, thus reducing further the isothermal characteristics commonly found in the vapor flow region.

Busse [23] presented an alternative approach by making the following assumptions: (1) one-dimensional, laminar and isothermal fluid flow, (2) the vapor behaves as an ideal gas, (3) only inertial effects are present. Hence, the final expression of the sonic limit is given by [237] :

$$Q_{son} = 0.745 D_v^2 h_{lv,a} \rho_{v,a} \sqrt{\gamma r_g T_{v,a}} \tag{1.18}$$

where γ is the vapor specific capacity ratio (c_p/c_v).

1.7.6 Entrainment limit

In a heat pipe, the liquid and vapor flow are moving in an opposite direction. The interaction between the counter-current two phase flow results in viscous shear forces occurring at the liquid-vapor interface. This may prevent liquid return to the evaporator zone. In such a case, waves are formed and the pressure drop, linked with the interfacial shear forces, becomes greater than the capillary forces. This results in the detachment of liquid droplets entrained by the vapor flow and pushed back to the condenser region. Many approaches [144, 249] have been developed and compared in order to estimate the entrainment limit in heat pipes, especially thermosyphons, but failed to prove reliability for the majority of cases. However, an evaluation of this limit can be given by two separate formulations depending on the interface structuring. For capillary pumping heat pipes, this interface is strongly influenced by the capillary forces. The approaches are then based on the Weber number which compares the inertial pressure with the capillary pressure:

$$We = \frac{Inertial forces}{Capillary forces} = \frac{\rho_v \bar{U}_v^2}{\frac{\sigma}{r_{eff}}} \tag{1.19}$$

We will retain for the driven power the expression provided by Prenger and Kemme [221]:

$$Q_{ent} = \sqrt{\frac{2\pi}{K_\alpha}} \sqrt{\frac{\sigma \rho_v}{r_{eff}}} \frac{r_{eff}}{r^*_{eff}} A_v h_{lv} \tag{1.20}$$

where $K_\alpha = 1.234$ for a laminar flow on the vapor phase and r^*_{eff} is the maximum size of validity of this equation.
Beyond this, the authors consider that capillary forces are not prominent. We retain the expression advocated by Faghri [66]:

$$Q_{ent} = K_e A_v h_{lv} \left(g\sigma \left(\rho_l - \rho_v\right)\right)^{\frac{1}{4}} \left(\rho_v^{-\frac{1}{4}} + \rho_l^{-\frac{1}{4}}\right)^{-2} \tag{1.21}$$

where $K_e = \left(\frac{\rho_l}{\rho_v}\right)^{0.14} \mathrm{th}^2 Bo^{\frac{1}{4}}$ and $Bo = d_{int} \left[\frac{g(\rho_l - \rho_v)}{\sigma}\right]^{1/2}$ is the Bond number.

1.8 A focus on heat pipe application in solar thermal collectors

1.8.1 Main solar collectors design and their performance

In solar heating devices, collectors are the components that capture the incident radiation and transfer it into the fluid flow [12]. The resulted energy is either used directly as a hot water or accumulated in a storage tank [33]. Indeed, solar systems can be coupled to other devices in a large range of applications, *e.g.* cogeneration or solar cooking [147].

Depending on the range of the desired temperature, different configurations of collectors are used they can be classified as concentrating and non-concentrating types. Concentrating solar collector, called compound parabolic collectors (CPC), consists of two parabolas and one absorber [72, 210, 320]. Due to their high performance, these systems are able to heat fluids up to 250°C [234]. Hence, such systems are used primarily for large level water heating in industrial applications. By contrast, non-concentrating type consists of flat plate collector (FPC) and evacuated tube collectors (ETC). These systems are commonly used for water heating applications in domestic solar water heaters (SWH) [8]. For FPC, the operating temperature ranges roughly between 20 and 80°C [256] while for ETC it ranges between 50 and 200°C [132]. Three main ETC types exist: Heat-pipe ETCs, U-tube glass [313] and water-in glass, the latter being used more commonly in solar collectors for domestic water heating [260]. Challenges do exist in the effective capture and storage of solar energy as solar radiation is available only during daytime. The mostly used and produced solar collectors are the conventional FPCs due to their simple design and low maintenance cost. However, FPCs suffer from major drawbacks which are heat loss through glass cover from the collector plate itself and absence of sunshine tracking specially in windy and cold days. In fact, FPCs are used mainly in warm and sunny climates [131]. This drawbacks can be overcame using ETCs as the pipes are under vacuum conditions which reduces greatly heat losses [275]. Hence, they are effective even in cold and unfavorable weather and are able to provide higher outlet fluid temperature [4, 4, 8, 131]. It was found that, under high solar irradiation, FPCs reach their maximum outlet temperature at 80°C. However, ETCs seem to be competitives devices with higher outlet temperature which leads to better performance and higher efficiency [8, 9, 124, 275]. From a comparative study conducted by Ayompe *et al.*, it was found that the annual average collector efficiency is 46.1% (resp. 60.7%) while the system efficiency is 37.9% (resp. 50.3%) for a FPC (resp. ETC) [8]. Eliminating (virtually) convective and conductive heat losses between the absorber surface and ambient air is the main advantage of ETCs over FPCs ones. These devices are currently of the most technologically advanced means for converting solar radiation into usable heat in a large range of applications.

1.8.2 Heat pipe evacuated tube solar collectors

Working principal

Typically a HPETC consists of two concentric glass tubes, *i.e.* an inner and an outer tube, fused at one end, an absorber, an aluminum fin and a heat pipe, see figure 1.8. The air in between the inner and outer tubes is evacuated to keep the device under vacuum condition which eliminates the convection heat loss and improves the thermal insulation [97, 201]. The inner tube is covered by a selective coating material. The absorber is characterized by a high absorptivity more than 92% of the incident radiation, and a low emissivity, less than 8% of radiation is sent back to the environment. The heat flux saved is transferred through aluminum fin, located inside the evacuated tube and in contact with it, to the HP. Heat pipes are separated where each one has a condenser zone inserted

in a well-insulated manifold exchanging heat with the working fluid.

FIGURE 1.8 – One tube HPETSC schematic description.

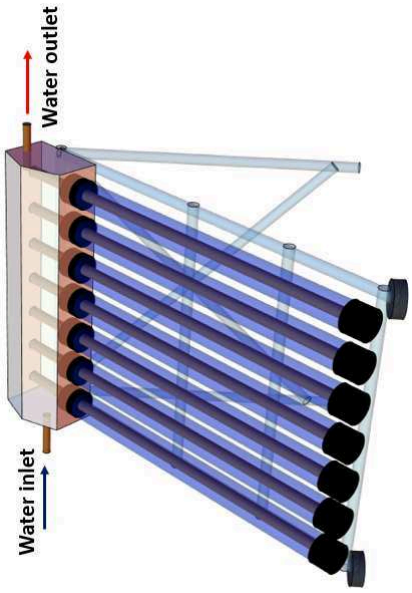

FIGURE 1.9 – Heat pipe evacuated tube solar collector.

Figure 1.9 shows an installation of HPETC for water heating systems. The main difference, in thermal performance, between a HPETSC and conventional one lies in the heat transfer mechanisms from the absorber tube wall to the energy transporting fluid. In the HPETC, the phase change (evaporation and condensation) convection and conduction are involved whereas for conventional solar collectors heat transfer involves no phase change. The key component of HPETC, namely the HP, is described in the next section.

Heat pipe: the main HPETSC component

There are two types of HP often used in HPETSC:
- Capillary driven heat pipe (CHP):

The CHP consists of a closed container where a wick structure is integrated along the inner wall of the HP. The purpose of the wick is to provide the necessary capillary pumping pressure for returning the condensate from the condenser to the evaporator section.
- Thermosyphon:
Compared to CHP, two-phase thermosyphon has the same working principal. The only difference is that thermosyphon uses the gravity forces to assure the liquid return from the condenser to the evaporator. Wicks may be incorporated in some parts of the unit in order to reduce entrainment and improve liquid distribution within the evaporator. However, the thermosyphon operation highly depends on the filling ratio of the working fluid.
Due to their suitable installation, good thermal performance and easy mobility, ETCs are commonly used through the world wide [132]. As it was mentioned in the introduction, ETCs have been designed in different models such as U-tube, glass-glass and heat pipe. Due to their intrinsic characteristics mentioned in section 1.2, heat pipe is a promising device with excellent heat transfer capacity in low-medium and high temperature range. Compared with forced-circulation or natural convection solar systems, the use of solar heat pipes has many advantages such as a higher rate of heat transfer with a low temperature difference, simple construction and large adjustability. Previous works showed disadvantages by using conventional solar collector [13, 182, 243], additional energy usage, extra charge for pumping, counter-flow circulation, water freezing at night, corrosion, and heat transfer limitation, in consequence of using water as working fluid. These drawbacks can be overcome utterly by using heat pipe in solar collector. In such a case, the efficiency of solar collector reaches 60% and in no way less than the conventional one. Through a comparative study [8, 129], evidence suggests that HPETSC presents less heat loss and better performance. Other advantages of the integration of HP are the high thermal conductance and its ability to work as a heat flow transmitter at isothermal level. Another advantage is that the freeze phenomenon is avoided in the solar collector in opposite to the common solar collector with water in-glass or U-tube [154].

State of knowledge

Although HPETSCs represent relatively a recent technology, their applications to SWH are increasing worldwide due to their high efficiency. However, the thermal performance of SWH using HPETSCs has not been well evaluated yet and is therefore not well known to end-users [43]. Hence, researchers are paying more attention and giving significant efforts to study numerically or experimentally HPETSCs in such applications. There have been many efforts over the last two decades to harness efficiently solar energy and reduce the operating and maintenance costs of devices using such a form of energy [135].

- Comparative study
In order to increase the rate of heat transfer, the use of heat pipes in solar collectors is one way of increasing the efficiency of solar hot water systems [12, 63, 234]. Due to its potential, several studies on HPSCs are reported in the literature. The first ones were focused on

FPCs using heat pipe technology [44, 126, 146]. The steady and, casually, transient state behavior was analyzed with regard to different design parameters: heat pipes with wick structure [44, 261] and without wick structure [44, 112–115, 126], the working fluid (water, methanol, acetone, ethanol, R-134a, R-407c, and R-410a) [44, 63], the absorber surface treatment [44], the number of heat pipes [112–115], the heat pipe filling ratio [60], the heat pipe tilt angle [112–115], the condenser length to the evaporator length ratio [10, 11], the inner diameter of the tubes to the total length of the tubes ratio [10, 11] and the solar radiation intensity [112].
Jun feng *et al.* [129] compared two types of all-glass vacuum tube collectors with and without heat pipe technology. It was necessary to implement a water circulation system. To analyze the performance, the instantaneous efficiency of the system was calculated. The findings proved that heat pipe solar water heaters had less heat loss and better performance. Based on experimental investigation, Hayek *et al.* [96] compared the thermal performance of two solar water heaters technology, water in glass and HPETC, under eastern Mediterranean climatic conditions at an altitude of 150 m in Zouk-Mosbeh located on the north of Beirut. Their results show that HPETC performs water-in-glass collectors by 15 to 20% of the total efficiency. However, their payback periods are almost three to four times much higher because of their larger initial cost in the local market. Ayompe *et al.* [8] presented the energy performance results of two SWH with 4 m^2 FPC and 3 m^2 HPETCs working under the same climates conditions along the year in Dublin, Ireland. The two collectors were oriented on the south and inclined at 53°. Through their experiments, they found that the annual average collector efficiency is 46.1% (resp. 60.7%) while the system efficiency is 37.9% (resp. 50.3%) for a FPC (resp. ETC). Through an economic analysis, they found that both solar water heaters systems are not viable with net present values ranging between -4264 € and -652 € while simple payback periods ranged from 13 to 48 years. Later, Ayompe *et al.* [9] developed a TRNSYS model for two systems of SWHs with FPCs and HPETSCs using a quasi steady state simulation utility. They claimed that this model can be used profitably to predict long-term performance of the solar water heating system in different locations at different operating conditions. More recently, Tong *et al.* [280] designed and tested two kinds of evacuated solar collectors: one with U-tubes and the other one with HPs under same weather conditions in Gwangju, Korea, at coordinates 35°N and 126°E. Through a theoretical investigation, the results obtained from a simplifed model show that each type of collector has its own advantages. In fact, the heat pipe type has an 8% higher effciency than the U-tube-type during the sunny day, while the U-tube-type shows steadier and better thermal performance on cloudy days. In what follows, a focus on HPETSC is made.

- Parametric study

Many studies deal with the impact of environment conditions on the performance of the HPETSC. Redpath [230] evaluated the thermal performance of three thermosyphon HPETSCs for SWHs under northern maritime climate conditions. He proposed a new correlation based on modified version of the F-chart design tool between the observed and expected performance for both systems which was successfully validated experimentally. For larger dwellings such as semi-detached and detached homes, a collector with an area

of 3 m^2 was found to be more appropriate to meet domestic hot water requirements. Jafarkazemi and Abdi [121] investigated theoretically and experimentally the performance of a HPETSC at coordinate 35°36'N; 51°24'E on the test center. The collector tilt angle was adjusted as 45°, facing south. A comparison between the theoretical and experimental results for two collectors with different numbers of heat pipes and different aperture areas was made. Good agreement was found for the efficiency, useful heat gain, and predicted outlet temperature prediction. They observed higher outlet temperature by decreasing the amount of flow rate. Also, they recommended to reduce the working fluid rate and to keep the inlet water temperature as near as possible to the ambient temperature in order to gain more heat, maximum outlet temperature and higher efficiency. Porras-Prieto *et al.* [218] designed a solar water heating system with a HPETC tested under Madrid, Spain, climate conditions (40°26'N; 3°43'W; altitude 600 m). They presented the effect of the required tank water temperature (rTWT) on the energy performance of the system. To ensure the best annual performance, the ETC was held at an angle 41°. They showed that as rTWT increases the net energy that can be stored by the system falls, with a difference over 1000W.h.m^{-2}.d^{-1} between rTWTs of 40°C and 80°C under incident solar radiation of 8000W.h.m^{-2}.d^{-1}(system efficiency ranging between 56 and 73%). This is due to the energy losses rising in the circuit's tubing. For a rTWT of 80°C, an important quantity of the incoming energy can be stored in the tank hot water. However, the required temperature will never be reached. To avoid nocturnal heat losses form the tank, auxiliary systems are required to make profit from this energy which can reduce up to 69% of the residual energy. Later, Jahanbakhsh *et al.* [122] investigated a HPETSC both theoretically and experimentally at the solar energy laboratory of Islamic Azad University on the South Tehran Branch (35°42'N; 51°25'E). They provided in details a theoretical approach for exergy and energy analysis. Good agreement between the experiment and theory was observed. Using the proposed theoretical model, effects of different parameters (absorptance of the absorber surface, water mass flow rate, inlet water temperature, transmittance of tubes) on the collector's energy and exergy efficiency were investigated. They found that all of the mentioned parameters have a direct effect on the overall energy and exergy efficiency. In fact, the increase of water inlet temperature decreases the amount of heat transfer rate between the HP's condenser region and water. Daghigh *et al.* [51] carried out theoretically and experimentally a study in order to evaluate the performance of a SWHs system with HPETCs located in Sanandaj city (46°59'N; 35°19'E and latitude 1450 m). They proposed a mathematical model involving thermal and exergy analysis to evaluate the collector performance and compared it with experimental tests. They found good agreement with maximum relative error of 8.4% and a maximum standard error of 1.91%. The reported results showed also that the optimal number of collector pipes was to be 15, the maximum efficiency around 5.4% at the end of the day and the maximum outlet temperature of collector about 64°C between 3 and 4 pm. They suggested an auxiliary system in the early morning until 2 pm so that the solar cycle supplies the required energy. More recently, Kumar *et al.* [148] designed a HPETSC made of Borosilicate glass with length 1.8 m, outer diameter 0.058 m and inner diameter 0.049 m of tubes under the Coimbatore climate (11°1'N; 76°57'E). They investigated the heat transfer of the device. They found that the length of evaporator to condenser section is a key parameter in HPETSC design. Also, they found that such a device is more sensitive to external

conditions like solar radiation and ambient temperature.

- The effect of the working fluid

The working fluid plays an important role on the heat transport from the evaporator to the condenser part. Hence, different working fluid were tested. Arab and Abbas [5] performed a model validation for a grooved type SWH system with experimental data under a typical weather data for the first of January at Sydney, Australia (33°52'N; 151°12'E). They studied the effects of different working fluid like water, ammonia, acetone, methanol and pentane during daily operation and identified water as the best working fluid. They found that higher performance of solar water heater (up to 84%) is achievable by solely improving the working fluid properties. They proposed an hypothetical working fluid that does not necessarily coincide with a real fluid or satisfy any chemical constraints. Also, they found that modifying the working fluid may lead to about 50% improvement in the efficiency of the solar water heater. Later, Jahanbakhsh *et al.* [123] investigated experimentally thermosyphon ETSC using ethanol-water mixture at different concentrations and tilt angles. The results indicated that the use of ethanol rises the HP performance even under low heat flux. They found also that the best thermal efficiency is observed for ethanol concentrations on the range of 50% -75%. Under these working conditions, the HPETSC gives an efficiency of about 52%. They concluded that the use of wick structure slightly enhances the heat pipe performance and that the collector has its highest heat transfer coefficient at a tilt angle of 35°. Based on the energy and exergy performance for a thermosyphon ETSC (THPETC), Ersoz [62] studied the effects of working fluids like hexane, petroleum ether, chloroform, acetone, methanol and ethanol under three air velocities as 2, 3 and 4 m.s^{-1} with the climatic conditions of Usak, Turkey (38°24'N; 29°14'E; altitude 919 m). The lowest energy and exergy efficiency occurs for the THPETC-Hexane at three different air velocities while the highest energy efficiency occurs for THPETC-acetone at air velocity of 2 and 3 m.s^{-1} and for THPETC-Chloroform at air velocity of 4 m.s^{-1}. The highest exergy efficiency appears for THPETC-acetone at air velocity of 2 m.s^{-1} and for THPETC-Chloroform at air velocity of 3 and 4 m.s^{-1}.

1.8.3 Development of collectors

In the last decade, many surveys have been conducted and released on the development of HPETSC technology specifically.

Maintaining the contact between the ET and HP

As already mentioned in section 1.8.2, an aluminum fin inside the evacuated tube (ET) is in contact with both the inner wall (absorber) of the evacuated tube and the HP. As a consequence, the efficiency of heat transfer from the ET to the HP is strongly dependent on the contact between the finned surface and the ET as well as the HP. However, irre-

gular thermal expansion of the fin usually occurs owing to the uneven exposure to solar radiation. In fact, the bottom side of the ET is exposed to a different radiation than the top one necessarily, in consequence of the ET orientation and Sunshine inclination. Also, excessive solar radiation in sunny countries may cause irreversible fin deformation. By taking into account this irregular expansion, the fins lose perfect contact with both the TE and HP and so increase significantly the thermal resistance of the device [158].

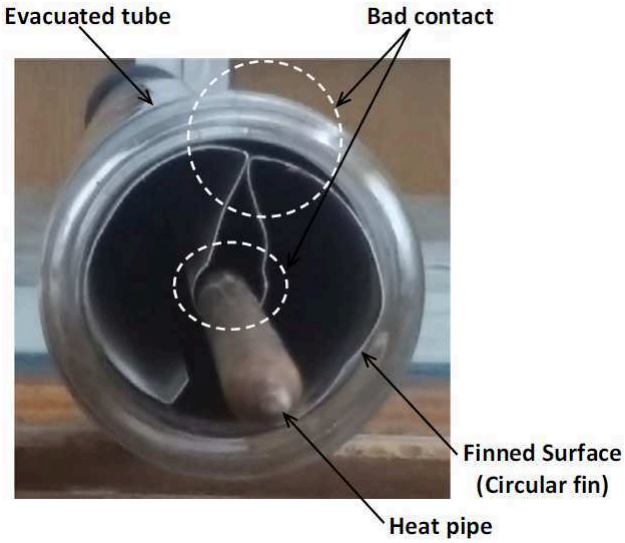

FIGURE 1.10 – HPETSC with bad contact between the finner and the inner tube [1].

Figure 1.10 shows a real photograph of a HPETSC with a fin locally in bad contact with both the ET and the HP. Hence, maintaining good contact between the finned surface and the ET as well as the HP can increase the overall performance. Recently, Abd-Elhady *et al.* [1] designed a new system to improve the heating capability of HPETSC by inserting thermal oil in the evacuated tube. Using such a configuration, the heat transfer from the inner surface of the ET to the HP occurs by convection through the oil and by conduction through the installed fin. In fact, the oil helps filling the gaps between finned surface and both tubes (ET and HP). In order to improve the conduction heat transfer, they also added foamed-copper into the finned surface. Through an experimental setup, three cases have been compared and studied as shown in figure 1.11. They mentioned that the bulb temperature HPETSC is increased by 30°C and the heating efficiency by 55.6% when inserting oil in the ET and replacing the finned surface with foamed copper. In fact, foamed metals let a better contact between the inner tube of the ET and the HP than finned surfaces. In addition, they do fill the wind gaps with a good heat transfer medium, which improves the heat transfer conductance. Such devices, provide heat energy by the ET even after Sun set.

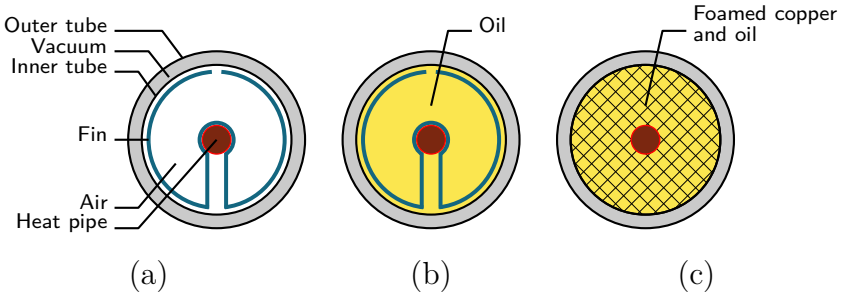

FIGURE 1.11 – Cross section of the evacuated tube heat pipe in case of inserting (a) finned surface (b) finned surface and oil and (c) foamed copper and oil. Courtesy of [1] (adapted).

Integrating PCM

Besides integrating phase change materials (PCM) in FPCs and ETSCs [3, 204, 303], several works attempted, recently, to integrate PCM in HPETSCs. An issue of SWHs system is the storage of solar energy; indeed this systems work appropriately during the day but its performance is reduced during the night time. Hence, storage systems can be useful when linked with SWH. Although costly and bulky, PCM integrated to solar collectors are considered as a promising solution in substitution for conventional storage units [28, 255, 278]. Naghavi *et al.* [192] modeled theoretically a solar hot water system consisting of an array of HPETSCs connected to a common manifold filled with PCM and acting as a latent heat thermal energy storage (LHTES) tank (see figure 1.12). The test bench was located in Kuala Lumpur International Airport meteorological station (2°26'N; 101°25'E).

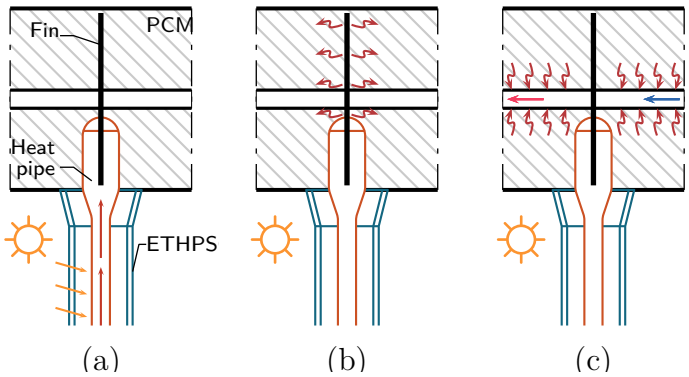

FIGURE 1.12 – Heat transfer process in LHTES tank. (a) solar heat absorption, (b) PCM charging and (c) PCM discharging and water supply heating. Courtesy of [192] (adapted).

The results show that for a large range of flow rates, the thermal performance of the HPETSC-LHTES system is remarkably higher. Furthermore, the analysis shows that

the efficiency of the introduced system is less sensitive to water flow rate draw off than conventional systems. They found that this system can be applicable as a complementary part to conventional HPETSC systems in order to produce hot water at night time or at times with weak radiation.
Later, Papadimitratos *et al.* [208] presented a novel approach to integrate PCMs within the HPETSCs for SWHs (see figure 1.13).

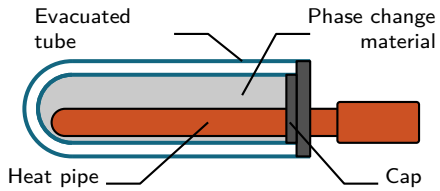

FIGURE 1.13 – Schematic of HPETSC filled with PCM. Courtesy of [208] (adapted).

In this approach, the heat pipe itself is immersed into the PCM, where heat is effectively accumulated and stored for a given period owing to the significant thermal insulation of ETs. The main benefit of this approach is providing sufficient hot water during bad weather conditions. The proposed HPETSC uses two PCMs: Tritriacontane and Erythritol. The investigation was performed during normal and on-demand working conditions. The feasibility of this technology was also tested via large-scale commercial solar water heaters. They found that the efficiency is improved to reach 26% for normal operation and 66% for on-demand mode in a comparison with standard SWHs. More recently, Naghavi *et al.* [193] investigated experimentaly the design of SWH employing HPETSCs and a latent heat storage (LHS) tank under charging or discharging operating modes see figure 1.14. In this design, sunshine irradiating the HPETSC is collected and stored in the LHS tank via a heat pipe with fins attached to the condenser ends inside the LHS tank. Then, the reserved heat is conducted to the working fluid through finned pipes inside the tank. The tests are done under weather conditions in a tropical region (3°6'N; 101°24'E). In sunny days, the thermal efficiency of the system is in the range of the 38%-42%. However, in cloudy-rainy days, this efficiency drops to the range 34%-36%, with a range of about 8% fluctuation in different conditions. They also illustrated that the flow rate impact appreciably the overall efficiency of the system in the tested ranges. Several advantages of using PCM can be drawn from the above research. Because of its low heat dissipation, this system can be adapted for hot water demands starting from night to next day early morning. Its large space capacity and isothermal behavior during melting decreases the heat loss from the LHS tank compared with the conventional tank. Hence, the mentioned advantages coupling HP and PCM cover the main drawbacks of each like HP overheating and low thermal conductivity of the PCM.

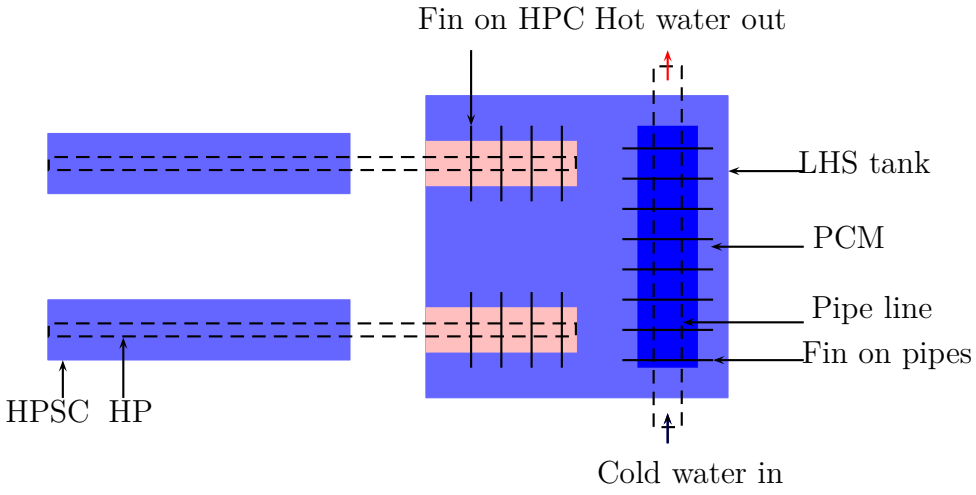

FIGURE 1.14 – HPSC-LHS system [193] (adapted).

Selective coating: new materials

One of the most important issues with SWH is the solar selective (absorber) coating (SSC) which transfers the incident solar radiation into heat. Therefore, its energy conversion efficiency acts like a conditioner of the whole device relevance [279]. So, an efficient way to increase the HPETSC efficiency is to integrate an efficient SSC to the collector. For optimal solar energy conversion, as show in figure 1.15, an appropriate SSC should be located between wavelengths of maximum emission of the solar spectrum and the evacuated tube spectrum. An ideal SSC is characterized by low reflectance and high absorption in the visible region, low thermal emissivity and high reflectance in the infrared region at a corresponding temperature.

For exemple, the optimal wavelength is on the range of 1-2 μm for a temperature of

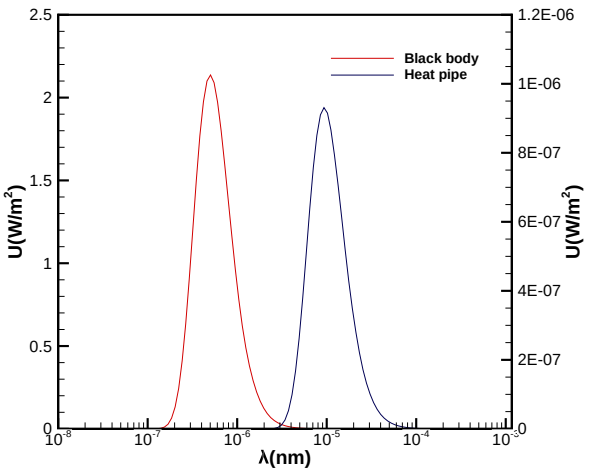

FIGURE 1.15 – Solar intensity for a black body at 5800K and a heat pipe at 310K.

100°C [139]. Black coatings are commonly used as absorber coatings in HPETSC with a high solar absorbance. However, they have a high thermal emissivity, too. Metals, like Au, Ag, Al and Cu, have a high reflectance and very low thermal emittance, between 0.01 and 0.04 up to temperatures of 300°C, in the high infrared region. But, they suffer from low solar absorbance. Based on a single element, transition metals and semiconductors are promising candidates. However, their composition requires to be greatly modified in order to achieve an ideal characterization [247]. Therefore, the absorber coatings often combine different materials in order to achieve the required performance. For example, the current integrated selective absorbers coatings are made of Aluminum-Nitride layers with 92% of solar absorbance. Hence, 8% of solar energy is lost because of the absorber material reflectivity. This requires the use of expensive and complex coating methods with careful control over the sputtering process (up to 12 sputtered layers for some designs). Compared to the black body, such a coating is less efficient. Recently, other kind of materials such as single and multi-walled carbon nanotubes (CNT) have been reported to be nearly-perfect optical absorbers with ultra-low theoretical reflectance within the range 0.01-0.10% in the visible spectrum [14, 174, 267]. In fact, CNT consists of an array of tube-shaped carbon material with a diameter of nanometer scale. CNT sheets is characterized by various structures, different thicknesses, lengths and number of layers. However, carbon-based materials integration faces two main issues: their poor heat conductivity and stability for medium and high temperature solar heaters. Very recently, Sobhansarbandi *et al.* [267] investigated a new HPETSC design using two technologies: the "dry-drawable" CNT sheet coatings in order to rise the absorption of solar energy and the PCMs in order to rise the heat storage. Using the dray-drawable techniques, the mentioned shortcoming of CNT is overcomed. The proposed solar collector uses Octadecane paraffin as a PCM. The combination (PCM and CNT) is found to be effective even on cloudy days and at night. In fact, the disadvantages of PCM like poor heat transfer rate, low thermal diffusivity and thermal conductivity are overbalanced by CNT layers with high thermal diffusivity and conductivity. With the proposed technology, a near ideal black body surface was designed with an absorbance of 98%, in the spectrum 600-1100 nm, of sunshine striking its surface.

The use of nanofluids

The conventional fluids used in HPETSC suffer from poor, thermal conductivity and critical heat fluxes [118, 164, 209, 272]. In order to increase their thermal performance, adding particles of nano size into these fluids (called then nanofluids) with high thermal conductivity like metal and metal oxide is a well mastered technique in the field of solar collectors [111, 166, 188, 272, 321]. This increases the over all conductivity of the working fluid. Hence, it improves the system thermal performance. Most of existing works are performed on a flat plate heat pipe solar collector. Few works studied the effect of nanofluids on the thermal performance of HPETSC. Effect of silver-water nanofluids was investigated by Ozsay *et al.* [205]. Once the stability of nanofluid verified, the experiments were performed at 35° tilt. They found that using silver-water nanofluid improves HPETSC efficiency between 20.7% and 40% compared to pure water. Iranmanesh *et al.* [118] stu-

died the effect of graphene nanoplatelets (GNP)- distilled water nanofluid mixture on the thermal performance of HPETSC water heater with a tilt of 33° in Kuala Lumpur, Malaysia. Different mass percentages of GNP were tested: 0.025, 0.5, 0.075 and 0.1wt% for different amounts of flow rate: 0.5, 0. 1 and 1.5 L/min. They found that the overall thermal efficiency reaches 90.7% for a flow rate of 1.5 L/min. More recently, Mahbubul *et al.* [166] analyzed the effect of Single Walled Carbon Nanotube (SWCNT)-water nanofluid on the collector performance compared to ordinary water working fluid. They found that the efficiency reaches 56.7% and 66% when the collector operates with water and 0.2 vol.% nanofluid, respectively. Also, they found that the highest outlet temperature reaches 120.6 °C at about 1:30 p.m. The evolution of the collector efficiency was found to be linear with thermal loss function. Moreover, SWCNT-water nanofluids of 0.05, 0.1, and 0.2 vol.% were considered for the performance enhancement and 10% higher efficiency was observed by using only 0.2 vol.% of SWCNT nanoparticles with water.

Heat loss reduction

Thermal performance is highly affected by heat losses from various sections. The upward region is totally exposed to environment. Hence, heat lost from this region is significant through convection and radiation. Unglazed and single-glazed collectors are highly exposed to heat losses due to natural winds. To study their impact, many wind tunnel tests have been performed in order to investigate the associated heat transfer coefficient [206, 207]. However, as the collector is exposed to the solar radiation, and thus to natural winds, wind tunnel seems in that case inappropriate.

Ayompe and Duffy [7] investigated the annual thermal performance of a HPETSC using the data obtained over a period of one year in Dublin, Ireland (53°20'N; 6°15'W). The average daily collector efficiency varies between 47.2% in December and 71.4% in May while the system efficiency varies between 41.7% in December to 58.7% in May. The annual average daily collector experimental efficiency is 63.0% while the experimental system efficiency is 52.0%. They found also that by reducing the pipe losses, which represent 17.7% of the energy collected and 21.5% of the energy delivered to the hot water tank, and by developing a more tuned pump control strategy for heavily overcast and intermittent cloudy covered days lead to system efficiency improvement up to 52%.

As one of the most relevant HPETSC component, the receiver's back surface can play an important role on the device performance. Hence, Zheng *et al.* [314] presented a heat transfer model that establishes the link between the heat loss and the back surface emissivity of the HPETSC. Through experimental tests, they measured the heat loss through HPETSC using different back surfaces. Their experimental results suggest that the heat loss increases with the increase of the back surface emissivity. For working temperature under 100°C, an rising from 0.03 to 0.12 of back surface emissivity led to a heat loss increasing up to 31%. However, for a temperature over 200°C, the heat loss rises up to 96%. Hence, the change of back surface emissivity can affect the performance of the HPETSC significantly at higher temperature but affects a little at moderate temperature. Based

on these conclusions, they performed a novel method by special coating of the receiver's back surface in order to overcome the overheating problem of HPETSC in summer. The test was performed for two SWH systems including 6 HPETSCs each one using standard and roughness-treated tubes.

The results show that, for water temperature below 60°C, the two collectors led to the same temperature range. However, for a temperature over 80°C, the collector with roughness-treated tube gives lower temperature increase compared with standard tube. Hence, it seems imperative to prevent SWH systems from overheating in hot weather conditions by using a back surface with a large roughness. Higher efficiency can be reached by preventing overheating issue, indeed.

Use of metal HPs

New research developments aim at using auxiliary devices in order to improve the thermal performance of HPETSCs. Most of previous works are heading toward designing a variety of liquid thermal solar collectors for SWH with copper HPs. It was reported by Rassamkin *et al.* [228] that metal HPs integrated to evacuated solar collectors is an efficient option for SWH systems. In addition, the majority of the existing thermal solar collectors does not meet the industrial requirements of small weight, design versatility, easy assembly and installation. In order to avoid the above-mentioned drawbacks, Rassamkin

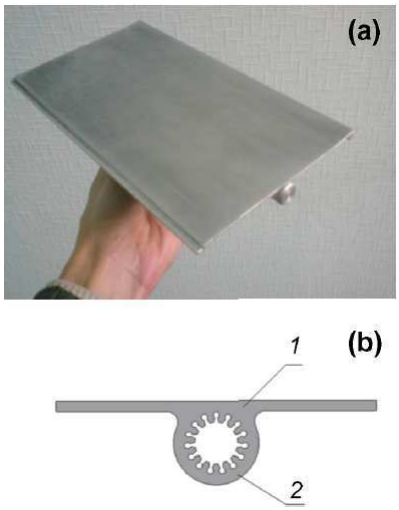

FIGURE 1.16 – Aluminum finned HP proposed by the authors: (a) outer view of the HP's fragment and (b) cross-sectional profile of the HP: 1-absorber and 2-grooved HP. [228].

et al. proposed to use an innovative extruded aluminum-alloy HPs. Its original cross-sectional profile is made with wide fins and longitudinal grooves (see figure 1.16). They used fins at the opposite end of the HP that serve as a heat sink surface. Through there tests, they proved that new lightweight and inexpensive heat pipes provide high thermal performance with maximum heat transfer power of one heat pipe is up to 210 W and

very low thermal resistance (from 0.02 to 0.07 °C/W). They also found that the hydraulic resistance of HPETSC utilizing aluminum profiled heat pipes could be reduced to less than 100 Pa while their thermal efficiency is may reach 72%.

Manifold structure

The currently known deficiencies of standard design manifolds are uneven heat consumption from the condenser, a high liquid volume, a serial connection of condenser casing and high thermal inertia [242]. These deficiencies are overcame partly using a new manifold design described by Rybar *et al.* [242], who carried out an experimental comparison between standard design HPETC and collector with manifold header under parallel flow made with metal foam material and developed by the authors in previous work (see figure 1.17). The experiments were done between April and May in Kosice (48°43'N; 21°15'E),

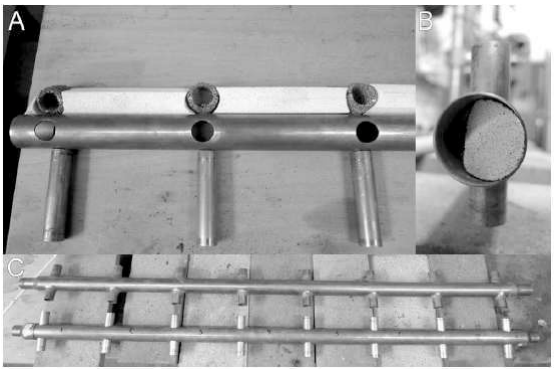

FIGURE 1.17 – Photography of manifold header prototype from different phase of manufacturing (A)-illustration of inner arrangement, (B)-front view of partially assembled manifold, (C)-comparison of standard manifold (top) and prototype of manifold header (bottom), where is clearly visible similar dimensions [242].

Slovakia, and under various weather conditions. They found that the proposed design yields a performance increase about 25% and reduces thermal inertia of the solar collector under different solar intensity insolation. This leads to an improvement of the system performance. In addition, they concluded that manifold header with metal foam structural element partly eliminates deficiencies of standard design manifold headers by: i) changing the heat transfer medium diffusing flow to each condenser, ii) decreasing the internal fluid volume and iii) introducing new materials to the manifold header design.

Micro-channel

Thermal analysis of minichannel-based HPETSC was investigated by Li *et al.* [154]. A theoretical and experimental study was performed to evaluate the system performance that shows many advantages, including the high heat transfer, low convective heat loss,

low contact thermal resistance and high thermal performance with addition of electricity production.

1.8.4 Challenges when using HPETSCs

State of the art of HPETSCs shows handicaps which currently lower their efficiency and reduce their application. The main challenges met are to increase durability and to reduce maintenance, cost and frequency. The presented challenges of HPETSCs shed light on both the need of and room for further improvement of such devices as well as development of collectors innovative concepts.

Economical, energy and environmental statement

Besides the high heat transfer ability of the HP itself, HPETSCs show a lower stagnation temperature of the solar fluid than other collectors. By introducing a dry connection between the HP and the manifold, the pipes exchange is feasible without draining the collector circuit. Thereby maintenance is ensured easily but is costly too. Because of the fluid flow circulation through the mainfold, HPETSC can be exposed to a low pressure drop causing slight percentage of leakage risk. Moreover, the HPETSC design requires a high degree of perfection which increases the installation cost. Despite those advantages, HPETSCs only account up to now for a minor market share due to their high cost compared to conventional collectors.

Mamouri *et al.* [169] studied the performance of HPET-SWH in the state of Michigan (42.73°; altitude 261m), USA, a region with particularity low solar resources, for year-round usage. Through an experimental investigation for 26 locations dispersed throughout the state, they found that an HPET-SWH can contribute up to 63.8% of the required energy for water heating, based on the typical household water usage profile with payback periods as low as 8 years. From an environmental point of view, CO_2-house emissions can be reduced by up to 1664 kg per year in Michigan. By varying the amount of hot water demands, they performed a study on the correspondent optimum collector area. Through this study, they identified a standard equation used for the estimation of the optimal collector area in Michigan. They found also that the performance of HPETSC depends mainly on the overall heat gain coefficient which should be taken into account in system design. Their analysis shows that through proper sizing of the system, high performance can be reached with a significant cost saving.

Snow removal

In very cold weather, when avoiding snow sticking on tubes is a hard task, much precaution should be taken to scrape off the accumulated snow which might make the

system ineffective without breaking it. The best plan of action for HPETSC is the angle of panel installation. Because of gravity, more tilt angle can help removing the snow from tubes. However and depending on the location, a particular tilt angle is recommend which is about 40° from level. Still, snow removal is an issue as longer as the sunlight can not rich the tube to keep normal working of HPETSC. Reversal usage of heat pipes, where the evaporator and condenser are switched, can address this particular issue.

Overheating

One of the intrinsic characteristics of HPETSCs and, in general ETSCs, is producing supplied water much hotter compared with other collectors. For SWH systems, keeping the temperature below 100°C is required to avoid overheating causing system damage. One of the required solution is integrating the HPETSC with PCM at the bottom of the solar collector. Once the daily demand is satisfied, the reset and the excess of the energy is stored in the PCM. Hence, such installation has following main advantages: i) controlling the overloading of the HP; ii) controlling the overheating of the supplied water in hot days especially in the middle of the day; iii) providing the required thermal energy to the HP at the end of the day until the next day morning.

1.9 Conclusions

Through this first chapter, we presented a brief introduction to heat pipe technologies: construction, applications, types, etc. We showed, also, that great efforts have been made, mainly during the last two decades, to develop solar water heater technologies. Through a literature review, we found that a continuous interest is increasing on the use of HP for solar water heaters. However, most heat pipes developed have a circular section with a wickless structure in HPETSC. In opposite, few studies have used evacuated tube solar collector with wick structure. Due to the lack of research on wicked HPETSCs, we get motivated to study such systems using numerical and experimental means presented in the next chapter.

Chapter 2

Lattice Boltzmann Method

Abstract

In this chapter, we present the most important tools required to build the Lattice Boltzmann method (LBM). We outline the theory behind the LBM: background, different approaches of Navier-Stockes equation derivation, Boltzmann equation and boundary conditions implementation.

Résumé

Dans ce chapitre, nous présentons les outils les plus importants nécessaires pour comprendre la méthode de Boltzmann sur réseau (LBM). Nous décrivons la théorie derrière la LBM: le contexte, les différentes approches de la dérivation des équations de Navier-stocks, l'équation de Boltzmann et l'implémentation des conditions aux limites.

2.1 Background and basics of Lattice Boltzmann method

In the last few decades several fundamental methods have been developed in order to solve fluid dynamics problems using molecular dynamics (MD) approach. These methods are able to simulate phenomena where the continuum assumption breaks down and the macroscopic properties are recovered using statistical mechanics. This procedure, however, requires calculating every particle's distribution functions, a long and complex process. This issue can be partially addresses by ignoring the molecular level interactions and grouping the molecules together into parcels. In such a way the kinetic equation can be simplified. For these reasons, the Lattice Gas Automata (LGA) was developed from cellular automata, with a history starting in 1973 [297]. Cellular automata are discrete computer models of a grid system with an evolution defined by some mathematical rules. This was a model for the motion of single particles in fluid using constitutive rules chosen as simple as possible deliberately. Hence, LGA can be seen as a simple method of molecular dynamics.

Lattice Gas Automata does work with a group of particles on the lattice nodes while colliding with particles located at the neighboring nodes and conserving the mass and the momentum. Each particle has a velocity whose direction is along the connection with one of the neighboring nodes. All the particles possess momentum and the collision between them is governed by a set of rules that change the particles velocity but conserves the total momentum of all the particles existing at a node. The particles then stream to their closest nodes according to the direction of their new velocity. At each time step and for each lattice node, there is collision between particles followed by motion. In the LGA, the occupation pattern of the cells is described by means of Boolean variables $n_i(x,t)$ (where i indicates the available directions for the particles). However, the LGA is not competitive compared to the classical macroscopic procedure with serious drawbacks. It suffers from the lack of precision and stability. In particular, the most important problem is the statistical fluctuations. Space and time averaging can reduce the statistical fluctuations, but this increases the computational time and memory requirements. This problem is magnified greatly in three-dimensional simulations.

In order to overcome this drawbacks, the Lattice Boltzmann method (LBM) has been developed. It finds its origin in intensive efforts made since 1997 toward the rigorous proof that the established Lattice Boltzmann algorithms could be interpreted as numerical solutions of the Boltzmann equation itself [2, 100, 217, 252]. It is a mesoscopic approach based on the kinetic theory expressed by the original Boltzmann equation. The method has its roots from the older LGA method [71] and later on was established as an independent numerical method derived from direct discretization of the Boltzmann, Bhatnagar-Gross-Krook (BGK) equation [100]. With respect to the Lattice Gas Automata, the LBM introduces a major improvement: the Boolean occupation variables are substituted by distribution functions, a procedure which eliminates statistical noise in the calculations. In fact, it was suggested to replace the Boolean occupation pattern of

the LGA with continuous distribution functions, one for every particle, which neglect single particle's motion and correlation. This constitutes the most significant change with respect to the LGA and is the foundation of the LBM.

2.2 Advantages of Lattice Boltzmann Method

As an alternative tool, the LBM has been developed into an efficient and powerful simulation method for a wide range of phenomena and processes, such as single-phase flows, multiphase flows, turbulence, heat transfer, and phase change, as well as a numerical tool for nonlinear partial differential equations. The LBM exhibits many distinctive advantages over conventional numerical methods . First, in the lattice Boltzmann equation the convective operator (the streaming process) is completely linear, whereas the convective terms of the Navier-Stokes equations are nonlinear. Second, in conventional numerical methods it is usually necessary and costly to solve Poisson equation for the pressure field of incompressible flows, while in the LBM the fluid pressure can be simply calculated with an equation of state. Third, complex boundary conditions in the LB method can be formulated with elementary mechanical rules such as bounce-back and reflection according to the interactions of the LB "molecules" with solid walls. Moreover, the LBM is ideal for parallel computing because of its explicit scheme, local interactions, and consequently very low communication/computation ratio. It is ideally situated to exploit the massively parallel supercomputers based on either CPUs or GPUs or heterogeneous architectures. For these reasons, we turned to the LBM as effective tool in both two and three-dimensional as in 2D simulations.

However, there are many issues that need more investigations and particular attention. Also, the method is used by some authors with less care to the limitations and constrains of the parameters in LBM. One of these issues is the proper treatment of the external forces.

2.3 The different approaches

The main issue with LBM is how to recover the macroscopic conservation equations from the kinetic Lattice Boltzmann equation based on the particle distribution function. To address this issue, two different approaches have been developed. The first was proposed by Grad in 1949 [80, 81] known as Grad's 13-moments-equations and the second one was developed later, in 1970, by Chapman and Cowling [30] which is known as Chapman-Enskog multiscale expansion. The last one was introduced mainly by Shan *et al.* [252] and is considered as a systematic approach.

2.3.1 Grad's representation approach

Grad [80, 81] claimed that continuity, momentum and energy equations are not sufficient to describe all the properties of the fluid. That is why he introduced another set of equations for stress tensor and energy flux, by projecting distribution function on Hermite polynomials. The main advantage of Grad's approach is its ability to achieve high order without loss of accuracy. Such an approach can go beyond Euler and Navier-Stockes equations easily. Despite its elegance, Grad's procedure has met with limited success in practical applications, mainly because the 13-moments truncation no longer guarantees positivity of the distribution function but also because it is hard to apply well-defined boundary conditions with, especially in wall bounded flows where more moments are needed to describe anisotropic transport terms.

2.3.2 Chapman-Enskog expansion approach

In this approach, Chapman and Cowling [30] expanded the distribution function as well as the physical space and time in different powers of Knudsen number then separate the system into multiple scales with respect to the Knudsen's order. By projecting the lattice Boltzmann equation on the lattice in different scales, the macroscopic equations such as Euler and Navier-Stokes equations, are recovered through mass and momentum conservation with respect to time and space [150]. The main drawback of this approach is its limitation to the derivation of differential system with moments less than second order. In fact, difficulty of derivation of high order problem is exponential with this approach.

2.3.3 Systematic approach

The derivation of the macroscopic equations from the Boltzmann equation is essentially based on Grad's moment method [81] together with the Gauss-Hermite quadrature in the velocity space [2,100,216,252,253]. This approach takes the advantages of Grad's approach and increases the expansion order, which helps going further ahead as required in variables describing far out-of-equilibrium phenomena.

2.4 Formulation

2.4.1 Boltzmann equation

From a statistical point of view, a given system can be presented by a distribution function $f(x, c, t)$ which represents the number of molecules at time t positioned between x and $x + dx$ which have velocities between c and $c + dc$.

If we suppose that an external force F (other than contact forces, *i.e.* collision) is applied on the fluid molecules, the velocity of molecules will change from c to $c + Fdt$ and their positions from x to $x + cdt$.
In the absence of collision, the number of molecules is conserved before and after applying the external force:

$$f\left(\mathbf{x}+\mathbf{c}dt, \mathbf{c}+\frac{\mathbf{F}}{m}dt, t+dt\right)d\mathbf{x}d\mathbf{c} - f\left(\mathbf{x},\mathbf{c},t\right)d\mathbf{x}d\mathbf{c} = 0 \tag{2.1}$$

While, in the presence of inter-molecules collisions, their will be no more conservation (This can be viewed as a deplet in of the population into region different from the position $(\mathbf{x}+\mathbf{c}dt, \mathbf{c}+\frac{\mathbf{F}}{m}dt)$. Hence, the evolution equation of the molecules number can be written as follows:

$$f\left(\mathbf{x}+\mathbf{c}dt, \mathbf{c}+\frac{\mathbf{F}}{m}dt, t+dt\right)d\mathbf{x}d\mathbf{c} - f\left(\mathbf{x},\mathbf{c},t\right)d\mathbf{x}d\mathbf{c} = \Omega(f)d\mathbf{x}d\mathbf{c}dt \tag{2.2}$$

where Ω represents the collision operator which is defined as the rate of change between the final and initial states of the distribution function. By dividing the previous equation by $d\mathbf{x}d\mathbf{c}dt$ and taking the limit $dt \to 0$, one finds:

$$\lim_{dt\to 0}\frac{f\left(\mathbf{x}+\mathbf{c}dt, \mathbf{c}+\frac{\mathbf{F}}{m}dt, t+dt\right)d\mathbf{x}d\mathbf{c} - f\left(\mathbf{x},\mathbf{c},t\right)d\mathbf{x}d\mathbf{c}}{d\mathbf{x}d\mathbf{c}dt} = \frac{df}{dt} = \Omega(f) \tag{2.3}$$

From the above equation, one can find that the total rate of change of the distribution function is equal to rate of the collision.
Since f is a function of $\mathbf{x}$, $\mathbf{c}$ and t, then its differential can be expanded as:

$$df = \frac{\partial f}{\partial t}dt + \frac{\partial f}{\partial \mathbf{x}}d\mathbf{x} + \frac{\partial f}{\partial \mathbf{c}}d\mathbf{c} \tag{2.4}$$

So, its total time derivative reads:

$$\frac{df}{dt} = \frac{\partial f}{\partial t} + \frac{\partial f}{\partial \mathbf{x}}\frac{d\mathbf{x}}{dt} + \frac{\partial f}{\partial \mathbf{c}}\frac{d\mathbf{c}}{dt} \tag{2.5}$$

Or:

$$\frac{df}{dt} = \mathbf{c}\frac{\partial f}{\partial \mathbf{x}} + \mathbf{a}\frac{\partial f}{\partial \mathbf{c}} + \frac{\partial f}{\partial t} \tag{2.6}$$

where $\mathbf{a}$ is the acceleration and can be related to force $\mathbf{F}$ by Newton's second law as $\mathbf{a} = \frac{\mathbf{F}}{m}$. By combining equation (2.3) and (2.6), the Boltzmann transport equation can be written as:

$$\mathbf{c}\frac{\partial f}{\partial \mathbf{x}} + \frac{\mathbf{F}}{m}\frac{\partial f}{\partial \mathbf{c}} + \frac{\partial f}{\partial t} = \Omega(f) \tag{2.7}$$

For a problem with dimension "D", $\frac{\partial f}{\partial \mathbf{x}}$ and $\frac{\partial f}{\partial \mathbf{c}}$ must be substituted by gradients $\nabla_x f$ and $\nabla_c f$ as follows:

$$\nabla_x f = \left(\frac{\partial f}{\partial x^1}, ..., \frac{\partial f}{\partial x^n}\right)^t \tag{2.8}$$

$$\nabla_c f = \left(\frac{\partial f}{\partial c^1}, ..., \frac{\partial f}{\partial c^n} \right)^t \tag{2.9}$$

Using the above expressions, the generalized Boltzmann equation is retrieved:

$$\mathbf{c} \cdot \nabla_x f + \frac{\mathbf{F}}{m} \cdot \nabla_c f + \frac{\partial f}{\partial t} = \Omega(f) \tag{2.10}$$

The relationships between the equation (2.10) and macroscopic quantities such as fluid density ρ, fluid velocity vector $\mathbf{u}$ and internal energy e, are given by:

$$\rho(x,t) = \int m f\,(x,c,t)\, d\mathbf{c} \tag{2.11}$$

$$\rho(x,t)\mathbf{u}(r,t) = \int m\mathbf{c} f\,(x,c,t)\, d\mathbf{c} \tag{2.12}$$

$$\rho(x,t)e(r,t) = \frac{1}{2}\int m\mathbf{u}_0^2 f\,(x,c,t)\, d\mathbf{c} \tag{2.13}$$

where m is the molecular mass and $\mathbf{u}_0$ is the peculiar velocity, $\mathbf{u}_0 = \mathbf{c} - \mathbf{u}$, which is the particle velocity relative to the local mean fluid velocity.

Equations (2.11), (2.12), and (2.13) are the equations of mass, momentum and energy conservation, respectively.
In kinetic theory, the internal energy is expressed by:

$$e = \frac{D}{2m} k_B T \tag{2.14}$$

Recall that D is the dimension of the problem, k_B is the Boltzmann constant and T is the temperature. The equation of state can be written as:

$$P = \rho \frac{k_B T}{m} = \rho R_g T = \rho c_s^2 \tag{2.15}$$

where P is the pressure, R_g is the gas constant and c_s is equivalent to the speed of sound.

2.4.2 Collision term

An expression of the collision operator Ω is required to solve the Boltzmann equation. The generalized form of the collision is given by [95, 211]:

$$\Omega(f) = \frac{1}{m}\int \|\mathbf{c}_1 - \mathbf{c}\| \left(f' f_1' - f f_1 \right) dS d\mathbf{c}_1 \tag{2.16}$$

where dS is the collision cross section. Before a binary collision, the number of molecular is $f' \equiv f(\mathbf{x}, \mathbf{c}', t)$ and $f_1' \equiv f(\mathbf{x}, \mathbf{c}_1', t)$ with velocity $\mathbf{c}'$ and $\mathbf{c}_1'$, respectively. After collision, the number of molecular becomes $f \equiv f(\mathbf{x}, \mathbf{c}, t)$ and $f_1 \equiv f(\mathbf{x}, \mathbf{c}_1, t)$ with velocity $\mathbf{c}$ and

$\mathbf{c}_1$, respectively.

The collision operator suggested by Bhatnagar, Gross and Krook [15] defines the collision process as a relaxation of the distribution function f toward the equilibrium state f^{eq}. The relaxation time is on order of the mean time between two successive collisions of particles. The expression of BGK-collision is given by:

$$\Omega(f) = \frac{(f - f^{eq})}{\tau} \tag{2.17}$$

This simplified expression is used henceforth in the manuscript. Not just for its simplicity but also because this expression is sufficient to define the fluid characteristics and to recover the macroscopic conservation of mass, momentum and energy.

2.4.3 From the Boltzmann equation to the lattice Boltzmann equation

Using the BGK approximation (2.17), in the absence of external force, the Boltzmann equation (2.10) becomes:

$$\frac{\partial f}{\partial t} + \mathbf{c} \cdot \nabla_x f = \frac{1}{\tau}(f - f^{eq}) \tag{2.18}$$

When a particular lattice is given, the discretization of the above equation for each lattice direction k reads:

$$\frac{\partial f_k}{\partial t} + \mathbf{c}_k \cdot \nabla_x f_k = \frac{1}{\tau}(f_k - f_k^{eq}) \tag{2.19}$$

where f_k is the discretized velocity distribution function along direction k.
Equation includes two terms fundamental to the theory behind this method. The term on the l.h.s. called propagation, modeling the displacement of a group of particles having the same lattice speed to another lattice in the domain of discretization. On the other hand, the term on the r.h.s. called collision, expresses the change in number of particles due to intermolecular short range interactions. So, computation can be split into collision then streaming steps.
Let us denote $\frac{Df_k}{Dt}$ the total derivative of f_k that reads:

$$\frac{Df_k}{Dt} = \frac{f_k(\mathbf{x} + \delta t c_k, t + \delta t) - f_k(\mathbf{x}, t)}{\delta t} \tag{2.20}$$

This derivative is equivalent to the substantial derivative with velocity c_k, *i.e.*

$$\frac{Df_k}{Dt} = \frac{\delta f_k}{\delta t} + c_k \cdot \nabla_x f_k \tag{2.21}$$

So approaching (2.20) and (2.21) and introducing into equation (2.19) leads the following equation:

$$f_k(\mathbf{x} + \mathbf{c}_k \delta t, t + \delta t) = f_k(\mathbf{x}, t) - \frac{\delta t}{\tau}(f_k(\mathbf{x}, t) - f_k^{eq}(\mathbf{x}, t)) \tag{2.22}$$

which can be discretized straightforwardly in space and time.
An example of a lattice used in the LBM is the D2Q9 lattice, see figure 2.1, where the velocity assumed only quantified values. More details are given in section 2.6. In the

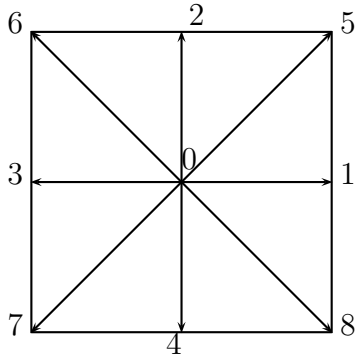

FIGURE 2.1 – Scheme of D2Q9 lattice.

presence of external forces, the generalized Lattice Boltzmann equation can be written as:

$$f_k(\mathbf{x} + \mathbf{c}_k\delta t, t + \delta t) = f_k(\mathbf{x}, t) + \frac{\delta t}{\tau}\left(f_k(\mathbf{x}, t) - f_k^{eq}(\mathbf{x}, t)\right) + \delta t\mathbf{F}_k \tag{2.23}$$

2.4.4 H-theorem

In order to introduce the equilibrium distribution function we define first the following function $H(t)$ as:

$$H(t) = \int f(\mathbf{x}, \mathbf{c}, t)\log\left(f(\mathbf{x}, \mathbf{c}, t)\right) d\mathbf{x}d\mathbf{c} \tag{2.24}$$

The following proof was given by Boltzamnn [83]. Differentiating the above expression with the respect to time and applying Reynolds transport theorem (velocity and space domains being time independent), the following form is got:

$$\frac{dH(t)}{dt} = \int \left(1 + \log\left(f(\mathbf{x}, \mathbf{c}, t)\right)\right)\frac{\partial f}{\partial t}d\mathbf{x}d\mathbf{c} \tag{2.25}$$

By supposing that system is space uniform, f depends only on t. Under this assumption, the above equation can be given by:

$$\frac{dH(t)}{dt} = \int \left(1 + \log\left(f(\mathbf{x}, \mathbf{c}, t)\right)\right)\Omega(f)d\mathbf{x}d\mathbf{c} \tag{2.26}$$

Introducing the expression of $\Omega(f)$ given in equation (2.16), one gets [211]:

$$\frac{dH(t)}{dt} = \frac{1}{m}\int \|\mathbf{c}_1 - \mathbf{c}\|\left(f'f_1' - ff_1\right) dSd\mathbf{c}_1\left(1 + \log\left(f\right)\right) d\mathbf{x}d\mathbf{c} \tag{2.27}$$

Identically for f_1, we get:

$$\frac{dH(t)}{dt} = \frac{1}{m}\int \|\mathbf{c}_1 - \mathbf{c}\|\left(f'f_1' - ff_1\right) dSd\mathbf{c}_1\left(1 + \log\left(f_1\right)\right) d\mathbf{x}d\mathbf{c} \tag{2.28}$$

Adding equation (2.27) to equation (2.28) side by side, we get:

$$\frac{dH(t)}{dt} = \frac{1}{2m}\int \|\mathbf{c}_1 - \mathbf{c}\| \left(f^{'} f_1^{'} - f f_1\right) dS d\mathbf{c}_1 \left(2 + \log\left(f f_1\right)\right) d\mathbf{x} d\mathbf{c} \tag{2.29}$$

The same holds for $f^{'} f_1^{'}$:

$$\frac{dH(t)}{dt} = \frac{1}{2m}\int \|\mathbf{c}_1^{'} - \mathbf{c}^{'}\| \left(f f_1 - f^{'} f_1^{'}\right) dS^{'} d\mathbf{c}_1^{'} \left(2 + \log\left(f^{'} f_1^{'}\right)\right) d\mathbf{x} d\mathbf{c}^{'} \tag{2.30}$$

As $dS = dS^{'}$,$\|\mathbf{c}_1^{'} - \mathbf{c}^{'}\| = \|\mathbf{c}_1 - \mathbf{c}\|$ and $d\mathbf{c}^{'} d\mathbf{c}_1^{'} = d\mathbf{c}_1 d\mathbf{c}$, by taking the difference of equations (2.29) and (2.30), we retrieve the following equation:

$$\frac{dH(t)}{dt} = \frac{1}{4m}\int \|\mathbf{c}_1 - \mathbf{c}\| \left(f^{'} f_1^{'} - f f_1\right) dS d\mathbf{c}_1 \left(\log\left(f f_1\right) - \log\left(f^{'} f_1^{'}\right)\right) d\mathbf{x} d\mathbf{c} \tag{2.31}$$

Since log is an increasing function, it comes immediately that:

$$\forall (a, b) \in \Re^2, (a - b)(\log(b) - \log(a)) \leq 0 \tag{2.32}$$

we find:

$$\forall t \in \Re_+^*, \frac{dH(t)}{dt} \leq 0 \tag{2.33}$$

Based on the above equation, H decreases until reaches an equilibrium value, when $\frac{dH(t)}{dt} = 0$. Hence, at equilibrium, this leads to:

$$f^{eq} f_1^{eq} = f^{'eq} f_1^{'eq} \tag{2.34}$$

Thus,

$$\log(f^{eq}) + \log(f_1^{eq}) = \log(f^{'eq}) + \log(f_1^{'eq}) \tag{2.35}$$

Hence, $\log(f^{eq})$ is an invariant summation function at the collision step which vanishes collision integrals given in equation (2.31). So, $\log(f^{eq})$ can be written as:

$$\log(f^{eq}) = a(x) + b(x)c + c(x)c^2 \tag{2.36}$$

and f^{eq} is deduced as:

$$f^{eq} = K^{'} exp(a(x) + b(x)c + c(x)c^2) \tag{2.37}$$

The coefficients a, b and c can be calculated with use of the macroscopic quantities as detailed in [102]. By noticing that the equilibrium function depends not on x, the equilibrium Maxwell distribution function reads:

$$f^{eq} = \frac{\rho}{(2\pi R_g T)^{\frac{3}{2}}} exp\left[-\frac{(\mathbf{c} - \mathbf{u})^2}{2R_g T}\right] \tag{2.38}$$

which can be written also as:

$$f^{eq} = \rho\left(\frac{m}{2\pi k_B T}\right)^{\frac{3}{2}} exp\left[-\frac{m(\mathbf{c} - \mathbf{u})^2}{2k_B T}\right] \tag{2.39}$$

where c_s is given by:

$$c_s^2 = \frac{k_B T}{m} = R_g T \tag{2.40}$$

The lattice Boltzmann equation can be viewed either as a special discrete case of the Boltzmann equation or a minimal form of the Boltzmann equation in which the microscopic kinetic principles are preserved so to recover the hydrodynamic behavior at macroscopic scale. Therefore, the LBM is based on a particle picture, but principally aims to predict macroscopic properties. This scale-bridging nature of the LBM is a fundamental advantage that leads to considering the essential microscopic or mesoscopic mechanisms while recovering the macroscopic laws and properties at affordable computational cost.

The discrete equilibrium moments are given by:

$$\rho = \sum_k f_k^{eq} \tag{2.41}$$

$$\rho \mathbf{u} = \sum_k \mathbf{c}_k f_k^{eq} \tag{2.42}$$

$$\Pi = \sum_k \mathbf{c}_k \mathbf{c}_k f_k^{eq} = p\mathbf{I} + \rho \mathbf{u}\mathbf{u} \tag{2.43}$$

2.4.5 Equilibrium distribution function

For low Mach number, the equilibrium distribution function can be written as follows [98]:

$$f^{eq} = exp\left[-\frac{(\mathbf{c}-\mathbf{u})^2}{2c_s^2}\right] = exp\left[-\frac{\mathbf{c}^2}{2c_s^2}\right] exp\left[-\frac{\mathbf{u}^2 - 2\mathbf{u}\cdot\mathbf{c}}{2c_s^2}\right] \tag{2.44}$$

Using Taylor series expansion, the very last exponential term of the above equation reads:

$$\begin{aligned} exp\left[-\frac{\mathbf{u}^2 - 2\mathbf{u}\cdot\mathbf{c}}{2c_s^2}\right] &\approx 1 - \frac{\mathbf{u}^2 - 2\mathbf{u}\cdot\mathbf{c}}{2c_s^2} + \frac{(\mathbf{u}^2 - 2\mathbf{u}\cdot\mathbf{c})^2}{8c_s^4} + O\left(u^3\right) \\ &\approx 1 - \frac{\mathbf{u}^2}{2c_s^2} + \frac{\mathbf{u}\cdot\mathbf{c}}{c_s^2} + \frac{(\mathbf{u}\cdot\mathbf{c})^2}{2c_s^4} + O\left(u^3\right) \end{aligned} \tag{2.45}$$

Introducing this expansion into the equilibrium distribution function (2.44), yields:

$$f^{eq} = \frac{\rho}{2\pi c_s^2} exp\left[-\frac{\mathbf{c}^2}{2c_s^2}\right]\left[1 - \frac{\mathbf{u}^2}{2c_s^2} - \frac{\mathbf{u}\cdot\mathbf{c}}{c_s^2} + \frac{(\mathbf{u}\cdot\mathbf{c}^2)}{2c_s^4}\right] + O\left(u^3\right) \tag{2.46}$$

Writing equation (2.46) in its discrete form in velocity space, we get the following expression of the equilibrium distribution function:

$$f^{eq} = \rho w_k \left(1 + \frac{\mathbf{c}_k\cdot\mathbf{u}}{c_s^2} + \frac{(\mathbf{c}_k\cdot\mathbf{u})^2}{2c_s^4} + \frac{\mathbf{u}^2}{2c_s^2}\right) \tag{2.47}$$

where w_k are the weight factors given by:

$$w_k = (2\pi c_s^2)^{-\frac{3}{2}} exp\left[-\frac{\mathbf{c}_k^2}{2c_s^2}\right] \tag{2.48}$$

2.4.6 The forcing schemes

Many physical problems require introducing extra or external body forces like gravity. The incorporation of external body forces in a lattice Boltzmann model was approached in different ways in the literature [22]. Mohamad and Kuzmin [184] presented a comparison between the most common schemes for incorporating forces:

— The scheme in which the force term is added to the collision operator as follows [165, 251]:

$$F_k = w_k \frac{\mathbf{F}_k \cdot \mathbf{c}_k}{c_s^2} \tag{2.49}$$

— The scheme in which the velocity expression is modified as follows [22]:

$$\mathbf{u}(\mathbf{x}, t) = \frac{1}{\rho} \sum_k \mathbf{c}_k f_k(\mathbf{x}, t) + \frac{\tau \mathbf{F}}{\rho} \tag{2.50}$$

This expression is based on Newton's second law where no extra terms are added to the collision process.

— Guo *et al.* [92] scheme for which:

$$F_k = w_k \left(1 - \frac{1}{2\tau}\right) \left(\frac{\mathbf{c}_k - \mathbf{u}}{c_s^2} + \frac{\mathbf{c}_k(\mathbf{c}_k \cdot \mathbf{u})}{\mathbf{c}_s^4}\right) \cdot \mathbf{F} \tag{2.51}$$

In this case the force term is added to the collision where the velocity is given by:

$$\mathbf{u} = \frac{1}{\rho} \sum_k \mathbf{c}_k f_k + \frac{\mathbf{F}\Delta t}{2\rho} \tag{2.52}$$

2.5 Initial and boundary conditions

2.5.1 Initial conditions

In transient simulations, correct definition of the initial conditions is of paramount importance in LBM simulations. Two cases arise. The first one is the case of zero initial velocity field. One should define flow and temperature fields then calculate the local equilibrium distribution function f_k^{eq} which is assigned to the distribution function f_k:

$$f_k = f_k^{eq} \tag{2.53}$$

The second case of velocity field different from zero, much attention must be taken there because it is important to calculate the initial density distribution functions properly. In this case, one has to calculate also the non-equilibrium part of the distribution function. Different approaches can be found in the literature [179, 265, 283].

2.5.2 Boundary conditions

Considering the boundary conditions is a critical step for both the accuracy and stability of the numerical method [37, 322]. The difficulty arises from the fact that there is no physical guideline about the behavior of the distribution function on the boundaries. Only the macroscopic information is defined at the boundaries and we need to transpose this information into the distribution functions. In order to overcome this issue, many approaches have been developed.
The unknown distribution functions at each boundary limits are represented in figure 2.2 with dashed arrows.

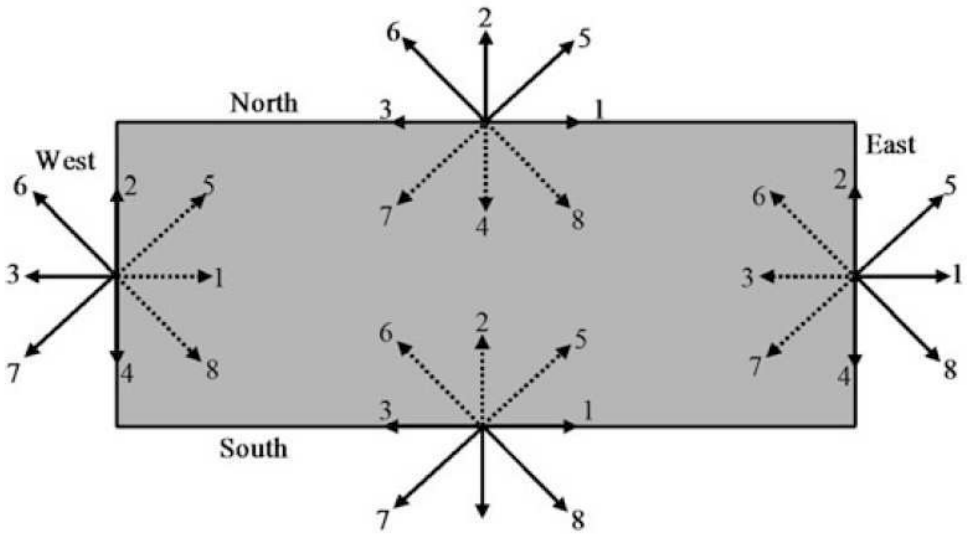

FIGURE 2.2 – Boundary distribution functions [186].

Bounce-Back or no-slip boundary condition

— Full way:

The most popular boundary condition for the LBM is the bounce-back scheme also called no-slip boundary or wall boundary condition. This scheme is suitable to model zero velocity components normal and tangential to the given boundary. It finds its origin from the boundary conditions of lattice gas and is well documented in the literature. The fundamental concept of this scheme is that the out-going distribution functions are reflected back into the domain. The main advantages of this configuration is its straightforwardness

to implement and the fact that it assures the conservation of mass and momentum on the wall nodes. This configuration requires just one time step to be performed and is the easiest ever. Taking the example of West boundary in figure 2.2, the explicit numerical expression for a D2Q9 model when applying this boundary condition is:

$$f_5 = f_7, f_1 = f_3, f_8 = f_6 \tag{2.54}$$

— Half way:
The wall condition can be carried out over one (simple bounce-back) or two steps (half-way bounce back) as described in [311]. The alternate interpretation is that the bounce-back condition corresponds to a zero-velocity boundary condition that is applied half-way from the wall and so between nodes (line at $\Delta y/2$ in figure 2.3). Thus, the unknown distribution functions at $\Delta y/2$ are calculated through the no-slip half-way aside the exact wall.

It is straightforward to implement and gives second-order accurate simulation results for flat boundaries aligned with the Cartesian axes of the lattice, although in more complex cases this degrades to first-order accuracy [196]. It is also computationally cheap and locally applicable.

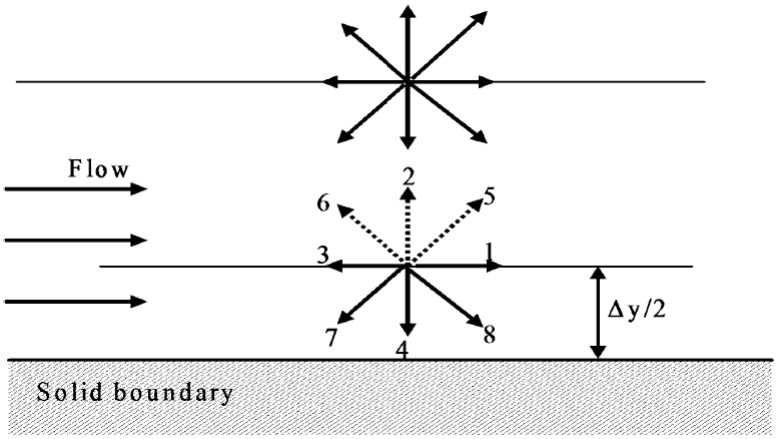

FIGURE 2.3 – Half way bounce back.

Zou-He boundary condition

In many situations, we would like to model flows with specified velocity or pressure at the boundary. This velocity/pressure boundary condition model was proposed by Zou and He in 1997 [322]. In this method, the local conservation of mass and momentum are used to find the missing particle distribution functions at the wall. However, to eliminate additional unknowns in the equations, they proposed to use the bounce-back scheme only for the non-equilibrium part of the distribution function normal to the wall. To illustrate this, we consider the case of an inlet boundary with known velocity or pressure. After the streaming step has been carried out, f_0, f_2, f_3, f_4, f_6 and f_7 are known. The undetermined distribution functions are f_1, f_5, f_8 and ρ or u.

These values are calculated in terms of the known distribution functions and the given inlet velocity or pressure as follows:

— Velocity boundary condition:

In the case of West boundary, the normal velocity u_w is imposed, while the other component of the velocity parallel to the boundary, v_w, is set to zero. The conservation equations are given by:

$$\rho_w = f_0 + f_1 + f_2 + f_3 + f_4 + f_5 + f_6 + f_7 + f_8 \tag{2.55}$$

$$\rho_w u_w = f_1 + f_5 + f_8 - f_6 - f_7 - f_8 \tag{2.56}$$

$$v_w = f_2 + f_5 + f_6 - f_4 - f_7 - f_8 \tag{2.57}$$

Gathering together the unknown distributions and setting $v_w = 0$, we obtain:

$$f_1 + f_5 + f_8 = \rho_w - (f_0 + f_2 + f_3 + f_4 + f_6 + f_7) \tag{2.58}$$

$$f_1 + f_5 + f_8 = \rho_w u_w - + f_6 + f_7 + f_8 \tag{2.59}$$

$$f_5 - f_8 = -f_2 - f_6 + f_4 + f_7 \tag{2.60}$$

Equations (2.58-2.60) are not sufficient to solve the problem as four unknowns have to be determined. The needed additional equation is obtained by assuming bounce back rule still hold for the non-equilibrium part of the particle distribution normal to the boundary, which can written in this case as follows:

$$f_1^{neq} = f_3^{neq} \tag{2.61}$$

that is

$$f_1 - f_1^{eq} = f_3 - f_3^{eq} \tag{2.62}$$

and

$$f_1 = f_3 - f_3^{eq} + f_1^{eq} \tag{2.63}$$

This yield finally the following solution:

$$\rho_w = \frac{1}{1 - u_w} \left(f_0 + f_2 + f_4 + 2\left(f_3 + f_6 + f_7\right)\right) \tag{2.64}$$

$$f_1 = f_3 + \frac{2}{3}\rho_w u_w \tag{2.65}$$

$$f_5 = f_7 - \frac{1}{2}\left(f_2 - f_4\right) + \frac{1}{6}\rho_w u_w + \frac{1}{2}\rho_w v_w \tag{2.66}$$

$$f_8 = f_6 + \frac{1}{2}\left(f_2 - f_4\right) + \frac{1}{6}\rho_w u_w - \frac{1}{2}\rho_w v_w \tag{2.67}$$

Following the same procedure, one can find the other boundary conditions.
- Pressure condition: Now let us turn to the pressure (density) flow boundary condition. The same case of the inlet boundary is studied in which the condition $\rho = \rho_w$ is applied, while the component of the velocity parallel to the boundary, v_w, is set to zero. The equations are given by:

$$\rho_w = f_0 + f_1 + f_2 + f_3 + f_4 + f_5 + f_6 + f_7 + f_8 \tag{2.68}$$

$$\rho_w u_w = f_1 + f_5 + f_8 - f_6 - f_7 - f_3 \tag{2.69}$$

$$v_w = f_2 + f_5 + f_6 - f_4 - f_7 - f_8 \tag{2.70}$$

Gathering together the unknown distributions and setting $v_w = 0$, we obtain:

$$f_1 + f_5 + f_8 = \rho_w - (f_0 + f_2 + f_3 + f_4 + f_6 + f_7) \tag{2.71}$$

$$f_1 + f_5 + f_8 = \rho_w u_w + f_6 + f_7 + f_8 \tag{2.72}$$

$$f_5 - f_8 = -f_2 - f_6 + f_4 + f_7 \tag{2.73}$$

Once more, consistency of the above equations and assuming that the bounce back rule holds for the non-equilibrium part of the particle distribution normal to the boundary, yield the following solution:

$$u_w = 1 - \frac{f_0 + f_2 + f_4 + 2\,(f_3 + f_6 + f_7)}{\rho_w} \tag{2.74}$$

$$f_1 = f_3 + \frac{2}{3}\rho_w u_w \tag{2.75}$$

$$f_5 = f_7 - \frac{1}{2}\,(f_2 - f_4) + \frac{1}{6}\rho_w u_w + \frac{1}{2}\rho_w v_w \tag{2.76}$$

$$f_8 = f_6 + \frac{1}{2}\,(f_2 - f_4) + \frac{1}{6}\rho_w u_w - \frac{1}{2}\rho_w v_w \tag{2.77}$$

Following the same procedure, one can find the other boundary conditions.

Symmetry boundary condition

The symmetry boundary condition is the same as slip boundary conditions. It is applied on a stress-free surface. Therefore, it's called also the free-slip boundary condition. The particular distribution functions normal to the boundary are reflected and those parallel to the boundary are propagated. In such a case, the physical boundary conditions are:

$$\mathbf{u}.\mathbf{n} = 0, \frac{\partial \mathbf{u}}{\partial n} = \mathbf{0} \tag{2.78}$$

In generally, this boundary condition is given by:

$$f_k(x^{'}, y) = f_{k_s}(x, y) \tag{2.79}$$

where k_s the direction symmetric to k and x' are the boundary positions that are symmetric to x across the physical boundary as shown in figure 2.4.

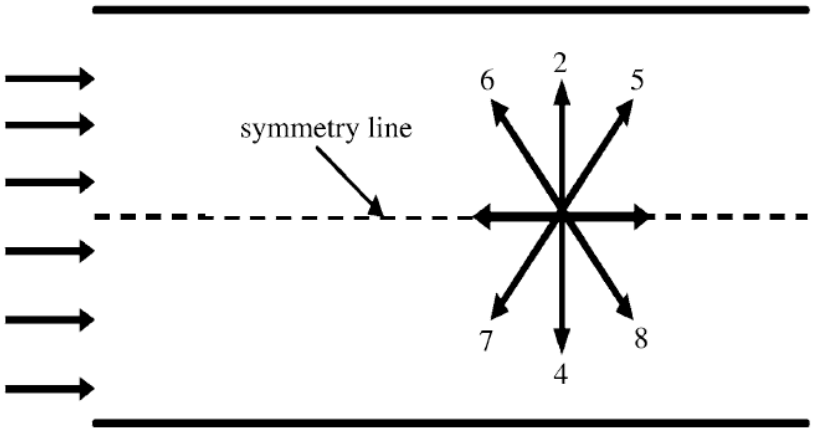

FIGURE 2.4 – Symmetry boundary condition.

Dirchlet boundary conditon

When using a Dirichlet boundary condition, one prescribes the value of a variable at the boundary, e.g. $T(y) = constant$. In the case of constant velocity, one can use the Zhou-He boundary condition 2.5.2. In the case of constant temperature ($T = T_w$), we can write the flux conservation equation at the boundary as follows:

$$g_5 - g_5^{eq} + g_7 - g_7^{eq} = 0 \tag{2.80}$$

$$g_1 - g_1^{eq} + g_3 - g_3^{eq} = 0 \tag{2.81}$$

$$g_8 - g_8^{eq} + g_6 - g_6^{eq} = 0 \tag{2.82}$$

where g^{eq} is the equilibrium distribution function at the boundary, function of T_w and g is the distribution function known from the streaming process. Thus, the missing distribution functions g_5, g_1 and g_8 can be calculated.

In the case of zero velocity at the same boundary, this condition reduces to:

$$g_5 = T_w(w(5) + w(7)) - g_7 \tag{2.83}$$

$$g_1 = T_w(w(1) + w(3)) - g_3 \tag{2.84}$$

$$g_8 = T_w(w(8) + w(6)) - g_6 \tag{2.85}$$

Following the same process, one can find the other boundary conditions.

Convective heat flux boundary condition

Taking into account the continuity of flux at the boundary, we write:

$$-\lambda \mathbf{n} \cdot \nabla T = h(T - T_a) \tag{2.86}$$

where $\mathbf{n}$ is the outward normal vector to the boundary, h is the convective heat transfer coefficient and T_a is the outside temperature. Then, it can be written as:

$$-\lambda \frac{\partial T}{\partial n} = h(T - T_a) \tag{2.87}$$

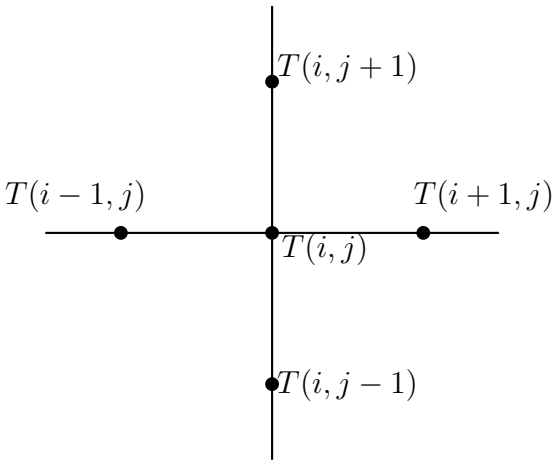

FIGURE 2.5 – Scheme of the implimented boundary condition.

Let us take the example of West boundary, see figure 2.5. By discretization of this last equation, we can write:

$$-\lambda \frac{T(i, j+1) - T(i, j)}{\triangle\, y} = h(T(i, j) - T_{envi}) \tag{2.88}$$

$$T(i, j+1) - T(i, j) = \frac{-h \triangle\, y}{\lambda}(T(i, j) - T_{envi}) \tag{2.89}$$

$$T(i, j)\left(1 - \frac{h \triangle\, y}{\lambda}\right) = T(i, j+1) + \frac{h \triangle\, y}{\lambda} T_{envi} \tag{2.90}$$

$$T(i, j) = \frac{1}{a} T(i, j+1) + \frac{b}{a} T_{envi} \tag{2.91}$$

where $a = \left(1 - \frac{h\triangle y}{\lambda}\right)$ and $b = \frac{h\triangle y}{\lambda}$.
Let us take the example of the North boundary in figure 2.2. By discretization of equation (2.5.2), we can write:

$$T(i,m) = \frac{1}{a}T(i,m-1) + \frac{b}{a}T_{envi} \tag{2.92}$$

In LBM, this boundary condition reads merely:

$$f_k(i,m) = \frac{1}{a}f_k(i,m-1) + \frac{b}{a}T_{envi} \tag{2.93}$$

Neumann boundary condition

The Neumann boundary condition consists of applying a constant flux at the boundary. Therefore, it is also called constant flux boundary condition. From a physical point of view, the normal gradient to the boundary of a variable, let us say the temperature T, at the boundary is set, e.g. $\partial_n T(n) = \text{constant}$. In LBM, this boundary condition is introduced by using a finite difference scheme. It can be written as flows:

$$-q = -\lambda\frac{\partial T}{\partial y} \tag{2.94}$$

using a finite difference scheme, we find:

$$q = \lambda\frac{T(i,j+1) - T(i,j)}{\Delta y} \tag{2.95}$$

This can be transposed in terms of distribution function immediately as follows:

$$q = \lambda\frac{g_k(i,j+1) - g_k(i,j)}{\Delta y} \tag{2.96}$$

$$g_k(i,j+1) = g_k(i,j) + \frac{q\Delta y}{\lambda} \tag{2.97}$$

where q is the value of the constant inward heat flux, λ the thermal conductivity.

Adiabatic boundary condition

The adiabatic boundary condition is a special case of Neuman boundary condition. In such a case, the wall is considered insulated with heat flux q equal to zero. To introduce this boundary condition in LBM, the same steps mentioned above are followed:

$$0 = \lambda\frac{T(i,j+1) - T(i,j)}{\Delta y} \tag{2.98}$$

$$T(i,j+1) = T(i,j) \tag{2.99}$$

It is description on LBM reads then:

$$g_k(i,j+1) = g_k(i,j) \tag{2.100}$$

Periodic boundary condition

When periodicity exists for a given system, periodic boundary condition is applied to a repeating flow condition allowing to calculate only a part of that system response by setting variables on the sides of it equal. As shown in figure 2.6, the flow boundary conditions above the line "a" and below the line "b" are exactly the same. For this reason, modeling the flow distribution between these two lines and using periodic boundary conditions the problem will be solved correctly. The applied periodic boundary is as follows:
Line a:

$$f_{4,a} = f_{4,b}; f_{7,a} = f_{7,b} \text{and} f_{8,a} = f_{8,b} \tag{2.101}$$

Line b:

$$f_{2,b} = f_{2,a}; f_{5,b} = f_{5,a} \text{and} f_{6,b} = f_{6,a} \tag{2.102}$$

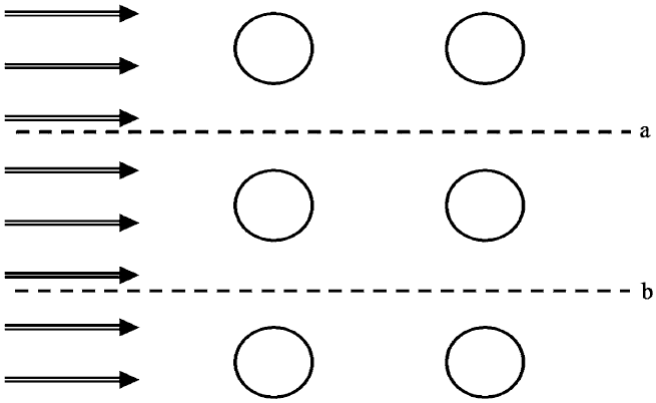

FIGURE 2.6 – Periodic boundary condition [186].

2.6 Lattice Models and isotropy

Numerous lattice Boltzmann equation (LBE) models have been presented in the literature in order to solve fluid flow problems. Each model has microscopic movement of the fluid particles. They are typically represented as DnQb where n is the number of dimensions and b is the number of microscopic velocity directions ($\mathbf{c}_k$). For example, D2Q9 represents a two-dimensional geometry with nine velocity directions. Particular attention must be paid to the choice of the numerical model because it may affect the entire theoretical framework.

2.6.1 Lattice structure

Wolf and Gladrow [297] presented a proof of necessary and sufficient conditions for lattice isotropy. Using the BGK model, Latt [150] found that there exists a constant c_s and a set of weights ω_k for the lattice velocities c_k such that the following equations are satisfied:

$$\sum_k \omega_k = 1 \tag{2.103}$$

$$\sum_k \omega_k \mathbf{c}_k = 0 \tag{2.104}$$

$$\sum_k \omega_k \mathbf{c}_{k\alpha} \mathbf{c}_{k\beta} = c_s^2 \delta_{\alpha\beta} \tag{2.105}$$

$$\sum_k \omega_k \mathbf{c}_{k\alpha} \mathbf{c}_{k\beta} \mathbf{c}_{k\gamma} = 0 \tag{2.106}$$

$$\sum_k \omega_k \mathbf{c}_{k\alpha} \mathbf{c}_{k\beta} \mathbf{c}_{k\gamma} \mathbf{c}_{k\delta} = c_s^4 \left(\delta_{\alpha\beta}\delta_{\gamma\delta} + \delta_{\alpha\gamma}\delta_{\beta\delta} + \delta_{\alpha\delta}\delta_{\beta\gamma}\right) \tag{2.107}$$

$$\sum_k \omega_k \mathbf{c}_{k\alpha} \mathbf{c}_{k\beta} \mathbf{c}_{k\gamma} \mathbf{c}_{k\delta} \mathbf{c}_{k\varepsilon} = 0 \tag{2.108}$$

where w_k is a set of lattice vector weights and must be selected for each lattice to fulfill these conditions. Several authors [71, 168] illustrated the lattices which fulfill these conditions such as D1Q3, D2Q7, D2Q9, D3Q15, D3Q19 and D3Q27. Let us take the example of a two-dimensional problem. In such a dimension, the D2Q9 is mostly used. In the D2Q9 lattice, three different w_k weights, see figure, are used:

— for w_k, k=0, is for the rest vector,
— for w_s, k=1,2,3,4, are for the short vectors,
— for w_l, k=5,6,7,8, are for the long vectors.

Then from the equations (2.103), (2.105) and (2.107), the following conditions arise:

$$\omega_0 + 4\omega_s + 4\omega_l = 1 \tag{2.109}$$

$$2\omega_s + 4\omega_l = c_s^2 \tag{2.110}$$

$$2\omega_s + 4\omega_l = 3c_s^4 \tag{2.111}$$

$$4\omega_l = c_s^4 \tag{2.112}$$

The solution for this system and for the other lattices used in this thesis are presented in the next subsections.

2.6.2 One-dimensional arrangements

Different one-dimensional arrangements exist in LBM, the most used is D1Q5, which is presented in figure 2.7 where the different parameters are as follows:
The sound speed: $c_s^2 = 1$ The weights: $w_k \begin{cases} \frac{1}{2}, & i = 0 \\ \frac{1}{6}, & i = 1, 2 \\ \frac{1}{12}, & i = 3, 4 \end{cases}$
The lattice velocity: $c_k \begin{cases} (0, 0, 0), & i = 0 \\ \left(\pm\frac{1}{3}c, 0, 0\right), & i = 1, 2 \\ \left(\pm\frac{1}{6}c, 0, 0\right), & i = 3, 4 \end{cases}$

FIGURE 2.7 – D1Q5 lattice.

2.6.3 Two-dimensional arrangements

Here w_k is defined as:

$$w_k = \begin{cases} \frac{4}{9}, & k = 0 \\ \frac{1}{9}, & k = 1, 3, 5, 7 \\ \frac{1}{36}, & k = 2, 4, 6, 8 \end{cases} \tag{2.113}$$

and c_k is as follows:

$$c_k = \begin{cases} (0, 0), & k = 0 \\ \lambda_k c \left[cos\left(\frac{(k-1)\pi}{4}\right), sin\left(\frac{(k-1)\pi}{4}\right)\right], & k \neq 0 \end{cases} \tag{2.114}$$

with λ_k is defined as:

$$\lambda_k = \begin{cases} 1, & k = 1, 3, 5, 7 \\ \sqrt{2}, & k = 2, 4, 6, 8 \end{cases} \tag{2.115}$$

In two-dimensional problems, D2Q9 arrangement is mostly used because it has a square grid of nodes and is easier to implement with good performance [199].
The speed of sound reads: $c_s^2 = \frac{1}{3}$. This expression can be derived from:

$$\sum_k w_k c_{k\alpha} c_{k\beta} = c_s^2 \delta_{\alpha\beta} \tag{2.116}$$

where $\delta_{\alpha\beta}$ is the Kronecker symbol. Thus, we have either $\sum_k w_k c_{kx} c_{kx} = c_s^2$ or $\sum_k w_k c_{ky} c_{ky} = c_s^2$. So, we can find in case of $\sum_k w_k c_{kx} c_{kx} = c_s^2$, for example, the following expression:

$$\sum_k w_k c_{kx} c_{kx} = 0 + \frac{1}{9}c^2 + 0 + \frac{1}{9}c^2 + 0 + \frac{1}{36}c^2 + \frac{1}{36}c^2 + \frac{1}{36}c^2 + \frac{1}{36}c^2 = \frac{1}{36}c^2 = c_s^2 \tag{2.117}$$

the weights: $w_k \begin{cases} \frac{4}{9}, & k = 0 \\ \frac{1}{9}, & k = 1..4 \\ \frac{1}{36}, & k = 5..8 \end{cases}$

and the lattice velocity: $c_k \begin{cases} (0,0,0), & k = 0 \\ (\pm c,0,0)\,(0,\pm c,0), & k = 1..4 \\ (\pm c,\pm c,0), & k = 5..8 \end{cases}$

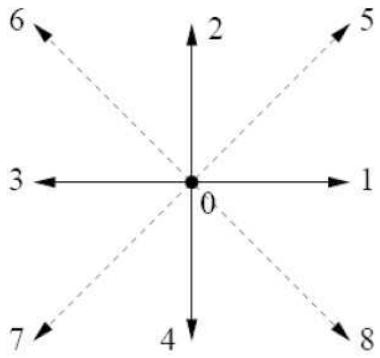

FIGURE 2.8 – D2Q9 lattice (recall of figure 2.1).

2.6.4 Three-dimensional arrangements

In three-dimensional problems, several arrangements are presented where the most representative is the D3Q19 [212]. It was shown that the D3Q15 arrangement has a small range of stability, while the D3Q27 model requires a higher computational effort. The D3Q19 arrangement is a good compromise.

The speed sound velocity: $c_s^2 = \frac{1}{3}$

The weights: $w_k \begin{cases} \frac{2}{9}, & k = 0 \\ \frac{1}{9}, & k = 1..6 \\ \frac{1}{72}, & k = 7..14 \end{cases}$

The lattice velocity: $c_k \begin{cases} (0,0,0), & k = 0 \\ (\pm c,0,0)\,(0,\pm c,0)\,(0,0,\pm c), & k = 1..6 \\ (\pm c,\pm c,\pm c), & k = 7..14 \end{cases}$

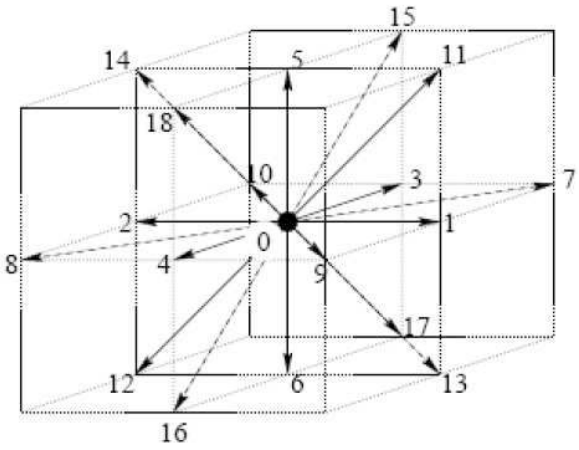

FIGURE 2.9 – D3Q19 lattice.

2.7 Unit conversion

When a given problem is dealt with, all physical quantities, such as pressure, temperature, velocity, density, are expressed in terms of physical unit using international system (IS) units, for instance. Using LBM technique, this quantities are provided in a dimensionless units called lattice units, instead. The translation between the physical and lattice units must therefore to be done. In order to achieve this conversion successfully, two conditions must be verified and satisfied. The first condition is the recovery of physical values in order to perform a correct simulation in relation with the "real world" system. The second one is to reach a high order of accuracy. There are two different ways to bind the lattice and physical units. The easiest method is to translate directly between the two sets of units by employing conversion factors for mass, time and length (and perhaps temperature). In the second method, the correspondence between the physical units and LBM units is achieved through dimensionless numbers (called also scale-independent numbers) via the principal of similarity. In this section, these two ways are discussed briefly.

2.7.1 Direct conversion

In this second approach, all physical quantities are given in lattice units. Thus, the translation between the lattice and physical units is made possible through the time step Δt and space step Δx. The physical velocity, speed of sound and viscosity are related to lattice units through:

$$u_{phy} = u_{lb}\frac{\Delta x}{\Delta t} \tag{2.118}$$

$$c_{s,phy} = c_{s,lb}\frac{\Delta x}{\Delta t} \tag{2.119}$$

$$\nu_p = \nu_{lb}\frac{\Delta x^2}{\Delta t} = c_{s,lb}^2\,(\tau - 1)\,\frac{\Delta x^2}{\Delta t} = c_{s,phy}^2\,(\tau - 1)\,\Delta t \tag{2.120}$$

here the subscript *phy* refers to physical quantities and the subscript *lb* refers to parameters expressed in lattice units. This leads to the expression of time step as follows:

$$\Delta t = \frac{\nu_{phy}}{c_{s,phy}^2\,(\tau - 1)} \tag{2.121}$$

Similarly, the space step is given by:

$$\Delta t = \frac{\nu_{phy}\sqrt{3}}{c_{s,phy}^2\,(\tau - 1)} \tag{2.122}$$

Any other physical quantities can be transformed into lattice units and vice versa.

2.7.2 Dimensionless formulation

Called also indirect conversion, this approach includes two-step. In the first step, the physical quantities are converted to a continuous dimensionless system which is independent of the simulation parameters with no physical unit associated. The second step, this dimensionless system is converted to a discrete lattice system which will be used in the simulation. The indirect conversion has shown to be much more appropriate compared to dimensional conversion [177]. This approach has the advantage that from the dimensionless units, the simulation result can be related to any physical system and so is much easier to work with.
In order to find the dimensionless numbers, it is required firstly to scale the governing equations, boundary conditions and all physical variables with characteristic values. Thus, the three systems: the physical scale (P), the dimensionless scale (D), and the discrete scale (LB), are defined in order to share the same values of the dimensionless numbers regardless the measurement units used to calculate them. First, the conversion from (P) to (D) is made through the choice of a characteristic length scale l_0 and time scale t_0. Second, the conversion from (D) to (LB) is made through the choice of a discrete space step Δx and time step Δt in order to maximize the accuracy of the simulation. Namely, the units are structured such that the dimensionless quantities are equivalent in all systems. Here is a graphical representation of this relationship:

$$\text{Physical scale(P)} \xrightarrow{l_0,t_0} \text{Dimensionless scale (D)} \xrightarrow{\Delta x,\Delta t} \text{Lattice scale (LB)}$$

Here we recall the dimensionless numbers which can be obtained from the governing equations and boundary conditions:

$$\text{Reynolds number} : Re = \frac{u_0 l_0}{\nu_{phy}} \tag{2.123}$$

$$\text{Mach number} : Ma = \frac{\nu_{phy}}{\nu_{sound}} \tag{2.124}$$

$$\text{Prandlt number} : Pr = \frac{C_{p,phy}\mu_{phy}}{\lambda_{phy}} \tag{2.125}$$

$$\text{Biot number} : Bi = \frac{h_{phy}l_0}{\lambda_{phy}} \tag{2.126}$$

In order to make the simulation consistent for different problems, and to get rid of physical units, it is better to rescale the problem from physical system to dimensionless system, in which we only care about values of variables and not their units. The conversion with dimensionless numbers, however, is preferred in this treatise, since it is much more convenient to show dimensionless results.

2.8 Lattice Boltzmann algorithm

The fluid flow simulations described in this thesis were performed by implementing a Lattice Boltzmann model using FORTRAN90 programming language. Figure 2.10 provides a flow chart scheme with the different steps of a standard LBM implementation which will be discussed in details in this section.

2.8.1 Discretization of the physical domain and making dimensionless the related parameters

As discussed in section 2.7, in this step, Lattice Boltzmann simulations should correctly model physical problems and so they should be able to correctly reflect the different mechanisms occurring there. This step proves challenging since all LBM simulations are performed with lattice variables and lattice units. In particular we have two constraints to observe when choosing the units for our simulations:

— The simulated system must be geometrically similar to the physical one,
— The chosen parameters must allow acceptable accuracy to be reached.

2.8.2 Choice of simulation parameters

In this step, some of the simulation parameters are already chosen from the previous step, such as the grid size, the Reynolds number, the density and viscosity, the relaxation time, the running time or the convergence criterion (whether a steady state exists). In

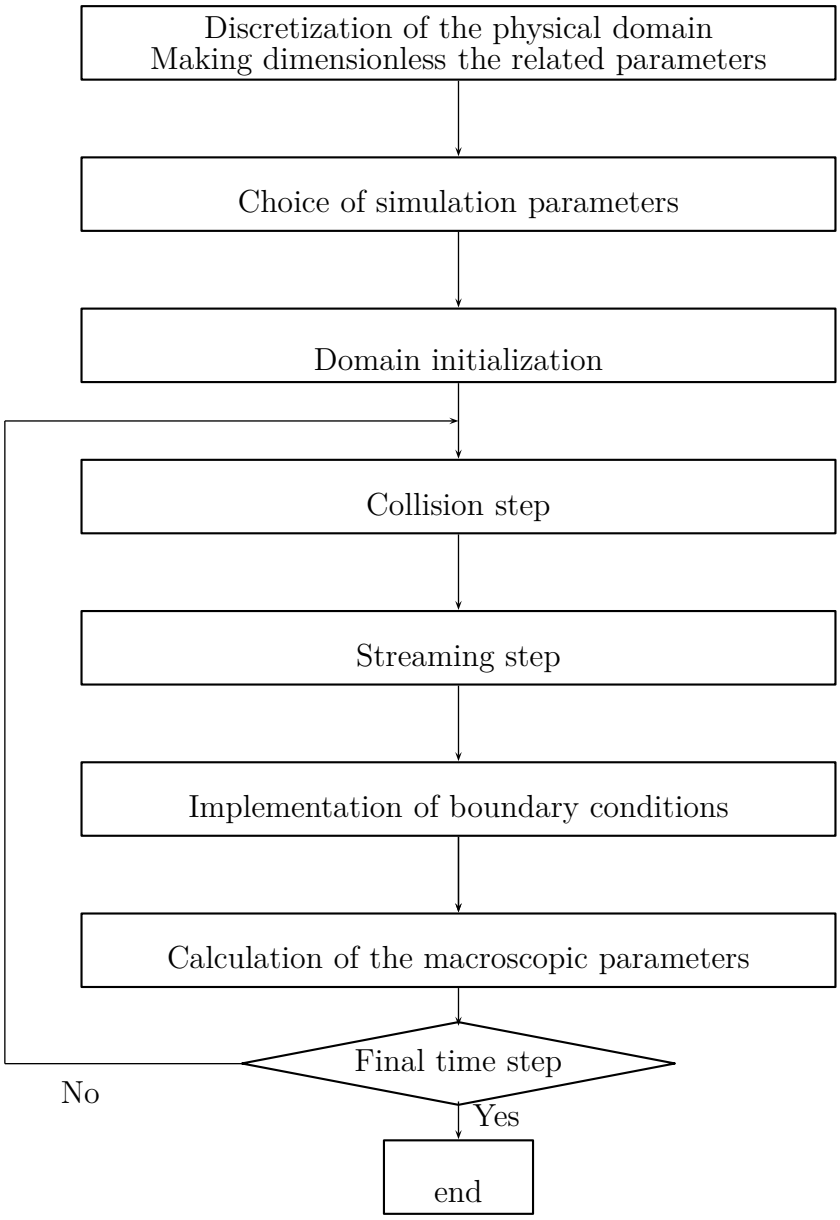

FIGURE 2.10 – LBM algorithm synoptic.

the LBM, the density is most commonly imposed as unity. In fact, the density can be expressed in lattice units as unitary via the normalization of the physical density by itself. This means that the initial density in the lattice will be unitary and that only small variations around the initial value are expected, given the incompressibility assumption of the method. The Reynolds number is chosen according to the physical case we want to model. The characteristic velocity of the lattice is set in order to be well below the compressibility limit, since the LBM is only valid for incompressible flows. The compressibility limit is related to the Mach number defined as the ratio between the maximum speed of the flow in lattice and the speed of sound in the lattice. The speed of sound (c_s) is a lattice constant and its squareis equal to the density variation over the pressure variations (at constant entropy) as defined in [150]:

$$c_s^2 = \frac{\partial p}{\partial \rho} \rightarrow c_s = \frac{1}{\sqrt{3}} \tag{2.127}$$

If the LBM computation leads to a velocity such that $u \geq 0.1c_s$, the solution will be rejected and the problem will be considered unsolvable with the present LBM and the corresponding set of parameters.

2.8.3 Domain initialization

The initial conditions for a typical CFD simulation are usually in terms of the velocity components, density and pressure. In the LBM, however, these conditions are not sufficient since a certain value must be assigned to the distribution functions. As discussed in section 2.5.1, one typical approach to solve this problem is to set the local initial distribution functions equal to the corresponding equilibrium distributions.
Just like any CFD simulation, we should then allow a transitory period necessary for reaching the steady state, whether the latter exists, to be performed. This way of implementing the initial conditions will be followed for all of the test cases presented in the next chapters.

2.8.4 Collision step

Entering the time loop, the post-collision state is calculated via the following equation:

$$f_k(x + c_k\Delta t, t + \Delta t) = f_k^{'}(x,t) - f_k^{neq}(x,t) \tag{2.128}$$

The collision of fluid particles is considered as a relaxation toward a local equilibrium. The distribution functions are calculated at each node as follows:

$$f_k^{neq}(x,t) = f_k(x,t) - f_k^{eq}(x,t) \tag{2.129}$$

$$f_k^{'}(x, t + \Delta t) = f_k^{eq}(x,t)) + \left(1 - \frac{1}{\tau}\right) f_k^{neq}(x,t) \tag{2.130}$$

2.8.5 Streaming step

In the streamingstep, the distribution functions resulting from the collision step are streamed to their neighbouring nodes according to their directions. If the lattice is uniform and the time step is set in order to achieve a lattice speed of 1, the distributions will travel exactly to their neighbouring nodes at every time step.
Applying equation (2.130) at time t, we find the distribution functions at time $t+1$ for the new location $x+c_k$. In fact, in equation (2.130), the streaming and collision processes are joined together in one equation only. However, from an implementation point of view, they are split into two separate processes as stated before. This means that, when we implement the method, we first calculate the distributions at time $t+1$ for the original positions x and successively stream them toward the new time step $(t+1)$ positions $x+c_k$. It can be presented by the following equation:

$$f_k(x + c_k\Delta t, t + \Delta t) = f_k^{'}(x, t + \Delta t) \tag{2.131}$$

2.8.6 Implementation of boundary conditions

As discussed in section 2.5.2, the boundary conditions are applied in this step depending on their type and on the macroscopic property (velocity, pressure or temperature) we want to apply. They are chosen in order to model correctly the physical boundaries of the problem and the main challenge consists in translating the macroscopic information to the microscopic distribution functions without affecting the numerical accuracy or stability.

2.8.7 Calculation of the macroscopic parameters

In this step the macroscopic parameters, typically density, velocity, pressure(and temperature) are calculated using equations ((2.41), (2.42) and 2.43).

2.8.8 Checking the convergence

If the convergence criterion or the maximum imposed simulation step are satisfied, the steady state is reached and the simulation is stopped. Otherwise, a new time step computation is performed by going back to the collision step 2.8.4.

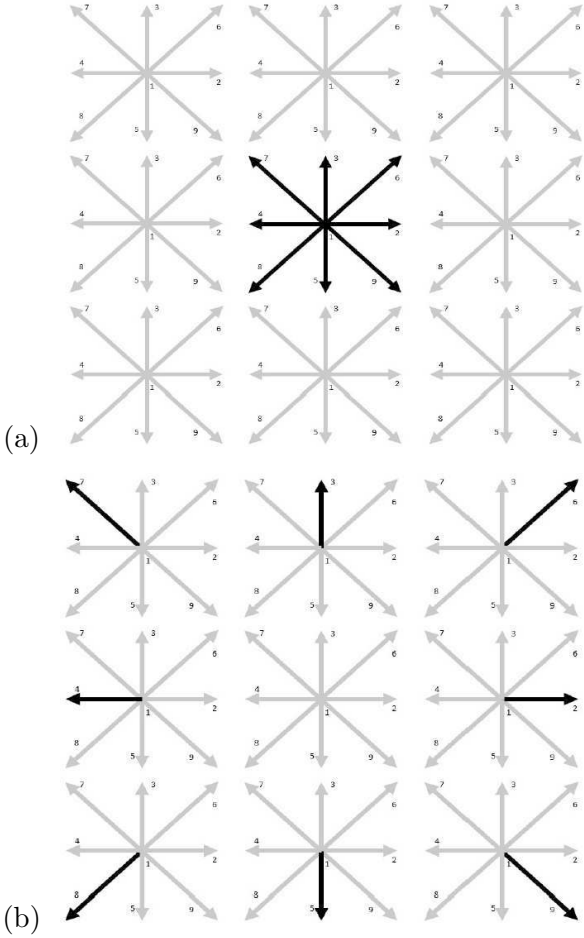

(a)

(b)

FIGURE 2.11 – pre-streaming step (a) and post-streaming step (b). Note the propagation of the information.

2.9 Conclusion

We outlined, in this chapter, the milestone of the LBM: background, different approaches of Navier-Stockes equation derivation, Boltzmann equation and boundary conditions implementation. The mentioned Chapman-Enskog approach is then used in the next chapter to develop an axisymmetric LBE for incompressible fluid flow in porous media.

Chapter 3

Axisymmetric Lattice Boltzmann model for fluid flow through porous media

Abstract

Since the main ideas behind the lattice Boltzmann method were presented in chapter 2, we focus in this chapter on using this tool to solve axisymmetric fluid flow through porous media.

Résumé

Maintenant que les idées clefs derrières la méthode de Boltzmann sur réseau ont été présentées au chapitre 2, nous nous concentrons dans ce chapitre sur l'utilisation de cet outil pour résoudre l'écoulement axisymétrique de fluides dans un milieu poreux.

3.1 Axisymmetric models

Compared with the three-dimensional models, the main advantages of two-dimensional axisymmetric LBE models lie in their case to implement and high computation efficiency. Actually, these models have been successfully applied to various flows, ranging from continuous single phase flows to microscale and two-phase flows [151, 189].

3.1.1 Literature review

In general, the resolution of three-dimensional problem requires large computation cost, high memory usage and handling curved boundaries. In order to overcome these drawbacks, an axisymmetric problem can degenerate into a pseudo two-dimensional problem using, in our case, the cylindrical coordinates system. In fact, several axisymmetric Lattice Boltzmann Equation (LBE) models have been proposed by many authors [35,89,94,107,151,155,190,213,220,231,232,290,315,317,318]. In the literature, four categories of axisymmetric LBE models can be found, namely, the Coordinate Transformation Method (CTM) [94,151], the Vorticity-Stream function Method (VSM) [107,213], the Hybrid Method (HM) [35] and the Double-Distribution-Function (DDF) method [290]. The main idea of CTM is the transformation of the axisymmetric Navier-Stokes Equations (NSE) into two-dimensional pseudo-Cartesian forms with some additional terms. The CTM was introduced by Halliday [94] who was the first to propose an axisymmetric LBE model involving space and velocity-dependent source terms. Following Halliday's work [94], Peng *et al.* [213] proposed a hybrid LBE model for incompressible axisymmetric thermal flows by solving the azimuthal velocity and the temperature field with a second-order center difference scheme. Subsequently, the numerical stability was improved by Huang *et al.* [107]. Lee *et al.* [151] pointed out that some important terms are missing in Halliday's model which leads to large errors in simulation. Thus, they developed a more correct axisymmetric LBE model. Later, further simplified models were presented by Reis [231, 232] and Zhou [317, 318]. Moreover, the method of Halliday *et al.* has been extended for the first time to multiphase flow by Premnath and Abrahamand [220]. Their model was improved to solve two-phase flow with large density ratio by Mukherjee and Abraham [190]. In this improved model, they incorporated additional source terms in the evolution equations for the density and pressure distribution functions combined with a multiple-relaxation-time (MRT) collision model that leads to a second order accuracy. Based on vorticity-stream function equations, Chen *et al.* [35] proposed a new LBE model including source terms with gradient terms which may leads to expensive computation and numerical instability. Based on continuous Boltzmann equation, Guo *et al.* [89] developed an effective LBE model for axisymmetric flow. Li *et al.* [155] suggested a new LBE model for axisymmetric thermal flows where the dimensionless relaxation time depends on the pipe radius. In order to avoid the above shortcomings, Zheng *et al.* [315] introduced another axisymmetric thermal model with second order accuracy in space. Recently, the DDF Lattice Boltzmann model was used by Wang *et al.* [290] to provide the local LB

solution at the cell interface, in which one distribution function is used for the axial and radial velocities while the other is adopted for the azimuthal velocity.

LBM has also been successfully used to simulate fluid flow through porous media [26,52,73,91,92,133,134,250,259,274,287]. Compared with the fluid scale, two approaches have been adopted in the literature: the pore scale [52,133,134,274] and the Representative Elementary Volume (REV) scale [26, 73, 91, 92, 250, 259, 287]. At the pore scale, detailed geometric information of the porous media is needed to be known while at the REV scale, only its statistical properties are needed. This makes the REV scale commonly used in numerical simulation of fluid flow through porous media. A large number of contribution have been made in this area. By introducing porosity into the equilibrium distribution in REV scale approach, Guo *et al.* [92] proved through their LBE model the relevance of LBM to study the isothermal flow in porous media. Later, they [91] extended the isothermal LBM to the thermal flows in porous media. Their model had been successfully applied in natural convection with heat transfer in porous media between two parallel plates [250], convective heat transfer in pipes filled with porous material [259] and mixed convection in a driven cavity packed with porous material [26]. By selecting appropriate equilibrium distribution functions and discrete source terms, Gao *et al.* [73] extended Guo's model [91] to heat and mass transfer under local thermal non-equilibrium conditions, in which several complex time-derivative terms were introduced into the evolution equations for solid and fluid temperatures. In this improved model, the compression work and viscous dissipation effects were ignored. Wang *et al.* [287] developed a more convenient lattice Boltzmann model in which both viscous dissipation and compression work were considered. In this model, a density distribution function was used to simulate the flow field and two total energy distribution functions were used to simulate temperature fields for both fluid and solid.

Recently, a particular attention has been paid to axisymmetric fluid flow and heat transfer through porous media [238–241]. By introducing porosity into the equilibrium distribution function in REV scale approach, Rong *et al.* [238] proposed a thermal LBE model where the conventional fluid flow in porous media has been successfully simulated directly without coordinate shift. In another work, Rong *et al.* [241] developed an algorithm dedicated to solve axisymmetric heat transfer and fluid flow problems in a pipe partially filled with porous media. The algorithm was implemented on the Graphics Processing Unit (GPU) using NVIDIA's CUDA for a massively parallel calculation. By weakening the coupling between the flow velocity and pressure, a new processing shape for external force was introduced by Rong *et al.* [239] to simplify the computation for macroscopic quantities. Later, Rong *et al.* [240] applied successfully the model presented in [241] to simulate heat and fluid flow in cylindrical pipe with porous blocks.

The existing literature shows that LBM can be used to study axisymmetric thermal flow through porous media. The main drawbacks of the previous methods are that the source term involves more complicated terms than the original equations and the added forces cause inconsistency in dimension with the lattice Boltzmann equation. In order to alleviate these issue, we propose a new LBM scheme, which inserts the position and time dependent source terms into the evolution equation of the standard LBM, and makes it

recover the continuity and Navier-Stockes equations on the cylindrical coordinate system by Chapman-Enskog expansion.

3.1.2 Governing equations

The analysis is carried out for a two-dimensional, incompressible, laminar and axisymmetric flow filled with porous medium. The porous structure is saturated with a single phase Newtonian fluid and is considered homogeneous and isotropic with a uniform porosity. Furthermore, the thermophysical properties of the working fluid and solid matrix are assumed constant. Moreover, the viscous dissipation and thermal radiation heat transfer are neglected. Under these assumptions, the final shape of the governing equations in the cylindrical coordinates system based on the Representative Elementary Volume (REV) scale is given by (3.1)-(3.4):

$$\frac{\partial u_r}{\partial r} + \frac{u_r}{r} + \frac{\partial u_z}{\partial z} = 0 \tag{3.1}$$

$$\begin{aligned} \frac{\partial u_z}{\partial t} + \frac{1}{\varepsilon}\left(u_r\frac{\partial u_z}{\partial r} + u_z\frac{\partial u_z}{\partial z}\right) &= -\frac{\varepsilon}{\rho}\frac{\partial p}{\partial z} \\ +\nu_e\left(\frac{\partial^2 u_z}{\partial r^2} + \frac{1}{r}\frac{\partial u_z}{\partial r} + \frac{\partial^2 u_z}{\partial z^2}\right) &+ F_{pz} \end{aligned} \tag{3.2}$$

$$\begin{aligned} \frac{\partial u_r}{\partial t} + \frac{1}{\varepsilon}\left(u_r\frac{\partial u_r}{\partial r} + u_z\frac{\partial u_r}{\partial z}\right) &= -\frac{\varepsilon}{\rho}\frac{\partial p}{\partial r} \\ +\nu_e\left(\frac{\partial^2 u_r}{\partial r^2} + \frac{1}{r}\frac{\partial u_r}{\partial r} + \frac{\partial^2 u_r}{\partial z^2} - \frac{u_r}{r^2}\right) &+ F_{pr} \end{aligned} \tag{3.3}$$

$$\sigma^{'}\frac{\partial T}{\partial t} + u_z\frac{\partial T}{\partial z} + u_r\frac{\partial T}{\partial r} = \alpha_e\left(\frac{\partial^2 T}{\partial r^2} + \frac{1}{r}\frac{\partial T}{\partial r} + \frac{\partial^2 T}{\partial z^2}\right) \tag{3.4}$$

where u_r, u_z, p and T are the volume averaged radial velocity, axial velocity, pressure and temperature, respectively. ν_e is the effective kinetic viscosity given by $\nu_e = \nu/\varepsilon$ [91], where ν is the kinematic viscosity of the fluid, the coefficient $\sigma^{'}$ represents the ratio between the heat capacity of the solid and fluid materials $\sigma^{'} = \left(\varepsilon\rho_l c_{pl} + (1-\varepsilon)\rho_s c_{ps}\right)/\left(\rho_l c_{pl}\right)$ and α_e is the effective thermal diffusion coefficient given by:

$$\alpha_e = \frac{\lambda_e}{\rho_l c_{pl}} \tag{3.5}$$

where λ_e is the effective thermal conductivity given by [20]:

$$\lambda_e = \frac{\lambda_l\left[\left(\lambda_l + \lambda_s\right) - \left(1-\varepsilon\right)\left(\lambda_l - \lambda_s\right)\right]}{\left[\left(\lambda_l + \lambda_s\right) + \left(1-\varepsilon\right)\left(\lambda_l + \lambda_s\right)\right]} \tag{3.6}$$

$\mathbf{F}_p = (F_{pz}, F_{pr})$ represents the total body force due to the presence of the porous medium and is given by:

$$\mathbf{F}_p = (F_{pz}, F_{pr}) = -\frac{\varepsilon\upsilon}{K}\mathbf{u} - \frac{\varepsilon F_\varepsilon}{\sqrt{K}}|\mathbf{u}|\mathbf{u} + \varepsilon\mathbf{G} \tag{3.7}$$

where $\mathbf{G}$ is the body force given by:

$$\mathbf{G} = -\mathbf{g}\beta(T - T_0) + \mathbf{a} \tag{3.8}$$

with the first term representing the buoyancy force (β is the thermal expansion coefficient, $\mathbf{g}$ the gravitational acceleration and T_0 the reference temperature), and the second term representing the acceleration. Worth to mention that the term $-\frac{\varepsilon F_\varepsilon}{\sqrt{K}}|\mathbf{u}|\mathbf{u}$ in equation 3.7 is called Forchheimer term.

The geometric function F_ε and the porous medium permeability K are related to the porosity ε based on Ergun's experimental investigations [61], which can be expressed as:

$$F_\varepsilon = \frac{1,75}{\sqrt{150\varepsilon^3}} \tag{3.9}$$

$$K = \frac{\varepsilon^3 d_p^2}{150\left(1-\varepsilon\right)^2} \tag{3.10}$$

where d_p is the mean diameter of the pores.

Equations (3.1-3.3) are combined and recast in pseudo-Cartesian shape plus extra terms to read:

$$\frac{\partial u_\beta}{\partial x_\beta} = -\frac{u_r}{r} \tag{3.11}$$

$$\begin{aligned}\frac{\partial u_\alpha}{\partial t} + \frac{1}{\varepsilon}\frac{\partial(u_\alpha u_\beta)}{\partial x_\beta} = -\frac{\varepsilon}{\rho}\frac{\partial p}{\partial u_\alpha} + \nu_e\frac{\partial}{\partial x_\beta}\left(\frac{\partial u_\alpha}{\partial x_\beta} + \frac{\partial u_\beta}{\partial x_\alpha}\right) \\ + \frac{\nu_e}{r}\left(\frac{\partial u_\alpha}{\partial r} + \frac{\partial u_r}{\partial x_\alpha}\right) - \frac{u_\alpha u_r}{\varepsilon r} - \frac{2\nu_e u_\alpha}{r^2}\delta_{\alpha r} + F_{p\alpha}\end{aligned} \tag{3.12}$$

$$\sigma'\frac{\partial T}{\partial t} + u_\alpha\frac{\partial T}{\partial x_\alpha} = \alpha_e\left(\frac{\partial^2 T}{\partial x_\alpha^2} + \frac{1}{r}\frac{\partial T}{\partial r}\right) \tag{3.13}$$

Here Einstein summation convention is used over repeated indices and α is the index standing for r or z.

Beside Reynolds and Prandtl number, defined in this case by $Re = \frac{LU}{\nu}$ and $Pr = \frac{\nu}{\alpha_e}$, the heat transfer problems governed by equations (3.1)-(3.4) is characterized by Darcy number, Da, defined as follows:

$$Da = \frac{K}{L^2} \tag{3.14}$$

where L is the characteristic length and U is the characteristic velocity.

3.2 Axisymmetric lattice Boltzmann equation for fluid flow through porous media

In what follows, we derive a new LBM scheme, which inserts the position-and time-dependent source terms into the evolution equation of the standard LBM, and makes it recover the exact mass and momentum equations on cylindrical coordinates system through Chapman-Enskog expansion. This new scheme combines the idea proposed by Halliday *et al.* [94] which uses the CTM approach with the one introduced by Guo *et al.* [92] to include the effect of porous media on fluid flow into the equilibrium distribution function. Compared with the existing LBE models for axisymmetric thermal flows through porous media [238–241], the proposed model has the following features: (i) the source terms are simply extra terms in the transformed pseudo-Cartesian equations where the velocity gradient calculations are avoided, (ii) the centered scheme is applied to remove the discrete lattice effects, (iii) it is easier to implement when compared to Rong *et al.*'s models [238–241] and the standard calculation of the macroscopic variables is preserved, (iv) it is applied on a uniform rectangular grid in the cylindrical coordinate system, which adheres to the inherit property of LBM, (v) the singularity problem at the axis can be appropriately handled, by presenting the discretization order, without affecting an important advantage of the lattice Boltzmann method: the easy processing of boundary conditions. The present approach is generally suitable for axisymmetric flows involving more physical phenomena, consequently.
Our method of adjustment is demonstrated by implementing the cylindrical coordinates form of the continuity and momentum equations on a rectangular lattice and generating results for pipe flow. By adopting the following mapping:

$$\begin{aligned}(z, r) &= (x, y)\\ (u_z, u_r) &= (u_x, u_y)\end{aligned} \tag{3.15}$$

we obtain a pseudo-Cartesian representation from (3.11) and (3.12). The right-hand side terms in continuity (3.11) and the three last terms in momentum equations (3.12) arise from the particular way in which our simulation has been adapted to cylindrical coordinates and we consider them as "non-rectangular" contribution.
In the following section, the LBE model based on the REV approach for axisymmetric thermal flows through porous media is introduced.

3.2.1 Lattice Boltzmann equation for the velocity field

In order to simulate the axisymmetric flows through porous media, we refer to [84] where we propose the following LBE model with source and force terms:

$$\begin{aligned}f_k\left(\mathbf{x}+\mathbf{c}_k\Delta t, t+\Delta t\right) - f_k\left(\mathbf{x}, t\right) &= \tau_e\left(f_k^{eq}\left(\mathbf{x}, t\right) - f_k\left(\mathbf{x}, t\right)\right)\\ &\quad + w_k\Theta\Delta t + \frac{\Delta t}{\chi c^2}\mathbf{c}_{k\alpha}F_\alpha + F_{pk}\Delta t\end{aligned} \tag{3.16}$$

where f_k is the density Distribution Function (DF) of particles; f_k^{eq} is the local Equilibrium Distribution Function (EDF) of particles; Δt is the time step; $\mathbf{x}$ is the position vector, *i.e.*, $\mathbf{x} = (z, r)$, $c = \frac{\Delta x}{\Delta t}$; $\mathbf{c}_{k\alpha}$ is the α-component of vector $\mathbf{c}_k$ which is the velocity vector of a particle in the link k; Δx is the lattice space; w_k is the weight, Θ is the source term defined as:

$$\Theta = -\frac{\rho u_r}{r} \tag{3.17}$$

F_α is the force term given by:

$$F_\alpha = -\frac{\rho u_\alpha u_r}{\varepsilon r} - \frac{2\rho\nu_e u_r}{r^2}\delta_{\alpha r} \tag{3.18}$$

χ is defined by:

$$\chi = \frac{1}{c^2}\sum_k \mathbf{c}_k\mathbf{c}_k \tag{3.19}$$

and τ_e is the effective relation time which is related to the single relaxation time τ by [316]

$$\tau_e = \begin{cases} \frac{1}{\tau} & , r = 0 \\ \frac{1}{\tau}\left(1 + \frac{(2\tau-1)c_{kr}\Delta t}{2r}\right) & , r \neq 0 \end{cases} \tag{3.20}$$

where τ is given by: $\tau = 3\upsilon + \frac{1}{2}$. The last term on the right-hand side of equation (3.16), $F_{pk}\Delta t$, accounts for the total force due to the presence of the porous medium and other external force fields and is given by [91]:

$$F_{pk} = w_k\rho\left(1 - \frac{1}{2\tau}\right)\left[\frac{\mathbf{c}_k \cdot \mathbf{F}_p}{c_s^2} + \frac{\mathbf{u}\mathbf{F}_p : (\mathbf{c}_k\mathbf{c}_k - c_s^2\mathbf{I})}{\varepsilon c_s^4}\right] \tag{3.21}$$

where c_s is the lattice speed of sound.

To include the effect of the porous medium, the Equilibrium Distribution Function (EDF) of the D_nQ_b models is defined as follows:

$$f_k^{eq} = w_k\rho\left[1 + \frac{\mathbf{c}_k \cdot \mathbf{u}}{c_s^2} + \frac{\mathbf{u}\mathbf{u} : (\mathbf{c}_k\mathbf{c}_k - c_s^2\mathbf{I})}{2\varepsilon c_s^4}\right] \tag{3.22}$$

We used the nine-velocity square lattice (D_2Q_9) arrangement , already illustrated in section 2.6.3.

From equation (3.19), we have $\chi = 6$.

Accordingly, the fluid density ρ and fluid velocity $\mathbf{u}$ can be given by:

$$\rho = \sum_k f_k \tag{3.23}$$

$$\rho\mathbf{u} = \sum_k \mathbf{c}_k f_k + \frac{\Delta t}{2}\rho\mathbf{F}_p \tag{3.24}$$

It is noted that the force term $\mathbf{F}_p$ of equation (3.7) contains the velocity $\mathbf{u}$, too. That means equation (3.24) is a nonlinear equation for the velocity $\mathbf{u}$. However, the velocity $\mathbf{u}$ could be obtained explicitly due to the quadratic nature of the equation (3.25) itself as [92]:

$$\mathbf{u} = \frac{\mathbf{v}}{c_0 + \sqrt{c_0^2 + c_1|\mathbf{v}|}} \tag{3.25}$$

where $\mathbf{v}$ is an auxiliary velocity defined as:

$$\rho\mathbf{v} = \sum_k \mathbf{c}_k f_k + \frac{\Delta t}{2}\varepsilon\rho\mathbf{G} \tag{3.26}$$

The two parameters c_0 and c_1 in equation (3.25) are given by:

$$c_0 = \frac{1}{2}\left(1 + \varepsilon\frac{\Delta t}{2}\frac{\nu}{K}\right) \tag{3.27}$$

$$c_1 = \varepsilon\frac{\Delta t}{2}\frac{F_\varepsilon}{\sqrt{K}} \tag{3.28}$$

The derivation of the velocity field equation (3.25) from the nonlinear equation (3.24) is detailed in Appendix A.

Through the Chapman-Enskog procedure, the effective viscosity is defined by:

$$\nu_e = c_s^2\left(\tau - \frac{1}{2}\right)\Delta t \tag{3.29}$$

3.2.2 Lattice Boltzmann equation for the temperature field

The governing equation (3.13) is a convection-diffusion equation (CDE). For most of the existing LBGK models for CDE, several unwanted deviation terms are ignored under the assumption of small Mach number in the Chapman-Enskog analysis to derive equation (3.13) [91]. In order to eliminate this restrictive assumption, two possible ways can be suggested. The first way is to add a source term in the evolution equation of the LBE model such that the CDE can be recovered correctly [42]. However, the collision process cannot be performed locally as discussed in section (2.8.4). To overcome the above constraint, a second way is proposed which consists in deriving a LBE model with a modified Equilibrium Distribution Function (EDF) and adding an appropriate source term in the evolution equation of the temperature field to ensure that the unwanted terms in the previous models can be eliminated safely [27]. Based on the idea of Chai and Zhao [27], the evolution equation of the present modified model for the temperature field is written as follows:

$$\begin{aligned} g_k\left(\mathbf{x} + \mathbf{c}_k\Delta t, t + \Delta t\right) - g_k\left(\mathbf{x}, t\right) = \frac{\Delta t}{\tau_g}\left(g_k^{eq}\left(\mathbf{x}, t\right) - g_k\left(\mathbf{x}, t\right)\right) \\ + \Delta t Q_k + w_k S\Delta t \end{aligned} \tag{3.30}$$

where g_k is the temperature distribution function, τ_g is the relaxation time which is related to the thermal diffusivity through the Chapman-Enskog expansion by:

$$\alpha_e = \sigma^{'} c_s^2 \left(\tau_g - \frac{1}{2}\right) \Delta t \tag{3.31}$$

and g_k^{eq} is the equilibrium temperature distribution function which is defined by:

$$g_k^{eq} = w_k T \left[\sigma^{'} + \frac{\mathbf{c}_k \cdot \mathbf{u}}{c_s^2} + \frac{\mathbf{uu} : (\mathbf{c}_k \mathbf{c}_k - c_s^2 \mathbf{I})}{2\varepsilon c_s^4}\right] + w_k \frac{\varepsilon p T}{c_s^2 \rho_0} \tag{3.32}$$

where $\sigma^{'}$ is the heat capacity ratio linked with the influence of porous media on heat distribution and ρ_0 is the average value of the fluid density.

The source term Q_k is taken as:

$$Q_k = w_k \left(1 - \frac{1}{2\tau_g}\right) \left[\frac{\mathbf{c}_k \cdot \left(\frac{\varepsilon p \nabla T}{\rho_0} + T \mathbf{F}_p\right)}{c_s^2}\right] \tag{3.33}$$

The last term in equation (3.30) represents the source term due to the axisymmetric configuration equal to:

$$S = \frac{\alpha_e}{r} \frac{\partial T}{\partial r} \tag{3.34}$$

This term can be easily approximated using Finite Difference Method (FDM).

Through the Temperature Distribution Function (TDF), the temperature T is defined by:

$$T = \frac{\sum_k g_k}{\sigma^{'}} \tag{3.35}$$

3.3 Lattice Boltzmann boundary conditions

In axisymmetric flows, the distribution functions which are pointed toward the inside of the domain are defined on all boundaries including the symmetry axis. In the discussed test cases, symmetry boundary conditions are applied on the axis as described in section 2.5.2. However, at such position ($r = 0$), the singularity emerges in the terms θ and F_α calculated from equations (3.17) and (3.18), respectively. Two approaches have been used to address this problem. The first one is based on the rearrangement of lattices: the first lattice line is set at $r = 0.5\Delta x$ such a way that the x axis is located both along the centerline of a pipe and in the middle of the two consecutive horizontal lattice lines. So the midgrid point specular reflection (halfway symmetry) boundary conditions is applied to a ghost lattice line located on $r = -0.5\Delta x$ (see figure 3.1) [89, 310, 317]. In such a way, the axis is located off lattices as a result the mentioned source terms are applied only at $r \neq 0$. The second approach is based on the evaluation of the singular source terms of type

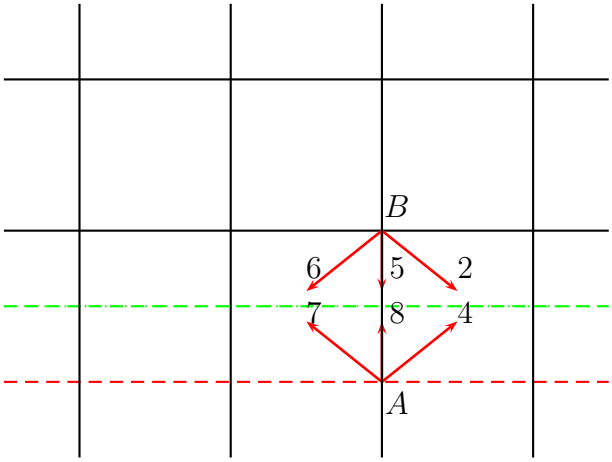

FIGURE 3.1 – Symmetry axis boundary; dashed-dotted line: symmetry axis; and dashed line: ghost boundary along symmetry axis.

$1/r$ using Taylor series expansion. After applying this approach, only terms containing a factor of $\partial_r(.)$ or u_r are got. Now, as $u(r = 0) = 0$ and so the resulting derivatives at $r = 0$ are zero, we get no source term [232, 318]. As a consequence, the two approaches lead to compute source terms only when $r \neq 0$.

3.4 From lattice Boltzmann equation to balances for axisymmetric fluid flow through porous media

The Chapman-Enskog analysis is applied to show that the macroscopic balances can be retrieved exactly from the LBE model.

3.4.1 Derivation of mass and momentum equations

To derive the governing equations (3.11) and (3.12) for incompressible axisymmetric fluid flows though porous media from the present LBE model, we first make the following ansatz:

$$\rho\mathbf{u} = \sum_k \mathbf{c}_k f_k + m\Delta t\mathbf{F}_p \tag{3.36}$$

where m is a constant to be determined by identification, as will be seen further bellow.

The forcing term F_{pk} in equation (3.16) can be written in a power series form as:

$$F_{pk} = w_k \left[A_p + \frac{\mathbf{B}_p \cdot \mathbf{c}_k}{c_s^2} + \frac{\mathbf{C}_p : (\mathbf{c}_k\mathbf{c}_k - c_s^2\mathbf{I})}{2c_s^4} \right] \tag{3.37}$$

where A_p, $\mathbf{B}_p$, and $\mathbf{C}_p$ are functions of $\mathbf{F}_p$ to be determined by requiring that the moments of F_{pk} are consistent with the hydrodynamic equations. After some algebra, we get the zeroth, first and second moments of F_{pk},

$$\sum_k F_{pk} = A_p, \quad \sum_k \mathbf{c}_k F_{pk} = \mathbf{B}_p, \quad \sum_k \mathbf{c}_k \mathbf{c}_k F_{pk} = \frac{1}{2}[\mathbf{C}_p + \mathbf{C}_p^T] \tag{3.38}$$

From the expression of f^{eq} in equation (3.22), we derive the following expression of the moments:

$$\begin{aligned}
\sum_k f_k^{(0)} &= \rho, \\
\sum_k \mathbf{c}_k f_k^{(0)} &= \rho \mathbf{u}, \\
\sum_k \mathbf{c}_{k\alpha} \mathbf{c}_{k\beta} f_k^{(0)} &= \rho c_s^2 + \frac{\rho \mathbf{u}_\alpha \mathbf{u}_\beta}{\varepsilon}, \\
\sum_k \mathbf{c}_{k\alpha} \mathbf{c}_{k\beta} \mathbf{c}_{k\gamma} f_k^{(0)} &= c_s^2 \rho \left(\mathbf{u}_\alpha \delta_{\beta\gamma} + \mathbf{u}_\beta \delta_{\alpha\gamma} + \mathbf{u}_\gamma \delta_{\alpha\beta}\right)
\end{aligned} \tag{3.39}$$

$$\sum_k \mathbf{c}_k f_k^{(1)} = -m\Delta t \mathbf{F}_p^{(1)} \tag{3.40}$$

$$\begin{aligned}
\textstyle\sum_k f_k^{(\eta)} &= 0 \quad &&, \text{for } \eta > 0 \\
\textstyle\sum_k \mathbf{c}_k f_k^{(\eta)} &= 0 \quad &&, \text{for } \eta > 1
\end{aligned} \tag{3.41}$$

The macrodynamic behavior arising from the LBE (3.16) can be found from a multiscale analysis using an expansion parameter ξ, which is proportional to the ratio of the lattice spacing to a characteristic macroscopic length:

$$f_k = f_k^{(0)} + \xi f_k^{(1)} + \xi^2 f_k^{(2)} + ... \tag{3.42}$$

$$\frac{\partial}{\partial t} = \xi \frac{\partial}{\partial t_1} + \xi^2 \frac{\partial}{\partial t_2} + ... \tag{3.43}$$

$$\nabla = \xi \nabla_1 \tag{3.44}$$

$$F_{pk} = \xi F_{pk}^{(1)} \tag{3.45}$$

$$\mathbf{F}_p = \xi \mathbf{F}_p^{(1)}, A_p = \xi A_p^{(1)}, \mathbf{B}_p = \xi \mathbf{B}_p^{(1)}, \mathbf{C}_p = \xi \mathbf{C}_p^{(1)} \tag{3.46}$$

The centered scheme is used for both mass Θ and momentum F_α source terms as [316]:

$$\Theta = \Theta\left(\mathbf{x} + \frac{1}{2}\mathbf{c}_k \Delta t, t + \frac{1}{2}\Delta t\right) \tag{3.47}$$

$$F_\alpha = F_\alpha\left(\mathbf{x} + \frac{1}{2}\mathbf{c}_k \Delta t, t + \frac{1}{2}\Delta t\right) \tag{3.48}$$

which can be also written, *via* Taylor's expansion, as:

$$\Theta\left(\mathbf{x}+\frac{1}{2}\mathbf{c}_k\Delta t, t+\frac{1}{2}\Delta t\right)=\Theta(\mathbf{x},t)+\frac{1}{2}\Delta t\left(\frac{\partial}{\partial t}+\mathbf{c}_k.\nabla\right)\Theta(\mathbf{x},t)+... \tag{3.49}$$

$$F_\alpha\left(\mathbf{x}+\frac{1}{2}\mathbf{c}_k\Delta t, t+\frac{1}{2}\Delta t\right)=F_\alpha(\mathbf{x},t)+\frac{1}{2}\Delta t\left(\frac{\partial}{\partial t}+\mathbf{c}_k.\nabla\right)F_\alpha(\mathbf{x},t)+... \tag{3.50}$$

Expanding $f_k\left(\mathbf{x}+\mathbf{c}_k\Delta t, t+\Delta t\right)$ in equation (3.16) about $\mathbf{x}$ and t, and applying the above multiscaling expansion to the resulting continuous equation, we get the following equations in successive powers of the parameter ξ:

$$O(\xi^0): f_k^{(0)}=f_k^{eq} \tag{3.51}$$

$$O(\xi^1): D_{1k}f_k^{(0)}=-\frac{1}{\tau\Delta t}f_k^{(1)}+w_k\Theta+\frac{c_{k\alpha}}{6c^2}F_\alpha+F_{pk}^{(1)} \tag{3.52}$$

$$O(\xi^2): \frac{\partial f_k^{(0)}}{\partial t_2}+D_{1k}\left[\left(1-\frac{1}{2\tau}\right)f_k^{(1)}\right]=-\frac{1}{\tau\Delta t}f_k^{(2)}-\left(1-\frac{1}{2\tau}\right)\frac{c_{kr}}{r}f_k^{(1)}-\frac{\Delta t}{2}D_{1k}F_{pk}^{(1)} \tag{3.53}$$

where $D_{1k}=\frac{\partial}{\partial t_1}+\mathbf{c}_k\cdot\nabla_1$.

Taking moments of equation (3.52), we get the following macroscopic equations on the $t_1=\xi t$ time scale and $\mathbf{x}_1=\xi\mathbf{x}$ space scale:

$$\frac{\partial\rho}{\partial t_1}+\nabla_1\cdot(\rho\mathbf{u})=\Theta+A_p^{(1)} \tag{3.54}$$

$$\frac{\partial(\rho\mathbf{u})}{\partial t_1}+\nabla_1\cdot\Pi_{\alpha\beta}^{(0)}=\mathbf{F}_\alpha+\mathbf{B}_p^{(1)}+\frac{m}{\tau}\mathbf{F}_p^{(1)}=\mathbf{F}_\alpha+\left(n+\frac{m}{\tau}\right)\mathbf{F}_p^{(1)} \tag{3.55}$$

where we assume that $\mathbf{B}_p^{(1)}=n\mathbf{F}_p^{(1)}$, and n is a constant to be determined. $\Pi_{\alpha\beta}^{(0)}$ is the zeroth-order momentum flux tensor given by:

$$\Pi_{\alpha\beta}^{(0)}=\sum_k\mathbf{c}_{k\alpha}\mathbf{c}_{k\beta}f_k^{(0)}=\varepsilon p\delta_{\alpha\beta}+\frac{\rho\mathbf{u}_\alpha\mathbf{u}_\beta}{\varepsilon} \tag{3.56}$$

In order to retrieve Euler equations from equations (3.54) and (3.55), we must set therefore:

$$A_p=0, n+\frac{m}{\tau}=1 \tag{3.57}$$

Similarly, the moments of equation (3.53) lead to the following equations:

$$\frac{\partial\rho}{\partial t_2}=\Delta t\left(m-\frac{1}{2}\right)\nabla_1\mathbf{F}_p^{(1)} \tag{3.58}$$

$$\frac{\partial(\rho\mathbf{u})}{\partial t_2}=\Delta t\left(m-\frac{1}{2}\right)\frac{\partial\mathbf{F}_p^{(1)}}{\partial t_1}+\nabla_1\cdot\Lambda_{\alpha\beta}+\frac{\Lambda_{\alpha r}}{r} \tag{3.59}$$

where $\Lambda_{\alpha\beta}$ is given by:

$$\Lambda_{\alpha\beta} = -\left(1-\frac{1}{2\tau}\right)\sum_k \mathbf{c}_{k\alpha}\mathbf{c}_{k\beta}f_k^{(1)} - \frac{\Delta t}{2}\sum_k \mathbf{c}_{k\alpha}\mathbf{c}_{k\beta}\mathbf{F}_{pk}^{(1)} \tag{3.60}$$

and

$$\Lambda_{\alpha r} = -\left(1-\frac{1}{2\tau}\right)\sum_k \mathbf{c}_{k\alpha}\mathbf{c}_{kr}f_k^{(1)} \tag{3.61}$$

The first-order momentum flux tensor $\Pi_{\alpha\beta}^{(1)} = \sum_k \mathbf{c}_{k\alpha}\mathbf{c}_{k\beta}f_k^{(1)}$ can be simplified using equation (3.53) and (3.54). After some standard algebra, we get [92]:

$$\Pi_{\alpha\beta}^{(1)} = -\tau\Delta t c_s^2\left(\nabla_{1\alpha}\mathbf{u}_\beta + \nabla_{1\beta}\mathbf{u}_\alpha\right) - \tau\Delta t\left[\frac{1}{\varepsilon}\left(\mathbf{u}_\alpha\mathbf{F}_{p\beta}^{(1)} + \mathbf{u}_\beta\mathbf{F}_{p\alpha}^{(1)}\right) - \frac{1}{2}(\mathbf{C}_{p\alpha\beta}^{(1)} + \mathbf{C}_{p\beta\alpha}^{(1)})\right] \tag{3.62}$$

Introducing this expression into equation (3.60), we obtain:

$$\begin{aligned}\Lambda_{\alpha\beta} = -\left(1-\frac{1}{2\tau}\right)\nabla_1\cdot\Pi_{\alpha\beta}^{(1)} - \frac{\Delta t}{4}\left(\mathbf{C}_{p\alpha\beta}^{(1)} + \mathbf{C}_{p\beta\alpha}^{(1)}\right) &= \nu_e\left(\nabla_{1\alpha}\mathbf{u}_\beta + \nabla_{1\beta}\mathbf{u}_\alpha\right) \\ &+ \Delta t\left[\frac{1}{\varepsilon}\left(\tau-\frac{1}{2}\right)\left(\mathbf{u}_\alpha\mathbf{F}_{p\beta}^{(1)} + \mathbf{u}_\beta\mathbf{F}_{p\alpha}^{(1)}\right) - \frac{\tau}{2}(\mathbf{C}_{p\alpha\beta}^{(1)} + \mathbf{C}_{p\beta\alpha}^{(1)})\right]\end{aligned} \tag{3.63}$$

where ν_e is the kinematic viscosity defined by:

$$\nu_e = c_s^2\Delta t(\tau - \frac{1}{2}) \tag{3.64}$$

To recover the correct governing equations (3.11) and (3.12) for the incompressible axisymmetric flows through porous media, the parameters A_p, $\mathbf{B}_p$ and m must be set as follows:

$$A_p = 0, n + \frac{m}{\tau} = 1, m = \frac{1}{2}, \mathbf{B}_p = m\left(2-\frac{1}{\tau}\right)\mathbf{F}_p \tag{3.65}$$

and $\mathbf{C}_p$ sets to:

$$\mathbf{C}_p = \frac{1}{\varepsilon}\left(1-\frac{1}{2\tau}\right)(\mathbf{u}\mathbf{F}_p + \mathbf{F}_p\mathbf{u}) = \frac{2}{\varepsilon}\left(1-\frac{1}{2\tau}\right)(\mathbf{u}\mathbf{F}_p) \tag{3.66}$$

Using the above results, we can find the following expression:

$$\nabla_1\Lambda_{\alpha\beta} = \nu_e\left[\nabla_{1\alpha}\mathbf{u}_\beta + \nabla_{1\beta}\mathbf{u}_\alpha\right] \tag{3.67}$$

The same method of calculation is used for $\Lambda_{\alpha r}$, too, which leads to:

$$\Lambda_{\alpha r} = \nu_e\left[\nabla_{1\alpha}\mathbf{u}_r + \nabla_{1r}\mathbf{u}_\alpha\right] \tag{3.68}$$

Combining the results on the $t_1 = \xi t$ and $t_2 = \xi^2 t$ time scales, equations (3.54), (3.55), (4.18) and (4.19) together with equations (3.65) and (3.66), we can easily check that the final macroscopic equations for incompressible flow through porous media given by equations (3.11) and (3.12) are retrieved.

3.4.2 Derivation of the energy equation

The energy equation can be derived from the proposed LBE model through Chapman-Enskog expansion procedure. First, the following multiscaling expansions are introduced:

$$g_k = g_k^{(0)} + \xi g_k^{(1)} + \xi^2 g_k^{(2)} + ... \tag{3.69}$$

$$\frac{\partial}{\partial t} = \xi \frac{\partial}{\partial t_1} + \xi^2 \frac{\partial}{\partial t_2} + ... \tag{3.70}$$

$$\nabla = \xi \nabla_1 \tag{3.71}$$

$$Q_k = \xi Q_k^{(1)} \tag{3.72}$$

$$\mathbf{F}_p = \xi \mathbf{F}_p^{(1)} \tag{3.73}$$

$$S = \xi^2 S^{(1)} \tag{3.74}$$

where ξ in this section is set to Δt which is a small expansion parameter proportional to Knudsen number.

Expanding $g_k\left(\mathbf{x} + \mathbf{c}_k \Delta t, t + \Delta t\right)$ in equation (3.29) about $\mathbf{x}$ and t, and applying the above multiscaling expansions to the resulting continuous equation, we retrieve the following equations in the successive powers of the parameter ξ:

$$O(\xi^0) : g_k^{(0)} = g_k^{eq} \tag{3.75}$$

$$O(\xi^1) : D_{1k} g_k^{(0)} = -\frac{1}{\tau_g \Delta t} g_k^{(1)} + Q_k^{(1)} \tag{3.76}$$

$$O(\xi^2) : \frac{\partial g_k^{(0)}}{\partial t_2} + D_{1k} g_k^{(1)} + \frac{\Delta t}{2} D_{1k}^2 g_k^{(0)} = -\frac{1}{\tau_g \Delta t} g_k^{(2)} + w_k S^{(1)} \tag{3.77}$$

where $D_{1k} = \frac{\partial}{\partial t_1} + \mathbf{c}_k \cdot \nabla_1$.

From the definitions of g^{eq} we get the following relationships:

$$\sum_k g_k^{(0)} = \sigma' T, \quad \sum_k \mathbf{c}_{k\alpha} g_k^{(0)} = \mathbf{u} T \sum_k \mathbf{c}_{k\alpha} \mathbf{c}_{k\beta} g_k^{(0)} = c_s^2 \sigma' T \mathbf{I} + \frac{T \mathbf{u}\mathbf{u}}{\varepsilon} + \frac{\varepsilon p T \mathbf{I}}{\rho_0} \tag{3.78}$$

$$\sum_k Q_k^{(1)} = 0, \quad \sum_k \mathbf{c}_{k\alpha} Q_k^{(1)} = \left(1 - \frac{1}{2\tau_g}\right) \left[\frac{\varepsilon p \nabla_1 T}{\rho_0} + T \mathbf{F}_p\right] \tag{3.79}$$

$$\begin{array}{ll} \sum_k g_k^{(\eta)} = 0 & , \text{for } \eta > 0 \\ \sum_k \mathbf{c}_k g_k^{(\eta)} = 0 & , \text{for } \eta > 1 \end{array} \tag{3.80}$$

From equation (3.76) and referring to the relationships (3.78) and (3.79), we get:

$$\begin{aligned}\sum_k \mathbf{c}_{k\alpha} g_k^{(1)} = &-\tau_g \Delta t \frac{\partial (T\mathbf{u})}{\partial t_1} - \tau_g \Delta t \nabla_1 \cdot \left(c_s^2 \sigma' T \mathbf{I} + \frac{T\mathbf{u}\mathbf{u}}{\varepsilon} + \frac{\varepsilon p T \mathbf{I}}{\rho_0} \right) \\ &+ \tau_g \Delta t \left(1 - \frac{1}{2\tau_g}\right) \left[\frac{\varepsilon p \nabla_1 T}{\rho_0} + T \mathbf{F}_p \right]\end{aligned} \tag{3.81}$$

Using equations (3.76) and (3.77), we get the macroscopic equations on the $t_1 = \xi t$ time scale and $\mathbf{x}_1 = \xi \mathbf{x}$ space scale:

$$\frac{\partial (\sigma' T)}{\partial t_1} + \nabla_1 \cdot (\mathbf{u} T) = 0 \tag{3.82}$$

$$\frac{\partial (\sigma' T)}{\partial t_2} + \nabla_1 \cdot \left[\left(1 - \frac{1}{2\tau_g}\right) \sum_k \mathbf{c}_{k\alpha} g_k^{(1)} \right] + \frac{\Delta t}{2} \nabla_1 \cdot \left[\sum_k \mathbf{c}_{k\alpha} Q_k^{(1)} \right] = S^{(1)} \tag{3.83}$$

After some algebra and making use of equations (3.79) and (3.80), the above equation (3.83) at the t_2 time scale are rewritten:

$$\frac{\partial (\sigma' T)}{\partial t_2} = \nabla_1 \cdot (\alpha_e \nabla_1 T) + S^{(1)} \tag{3.84}$$

where α_e is given by:

$$\alpha_e = \sigma' c_s^2 \left(\tau_g - \frac{1}{2}\right) \Delta t \tag{3.85}$$

Combining the macroscopic equations at the $t_1 = \xi t$ and $t_2 = \xi^2 t$ scales, we get:

$$\xi \frac{\partial (\sigma' T)}{\partial t_1} + \xi^2 \frac{\partial (\sigma' T)}{\partial t_2} + \xi \nabla_1 \cdot (\mathbf{u} T) = \xi^2 \nabla_1 (\alpha_e \nabla_1 T) + \xi^2 S^{(1)} \tag{3.86}$$

which leads to the following energy equation:

$$\frac{\partial (\sigma' T)}{\partial t} + \nabla (\mathbf{u} T) = \nabla \cdot (\alpha_e \nabla T) + S \tag{3.87}$$

where S is the source terme given by equation (3.34), QED.

3.5 Model validation

In order to validate the proposed LBE, four flow problems are carried out:

1- The incompressible isothermal fluid flow driven by constant forces in a clear pipe,
2- The incompressible isothermal fluid flow driven by constant forces in a porous pipe,
3- The incompressible isothermal fluid flow in a porous pipe which wall is drifted at a constant velocity on the pipe wall and parallel to its axis,

4- The incompressible thermal flow driven by constant flow rate in a pipe partially filled with porous media.

The approach here is to check the relevance of the model starting from the simplest case to the closest one to the target configuration; the capillary heat pipe. All the numerical tests are simulated with a uniform lattice size of 100×100 except the last test case where we took 200×4000 lattices. For our LBM simulations, we use unit time step ($\Delta t = 1$), unit grid spacing ($\Delta z = \Delta r = 1$) and unit relaxation time ($\tau = \tau_g = 1$).

In each run, the following inequality is used to check whether the steady state is reached:

$$\frac{\sum_x \parallel \phi(\mathbf{x}, t + \Delta t) - \phi(\mathbf{x}, t) \parallel}{\sum_x \parallel \phi(\mathbf{x}, t) \parallel} \leq 10^{-6} \tag{3.88}$$

where $\parallel . \parallel$ is the L_2 norm, ϕ represents $\mathbf{u}$ or T. Typically, it takes about $50,000$ time steps for each case to achieve the above criterion.

Numerical computations are carried out using dimensionless variables. Thus, all results are given in dimensionless units.

3.5.1 The incompressible isothermal fluid flow in a clear pipe driven by a constant force

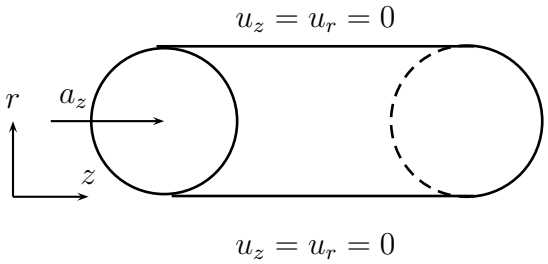

FIGURE 3.2 – Illustration of the first (clear pipe) and second (porous pipe) test cases.

In the first test case, the incompressible isothermal fluid flows through a pipe and is driven by a constant external force $\mathbf{a} = (a_z, 0)$. Figure 3.2 shows an illustration of the proposed problem. The operating conditions are: $K \to \infty$, $\varepsilon \to 1$, which represent the fluid flow in a clear pipe. The fluid is assumed at rest initially and its density is taken constant $\rho = \rho_0 = 1$. Thus, the boundary conditions read:

$$\begin{cases} \frac{\partial u_z}{\partial r} = \frac{\partial u_r}{\partial r} = 0 & , r = 0 \\ u_z = u_r = 0 & , r = R \end{cases} \tag{3.89}$$

Periodic conditions are applied at the inlet and outlet boundaries. At $r = 0$, we apply the symmetric boundary condition (impermeability and slip conditions) and no-slip boundary condition at the solid wall for $r = R$, as shown in figure 3.2.

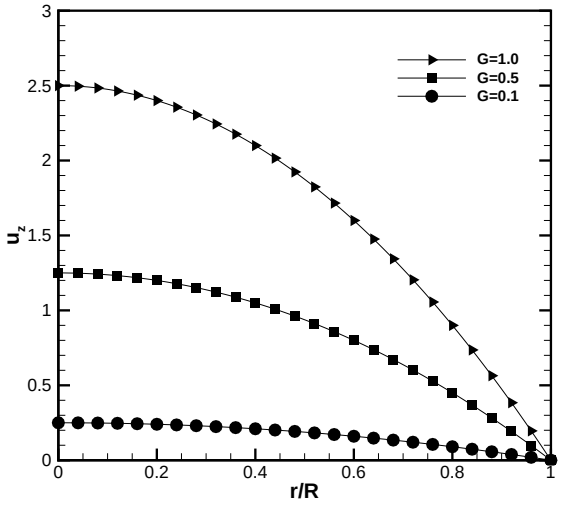

FIGURE 3.3 – A comparison of the axial velocity profiles for different external forces of the first test as obtained from the present LBE model simulation (solid lines) versus the closed-form solution (symbols) for the first test case.

The analytical solution for the axial velocity of the Hagen-Poiseuille flow is given by:

$$u_z(r) = u_0 \left(1 - \frac{r^2}{R^2}\right) \tag{3.90}$$

where $u_0 = a_z R^2/4\nu$ is the maximum velocity where a_z is a constant external body force applied on the fluid and R is the radius of the pipe.

Three test cases are conducted by the present LBE model for different flow rates under the same working condition: $\nu = 0.1$. Excellent agreement with closed-form solution is noticed from figure 3.3. To be consistent with such a flow, the inertia term is deactivated in the numerical model. Also, it can be seen that external force term affects directly the resulted velocity. This can be seen from the analytic solution: increasing the force term increases the maximum velocity, too. Either adverse or favorable, this force is a key element in fluid flow behavior.

3.5.2 The incompressible isothermal fluid flow in a porous pipe driven by a constant force

The second test deals with the incompressible isothermal fluid flow in a porous pipe driven by a constant force as shown in figure 3.2. The initial and boundary conditions are the same as those of the first test case. The porous medium parameters are chosen as: $\nu = 0.01$, $\varepsilon = 0.1$ and $a_z = 10$. Neglecting the effect of Forchheimer term in equation

(3.7), the governing equations can be written as follows:

$$\frac{\nu}{\varepsilon}\left[\frac{\partial^2 u_z}{\partial r^2}+\frac{1}{r}\frac{\partial u_z}{\partial r}\right]=\frac{\nu}{K}u_z-a_z \tag{3.91}$$

The corresponding closed-form solution reads [239]:

$$u_z(r)=\mathfrak{Re}\left\{\frac{a_z K}{\nu}-\frac{a_z K J_0((-\varepsilon/K)^{1/2}r)}{J_0((-\varepsilon/K)^{1/2}R)\nu}\right\} \tag{3.92}$$

where J_0 is the zeroth-order Bessel function of the first kind and $\mathfrak{Re}$ means the real part of the complex variable.

The numerical results of the present LBE applied to equation (3.91) are compared in figure 3.4 with closed-form solution. Very good agreement between them is observed from this figure. As it can be seen, the permeability has a significant effect on the velocity. In fact, increasing the porous medium permeability leads to increasing the maximum velocity. This is due to the diminution of the Darcy force effect resulting in the increasing ability of the porous media to transmit even easier the fluid throufh its porous network.

For flows in porous medium, inertial effects can also become significant which is known as Forchheimer term. This term takes into account the non-linear behavior of the pressure difference. For low flow velocities ($Re \leq 10$), Darcy's law correctly describes the flow in porous media [262]. However, as velocities become larger ($Re > 10$), a discrepancy between experimental data and results obtained from Darcy's law was found by Forchheimer [145]. He linked this discrepancy to inertial effects and suggested to add the term representing kinetic energy bearing his name. Based on what was found previously, the effect of Forchheimer term is also studied. Due to the difficulty in obtaining the analytical solution in the presence of inertia effect, we compared our numerical results (with inertia activated) with those obtained by Rong *et al.* [238]. As it can be seen, good agreement is obtained. The effect of permeability is figured here also as discussed before. By comparing figures 3.4 and 3.5, we can see that, for the same working conditions, adding Forchheimer force term greatly affects the evolution of the axial velocity. For example, for $K = 10^{-2}$ at position $r = 0$, the axial velocity in the case with and without Forchheimer force is equal to 8.14 and 0.46, respectively. This effect is decreasing as the permeability increases. The Forchheimer can not therefore be neglected and should be taken into account in such problems.

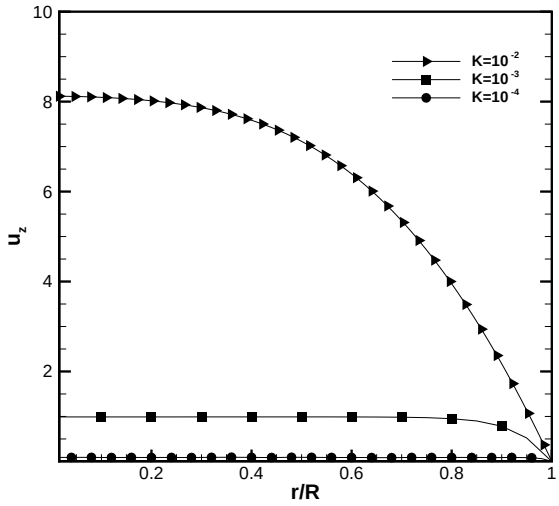

FIGURE 3.4 – A comparison of the axial velocity profiles for different permeabilities as obtained from the present LBE model simulation (solid lines) and the closed-form solution (symbols) for the second test case with Forchheimer term.

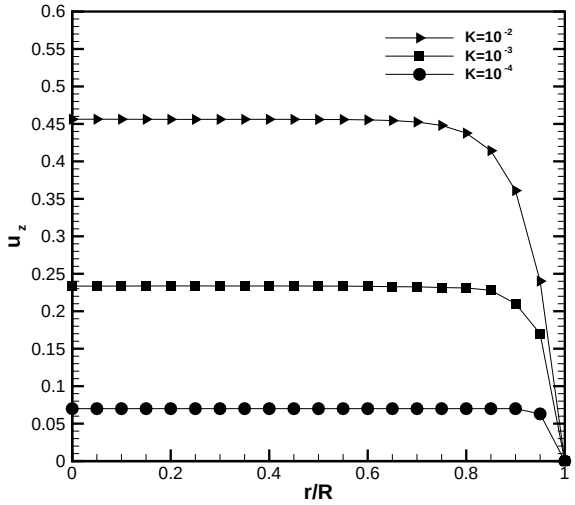

FIGURE 3.5 – A comparison of the axial velocity profiles for different permeabilities as obtained from the present LBE model simulation (solid lines) and the numerical solution by Rong *et al.* [238] (symbols) for the second test case without Forchheimer term.

3.5.3 The incompressible isothermal fluid flow in a porous pipe driven by a constant velocity on the pipe wall

The third test case is the incompressible isothermal fluid flow in a porous pipe driven by constant velocity u_0 on the pipe wall. The configuration of the problem is shown in figure 3.6 where the velocity is set to 1.0 in the simulations.
The governing equations (3.91) can also be used to describe this problem without external

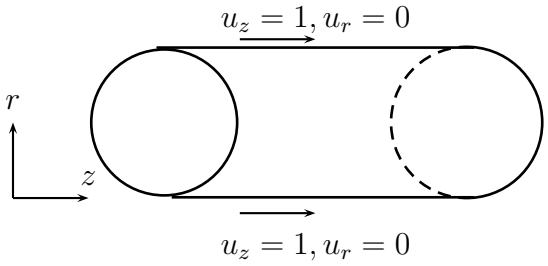

FIGURE 3.6 – Illustration of the third case test.

force ($a_z = 0$). The only difference from the above test is the velocity boundary condition on the pipe wall which is deal with using Zou-He BC described in 2.5.2. All tests were carried out with the same working conditions: $\nu = 0.01$ and $\varepsilon = 0.1$.

Similar to the above discussions, the problem without Forchheimer term is first studied, and the closed-form solution reads:

$$u_z(r) = \mathfrak{Re}\left\{\frac{u_0 J_0((-\varepsilon/K)^{1/2} r)}{J_0((-\varepsilon/K)^{1/2} R)}\right\} \tag{3.93}$$

The numerical results are compared with the closed-form solutions in figure 3.7 where remarkable agreement is got in this case too. The axial velocity increases along the radial axis until it reaches the maximum velocity at the pipe wall. As it can be seen, the decreases of permeability leads to get closer to the wall velocity all along the axis. This can be explained by the fact that permeability of the porous medium affects the fluid flow by slow motion its circulation.

The same test case is considered now when Forchheimer term is included in the momentum equations (3.91). As shown in figure 3.8, the numerical results agree quite well with those found by central difference solutions by Rong *et al.* [238] for different permeability. Compared to figure 3.7, the velocity profile is flatter when Forchheimer term is considered than when it is not. By taking the example at position $r/R = 0.2$ and $K = 10^{-3}$, the axial velocity is equal to 0.91 and 0.83 in the case with and without Forchheimer term, respectively. From this example, we can conclude that considering this term leads to increasing the axial velocity. Changing the flow topology considerably, this term must therefore not be neglected.

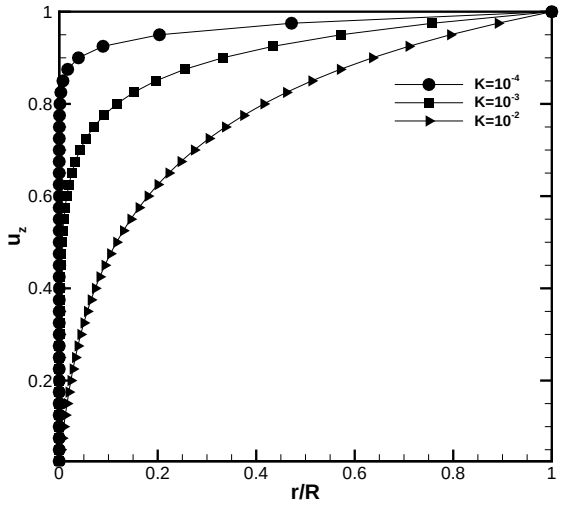

FIGURE 3.7 – A comparison of the axial velocity profiles for different permeability as obtained from the present LBE model simulation (solid lines) without Forchheimer term versus the closed-form solution (symbols) for the third test.

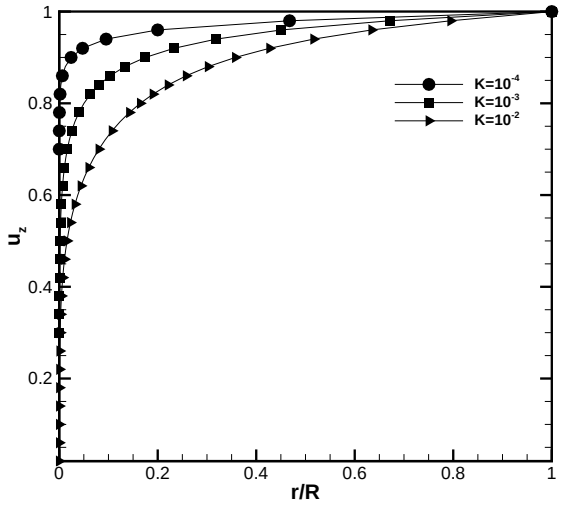

FIGURE 3.8 – A comparison of the axial velocity profiles for different permeability of the third test case as obtained from the present LBE model simulation (solid lines) with Forchheimer term versus numerical solution by Rong *et al.* [238] (symbols).

3.5.4 The incompressible heated fluid flow in a porous pipe partly filled with porous medium

The last test case is the incompressible thermal fluid flow in a pipe partly filled with porous medium. The configuration is presented in figure 3.9 where the velocity is set to 1.0 in the simulations. The initial and boundary conditions are the same as described in [241]. The dimensionless pipe radius is R_0. The dimensionless porous medium radius inset in the pipe is R_p. R is the pipe dimensionless current radius. U_{in} and T_{in} are the unit inlet velocity and temperature, respectively.
The numerical results of the present LBE model are compared with the results of Rong *et*

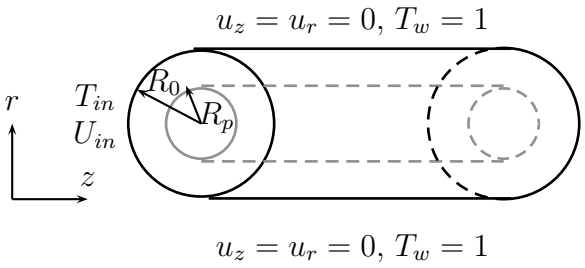

FIGURE 3.9 – Schematic diagram of the fourth case test.

al. [241] given for $\varepsilon = 0.4$, $Da = 10^{-3}$ to $Da = 10^{-5}$, $Rp = 0.5$, $Pr = 0.7$ and $Re = 100$. Very good agreement can be seen from figures 3.10 between the present work results and the results of the model proposed by Rong *et al.* [241]. As shown from figure 3.10a, the variations of axial velocity are lower in the region filled with the porous medium. In fact the presence of such structure involves forces that help fluid circulation more uniform along the pipe. While in the region without porous medium, equivalent viscosity is smaller and so the velocity gradients can be larger while shear stress is comparable. From figure 3.10b, we can see that the temperature is virtually constant in the porous region and increases rapidly in the clear region to reach the wall temperature. As the temperature and velocity profiles are deeply related, this can be explained also by the small velocity gradient in the porous region.

The LBM used in these test cases is relevant only for weakly compressible flows. In fact, through multiscaling expansion, the incompressible Navier-Stokes equations were recovered from the proposed lattice Boltzmann equation on the assumptions of small Mach number and slow density variation in a manner that the density fluctuation can be neglected. However, these two conditions can't always be satisfied in numerical simulation using the proposed models.

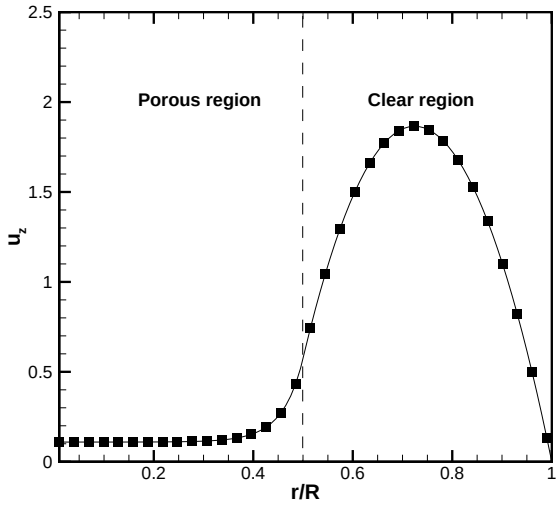

(a)

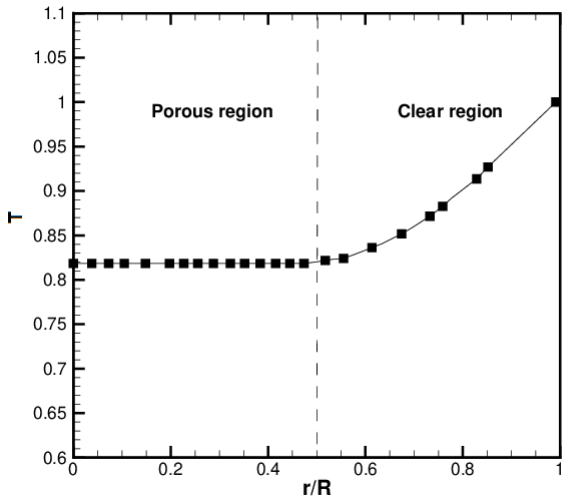

(b)

FIGURE 3.10 – A comparison of the 3.10a axial velocity and 3.10b temperature profiles of the fourth test case as obtained from the present LBE model simulation (solid lines) versus the results of Rong *et al.* [241] (symbols).

3.6 Enhanced axisymmetric model

3.6.1 Compressibility problem statement

The point is that the compressibility effect in the existing LBE models may produce uncontrollable error. Therefore, most of these models can be used only to simulate compressible flows in the incompressible limit. That is why it is considered as an artificial compressible model for the incompressible Navier-Stokes equations. In many previous studies, the compressibility effect of incompressible LBE model has been highlighted. Efforts have been made to either reduce or eliminate such errors [90, 98, 151, 310]. By neglecting terms of higher order Mach number in the equilibrium density distribution function, He and Luo [98] proposed an incompressible LBGK model in which the distribution function is for pressure representation. The incompressible Navier-Stokes equations in artificial compressible form were derived from this model. However, before the model is used, the average pressure of the flow must be specified in advance. In some cases, especially in practical problems, the average pressure is not known or cannot be prescribed precisely. Furthermore, when it is used to simulate unsteady incompressible flows, the model requires an additional condition, $\frac{L}{Tc_s} \ll 1$(T and L are characteristic time and length, respectively), to neglect the artificial compressibility effect. To derive a more accurate axisymmetric model, Lee *et al.*'s model [151] started from the incompressible LBE proposed by He and Luo [98]. In their model, the compressibility effect of $O(M^2)$ order is explicitly eliminated. When the model proposed in [151] is used to simulate unsteady incompressible axisymmetric flows, in order to neglect the artificial compressible effect, the condition aforementioned, $L/Tc_s \ll 1$, is required. Equally the average pressure of the flow must be specified in advance in this model, too. In order to avoid the above shortcomings, Zhang *et al.* [310] developed a new axisymmetric LBE model with second order accuracy in space. This model can eliminate the compressibility effects only within the small Mach number limit and has no velocity gradients in source terms. Following the same idea and by reducing the coupling between flow velocity and pressure, Rong *et al.* [239] successfully recovered the incompressible fluid flow through porous media for isothermal flow. Although the above axisymmetric LBGK models have been used to simulate various flows, they still suffer some limitations. Firstly, in the case where the fluids are liquids, the pressure drop that drives the fluid to flow through a porous media is usually very large. That means large density variations, for a given computational speed of sound, occur in the simulation which causes numerical instability. However, the density may fluctuate to a great extent in flows with large pressure gradient because the pressure and density variations satisfy the ideal gas equation of state. Thus, in such a case, the Navier-Stokes equations of incompressible fluid are not satisfied exactly. Secondly, these models almost include many velocity gradients in the source terms. The discretization of these gradient terms may lead to additional errors and numerical instability. Finally, most of these models are built from the standard LBE, so they can only be viewed as artificial compressible methods for simulating incompressible axisymmetric flows. Considering the significance of the incompressible Navier-Stokes equations in theory and applications, it is

necessary to establish a LBGK model which can recover the incompressible Navier-Stokes equations exactly through porous media. It is well known that the small Mach number limit is equivalent to the incompressible limit, so it is possible to set up a LBE model which can properly model the incompressible Navier-Stokes equations only with the small Mach number limit. Based on this idea, the LBE for the incompressible axisymmetric flows in porous media, described in the previous section is improved to overcome the above limitations. This model combines the idea in [84] with the one of Zhang *et al.* [310]. Compared with the existing LBE models and the one in [84] for axisymmetric incompressible thermal flows through porous media, the proposed model has the following features: (i) The Navier-Stokes equations for incompressible fluid flow are recovered correctly up to second-order; (ii) It still retains the inherent features of the standard LB method; (iii) Its implementation is in noway more complicated than the original model.

3.6.2 Lattice Boltzmann equation for the velocity field

In order to correctly simulate the axisymmetric incompressible fluid flows through porous media, we propose the following modified LBE model:

$$\begin{aligned} f_k\left(\mathbf{x}+\mathbf{c}_k\Delta t, t+\Delta t\right) - f_k\left(\mathbf{x},t\right) = \tau_e\left(f_k^{eq}\left(\mathbf{x},t\right) - f_k\left(\mathbf{x},t\right)\right) \\ + w_k\Theta\Delta t + \frac{\Delta t}{\chi c^2}\mathbf{c}_{k\alpha}F_\alpha + F_{pk}\Delta t \end{aligned} \tag{3.94}$$

where f_k is the pressure distribution functions; f_k^{eq} is the pressure equilibrium distribution function; Θ is the source term defined as:

$$\Theta = -\frac{u_r}{r} \tag{3.95}$$

F_α is the force term given by:

$$F_\alpha = -\frac{u_\alpha u_r}{\varepsilon r} - \frac{2\nu_e u_\alpha}{r^2}\delta_{\alpha r} \tag{3.96}$$

χ, τ_e and F_{pk} are kept the same as in (3.19), (3.20) and (3.21), respectively.
To include the effect of the porous medium and to recover, the EDF of the D_nQ_b models is defined as follows:

$$f_k^{eq} = \begin{cases} \rho_0 - \frac{4\varphi\varepsilon P}{\rho_0 c^2} + s_0(u) & , \quad k=0 \\ \frac{\phi\varepsilon P}{\rho_0 c^2} + s_k(u) & , \quad k=1,2,3,4 \\ \frac{\psi\varepsilon P}{\rho_0 c^2} + s_k(u) & , \quad k=5,6,7,8 \end{cases} \tag{3.97}$$

where the constant ρ_0 is the fluid average density, and s_k is given by:

$$s_k(\mathbf{u}) = w_k\left[\frac{\mathbf{c}_k.\mathbf{u}}{c_s^2} + \frac{\mathbf{uu}:\left(\mathbf{c}_k\mathbf{c}_k - c_s^2\mathbf{I}\right)}{2\varepsilon c_s^4}\right] \tag{3.98}$$

The parameters φ, ϕ and ψ satisfy the following relationships [310]:

$$\begin{cases} \phi + \psi = \varphi \\ \phi + 2\psi = \frac{1}{2} \end{cases} \tag{3.99}$$

Accordingly, the fluid pressure p and velocity $\mathbf{u}$ can be defined by:

$$p = \frac{c^2}{4\varphi\varepsilon}\left[\rho_0 + \sum_k f_k + s_0(u)\right] \tag{3.100}$$

$$\rho\mathbf{u} = \sum_k \mathbf{c}_k f_k + \frac{\Delta t}{2}\mathbf{F}_p \tag{3.101}$$

The new equation of state recovered here, called the perfect fluid equation of state, is more suitable to describe liquids than the perfect gas equation of state.
As it was mentioned in equation (3.25), the velocity is kept the same where $\mathbf{v}$ is an auxiliary velocity defined by 3.26. Through the Chapman-Enskog procedure, the effective viscosity is kept the same as in (3.29).

3.6.3 From lattice Boltzmann equation to mass and momentum equations for axisymmetric fluid flow through porous media

In order to reduce the errors due to the compressibility effect in the above model described in section 3.2, we first suppose that:

$$\mathbf{u} = \sum_k \mathbf{c}_k f_k + m\Delta t\mathbf{F}_p \tag{3.102}$$

where m is constant to be determined by the identification.

The forcing term F_{pk} in equation (3.16) can be written in a power series in a generalized form as mentioned in (3.37) and with the same proprieties as in (3.38). From the expression of f^{eq} in equation (3.98), we get the following expression of moments:

$$\sum_k f_k^{(0)} = \rho_0,$$

$$\sum_k \mathbf{c}_k f_k^{(0)} = \mathbf{u},$$

$$\sum_k \mathbf{c}_{k\alpha}\mathbf{c}_{k\beta} f_k^{(0)} = \frac{\varepsilon P}{\rho_0} I + \frac{\mathbf{u}_\alpha \mathbf{u}_\beta}{\varepsilon},$$

$$\sum_k \mathbf{c}_{k\alpha}\mathbf{c}_{k\beta}\mathbf{c}_{k\gamma} f_k^{(0)} = \frac{c^2}{3}\left(\mathbf{u}_\alpha\delta_{\beta\gamma} + \mathbf{u}_\beta\delta_{\alpha\gamma} + \mathbf{u}_\gamma\delta_{\alpha\beta}\right) \tag{3.103}$$

$$\sum_k \mathbf{c}_k f_k^{(1)} = -m\Delta t\mathbf{F}_p^{(1)} \tag{3.104}$$

$$\begin{array}{ll} \sum_k f_k^{(\eta)} = 0 & \text{, for } \eta > 0 \\ \sum_k \mathbf{c}_k f_k^{(\eta)} = 0 & \text{, for } \eta > 1 \end{array} \tag{3.105}$$

As before, the macrodynamic behavior arising from the LBE (3.94) is found from a multiscaling analysis using an expansion parameter ξ, which is proportional to the ratio of the lattice spacing to a characteristic macroscopic length:

$$f_k = f_k^{(0)} + \xi f_k^{(1)} + \xi^2 f_k^{(2)} + ... \tag{3.106}$$

$$\frac{\partial}{\partial t} = \xi \frac{\partial}{\partial t_1} + \xi^2 \frac{\partial}{\partial t_2} + ... \tag{3.107}$$

$$\nabla = \xi \nabla_1 \tag{3.108}$$

$$F_{pk} = \xi F_{pk}^{(1)} \tag{3.109}$$

$$\mathbf{F}_p = \xi \mathbf{F}_p^{(1)}, A_p = \xi A_p^{(1)}, \mathbf{B}_p = \xi \mathbf{B}_p^{(1)}, \mathbf{C}_p = \xi \mathbf{C}_p^{(1)} \tag{3.110}$$

The centered scheme is used for both source term Θ and force term F_α as [316]

$$\Theta = \Theta \left(\mathbf{x} + \frac{1}{2} \mathbf{c}_k \Delta t, t + \frac{1}{2} \Delta t \right) \tag{3.111}$$

$$F_\alpha = F_\alpha \left(\mathbf{x} + \frac{1}{2} \mathbf{c}_k \Delta t, t + \frac{1}{2} \Delta t \right) \tag{3.112}$$

which are written, via Taylor's expansion, as:

$$\Theta \left(\mathbf{x} + \frac{1}{2} \mathbf{c}_k \Delta t, t + \frac{1}{2} \Delta t \right) = \Theta(\mathbf{x}, t) + \frac{1}{2} \Delta t \left(\frac{\partial}{\partial t} + \mathbf{c}_k \cdot \nabla \right) \Theta(\mathbf{x}, t) + ... \tag{3.113}$$

$$F_\alpha \left(\mathbf{x} + \frac{1}{2} \mathbf{c}_k \Delta t, t + \frac{1}{2} \Delta t \right) = F_\alpha(\mathbf{x}, t) + \frac{1}{2} \Delta t \left(\frac{\partial}{\partial t} + \mathbf{c}_k \cdot \nabla \right) F_\alpha(\mathbf{x}, t) + ... \tag{3.114}$$

Expanding $f_k \left(\mathbf{x} + \mathbf{c}_k \Delta t, t + \Delta t \right)$ in equation (3.16) about $\mathbf{x}$ and t, and applying the above multiscaling expansion to the resulting continuous equation, we get the following equations in successive powers of parameter ξ:

$$O(\xi^0) : f_k^{(0)} = f_k^{eq} \tag{3.115}$$

$$O(\xi^1) : D_{1k} f_k^{(0)} = -\frac{1}{\tau \Delta t} f_k^{(1)} + w_k \Theta + \frac{c_{k\alpha}}{6c^2} F_\alpha + F_{pk}^{(1)} \tag{3.116}$$

$$O(\xi^2) : \frac{\partial f_k^{(0)}}{\partial t_2} + D_{1k} \left[\left(1 - \frac{1}{2\tau} \right) f_k^{(1)} \right] = -\frac{1}{\tau \Delta t} f_k^{(2)} - \left(1 - \frac{1}{2\tau} \right) \frac{c_{kr}}{r} f_k^{(1)} - \frac{\Delta t}{2} D_{1k} F_{pk}^{(1)} \tag{3.117}$$

where $D_{1k} = \frac{\partial}{\partial t_1} + \mathbf{c}_k \cdot \nabla_1$.

Taking moments of equation (3.116), we get the following macroscopic equations on time scale $t_1 = \xi t$ and space scale $\mathbf{x}_1 = \xi \mathbf{x}$:

$$\nabla_1.(\rho \mathbf{u}) = \Theta + A_p^{(1)} \tag{3.118}$$

$$\frac{\partial(\mathbf{u})}{\partial t_1} + \nabla_1.\Pi_{\alpha\beta}^{(0)} = \mathbf{F}_\alpha + \mathbf{B}_p^{(1)} + \frac{m}{\tau}\mathbf{F}_p^{(1)} = \mathbf{F}_\alpha + \left(n + \frac{m}{\tau}\right)\mathbf{F}_p^{(1)} \tag{3.119}$$

where we assume that $\mathbf{B}_p^{(1)} = n\mathbf{F}_p^{(1)}$, and n is a constant to be determined. $\Pi_{\alpha\beta}^{(0)}$ is the zeroth-order momentum flux tensor given by:

$$\Pi_{\alpha\beta}^{(0)} = \sum_k \mathbf{c}_{k\alpha}\mathbf{c}_{k\beta} f_k^{(0)} = \frac{\varepsilon P}{\rho_0} I + \frac{\mathbf{u}_\alpha \mathbf{u}_\beta}{\varepsilon} \tag{3.120}$$

In order to recover Euler equations from equations (3.118) and (3.119), we must set:

$$A_p = 0, n + \frac{m}{\tau} = 1 \tag{3.121}$$

Similarly, the moments of equation (3.117) lead to the following equation:

$$0 = \Delta t \left(m - \frac{1}{2}\right) \nabla_1 \mathbf{F}_p^{(1)} \tag{3.122}$$

Thus, $m = \frac{1}{2}$, necessarily.
It leads also to:

$$\frac{\partial \mathbf{u}}{\partial t_2} = \Delta t \left(m - \frac{1}{2}\right) \frac{\partial \mathbf{F}_p^{(1)}}{\partial t_1} + \nabla_1 \cdot \Lambda_{\alpha\beta} + \frac{\Lambda_{\alpha r}}{r} \tag{3.123}$$

where $\Lambda_{\alpha\beta}$ is given by:

$$\Lambda_{\alpha\beta} = -\left(1 - \frac{1}{2\tau}\right) \sum_k \mathbf{c}_{k\alpha}\mathbf{c}_{k\beta} f_k^{(1)} - \frac{\Delta t}{2} \sum_k \mathbf{c}_{k\alpha}\mathbf{c}_{k\beta}\mathbf{F}_{pk}^{(1)} \tag{3.124}$$

and

$$\Lambda_{\alpha r} = -\left(1 - \frac{1}{2\tau}\right) \sum_k \mathbf{c}_{k\alpha}\mathbf{c}_{kr} f_k^{(1)} \tag{3.125}$$

The first-order momentum flux tensor $\Pi_{\alpha\beta}^{(1)} = \sum_k \mathbf{c}_{k\alpha}\mathbf{c}_{k\beta} f_k^{(1)}$ can be simplified using equation (3.117) and (3.118). After some algebra, we obtain [92]:

$$\Pi_{\alpha\beta}^{(1)} = -\tau \Delta t c_s^2 \left(\nabla_{1\alpha}\mathbf{u}_\beta + \nabla_{1\beta}\mathbf{u}_\alpha\right) - \tau \Delta t \left[\frac{1}{\varepsilon}\left(\mathbf{u}_\alpha \mathbf{F}_{p\beta}^{(1)} + \mathbf{u}_\beta \mathbf{F}_{p\alpha}^{(1)}\right) - \frac{1}{2}(\mathbf{C}_{p\alpha\beta}^{(1)} + \mathbf{C}_{p\beta\alpha}^{(1)})\right] \tag{3.126}$$

Combining the above equation with equation (3.124), we obtain:

$$\begin{aligned}\Lambda_{\alpha\beta} = -\left(1 - \frac{1}{2\tau}\right) \nabla_1.\Pi_{\alpha\beta}^{(1)} - \frac{\Delta t}{4}\left(\mathbf{C}_{p\alpha\beta}^{(1)} + \mathbf{C}_{p\beta\alpha}^{(1)}\right) = \nu_e \left(\nabla_{1\alpha}\mathbf{u}_\beta + \nabla_{1\beta}\mathbf{u}_\alpha\right) \\ + \Delta t \left[\frac{1}{\varepsilon}\left(\tau - \frac{1}{2}\right)\left(\mathbf{u}_\alpha \mathbf{F}_{p\beta}^{(1)} + \mathbf{u}_\beta \mathbf{F}_{p\alpha}^{(1)}\right) - \frac{\tau}{2}(\mathbf{C}_{p\alpha\beta}^{(1)} + \mathbf{C}_{p\beta\alpha}^{(1)})\right]\end{aligned} \tag{3.127}$$

where ν_e is the kinematic viscosity defined by:

$$\nu_e = c_s^2 \Delta t(\tau - \frac{1}{2}) \tag{3.128}$$

To retrieve the governing equations (3.11) and (3.12) for the incompressible axisymmetric flows through porous media, the following relations must hold:

$$A_p = 0, n + \frac{m}{\tau} = 1, m = \frac{1}{2}, \mathbf{B}_p = m\left(2 - \frac{1}{\tau}\right)\mathbf{F}_p \tag{3.129}$$

and $\mathbf{C}_p$ set as:

$$\mathbf{C}_p = \frac{1}{\varepsilon}\left(1 - \frac{1}{2\tau}\right)(\mathbf{u}\mathbf{F}_p + \mathbf{F}_p\mathbf{u}) = \frac{2}{\varepsilon}\left(1 - \frac{1}{2\tau}\right)(\mathbf{u}\mathbf{F}_p) \tag{3.130}$$

Using the above results, we can find the following expression:

$$\nabla_1 \Lambda_{\alpha\beta} = \nu_e \left[\nabla_{1\alpha}\mathbf{u}_\beta + \nabla_{1\beta}\mathbf{u}_\alpha\right] \tag{3.131}$$

The same method of calculation is used also for $\Lambda_{\alpha r}$, which leads to:

$$\Lambda_{\alpha r} = \nu_e \left[\nabla_{1\alpha}\mathbf{u}_r + \nabla_{1r}\mathbf{u}_\alpha\right] \tag{3.132}$$

Combining the results on the $t_1 = \xi t$ and $t_2 = \xi^2 t$ time scales, equations (3.118), (3.119), (3.122) and (4.19) together with equations (3.129) and (3.130), we can easily check that the final macroscopic equations for incompressible flow through porous media given by equations (3.11) and (3.12) are obtained.

3.6.4 Performance of the enhanced model

In order to evaluate the performance of the new model, a precision and accuracy test is performed using the L_2-norm of the velocity error defined as:

$$E(U) = \frac{\|U - U_{analytical}\|_2}{\|U_{analytical}\|_2} \tag{3.133}$$

where $U_{analytical}$ is the closed-form solution value of velocity.

Figure 3.11 shows the variations of this global L_2-norm error with respect to mesh resolution for the four test cases. Results are presented in log-log scale so that slope indicates the consistency order of the two models. The slope is equal to 2 for the enhanced model and between 1.8 and 1.95 for previous model. Hence, L_2-norm shows clearly a second order accuracy in space for the enhanced model. Since the time step Δt in LBE is equal to the spatial resolution Δx, the accuracy of the enhanced model in time is also of second-order. Hence, it is demonstrated that: (i) the global errors from both LBE models converge at a quasi same rate; (ii) the two original models agree numerically and (iii) the incompressible enhanced model is more accurate than the original model.

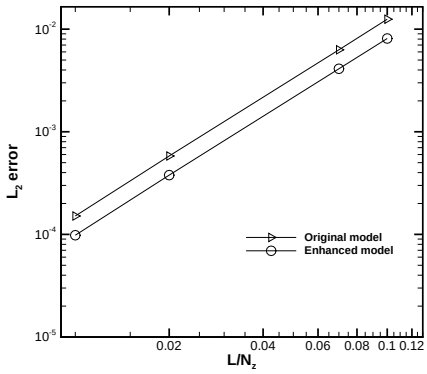

(a) First test case

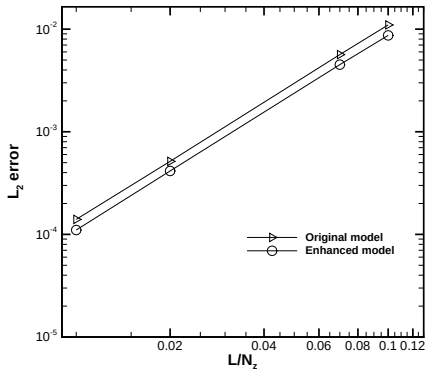

(b) Second test case

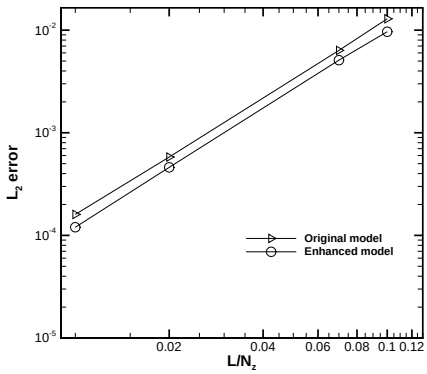

(c) Third test case

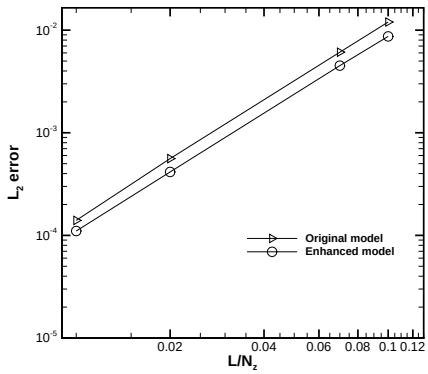

(d) Fourth test case

FIGURE 3.11 – L_2-norm errors with respect to mesh resolution for the different test case for the proposed LBE model ($\triangleright$ symbols) and its enhanced version ($\circ$ symbols).

3.7 Conclusion

In this chapter, we proposed a new LBM scheme, which inserts the position and time dependent source terms into the evolution equation of the standard LBM, and makes it recover the continuity and Navier-Stockes equations on the cylindrical coordinate system by Chapman-Enskog expansion. The presented model overcomes the existing methods drawbacks which involve more complicated terms than the original equations and add forces causing inconsistency with the lattice Boltzmann equation. An enhanced derived model was then proposed which avoids the compressibility effect in the existing LBE models. Then, we presented the detailed derivation of both models and their validation through many test cases. The effect of Forchheimer term was analyzed, too. This analysis is a guidance in the heat pipe modeling discussed in the next chapter.

Chapter 4

Numerical analysis of the heat pipe

Abstract

In the present chapter, the model developed in chapter 3 is used to simulate wicked heat pipe. The validations with analytical, experimental and numerical data are presented first. The effect of various parameters is investigated and the performance of a wicked heat pipe used in solar collectors is discussed. Then, the proposed HP is tested for different working conditions (working fluid, wick structure, wick thickness, heat input, evaporator length and tilt). Finally, an optimum configuration is suggested for HPSC manufacturing.

Résumé

Dans le présent chapitre, le modéle proposé au chapitre 3 est utilisé pour modéliser un caloduc à méche souvent rencontré dans les capteurs solaires. La validation avec les données analytiques, expérimentales et numériques est présentée. L'effet de plusieurs paramètres est investigé et la performance de caloduc est discutée. Le caloduc candidat est testé dans différentes conditions de travail (fluide de travail, structure de la mèche poreuse et son épaisseur, apport de chaleur, longueur de l'évaporateur et inclinaison). Enfin, une configuration optimale est esquissée pour la fabrication des HPSC.

4.1 Heat pipe modeling using Lattice Boltzmann method

The configuration of the considered heat pipe is illustrated in figure 4.1 with the coordinates system.

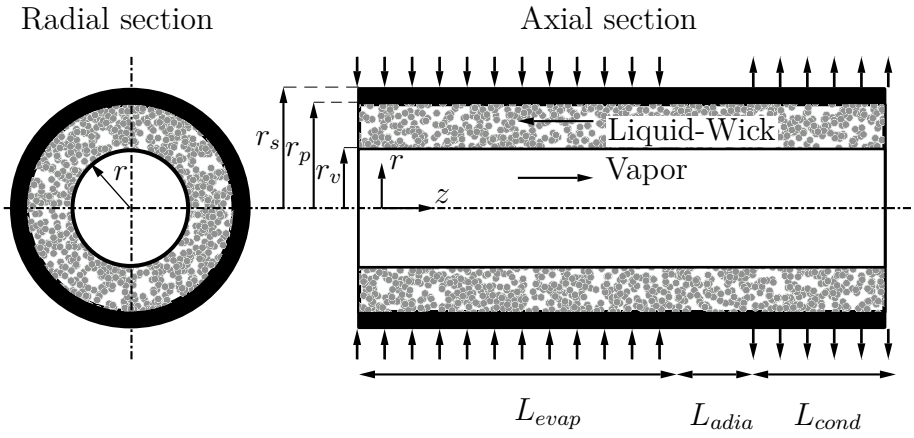

FIGURE 4.1 – Heat pipe schematic description. (Lengths are not to scale.)

4.1.1 Assumptions

The analysis is carried out for:
- An incompressible, laminar and axisymmetric flow;
- All thermophysical properties of the working fluid and solid matrix are assumed constant;
- Viscous dissipation and radiative effects are neglected;
- When considered, the gravitational acceleration is assumed acting in axial direction;
- The liquid and vapor phases are coupled through the (radially) stagnant liquid-vapor interface;
- The porous structure (or wick) is saturated with a single phase. Newtonian liquid is considered homogeneous and isotropic (*i.e.*, with uniform porosity and permeability).

4.1.2 Governing equations

The problem is split into three distinct regions:

— Solid region: The heat transfer through the wall is transferred purely by diffusion where $u_r = u_z = 0$. The corresponding energy equation is that of equation (3.4) where $\sigma^{'}$ is equal to 1.
— Liquid/porous region: Equations (3.1), (3.2), (3.3) and (3.4) are kept the same.
— Vapor region: Equations (3.1), (3.2), (3.3) and (3.4) are given for $\varepsilon = 1$ and $K \to \infty$.

4.1.3 Boundary conditions

In order to close the problem, boundary conditions must be provided for each region.

1. For the wall region:

— at $r = r_s$, $\begin{cases} -\lambda_s \frac{\partial T_s}{\partial r} = -q, 0 \leq z \leq L_{evap} \\ -\lambda_s \frac{\partial T_s}{\partial r} = 0, L_{evap} < z < L_{adia} \\ -\lambda_s \frac{\partial T_s}{\partial r} = h_{conv} \left(T_s - T_{in}\right), L_{adia} \leq z \leq L_{tot} \end{cases}$

— at $r = r_p$ and $0 \leq z \leq L_{tot}$, $\lambda_e \frac{\partial T_l}{\partial r} = \lambda_s \frac{\partial T_s}{\partial r}$

— at $z = 0$ and $r_p \leq r \leq r_s$, $\frac{\partial T_s}{\partial z} = 0$

— at $z = L_{tot}$ and $r_p \leq r \leq r_s$, $\frac{\partial T_s}{\partial z} = 0$

2. For the liquid/porous medium region:

— at $r = r_p$ and $0 \leq z \leq L_{tot}$, $u_{z,l} = u_{r,l} = 0, T_l = T_s$

— at $r = r_v$ and $0 \leq z \leq L_{tot}$,$u_{z,l} = 0, u_{r,l} = \dot{m}/\rho_l, T_l = T_{sat}\left(p_v\right)$

— at $z = 0$ and $r_p \leq r \leq r_s$, $u_{z,l} = u_{r,l} = 0$, $\frac{\partial T_s}{\partial z} = 0$

— at $z = L_{tot}$ and $r_p \leq r \leq r_s$, $u_{z,l} = u_{r,l} = 0$, $\frac{\partial T_s}{\partial z} = 0$

3. For the vapor region:

— at $r = r_v$ and $0 \leq z \leq L_{tot}$, $u_{r,v} = \dot{m}/\rho_v, \mu_v \frac{\partial u_{z,v}}{\partial r} = \mu_e \frac{\partial u_{z,l}}{\partial r}, T_v = T_{sat}(p_v)$

— at $r = 0$ and $0 \leq z \leq L_{tot}$, $\frac{\partial u_{z,v}}{\partial r} = 0$, $u_{r,v} = 0$, $\frac{\partial T_v}{\partial r} = 0$

— at $z = 0$ and $0 \leq r \leq r_v$, $u_{z,v} = u_{r,v} = 0, \frac{\partial T_s}{\partial z} = 0$

— at $z = L_{tot}$ and $0 \leq r \leq r_v$, $u_{z,v} = u_{r,v} = 0, \frac{\partial T_v}{\partial z} = 0$

4.1.4 LB implementation

In LBM, care should be taken when dealing with different media, because the lattice speed depends on the properties of the medium. Hence, the interface should be handled carefully, especially for unsteady-state problems. There are two ways to handle the interface problem either on a two separated media or on a single medium.

Analysis of the solid-liquid interface

Using the boundary conditions described in section 2.5, the different heat pipe boundaries are implemented. For the continuity boundary condition between the wall and the liquid/porous medium, at $r = r_p$ and $0 \leq z \leq L_{tot}$, $\lambda_e \frac{\partial T_l}{\partial r} = \lambda_s \frac{\partial T_s}{\partial r}$, it can be reached mainly by three methods which treat the generalized fluid solid interface conditions:
- First method [285]: It is considered as the easiest way to deal with this BC. The main idea is to use the half lattice division scheme for the interface as shown in figure 4.2. Hence, for the flow evolution, the half way bounce back model is applied at the interface, while, for the heat transfer evolution, only local properties either for fluid or solid need to be determined. However, this scheme is limited to the steady state cases as the continuity is insured after convergence [38, 277, 285, 288]. Otherwise, it actually gains much more computational efficiency with much less coding efforts than classical CFD methods and other LB schemes.
- Second method [185]: Each phase is processed separately by artificially splitting the domain into two sections (see figure 4.3). Then, the interface value is obtained, from conservation principles (energy balance), by matching flux and temperature at the interface using finite-difference scheme with first or second-order approximations.
- Third method The problem is processed as one single medium by scaling the distribution function at the interface properly. This is done by letting the relaxation time at the interface be equal to the average of the relaxation times of the underlying media.

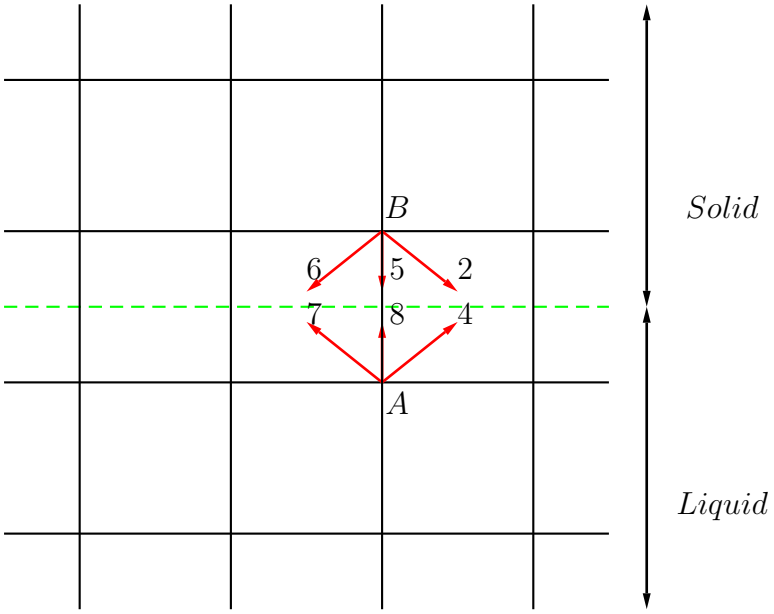

FIGURE 4.2 – Half lattice division for the solid/fluid interface processing; dashed line: solid/fluid interface; A: one lattice on the liquid; B: one lattice on the solid.

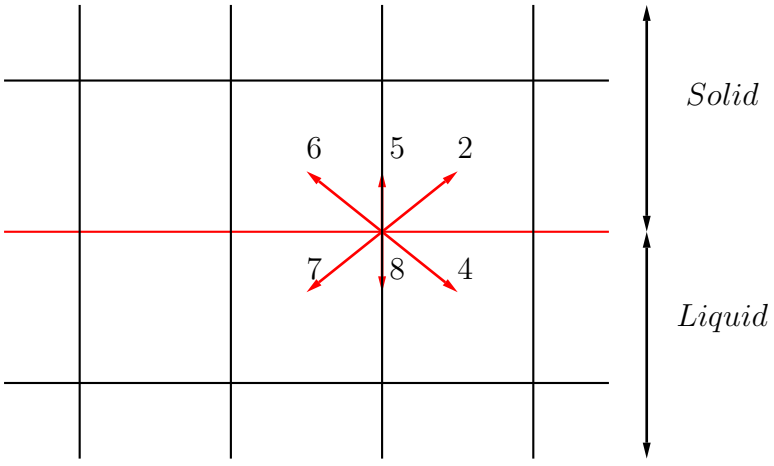

FIGURE 4.3 – Artificial seperation of the domain into two parts at the solid/fluid interface; solid red line: solid/fluid interface.

Analysis of the vapor-liquid/wick interface

Phase change from liquid to vapor or vice-versa is assumed to occur at the vapor-liquid/wick core interface as shown in figure 4.4.

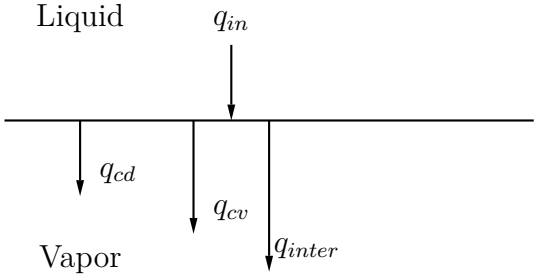

FIGURE 4.4 – Vapor-liquid interface.

The energy balance at the interface can be written as:

$$q_{in} = q_{inter} + q_{cd} + q_{cv} \tag{4.1}$$

where q_{in} is the total heat flux into the liquid given by:

$$q_{in} = q_{cd,l} + q_{cv,l} = -\lambda_{eff}\frac{\partial T_l}{\partial y} + \dot{m}_{inter}C_{pl}T_{inter} \tag{4.2}$$

q_{inter} is the latent heat of vaporization given by:

$$q_{inter} = \dot{m}_{inter}h_{lv} \tag{4.3}$$

q_{cd} is the conductive heat flux into the vapor given by:

$$q_{cd} = -\lambda_v\frac{\partial T_v}{\partial y} \tag{4.4}$$

q_{cv} is the convective heat flux due to the vapor velocity at the interface given by:

$$q_{cv} = \dot{m}_{inter}C_{pv}T_{inter} \tag{4.5}$$

The energy balance leads then to the following equation:

$$-\lambda_{eff}\frac{\partial T_l}{\partial y} + \dot{m}_{inter}C_{pl}T_{inter} = -\lambda_v\frac{\partial T_v}{\partial y} + \dot{m}_{inter}C_{pv}T_{inter} + \dot{m}_{inter}h_{lv} \tag{4.6}$$

Here by convention, $m_{inter} < 0$ denotes evaporation and $m_{inter} > 0$ denotes condensation. At this interface, the temperature is set to the saturation temperature at the running pressure. Thus, by applying Clausius-Clapeyron equation, the saturation temperature can be determined by:

$$T_{sat} = \left(\frac{1}{T_0} - \frac{R_g}{h_{lv}}\log\left(\frac{p_v}{p_0}\right)\right)^{-1} \tag{4.7}$$

where R_g is the gas constant of the working fluid, T_0 and P_0 are the reference temperature and pressure at the saturation conditions (1.01×10^5Pa and 373 K). Thus, the evaporation/condensation condition is applied through the equation based on the kinetic theory that relates the evaporation/condensation rate to the liquid-vapor interface temperature and the state properties of the vapor as follows [246]:

$$\dot{m} = \frac{2\widetilde{\sigma}}{2-\widetilde{\sigma}} \left(\frac{M}{2\pi R_g}\right)^{0.5} \left(\frac{p_{sat}(T_{lv})}{T_{lv}^{0.5}} - \frac{p_v}{T_v^{0.5}}\right) \tag{4.8}$$

where $\widetilde{\sigma}$ is the accommodation coefficient, M is the molar weight of the working fluid, and R_g is the universal gas constant. The above expression has been obtained with the assumption of equal mean evaporation condensation accommodation coefficient, where their variation with temperature and pressure is assumed to be small [171]. A value of unity for the accommodation coefficient is widely used [64, 128, 286].

As it was explained in section 4.1.4, processing with vapor-liquid/wick interface can be done following the same idea.

Algorithm

The LB algorithm, as it was described in section 2.8, is used for each part of heat pipe as follows.

4.1.5 Validations

A FORTRAN90 code has been written to solve the discretized lattice Boltzmann equations. In this section, the method implemented to assessing capillary heat pipe is first tested through comparison with data available in the literature.

Numerical validation

To illustrate the reliability of the written code, numerical simulations are performed for copper-water wicked heat pipe 1 m long and 0.022 m of diameter, see table 4.1.
The dimensionless vapor axial and radial velocity profiles are plotted in figure 4.6 where a heat input of 5000 W.m^{-2} is applied at the evaporator. The comparison of the present study with the work of Brahim *et al.* [20] shows excellent agreement.

As it can be seen from figure 4.6a, the evolution of the axial velocity at the vapor core center in the evaporator and condenser is slightly nonlinear. This is probably due to the pressure drop in the heat pipe. In addition, as we can see from 4.6b, the evaporation process reaches its maximum in the location of the evaporator region close to the adiabatic

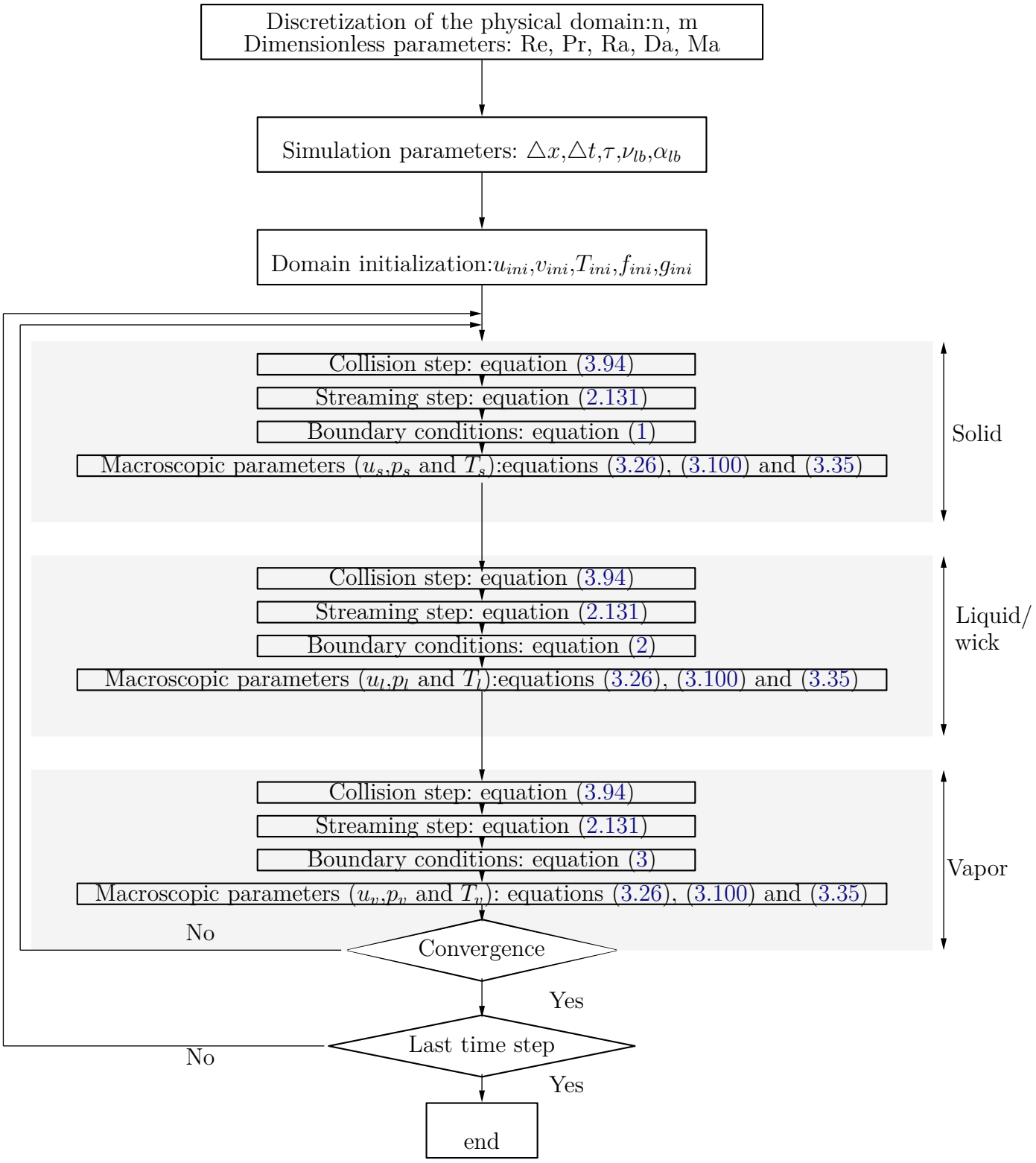

FIGURE 4.5 – LBM algorithm synoptics applied to HP.

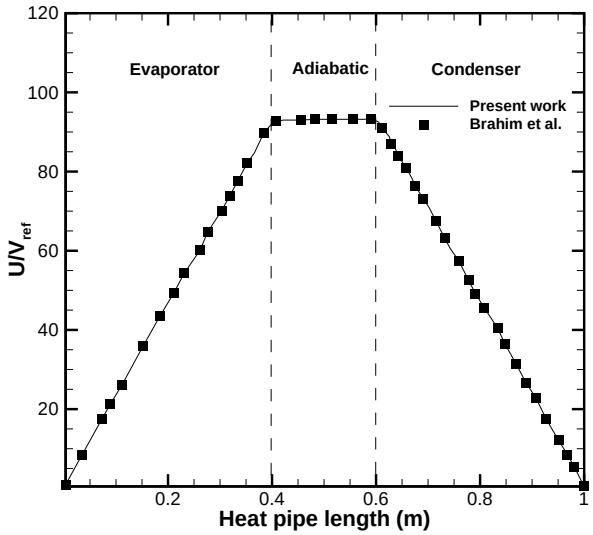

(a)

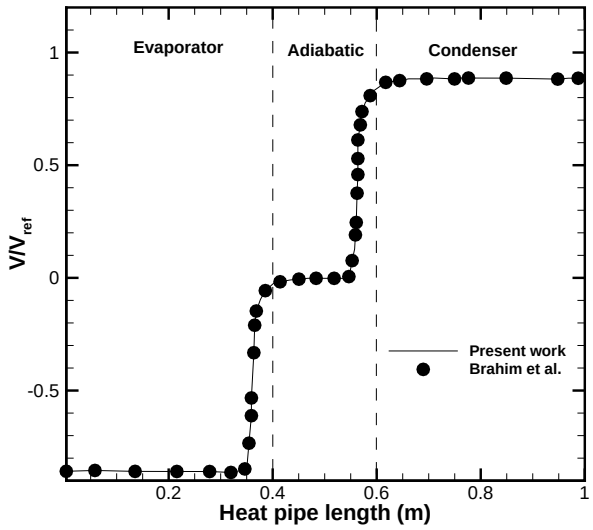

(b)

FIGURE 4.6 – Comparison between velocity profiles obtained from the present LBE model simulation (solid line) and from the results of Brahim *et al.* (symbols) [20]. (a) the axial velocity along the vapor core center, (b) the radial velocity along the liquid-vapor interface.

Heat pipe dimensions	
Evaporator length	0.4 m
Adiabatic length	0.2 m
Condenser length	0.4 m
Wall radius	0.022 m
Wick radius	0.02 m
Vapor radius	0.0127 m
Wick structure	
Porosity	0.46
Permeability	0.267×10^{-10} m^2
Material	sintered copper
Heat exchanger	
Heat input	5000 W.m^{-2}
Convective transfer coefficient	800 W.m^{-2}.K^{-1}
Material	
Wall	copper
Wick	copper

TABLE 4.1 – Heat pipe validation parameters [20].

region.

Analytic and experimental validation

Another validation test is performed based on the analytical work of Zhu *et al.* [319] and the experimental work of Huang *et al.* [159] for copper-water wicked heat pipe 0.89 m long and 0.00955 m of diameter, see table 4.2.

Figure 4.7a compares the LBE model predictions with the analytical and experimental results of the wall temperature distributions along the heat pipe. A good agreement can be seen with the analytical and the experimental results. However, there is a discrepancy between the calculated wall temperature and the experimental data at the beginning and the end of the condenser section. As same parameter values for the convective cooling boundary condition are used in the present model as those used in the analytical model, the good agreement between both results of the wall temperatures is observed. This further demonstrates that the present LBE model provides accurate predictions of the low-temperature heat pipe operations.

Figure 4.7b compares the present LBE model with the analytical results for vapor and liquid pressure distributions along the heat pipe. Good agreement between both results is noticeable. The variations of the vapor pressure along the heat pipe are small compared

Heat pipe dimensions	
Evaporator length	0.6 m
Adiabatic length	0.09 m
Condenser length	0.2 m
Wall radius	0.00955 m
Wick radius	0.0094 m
Vapor radius	0.00865 m
Wick structure	
Porosity	0.9
Permeability	1.5×10^{-9} m^2
Material	sintered copper
Heat exchanger	
Heat input	455 W
Convective transfer coefficient	1800 W.m^{-2}.K^{-1}
Material	
Wall	copper
Wick	copper

TABLE 4.2 – Heat pipe validation parameters [319].

with liquid pressure. As a consequence, a uniform vapor temperature is expected along the heat pipe length.

Figure 4.7c and 4.7d compare the maximum vapor and liquid velocity distributions along the heat pipe from the present LBE model with the analytical results of Zhu *et al.* [319]. A good agreement with the analytical results is shown here as well.

4.2 Numerical analysis of a wicked heat pipe

To assess the numerical solutions sensitivity to grid spacing, the grid-dependence test is performed using the L_2-norm of the temperature error defined as:

$$E(T) = \frac{\|T - T_0\|_2}{\|T_0\|_2} \tag{4.9}$$

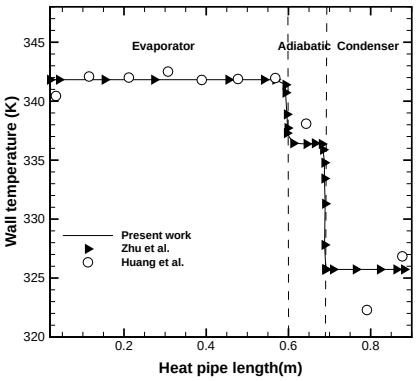

(a) Wall temperature

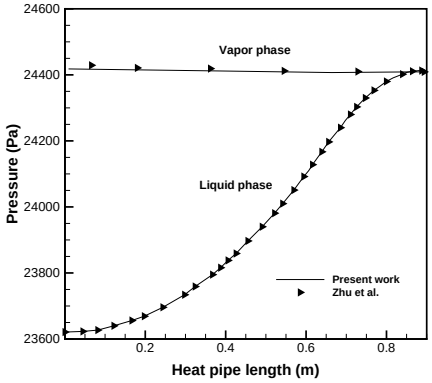

(b) Liquid and vapor pressure

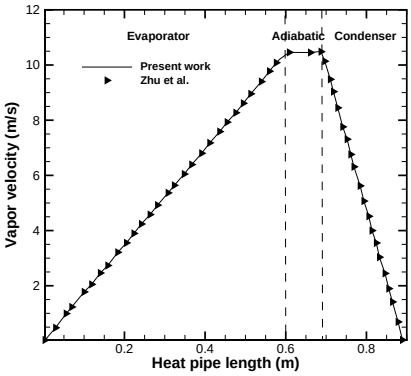

(c) Maximum vapor velocity

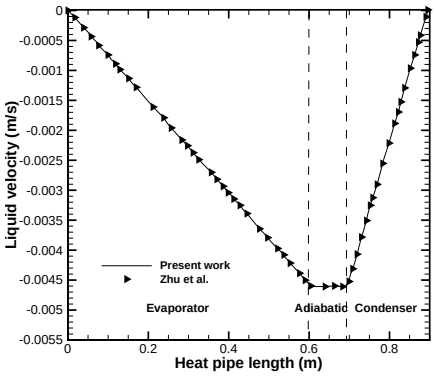

(d) Maximum liquid velocity

FIGURE 4.7 – A comparison of the present LBE model simulation (solid line) with the analytical results of Zhu *et al.* [319] (▷ symbols) and the experimental results of Huang *et al.* [159] (○ symbols).

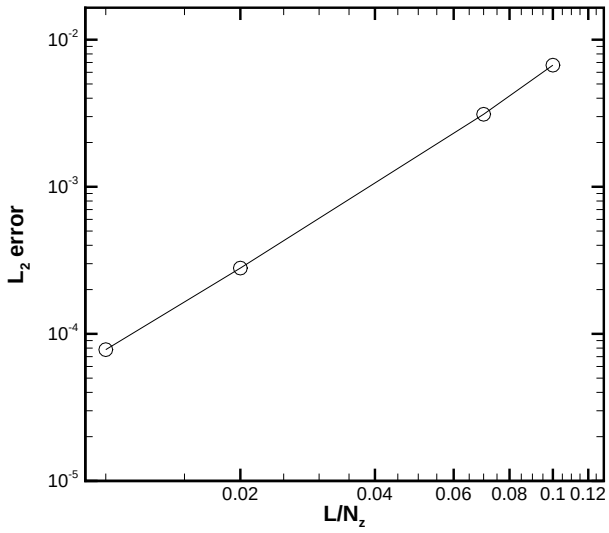

FIGURE 4.8 – L_2-norm errors versus the grid spacing.

where T_0 is the temperature field obtained with an extremely fine grid. Figure 4.8 shows the variations of this error versus the grid spacing.
Results are presented in log-log scale so that slope indicates the consistency order of the method. L_2-norm shows second-order, thus the present model is second-order accurate. In addition, the results indicate that solution is acceptable for grid space on order 10^{-2}.

4.2.1 Analysis of working fluid potential

The design of heat pipes begins with appropriate selection of the working fluid candidates. As mentioned in section 1.3.2, the selection of the working fluid must be done carefully and take several factors into consideration. Many working fluids are compatible with copper due to their wetability. In water heating systems operating near 60°C, acetone, methanol, ethanol and water are selected and tested as possible candidates. In addition, the fluid must be chemically stable over the operating range of the system and also be non-freezing at very low ambient temperatures. In general, the fluid should be in the liquid phase at the cooler end of the heat pipe and in the vapor phase at the hotter end of the pipe and must be compatible with the outer heat pipe material. Vaporization temperature is controlled by pressure and so is adjustable by the filling ratio, but the freezing temperature is not. Despite the beneficial characteristics of heat pipes, their effectiveness can be limited by poor thermal properties of the working fluid. To overcome such an issue, the thermal properties of the working fluids need to be enhanced [248].

In order to study the effect of the working fluid, it is still reasonable, before performing simulations, to make qualitative analysis and discussions based on its physical propriety only. Table 4.3 lists the most important thermophysical properties of the four working fluids that are thought to affect the heat transfer performance of the heat pipe. Previous works [229] showed that the working fluids applied in a heat pipe should have the following characteristics: high value of $(dp/dT)_{sat}$, high latent heat of vaporization, high specific heat, high surface tension, and low liquid dynamic viscosity. As it can be seen from Table 4.3, water has the most interesting thermophysical properties and the lowest $(dp/dT)_{sat}$ compared with ethanol, methanol and acetone. Higher dynamic viscosity requires higher force to drive the fluid. Higher boiling point and higher latent heat of vaporization lead to higher amount of heat exchanged with a minimum fluid flow. This maintains low pressure drops within the heat pipe. Higher thermal conductivity induces minimum radial temperature gradient and reduces the possibility of nucleate boiling at the wick/wall interface.
A high value of $(dp/dT)_{sat}$ implies that a small rise in temperature can generate a large pressure difference and accordingly greater driving force necessary for vapor motion. Under the same flow condition, higher specific heat may result in better sensible heat transfer

Properties \ Working fluid	Water	Methanol	Ethanol	Acetone
Vapor density ($kg.m^{-3}$)	0.017	0.21	0.78	0.63
Liquid density ($kg.m^{-3}$)	998	791	789	792
Thermal conductivity ($W.m^{-1}.°C^{-1}$)	0.599	0.212	0.172	0.170
Latent heat of vaporization ($kJ.kg^{-1}$)	2257	1101	846	523
Liquid specific heat ($kJ.kg^{-1}.°C^{-1}$)	4.18	2.48	2.39	2.35
Kinematic viscosity $\times 10^6$ ($m^2.s^{-1}$)	1.01	0.60	1.15	0.32
$(dp/dT)_{sat} \times 10^{-3}$ ($Pa.°C^{-1}$)	0.99	4.05	2.32	6.39
Molar mass($g.mol^{-1}$)	18	32	46	58
$P_{sat}(T$=20°C) kPa	2.3	16.9	5.4	30
Surface tension $\times 10^3$ (N/m)	72.8	22.6	22.8	23.7

TABLE 4.3 – Thermophysical properties of the working fluids at standard conditions.

and so in small thermal resistance. Note however that: (*i*) higher heat of vaporization will hinder the generation and growth of bubbles for the start-up of heat pipe and (*ii*) in heat pipe design, a high value of surface tension is desirable in order to generate a high capillary driving force and so to enable the heat pipe in order to operate against gravity and friction. In addition, the contact angle in our case is equal to 0° that means that the working fluid wets the wick and container material, an appreciable property.

The thermal resistance of the heat pipe is considered here as an indicator of heat pipe efficiency. The thermal resistance of heat pipe is given by:

$$R_{th} = \frac{(\bar{T}_{evap} - \bar{T}_{cond})}{Q} \tag{4.10}$$

It is defined as the ratio of the difference of average evaporator temperature, $\bar{T}_{evap}$, and average condenser temperature, $\bar{T}_{cond}$, to the heat input Q when steady state is reached. To explain its computation, the thermal resistance circuit shown in figure 4.9 is suggested.

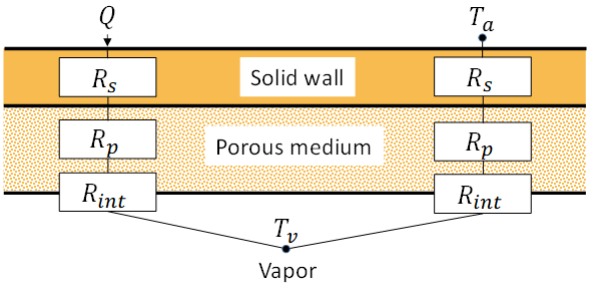

FIGURE 4.9 – Resistance circuit equivalent to the heat pipe.

The resulting total resistance is equal to:

$$R_{th} = R_{s,evap} + R_{p,evap} + R_{int,evap} + R_{int,cond} + R_{p,cond} + R_{s,cond} \tag{4.11}$$

Each term can be evaluated exactly, if advective effects are assumed negligible. At evaporator section, three thermal resistances occur causing by temperature drop: container wall ($R_{s,evap}$), liquid/ wick conduction resistances ($R_{s,evap}$) and vapor-liquid interfacial resistance ($R_{int,evap}$). These can be expressed, respectively, as follows:

$$R_{s,evap} = \frac{\log\left(r_s/r_p\right)}{2\pi\lambda_s L_{evap}} \tag{4.12}$$

$$R_{p,evap} = \frac{\log\left(r_p/r_v\right)}{2\pi\lambda_{eff} L_{evap}} \tag{4.13}$$

$$R_{int,evap} = \frac{2\pi T_v}{\frac{2\sigma}{2-\sigma} S_{evap}\sqrt{M} h_{lv} \frac{dP_{sat}}{dT}} \tag{4.14}$$

The resulting vapor on the inner wall of the condenser releases its latent heat of condensation. Thus, the heat is evacuated through the container wall to the outer wall surface. Similarly, at the condenser, three thermal resistances occur: container wall ($R_{s,cond}$),liquid/ wick conduction resistances ($R_{s,cond}$) and vapor-liquid interracial resistance ($R_{int,cond}$). These can be expressed, respectively, as follows:

$$R_{s,cond} = \frac{\log\left(r_s/r_p\right)}{2\pi\lambda_s L_{cond}} \tag{4.15}$$

$$R_{p,cond} = \frac{\log\left(r_p/r_v\right)}{2\pi\lambda_{eff} L_{cond}} \tag{4.16}$$

$$R_{int,cond} = \frac{2\pi T_v}{\frac{2\sigma}{2-\sigma} S_{cond}\sqrt{M} h_{lv} \frac{dP_{sat}}{dT}} \tag{4.17}$$

To validate the thermal resistance found numerically from the evaporator section to the condenser section, we compared it with this simple resistive model.

4.2.2 Effect of working fluid

The effects of the working fluid thermophysical properties on the performance of a capillary pumped heat pipe are investigated here. Four pure fluids (water, methanol, ethanol and acetone) are compared using sintered copper as wick structure which properties are given in table 4.6. Thermophysical proprieties of each fluid are presented in table 4.3. The heat pipe sizes are given in table 4.4. The effect of the working fluid on the wall temperature, liquid pressure drop, axial liquid and vapor velocity is shown in figure 4.10 for the tested working fluids. As it can be seen from figure 4.10a, a lower wall temperature difference between the evaporator and the condenser is observed for water. However, the highest wall temperature difference is observed for acetone. From figure 4.10b, the highest liquid pressure drop is observed for water. In the vapor core, the only end-to-end temperature variations are associated with changes in vapor pressure caused by vapor

Heat pipe dimensions	
Evaporator length	0.4 m
Adiabatic length	0.2 m
Condenser length	0.4 m
Wall radius	0.022 m
Wick radius	0.02 m
Vapor radius	0.0127 m
Heat exchanger	
Heat input	5000 $W.m^{-2}$
T_{out}	40°C
Material	
Wall	copper
Wick	copper

TABLE 4.4 – Heat pipe parameters.

Working fluids	Water	Methanol	Acetone	Ethanol
$R_{th_{model}}(K.W^{-1})$	0.18	0.19	0.21	0.20
$R_{th_{theoretical}}(K.W^{-1})$	0.178	0.186	0.205	0.198

TABLE 4.5 – Thermal resistance, R_{th}, for different working fluids.

flow pressure drops. These pressure drops are very small, and the vapor core is assumed to operate close to saturation conditions. However, since heat is transferred radially into and radially out of the heat pipe, temperature drops occur. In steady state, the total heat provides to the evaporator section must be extracted at the condenser section. Obviously, the absolute value of the liquid axial velocity, as well as the vapor axial velocity, decreases when increasing the working fluid propriety, *i.e.*, latent heat of vaporization and liquid specific heat, within the working fluid. This reduces the liquid velocity and the vapor axial velocity as explained previously and yields ultimately a lower pressure drop due, this time, to lower dynamic viscosity. From figure 4.10d and 4.10c, the highest axial liquid and vapor velocity are given for water while the lowest one is observed for acetone. Referring to the above analysis in section 4.2.1, water gives higher performance due to its intrinsic proprieties. Using now the thermal resistance as a performance criterion, water shows the best performance compared to the other working fluids, see table 4.5. Particularly, this fluid is able to transfer about 16% more heat flux than acetone at the same temperature difference. The LBE model provides good prediction of thermal resistance compared to the theoretical one.

4.2.3 Effect of wick structure

Besides the working fluid, the heat pipe wall and the heat pipe materials, the wick structure is an important element determining the performance of the heat pipe. The

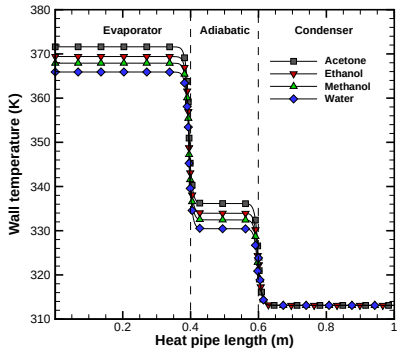

(a) Wall temperature

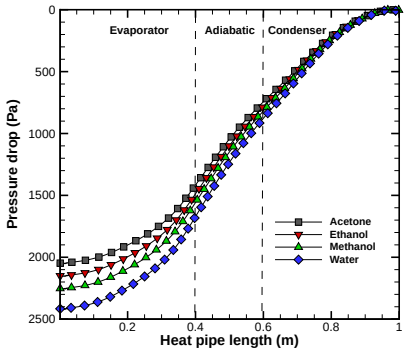

(b) Liquid pressure

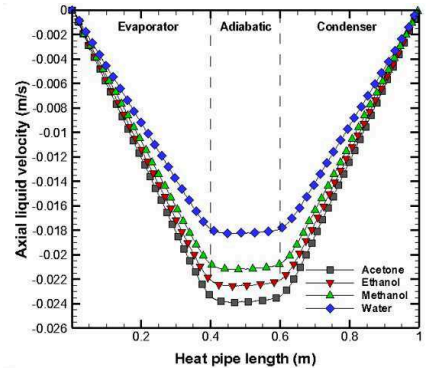

(c) Maximum axial liquid velocity

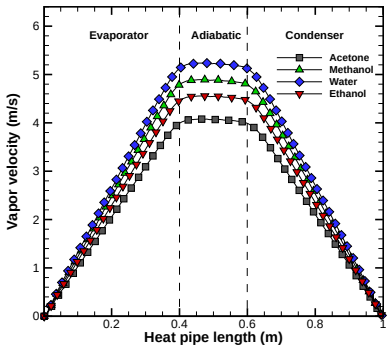

(d) Maximum axial vapor velocity

FIGURE 4.10 – Profiles for different working fluid.

wick structure works as a capillary pump driving the liquid from the condenser into the evaporator through the adiabatic section. A wick has to satisfy two apparently contrasting requirements in order to work effectively and efficiently. Provision of a flow path with low resistance for the vaporization, condensation and liquid flow requires as much open as possible porous structure with high permeability. In the opposite, and according to equation (3.9), a small pore size of the wick is desired for high capillary pumping pressure. It must also facilitate the evenly distribution of the working fluid over the entire area of the evaporator. These two facts need a special care because small pore structure creates larger capillary pressure, whereas larger permeability requires larger pores. Wick structures that satisfy adequately all these demands can contribute to optimize heat pipe performance. Selecting an appropriate wick generally implies a trade-off between a material with a high permeability and a high capillary pumping effect, therefore. Hence, the influence of porosity and permeability is investigated when water is used as working fluid by simulating three different wick structures: case (I) sintered steel, case (II) sintered copper and case (III) screen copper. More details are given in table 4.6.

The effect of the wick structure on the wall temperature, liquid pressure drop, axial

Cases	Wick type	Porosity (-)	Permeability (m^2)
Case (I)	Sintered steel	0.6305	3×10^{-10}
Case (II)	Copper screen	0.9	1.5×10^{-9}
Case (III)	Sintered copper	0.4	1.17×10^{-11}

TABLE 4.6 – Proprieties of the different wick structure.

Wick structure	Copper screen	Sintered Steel	Sintered Copper
$R_{th}(\mathrm{K.W^{-1}})$	0.21	0.19	0.18
$R_{th_theoretical}(\mathrm{K.W^{-1}})$	0.212	0.189	0.178

TABLE 4.7 – Thermal resistance, R_{th}, for different wick structure.

liquid and vapor velocity is shown in figure 4.11 for the three different wick proprieties using water as working fluid. Figure 4.11a shows wall temperature distribution for different wick structures. A lower temperature difference between the evaporator and the condenser is noticeable for sintered copper. A decrease of heat pipe temperature in the entrance leads to an increase in the absolute liquid pressure 4.11b. In fact, the wick thermal conductivity affects significantly the wall temperature and leads consequently to a lesser pressure drop. The effect of the wick structure on the axial liquid and vapor velocity profiles is given in figure 4.11c and 4.11d, respectively. As seen, the absolute value of the liquid axial velocity, as well as the vapor axial velocity, decreases when increasing the propriety, *i.e.*, porosity and permeability, within the wick structure. On the one hand, because of hydrodynamic resistance, a decrease in permeability reduces the liquid velocity. On the other hand, the decrease of the porosity leads to an increase of the vapor axial velocity. This can be explained by the fact that, in this case, a smaller area of liquid contributes to phase change so in order the same heat input power to be exchanged (the heat flux density being fixed), the vapor axial velocity must be larger, necessarily.

According to the above mentioned criterion, sintered copper wick HP shows the best performance of the three cases under the same heat input power and cooling conditions, see table 4.7. These results show that for the same heat input power, sintered copper HP is able to transfer almost twice as much heat power as copper screen HP at the same temperature difference. By comparing the model resistance to the theoretical one, good predictive feature is found.

4.3 Numerical study of heat pipe performance used in solar applications

The results of the flow and heat transfer in a typical cylindrical heat pipe, usually encountered in solar applications, are presented. The effect of the evaporator region, working fluid, wick structure and inclination angle are discussed. In the numerical results

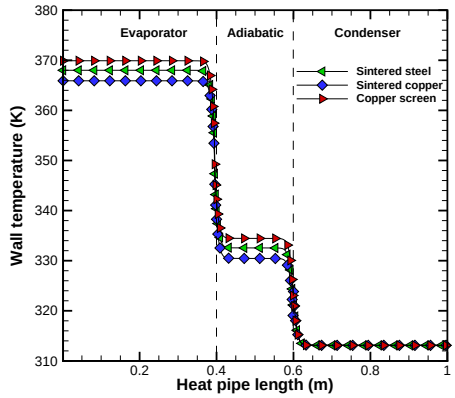

(a) Wall temperature

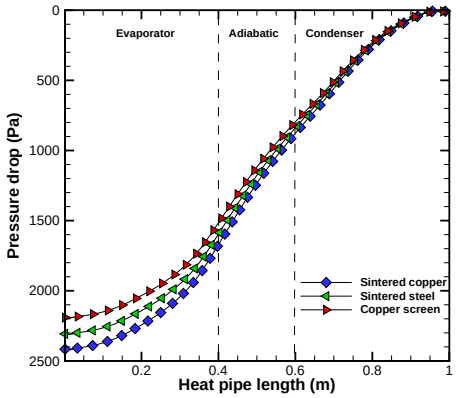

(b) Liquid pressure

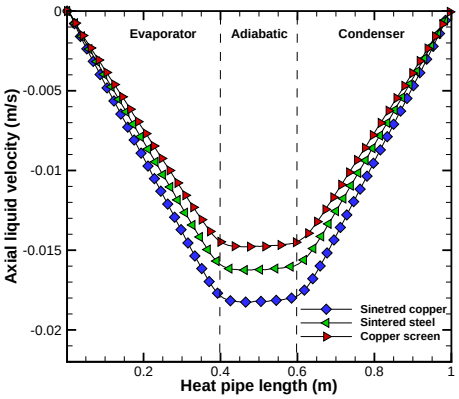

(c) Maximum axial liquid velocity

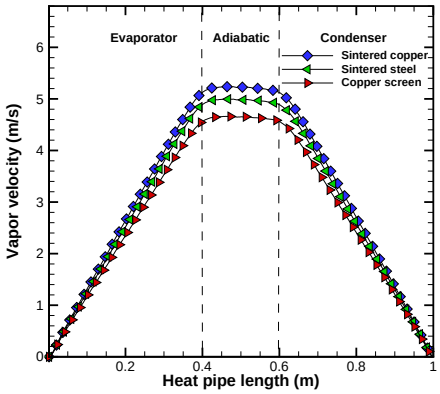

(d) Maximum vapor axial velocity

FIGURE 4.11 – Profiles in the liquid/wick region for different wick structures.

presented here, the thermal properties of the working fluids are calculated at the reference temperature and are assumed constant. The input heat flux density q is set to 700 W.m^{-2}. The coolant water enters the condenser cooling jacket at 22°C and 4 g.s^{-1}, see figure 4.21. The temperature of the coolant water at the exit of the cooling jacket is calculated using the balance $Q = \dot{m}Cp(T_{out} - T_{in})$. The convective heat transfer coefficient in the cooling jacket is set to 1400 W.m^{-2}.K^{-1}. Table 4.8 includes the default value of parameters used in this work unless otherwise specified.

As initially the porous media is totally filled with liquid and the vapor region is totally filled with vapor only, the definition of the filling ratio is as follow:

$$\text{Filling ratio}(\%) = \frac{V_l}{\left(L_{tot}\pi\varepsilon\left(r_p - r_v\right)^2 + L_{tot}\pi r_v^2\right)} \times 100 \tag{4.18}$$

Heat pipe dimensions	
Evaporator length	1.4 m
Adiabatic length	0.06 m
Condenser length	0.3 m
Wall radius	0.022 m
Wick radius	0.02 m
Vapor radius	0.0127 m
Wick structure	
Porosity	0.4
Permeability	1.17×10^{-11} m^2
Effective heat capacity	4216 J.kg^{-1}.K^{-1}
Effective diffusivity	3.0476 W.m^{-1}.K^{-1}
Material	sintered copper
Heat exchanger	
Heat input	700 W.m^{-2}
Convective transfer coefficient	1400 W.m^{-2}.K^{-1}
Inlet temperature	22°C
Mass flow	4×10^{-3} kg.s^{-1}
Material	
Wall	copper
Wick	copper

TABLE 4.8 – Heat pipe parameters.

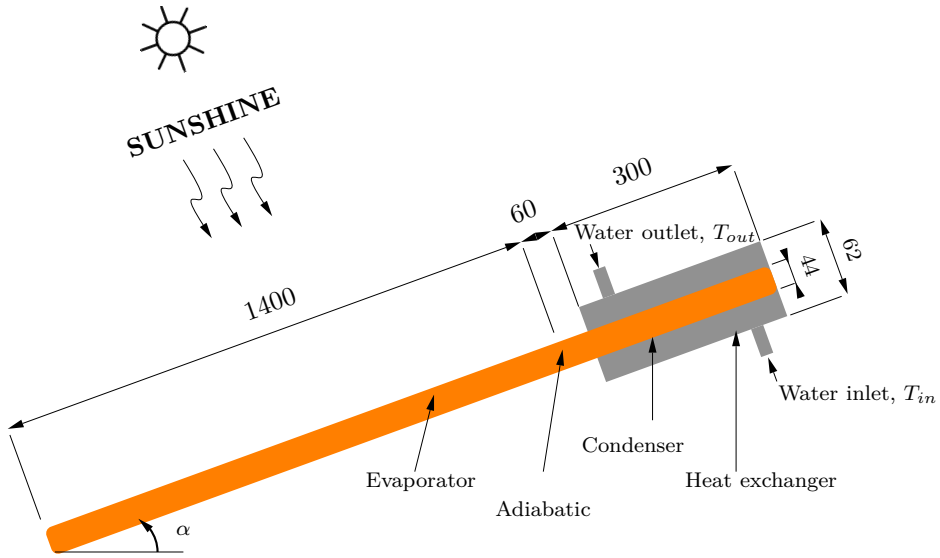

FIGURE 4.12 – Heat pipe coupled to heat exchanger. (All sizes are given in mm.)

where $L_{tot} = L_{evap} + L_{adia} + L_{cond}$ and V_l is liquid volume and is defined as:

$$V_l = \frac{V_p \rho_l + V_v \rho_v}{\rho_l} \tag{4.19}$$

where V_p is the volume of the liquid saturating the porous medium and V_v is vapor phase volume.

For the required operating temperature range in the neighborhood of 60°C for water heating systems, acetone, methanol, ethanol and water are selected and tested as possible candidates.

4.3.1 Heat input effect

The variations of the thermal resistance of the heat pipe with different working fluids as a function of the applied heat flux density is shown in figure 4.13. The variations are of similar pattern for all the cases. At lower heat input, Q=600 W.m^{-2}, heat transfer mechanism is dominated by pure conduction and as much depends on fluid properties and is less efficient, hence the large thermal resistance. However, the latter decreases appreciably when heat input increases. This feature of the thermal resistance is a typical characteristic of heat pipes. The decrease of the thermal resistance is due to the liquid motion onset that reduces significantly the film resistance both at the evaporator and the condenser. The thermal resistance for water is calculated as 0.237 K.W^{-1} and for acetone as 0.2 K.W^{-1} at heat input of 600 W.m^{-2}. Hence, thermal resistance is observed highest for water and lowest for acetone whereas it falls in-between for ethanol and methanol, respectively.

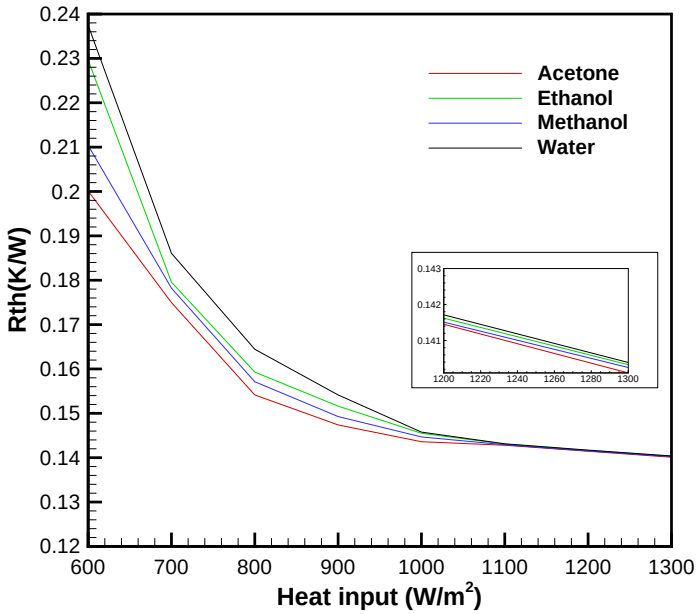

FIGURE 4.13 – Variations of thermal resistance versus heat input density for different working fluids.

4.3.2 Porosity and permeability effect

The influence of permeability and porosity is investigated for different working fluids. In order to distinguish their effect, the evolution of porosity as well as the permeability are shown in figure 4.14 to 4.15 in the range of 0.1 to 0.9 and 5×10^{-11} to 5×10^{-9}m^2, respectively. Worth noting here that changing further the value of these parameters does not change the thermal resistance trend. As we can see from figure 4.14, the increasing of porosity leads to smaller thermal resistance. This may be explained by the increase of pores diameter which leads to the decreases of the global resistance to the flow of working fluid in the porous medium. The same trend can be seen from figure 4.15 where the decrease of permeability leads to obstructing the fluid circulation in the porous medium. Note that one can retrieve the thermal resistance of any wick structure in the mentioned porosity and permeability range using the tested working fluids.

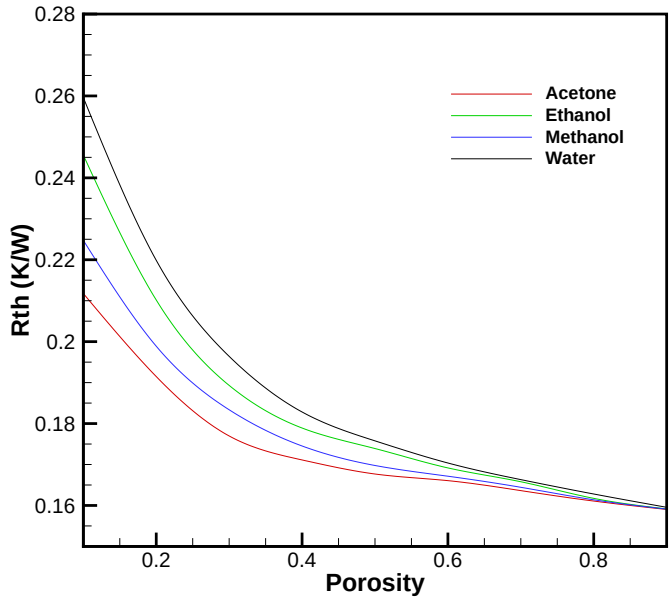

FIGURE 4.14 – Variations of thermal resistance versus the porosity for different working fluids and permeability equal to $1.17 \times 10^{-11}\mathrm{m}^{-2}$.

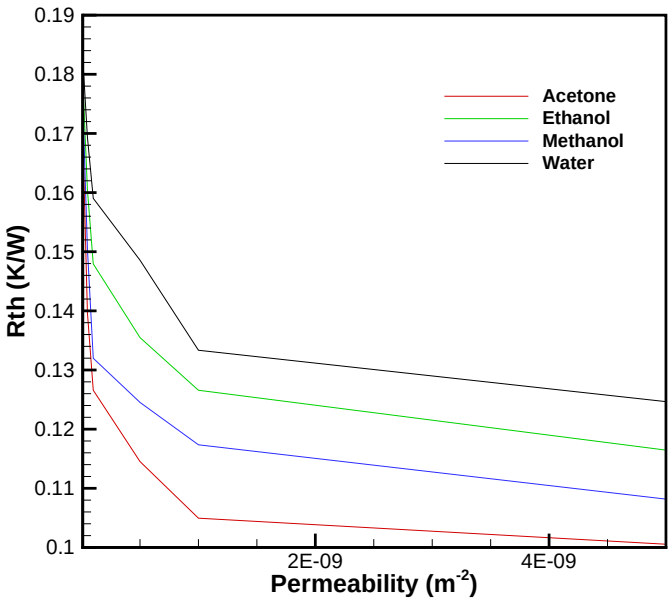

FIGURE 4.15 – Variations of thermal resistance versus the permeability for different working fluids and porosity set to 0.4.

Let us discuss three wick structure cases mentioned previously in 4.2.3: case (I) sintered

steel, case (II) sintered copper and case (III) screen copper, which properties are given in table 4.6. Using the thermal resistance, as a performance criterion, case (II) shows the best performance under the same heat input and cooling conditions.
From figure 4.14 and 4.15 the thermal resistance using water as working fluid is 0.182K.W^{-1} for cases III. For the two other cases, case (I) and (II), the thermal resistance is 0.217K.W^{-1} and 0.194K.W^{-1} respectively. The thermal resistance is calculated for the four tested working fluids, for the three porous medium cases, and is given table 4.9. These results show that for the same heat input, case (III) has the lowest thermal resistance and is able to transfer higher heat flux compared to case (I) at the same temperature difference. A wick with features like those for case (III) seems to be more suitable for heat pipes designed for solar collectors, where the density of solar heat flux within a sunny day increases rapidly. Additionally, it seems to provide means to rapidly produce hot water in cold days thus increasing the annual thermal performance of the solar collector.

	Acetone	Ethanol	Methanol	Water
Case (I)	0.176	0.189	0.180	0.194
Case (II)	0.197	0.218	0.199	0.217
Case (III)	0.170	0.179	0.175	0.182

TABLE 4.9 – Thermal resistance (Rth(K.W^{-1})) of each case for different working fluids and different wick structures.

The performance of heat pipe used in solar collectors can also be controlled by proper design including appropriate wick thickness, evaporator length and inclination angle. This analysis is performed in what follows.
The evolution of temperature in the wall/liquid-wick region is presented in figures B.1, B.2 and B.3 for each case and with different working fluids when steady state is reached. The porosity and the permeability are given in table 4.6. The heat flux density q is set to 700 W.m^{-2}. Obviously, the evaporator, adiabatic and condenser regions are well distinguishable, while the vapor core is almost isothermal. For the three cases, a lower temperature difference between the evaporator and the condenser can be observed for acetone as working fluid. A decrease of heat pipe temperature in the entrance leads to performance degradation. In fact, the wick thermal conductivity significantly affects the wall temperature and consequently leads ultimately to less pressure drop. The evolution of axial velocity in the vapor region is presented in figures B.4, B.5 and B.6 for each case and with different working fluids in the same conditions as in figures B.1, B.2 and B.3. Independently of the case considered, a lower axial velocity can be observed for acetone as working fluid. A decrease of heat pipe velocity leads to increasing the temperature which in turn affects negatively the performance of heat pipe solar collector.

4.3.3 Wick thickness effect

The effect of the wick thickness on the thermal resistance is illustrated for different working fluids in figure 4.16. For all working fluids, the thermal resistance is maximum for smaller thickness and decreases slightly for larger wick thickness. The impact of wick layer thickness on the performance is therefore modest within the thickness range investigated here. Li *et al.* [153] also reported on the virtual independence of thermal performance on wick thickness from their tests under similar fluid conditions. This wick independence may be the consequence of the intrinsic proprieties, high porosity and low permeability that balances the relative small wick thickness.

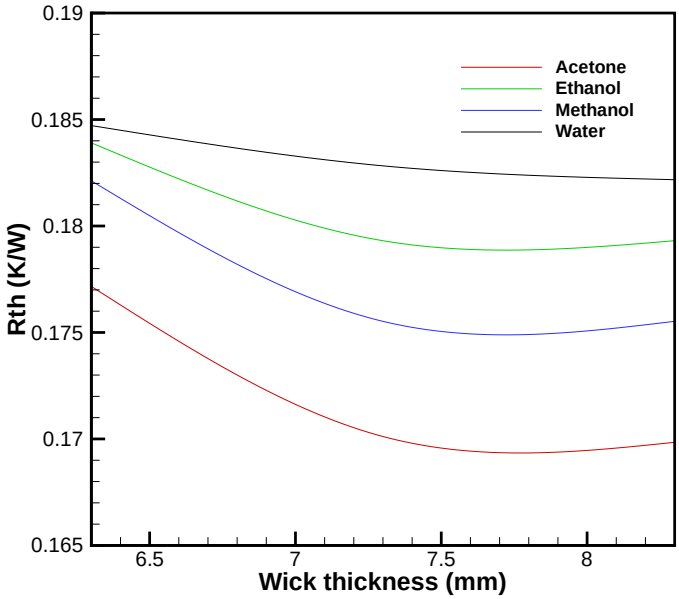

FIGURE 4.16 – Variations of thermal resistance versus the wick thickness for different working fluids.

4.3.4 Evaporator length effect

The effect of evaporator length on the thermal performance of the heat pipe is investigated with different working fluids and shown in figure 4.17. This effect is assessed using the relative deviation of the thermal resistance R_{th} compared with the thermal resistance of the heat pipe standard configuration, R_{th0}, *viz.* when the evaporator length equals 1.4 m. So this ratio is given by $(R_{th} - R_{th0})/R_{th0}$. All other parameters given in table 4.3 are unchanged. It should be noticed here that the total heat pipe length and condenser length are kept constant while the adiabatic length is constrained by the other lengths. As we can see from figure 4.17, evolution of the ratio is linear in terms of the

evaporator length. Under the same conditions, the performance seems marginally affected by the evaporator length. This can be explained by the fact that the evaporator occupies already a large region of the heat pipe in the context of solar applications. So increasing or decreasing slightly the evaporator length seems not having noticeable effect on the device performance.

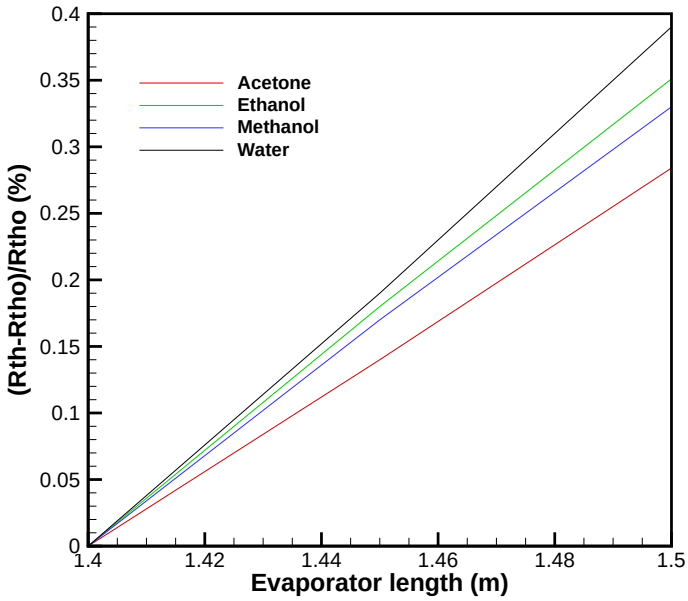

FIGURE 4.17 – Variations of the ratio of thermal resistance versus the evaporator length for different working fluids.

4.3.5 Inclination effect

The effect of inclination angle, with respect to the horizontal, of the heat pipe on its thermal resistance is illustrated in figure 4.18 for different working fluids. All other parameters are given in table 4.3. The tests are carried out with heat pipes tilted at four different angles (0°, 30°, 45° and 90°) with respect to the horizontal, all favorable. It is obvious that increasing the inclination angle (setting the evaporator lower than the condenser) causes the condensed liquid returns easier to the evaporator section by means of favorable gravity and consequently lower thermal resistances is gotten. So the thermal resistance decreases with increasing angle for all working fluids, independently of their capillary potential. At 30° inclination angle, after condensation the working fluid flows back to the evaporator section at a moderate rate so the heat exchange coefficient at both the evaporator and the condenser is still more important than at no inclination, which decreases the global resistance moderately, too. At even larger inclination angles ($\geq 45°$) superior thermal performance is observed. In water heating collector application, the heat

pipe performance depends also on the solar orientation. Thus, the existing sintered mesh in contact with the inner wall of the heat pipe reduces the non-uniform heat transfer along the circumference direction and makes 45° to be the optimal inclination angle for the different working fluids. In fact, the phenomenon of overheating for solar collectors in summer is an important issue. Excess energy in summer should be avoided. Thus, it is advisable to balance the supply of solar energy throughout the year. For this reason, it is necessary to adopt a midway inclination, say 45°. This favors the heat input in winter and reduces it in summer. (Note here that it is assumed that the solar radiation is not affected by the inclination angle, a quite strong assumption). Thus, referring to figure 4.18, the optimum inclination angle is 45° for the four working fluids tested here. Smaller inclination angles will decrease gravity effect, creating a more disturbed vapor flow. Larger inclination angle will cause too much large gravity effect in the porous medium, leading to subcooling phenomenon at the evaporator potentially preventing phase change at the evaporator region.

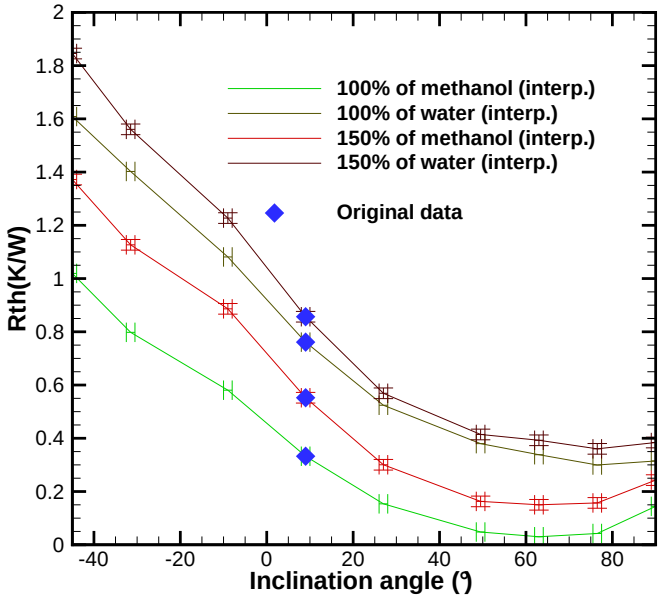

FIGURE 4.18 – Variations of thermal resistance versus the sine of inclination angle for different working fluids.

4.3.6 Working fluid effect

Compared to the study mentioned in section 4.2, acetone seems to be the most suitable fluid for efficient heat pipes in solar applications among the tested fluids and not water. Why such a behavior can be possible as long as no particular new phenomena are involved in the latter HP configuration ?

If we recall the expression (4.20) of the total resistance, we can see that the assumptions (linearity of the temperature profile within each zone) leading to it still hold but for the condenser, where the ratio of its length to the evaporator length is very large compared to the former HP configuration (this ratio is equal to 8). This means that the porous medium experiences here much larger flow in the condenser zone than formally. The direct consequence of this is that the advective effect becomes not negligible anymore compared to the (linear) diffuse effect. Making reference to table 4.3, we can see for acetone and water that:

i) the viscosity ratio is 1/3
ii) the latent heat of vaporization ratio is 1/4
iii) the liquid density ratio is 4/5

So the ratio of temperature gradient at the interface separating the solid wall and the porous medium at th condenser zone (between acetone and water) and due to advection is equal: $\frac{1}{\frac{1}{4}\times\frac{4}{5}\times\frac{1}{3}} = 15$. The condenser resistance is 5 times lower for acetone than for water at the same heat flux when advection is considerable, hence the trend found in this HP configuration.

4.4 HPETSC thermal analysis

4.4.1 HPETSC configurations

There is mainly two technologies of HPETSC used in SWH. Thermal losses occur for two types by radiation from the absorber tube/plate. In this study, we focus on the HP systems integrated in such devices.

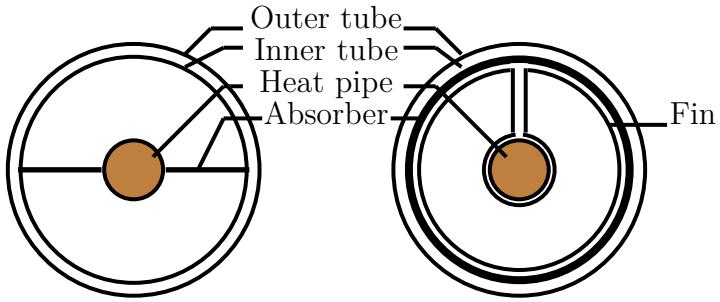

FIGURE 4.19 – Cross section of heat pipe evacuated tube solar collector.

From the mentioned literature in section 1.8, it can be noticed that all the researches have been led on ETSCs based on thermosyphon HPs [154]. When HP is operating in gravity-assisted mode, a high heat transfer capability can be achieved. However, a wick

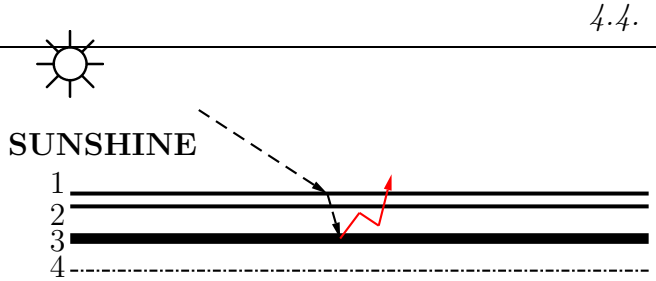

FIGURE 4.20 – General description of heat pipe evacuated tube solar collector.

structure is required for circumferential distribution of liquid along the HP. In addition, most of the aforementioned studies were performed on the basis of energy analysis. However, exergy analysis is as much important for performance evaluation. Moreover, ETSC based CHP with both energy and exergy analysis is unavailable to the best knowledge of the authors. Hence, this study is performed on both the exergetic and energetic efficiency of a ETSC based on CHP using such a heat transfer enhancer.

4.4.2 Single pipe thermal analysis

For a single HP, the useful energy gained is equal to the difference between solar energy absorbed and the heat loss to the ambient over the length of the absorber. Hence, the

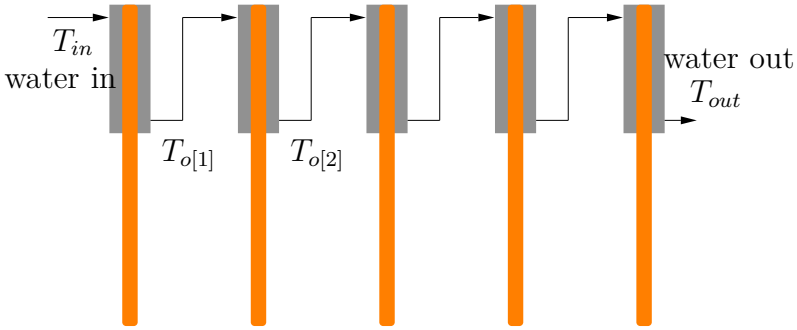

FIGURE 4.21 – Heat pipe evacuated tube solar collector.

rate of the useful energy collected can be modeled using the Hottel-Willer [105] equation given by:

$$Q_{u[n]} = A_{c[n]} F_R \left[I \left(\tau\alpha \right)_e - U_L \left(T_{evap[n]} - T_a \right) \right] \tag{4.20}$$

where A_c is the collector aperture area, I is the solar radiation intensity, $(\tau\alpha)_e$ is the collector effective transmittance-absorptance product, F_R is the removal factor, U_L is the heat loss coefficient and T_a is the environmental temperature. The useful energy extracted in the form of heat by the fluid flowing in the heat is given by:

$$Q_{u[n]} = \dot{m} C_p \left(T_{o[n]} - T_{i[n]} \right) \tag{4.21}$$

where $\dot{m}$ is the mass flow rate of the working fluid in the manifold. From (4.20) and (4.21), $T_{o[n]}$ can be deduced:

$$T_{o[n]} = T_{i[n]} + \frac{A_c F_R}{\dot{m} C_p} \left[I \left(\tau\alpha \right)_e - U_L \left(T_{evap[n]} - T_a \right) \right] \tag{4.22}$$

Energy efficiency

The energy analysis represents the way energy is used in a given application. It is related to the first law of thermodynamics through the energy efficiencies and balances. A generalized energy balance is given by:

$$\sum \dot{E}_{in} = \sum \dot{E}_{out} \tag{4.23}$$

The thermal or energy efficiency of solar collector is defined by the ratio of the net heat gained to the received solar ration by the HP. Based on this definition, the thermal efficiency is given by:

$$\eta_{energy} = \frac{Q_u}{A_c I} \tag{4.24}$$

$$= \frac{\dot{m} C_p \left(T_o - T_i \right)}{A_c I} \tag{4.25}$$

where $\dot{m}$ is the mass flow rate of the working fluid in the manifold. Using equation (4.20), the energy efficiency reads:

$$\eta_{energy} = F_R \left(\tau\alpha \right)_e - F_R U_L \frac{\left(T_{evap[n]} - T_a \right)}{I} \tag{4.26}$$

Exergy efficiency

In thermodynamics, the calculation of exergy efficiency starts by finding out the exergy sources and sinks. For solar collectors, the exergy of the sun radiation is considered as the source of exergy and the header water which is heated in the top of manifold is considered as the exergy sink.

The exergy of the thermal radiation is given by [25]:

$$\dot{E}x_{heat} = A_c I \left(1 - \frac{T_a}{T_{sol}} \right) \tag{4.27}$$

where T_{sol} is the temperature (in Kelvin) of the exergy source which is considered to be 75% of the black body temperature of the sun assumed to be 4500 K [215]. The rate of exergy given in the above equation represents the exergy source.

The exergy of the inlet and outlet water are given by:

$$\dot{E}x_{w,in} = \dot{m}C_p \left[(T_{in} - T_a) - T_a ln\left(\frac{T_{in}}{T_a}\right)\right] \tag{4.28}$$

$$\dot{E}x_{w,out} = \dot{m}C_p \left[(T_{out} - T_a) - T_a ln\left(\frac{T_{out}}{T_a}\right)\right] \tag{4.29}$$

Thus, the rate of exergy can be calculated by subtracting equation (4.29) from equation 4.28 as follows:

$$\Delta\dot{E}x_w = \dot{m}C_p \left[(T_{out} - T_{in}) - T_a ln\left(\frac{T_{out}}{T_{in}}\right)\right] \tag{4.30}$$

The rate of exergy given in equation (4.31) represents the exergy sink.
The exergy efficiency is defined by the ratio of absorbed exergy in the exergy sink which is delivered to the exergy source. For a solar collector, it can be expressed as:

$$\eta_{ex} = \frac{\dot{m}C_p \left[(T_{out} - T_{in}) - T_a ln\left(\frac{T_{out}}{T_{in}}\right)\right]}{A_c I\left(1 - \frac{T_a}{T_{sol}}\right)} \tag{4.31}$$

4.5 Energy and exergy analysis

In this study, the effect of solar radiation intensity and the number of tubes is investigated.

4.5.1 Effect of solar radiation intensity

The weather conditions are represented generally by two extreme seasons (cold and hot). The cold season, winter, expands, from 15 December to 15 February in Northern hemisphere. The hot season, summer, extends for the rest of the year. However, the period from first of Mars to the end of May is characterized by a moderate ambient temperatures and solar radiation. In this study, three solar radiations were selected to introduce the main existing climate conditions. Figures 4.22b and 4.22c illustrate the impact of the solar energy increasing from 300 to 1000 W/m^2 on the energetic and exergetic efficiencies of HPETSC. They show that both efficencies trend upward. Also, the exergetic performance rate of solar collector is increased nearly by 30% as well as the outlet water temperature T_{out}. When the solar radiation is about 300 W/m^2, the solar collectors can not collect enough heat to recover the basic heat loss. Therefore, a critical value of efficiency is observed. In addition, for high flux density an increase in solar radiation results not in a significant increase in energy and exergy efficiency. For modest heat flux density, however, an increase in solar radiation can promote noticeably phase-change heat transfer in the heat pipe and hence the solar collector efficiency. In both cases, an increase in solar radiation will cause a higher output water temperature.

Evacuated tubes parameters	
Length of glass tube	1.46 m
Outer diameter of glass tube	0.047 m
Inner diameter of glass tube	0.037 m
Transmittance	≥ 91
Absorptivity of absorber	≥ 94
Emissivity of absorber	≤ 7
Collector tilt	45°
Heat pipe dimensions	
Evaporator length	1.4 m
Adiabatic length	0.06 m
Condenser length	0.3 m
Wall radius	0.022 m
Wick radius	0.02 m
Vapor radius	0.0127 m
Wick structure	
Porosity	0.4
Permeability	1.17×10^{-11} m^2
Effective heat capacity	4216 J.kg^{-1}.K^{-1}
Effective diffusivity	3.0476 W.m^{-1}.K^{-1}
Material	sintered copper
Heat exchanger	
Heat input	700 W.m^{-2}
Convective transfer coefficient	1400 W.m^{-2}.K^{-1}
Inlet temperature	22°C
Mass flow	4×10^{-3} kg.s^{-1}
Material	
Glass tube	Borosilicate glass
HP wall	copper
Wick structure	copper

TABLE 4.10 – HPETSC parameters.

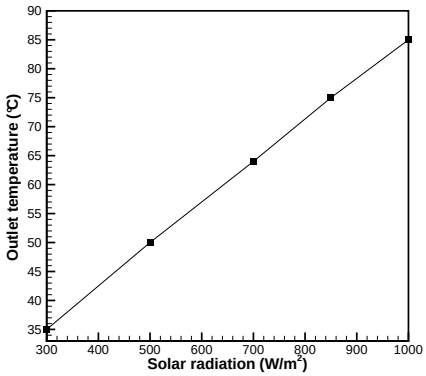

(a) Outlet temperature

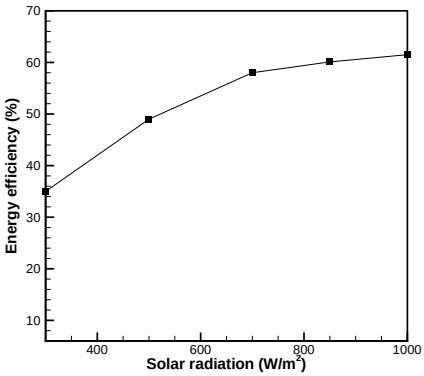

(b) Energy efficiency

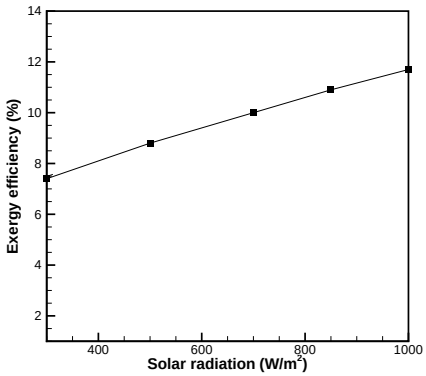

(c) Exergy efficiency

FIGURE 4.22 – The evolution of (4.22a) outlet temperature, (4.22b) energy efficiency and (4.22c) exergy efficiency for different solar radiations.

4.5.2 Effect of the number of tubes

The comparison of efficiencies of HPETSC using different numbers of tubes is given in figures 4.23b and 4.23c. When the number of tubes increases, both efficiencies increase by 20.7% and 40%, respectively. These results show that using more tubes causes a significant improvement in HPETSC efficiency but a saturation effect occurs, at very large number of tubes, here about 16, for energy but curiously exergy still goes on increasing without exceeding that of energy. The considerable improvement results from the fact that when many HPs used, the temperature difference between the evaporator and the condenser for each will be smaller. This raises the outlet temperature and compensate the heat loss. Hence, an improvement of the collector efficiencies is observed. However, from a cost point of view, HP with 15 tubes is chosen as the best price/performance ratio.

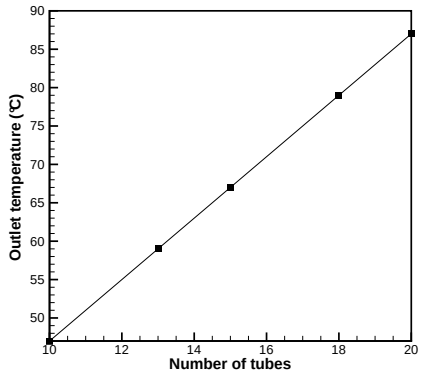

(a) Outlet temperature

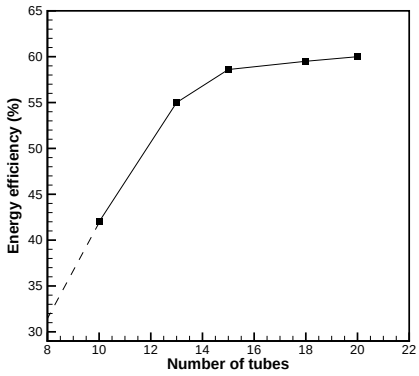

(b) Energy efficiency

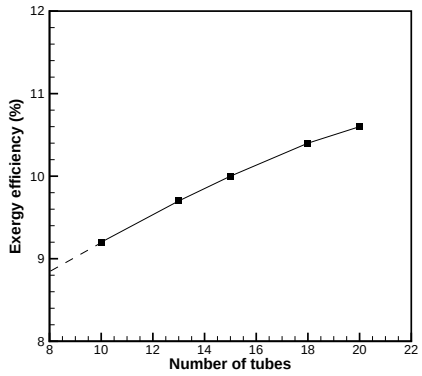

(c) Exergy efficiency

FIGURE 4.23 – The evolution of (4.23a) outlet temperature, (4.23b) energy efficiency and (4.23c) exergy efficiency for different tubes numbers.

4.6 Conclusion

In this chapter, the performance of a capillary driven HP used in solar collectors was investigated. The analysis includes the wall, the liquid-wick material and the vapor regions. Comparison between the present model results and experimental, numerical and analytical results available in the literature shows very good agreement. The effect of working fluid, wick structure, evaporator length and inclination angle on the system behavior was addressed. Among these results, some suggest the superior performance of acetone heat pipe with sintered copper structure of 7.3 mm of thickness in 45° inclination. Numerical results under those working conditions was presented, which provides guidance for the heat pipe design used in solar collectors. Then, a HPETSC has been investigated numerically. A detailed theoretical method for energy and exergy analysis of the collector was provided. Based on the numerical results of lattice Boltzmann method, the effect of inci-

dent solar radiation intensity and number of tubes was analyzed. For a price/performance ratio, a heat pipe evacuated tube with about 15 tubes is recommended with both exergy and energy efficiency. This study can be helpful in designing actual solar collector systems.

Chapter 5

Experimental analysis of heat pipe

Abstract

As a part of the present work, an experimental bench was developed. The instrumentation, the heat pipe conception and the procedure of start up are presented in details in this chapter. The experimental results under different working conditions (working fluid, filling ratio, tilt, heat input, evaporator length and condenser temperature) are discussed. The LB model results are compared to experimental data. Finally, an optimal HP configuration is recommended.

Résumé

Dans le cadre de ce travail, un banc expérimental a été développé. L'instrumentation, la conception du caloduc et la procédure de démarrage des essais sont présentées en détail dans ce chapitre. Les résultats expérimentaux dans différentes conditions de fonctionnement (fluide de travail, taux de remplissage, inclinaison, apport de chaleur, longueur de l'évaporateur et température au condenseur) sont analysés et discutés. La validation du modèle LB est effectuée. Enfin, une configuration optimale du caloduc est proposée.

5.1 Heat pipe design

The heat pipe used in the experimental tests is made by Atherm factory (see the plan in appendix C). It is a copper cylindrical heat pipe with 500 mm long and 8 mm diameter. More characteristics details are given in table 5.1.

Heat pipe dimensions	
Evaporator length	0.4 m
Adiabatic length	$0 - 0.05$ m
Condenser length	$0.05 - 0.1$ m
Wall radius	0.004 m
Wick radius	0.0034 m
Vapor radius	0.002 m
Wick structure	
Porosity	0.5
Permeability	2.03×10^{-11} m^2
Mean pore radius	3.15×10^{-5} m
Material	sintered copper
Heat exchanger	
Heat input	$5 - 50$ W
T_{ou}	$20 - 40$°C
Material	
Wall	copper

TABLE 5.1 – Heat pipe characteristics parameters.

5.2 Instrumentation

We have seen in previous chapters that the performance of a heat pipe depends strongly on the nature of the working fluids, the condenser length, the inclination angle, etc. Hence, we choose to study experimentally the influence of these parameters.
We briefly present the techniques adopted for the design of the condenser and evaporator zones (see Appendix D, figure D.5).

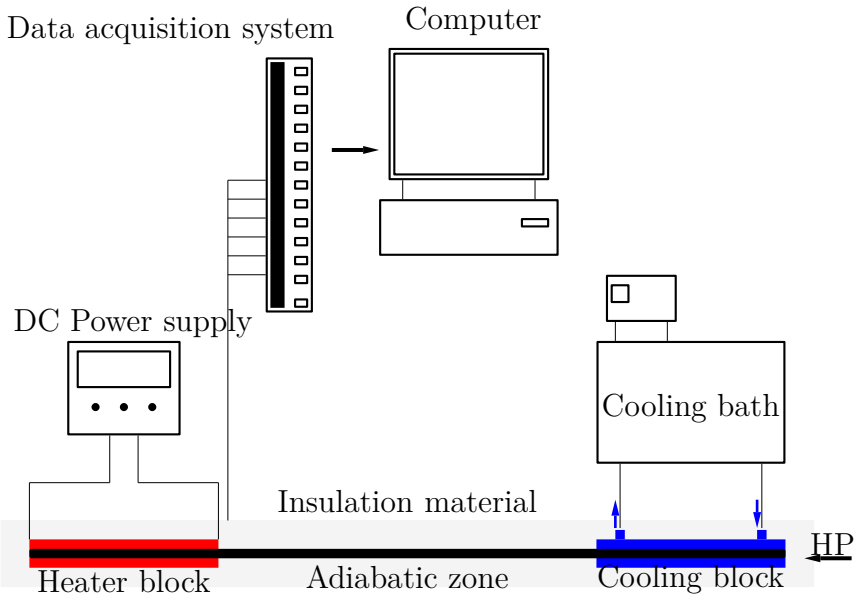

FIGURE 5.1 – Schematic of the heat pipe experimental system.

5.2.1 Condenser

In order to limit process costs and time, we have first developed a tubular condenser with a spiral shape made by copper (see Appendix D, figure D.3). The condenser block is soldered to the HP using tin to ensure good thermal contact. In a second attempt, we have developed a heat exchanger bundles (see Appendix D, figure D.4). The block is in contact with the HP through thermal grease which eliminates the air gaps. (that acts as a thermal insulator, in order to optimize heat transfer). Figure 5.2 presents the second configuration of the condenser used.

(a) Front side with intern pipes.

(b) Condenser block.

FIGURE 5.2 – Condenser bundles.

5.2.2 Evaporator

The main role of the evaporator block is to produce heat flux to a given surface. Due to the implantation constraints, the solution chosen for the heating block is heating wire. It is wrapped around the evaporator block and soldered using thin heating film which makes it represent a unique heating solution with many advantages. It is composed of plastic film reinforced micro plates of carbon resistors. Carbon plates produce radially directed heat in contact with a silver electrical conductor. The use of a heating film allows the setup saving up to 50% on the energy consumption. The design of the first configuration is given in Appendix D, figure D.1. A second conception of the evaporator block has been proposed (see Appendix D, figure D.2). The main advantages are its flexibility and mobility. It consists of half shells where heating wire is integrated through grooves. Figure 5.3 presents the two evaporator block designs.

(a) Spiral configuration.

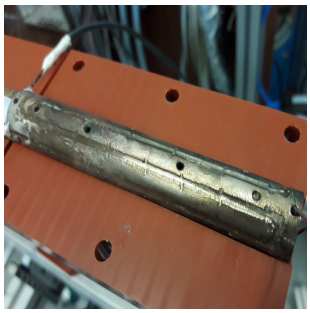

(b) Groove configuration.

FIGURE 5.3 – Evaporator block.

5.2.3 Temperature measurement

The choice of thermocouple type T for temperature measurements has been guided by many parameters related to the implantation of these thermocouples. First, the temperature range is large and ranges from approximately -30°C to 150°C which excludes the possibility of using thermistors. In addition, measurement points are on the wall of the heat pipe. Thus, they are located in a zone with a very high gradient (except for the adiabatic zone). That is why it is important to ensure good thermal contact. So, we used thermocouples type T with 0.1 mm of diameter for all of our experiments which gives good accuracy and low noise. The HP performance characterization requires a precise measurement of the temperature at the interfaces between the HP external wall and the evaporator block or the condenser block.
Ideally, the introduction of a thermocouple should be done according to the isotherms to limit disturbances. But in our case, for technical reasons, the thermocouples are implanted by radial penetration of the wires through the copper blocks. Thus, this implantation is

unfavorable because it was fixed almost parallel to the temperature gradients. However, the influence in our case is very small. The details of the uncertainties model and calculations can be found in Appendix E in the section dealing with temperature measurement uncertainties.

Implementation of thermocouples

The thermocouples implementation is taken in two ways:
- For the first configuration: using the HP weld of connection and copper blocks in the condenser region. For evaporator region, we tried to use the hot welds but it doesn't work due to the complicated geometry and the large number of thermocouples. So we used black glue in order to stick the thermocouples to the evaporator block in contact with the heat pipe interface. The same procedure has been adapted for the adiabatic region (see figure 5.4a).
- For the second configuration: as we are aiming to implement a heat pipe with moving blocks, the thermocouples were fixed by a piece of copper which plays double role: mounting and fair contact (see figure 5.4b).

(a) First implementation. (b) Second implementation.

FIGURE 5.4 – Thermocouple implementation.

Positioning of thermocouples

The positions have been carefully selected in order to represent correctly the profiles of wall temperature along the heat pipe. As the condenser and evaporator zone show the most significant variations and temperature difference and that the evaporator zone is the area where the onset of drying is likely to occur, this regions have been more intensively instrumented with thermocouples. The positions of the used thermocouples are presented in figure 5.5. We have presented only the top thermocouples. The evaporator is surrounded by 34 thermocouples : 8 in the top (E1..E8), 8 in the bottom (E9..E16), 9 in the right (E17..E25) and 9 in the left (E26..E34). The distance between each thermocouple is equal to 10mm. The condenser is surrounded by 24 thermocouples: 6 in the upper (C1..C6),

6 in the bottom (C7..C12), 6 in the right (C13..C18) and 6 in the left (C19..C24). The distance between each thermocouple is equal to 12mm. We implimented a large number of thermocouples in this two regions in order to be able to capture as soon as possible the functioning limit. While the adiabatic region is surrounded by only 6 thermocouples as the temperature there is virtually uniform: 2 in the center (A1,A2), 2 in the right near the condenser (A5,A6) and 2 in the left near the evaporator (A3,A4) in order to get information about the temperature evolution there.

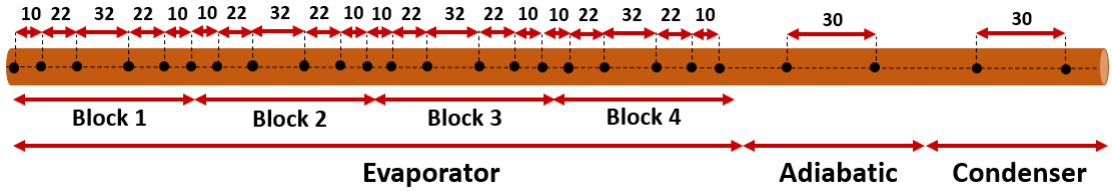

FIGURE 5.5 – Details of thermocouple locations in test bench in cm.

5.2.4 Leak test and envelop degassing

Before starting, the heat pipe leakage must be checked. The device is connected to a vacuum pump with a valve that seals the system, as it can be seen in figure 5.6. In order to eliminate the incondensable gases and ensure a good envelop degassing the vacuuming lasts 24 hours. After 24 hours, the measured pressure was about 4.7×10^{-11} Pa. Above this value, we consider that heat pipe is leaking. After this test, the device is under vacuum condition and could be filled with working fluid.

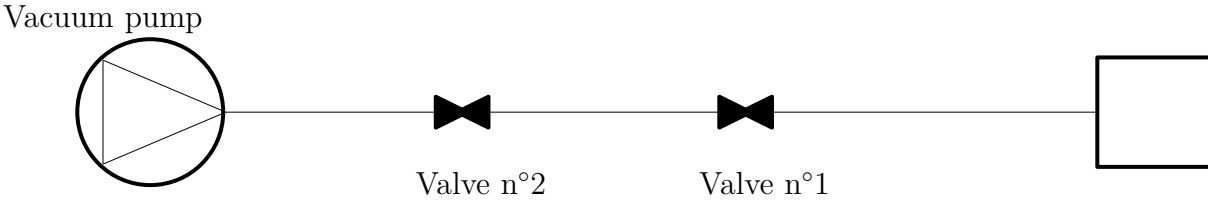

FIGURE 5.6 – Leak test

5.2.5 Inclination

Horizontal adjustment

In order to minimize the effect of the HP uncertainty alignment, the device is supported by two brackets hooked to horizontal axes. In fact, a misalignment greater than 1 mm/m

can cause an uncertainty of plus or minus 5 to 7 Pa on the driving pressure available in the heat pipe. The gravity force exerted on the liquid flow thus counteracts or favors the capillary action of the capillary structure, according to the sign of the tilt (inclination). Flatness characterizes the defects of a surface with respect to a plane. This setting is performed horizontally using an automatic level.

Inclination adjustment

The HP heat transport performance dependents substantially on its capillary pumping capacity. Therefore, the tilt can reveal useful information. Indeed, the extrapolation of measurements for different tilts allows to estimate the performance in flight for spacial applications, for instance. In unfavorable configuration, the evaporator is raised relative to the condenser thus limiting the return of the liquid phase. In this case, the heat pipe is able to evacuate the imposed heat flow until it reaches its capillary limit.

In order to study the effect of inclination on the performance of HP, we used a pivot support fixed below the center and the evaporator zone. In addition, the HP support is related to the whole frame by axis of rotation where the graduation is entirely visible.
Using the system described above, we can easily change the HP orientation by 5 ° in the range between -90 ° and +90 ° .

5.2.6 Calibration

To reach the desired high level of precision (0.1 ° C) on the measuring chain, the choice of temperature thermocouples was focused on type T thermocouples (Copper/Constantan) characterized by a good sensitivity (of the order of 46μ V / ° C for a temperature ranging between of -180 and 300 ° C). In addition, the cold junction is maintained at a reference temperature of 20 ° C which corresponds to a glycoled water cryostat. Indeed, the reference points are plunged directly into this bath. At the same time, a circulation of fluid makes it possible to keep the connection points permanently at the same temperature (*i.e.* 20 ° C). Figure 5.7 illustrates the basic principle of the chosen measurement technique.

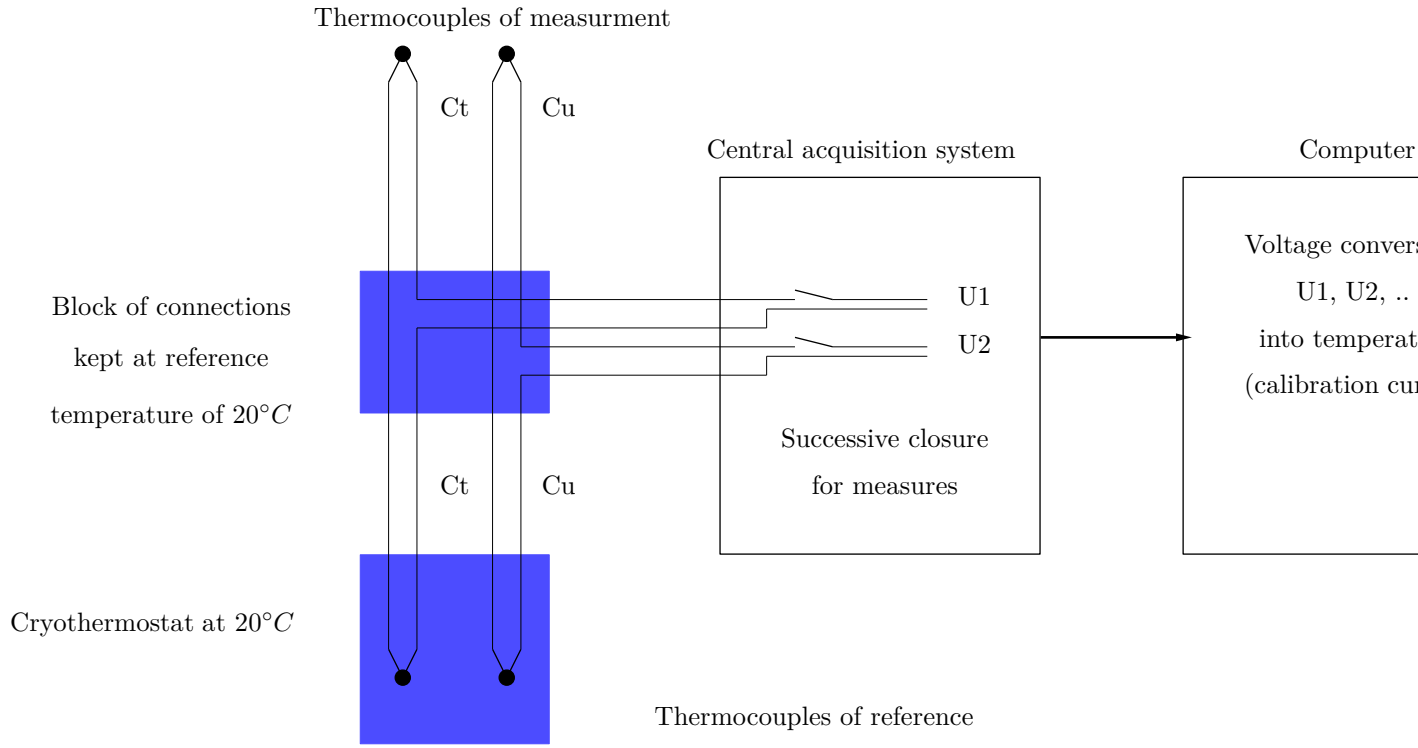

FIGURE 5.7 – Temperature measurement technique.

It is based on the measurement of the potential difference U between the measuring point and the cold junction by closing the paths at the central acquisition. These pathways are connected to a computer for storage and data processing. Thus, each voltage measurement is converted into temperature through the calibration curve of the corresponding thermocouple. Therefore, it is necessary to calibrate the entire measurement chain before proceeding with the thermocouple bonding and start the experimental study.

A calibration bench test makes it possible to record the voltage measurements of all the thermocouples under known temperature conditions (see figure 5.8). Thermocouples are collected in an aluminum block which is immersed in a bath of silicone oil. The latter is regulated at a temperature of $0.01°C$. A PT100 probe reference, calibrated to 1/10th of a degree, gives a direct measurement of bath temperature via a digital voltmeter. A measurement series is thus carried out from -20 to $150°C$, in steps of $5°C$. At each stage, the temperature stability is expected (a slope of $0.001°C$/min, at most, is required) before recording the voltage measurements. The average time required to achieve single-level data acquisition is 45 minutes.

FIGURE 5.8 – Calibration bench test.

The variations of the potential difference across each thermocouple as a function of the temperature are obtained. A six-order polynomial is used to smooth the calibration curves (temperature as a function of voltage). The reliability of these parameters is then checked: a maximum error of $0.01°C$ is tolerated for all measurements of all calibrated pairs. These data were used to convert the measurements temperature voltages throughout the experimental tests.

5.2.7 Thermal insulation

The thermal insulation of the test bench is an important issue of the HP characterization. In order to limit as much as possible the heat exchanges with the environment, a good insulation is adopted in the design of the experimental device.

Static insulation minimizes thermal losses by diffusion within the experimental bench. Indeed, the supports that holds the heat pipe are made with ERTALON, an insulating material ($\lambda = 0.3$ W.m^{-1}.K^{-1}) and characterized by good mechanical performance up to 150°C.

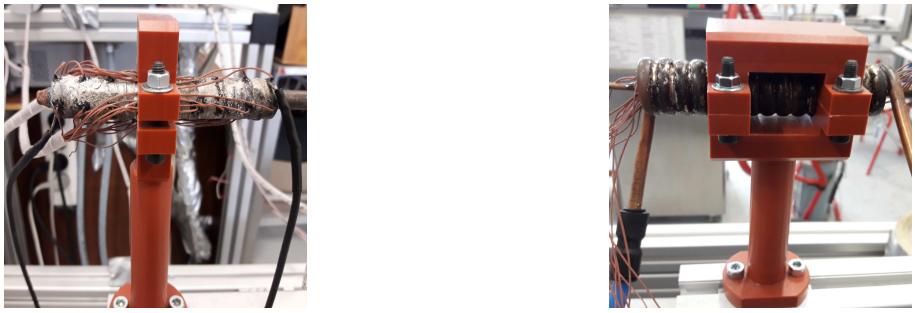

(a) Evaporator support. (b) Condenser support.

FIGURE 5.9 – Ertalon support.

The heating and condensing blocks are covered with a cover in ERTALON thus mini-

mizing heat losses at this level (see figure 5.9). In addition, the entire heat pipe is filled with glass wool (λ= 0.04 W.m^{-1}.K^{-1}) which makes it possible to eliminate the convective and radiative exchanges between the various elements of the bench (see figure 5.10). Nevertheless, this thermal insulation device is insufficient to limit the effect of external environment since temperature differences can reach values above 100°C. This type of problem can thus cause two defects of the insulation which limit the effectiveness of the HP fine characterization procedure. The first defect, the existence of a parasitic flow between the evaporator and the environment, consequence of distorting the imposed power measurements. The second defect is the result of the difficulty of regulating the insulation, because of its large mass and low exchange coefficient. In addition, the heat pipe is equipped with many thermocouples type T passing through the insulation. The thermocouple wires may generate then significant thermal leakage between the HP and the surrounding environment. That is why the use of insulation that adapts and directly limits the heat flows exchanged with the environment is necessary to obtain reliable measurements characterizing the heat pipe functioning.

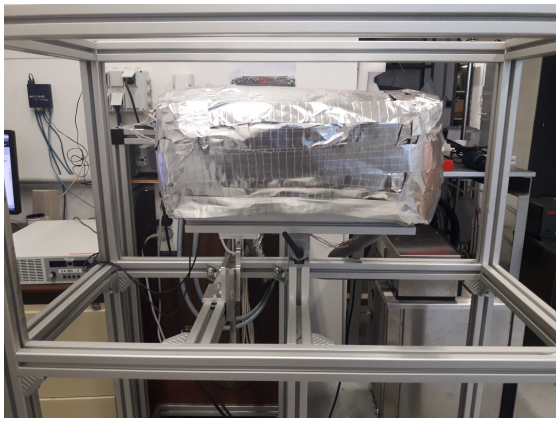

Figure 5.10 – Isolated heat pipe.

5.3 Data acquisition and control devices

In order to facilitate the control of the operating parameters through the experimental device, the computer communicates with each element of the bench via Labview software. In this section, we proceed to the description of the implemented software and instrumentation for the acquisition of temperatures, the measurement and control of electrical powers.

5.3.1 Labview software

Due to the number of devices controlled during the experimental tests, we have centralized data acquisition and control of equipment on a central computer using Labview software (National Instrument®). This object oriented language presents the benefit of having an intuitive graphical programming interface and a large library database of extensive instrument devices drivers. Moreover it allows to realize a personalized graphical interface allowing to visualize all the relevant parameters. The completed interface includes the choice of configuration instruments, acquisition of control and acceleration, the criteria for the end of the measuring point, the temperatures of the heat pipe, ambient temperatures and heat input power.

5.3.2 Temperature measurement

As described in section 5.2.3, the temperature measurements at the heat pipe wall are realized using T-type thermocouples after calibration. The measurement of the voltage delivered by the thermocouple is generally delicate because it is a low level signal. The temperature is measured by relating each polynomial coefficient, found by calibration, to the correspondent voltage of each central line.

5.3.3 Power control and measurement

The control of the electrical power, dissipated in the heating wire of the evaporator, requires special care in order to impose optimal conditions with an accurate and controllable voltage measurement.

5.4 Measurement uncertainty

The instrumentation of the heat pipe in the test procedure was the object of much attention in order to get accurate temperature measurements. However, in any experimental characterization, the uncertainties must be evaluated in order to verify the accuracy level of the measurements made. In this section, the parameters affecting the temperature and power measurements are presented. General notions, based on methods recommended by AFNOR, allowing to define the uncertainties are presented in Appendix E.

5.4.1 Uncertainties on the measured temperature

Uncertainties in thermocouple measurements involve several parameters including:

Uncertainty type	Error source	Expanded uncertainty(°C)
Calibration	PT100	1.05
	Cold junction	0.01
	Polynomial coefficient	0.02
Voltage	sensitivity	0.002
	Acquisition	0.03
Position	$Q_{e_max} =$	0.0007
	Total	0.6

TABLE 5.2 – Uncertainty of temperature measurement.

— Calibration of the measurement chain;
— The measurement and acquisition of the voltage;
— Thermocouple position;
— Thermocouple type.

As a consequence, the temperature uncertainty is given by:

$$\varepsilon_T = \varepsilon_{Calibration} \oplus \varepsilon_{Voltage} \oplus \varepsilon_{Position} \oplus \varepsilon_{Type} \tag{5.1}$$

where the $\oplus$ symbolizes the composition of the variances in AFNOR standard. Table 5.2 summarizes the calculation results of uncertainties. So, the global uncertainty on the temperature measurement is estimated to 0.6 °C for temperatures that can reach, locally, more than 150 °C. Based on this correction, the comparison of measurements for different test configurations, can be carried out with good confidence.

Details of the different corrections

— Calibration of the measurement chain

The uncertainty of the PT100 probe, used in the measurement of the temperature in the calibration stage, is estimated from the curve given by the manufacturer. The cold junction of each thermocouple is immersed in a thermostatic bath. This method avoids the appearance of leakage voltage or the formation of an undesirable point of measurement. The uncertainty of regulation and homogeneity of the bath fluid temperature is of the order of one hundredth of degree. Conversion of voltage measurements to temperature using curves of calibration generates errors of the same order of magnitude. The error margin of the reconstitution of temperature measurements (using a polynomial of order 6 in comparison with the values recorded by the reference thermometer) is equal to 0.04°C for the 68 used thermocouples. The global uncertainty due to the calibration of the thermocouples is then estimated at the tenth of degree.

— The measurement and acquisition of the voltage

The uncertainty due to the measurement of the voltage comes, on the one hand, from the sensitivity limit of T-type thermocouples ($46\mu V.°C^{-1}$) and from acquisition, on the other hand. The first type of uncertainty, estimated to 0.1 μV in increased value, gives rise to a temperature measurement error of the order of 0.002 °C. On the other hand, the second type of uncertainty is composed of the range error which is reduced to the

reproductibility error (≈1 μV) and inaccuracies resulting from the measurement function, by data acquisition, of the input signal. These are less than 0.5 μV for the considered temperature range. The uncertainty of voltage acquisition is then estimated to 1.5 μV; which corresponds to a temperature measurement error of the order of 0.03 °C.

— Thermocouple positioning accuracy

The positioning uncertainty remains, nevertheless, a major obstacle to judge the spatial behavior of the heat pipe for a given operation point. The uncertainty generated by the positioning error of the thermocouples is considered for the maximum transferable flow, in value increased (more than 1 °C in this case). Note that the uncertainties due to the thermocouple positioning increases with the increase of the imposed flow heat.

5.4.2 Uncertainties on power measurement and applied power

Recall that the applied power at the evaporator is generated by the heated wire which is under continuous power supply. Hence, the power measurement is calculated from the measured voltage and intensity. However, the received power by the HP doesn't exactly correspond to the generated power. In fact, a part of this power is evacuated, mainly, to the environment. Then, the received power by the HP is expressed as:

$$P = UI \tag{5.2}$$

where U is the measured tension and I is the measured intensity.
Hence, the standard deviation can be written as:

$$\frac{U(P)}{P} = \sqrt{\left(\frac{U(U)}{U}\right)^2 + \left(\frac{U(I)}{I}\right)^2} \tag{5.3}$$

As we used EA PS 8000T model which gives an accuracy of 0.2% for both voltage and intensity, we found an uncertainty of 0.006W for the maximum used heat input of 50W.

5.4.3 Uncertainties on the thermal resistance

As it was defined in equation (4.10), the relative uncertainty can be written as:

$$\frac{U(R_{th})}{R_{th}} = \sqrt{\left(\frac{U(\Delta T)}{\Delta T}\right)^2 + \left(\frac{U(Q)}{Q}\right)^2} \tag{5.4}$$

Hence, the extended relative uncertainty can be written as:

$$U(R_{th}) = R_{th}\sqrt{\left(\frac{U(\Delta T)}{\Delta T}\right)^2 + \left(\frac{U(Q)}{Q}\right)^2} \tag{5.5}$$

By taking into account the maximum thermal resistance and temperature difference, the uncertainty is found equal to 0.02K/W.

5.5 Heat pipe filling

The filling operation, as it can be seen in figure 5.11, is carried out in several stages aiming to avoid incondensable gases inside the heat pipe. In the case of wicked heat pipes, the presence of incondensable gases is a major problem, which severely affects their performance. The sources of incondensable gases are the molecules adsorbed in its internal walls and the gases dissolved in the injected fluid. This can cause the formation of gas plug which prevents the passage of vapor and decreases the condensation zone area. Hence, much care has been taken while filling and degassing the heat pipe which is described in what follows.

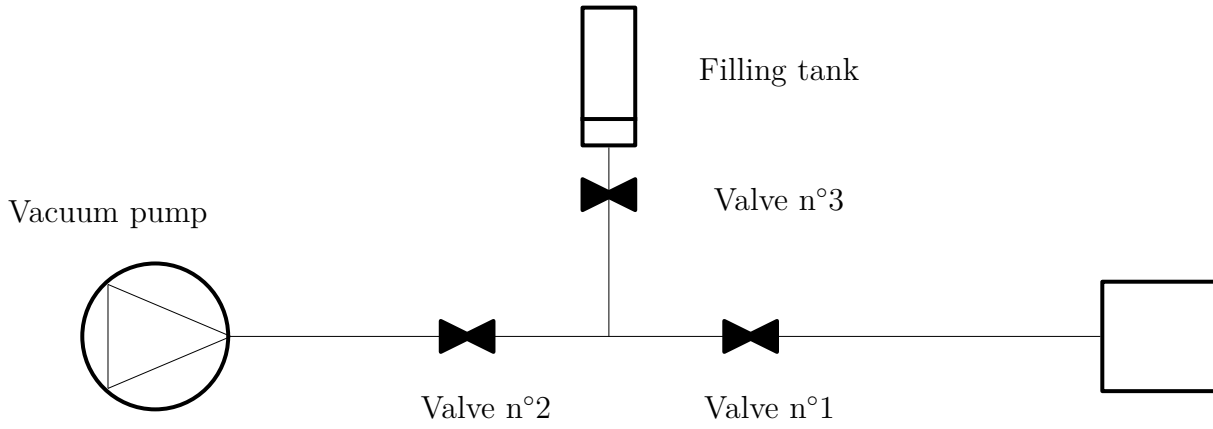

FIGURE 5.11 – Filling system.

The filling procedure of the heat pipe is very important for appropriate heat pipe operation, reliability and reproductibility (see figure 5.11). That is why, special care has been taken during this process. Once the working fluid is selected, the mass of the fluid is calculated based on the desired filling ratio. To avoid any significant leakage, the filling pipe closure must be perfectly sealed. Inappropriate sealing causes degradation of the HP operation. Using a scale, we measure the filling tank mass. Then, we introduce the calculated quantity of mass. The uncertainty associated with the measurement of this mass quantity is less than one gramme, which generates an uncertainty of about 10% on the filling ratio, approximately. Before filling the heat pipe, the fluid must be degassed carefully to eliminate any residuals incondensable gas. The degassing is obtained through many operations of sublimation and condensation. The fluid is first solidified in a helium tank in liquid state. The incondensable gases are evacuated by the pumping unit. The liquid charge can then be adjusted using this vacuum pump that allows extracting a portion of the fluid to be performed while preventing incondensable gases from entering the system. The solid is then sublimated by heating it. The operation is repeated several times in order to obtain maximum purity of the fluid. Before injecting the fluid, we remeasure the fluid mass. Then, the filling of the HP is carried out immediately to

maintain the quality of the fluid. While heating the filling tank, the valves are opened. Due to the pressure difference, the fluid flows through the connections then condenses in the HP. The quantity of fluid introduced in the HP is recalculated based on the mass of the filling tank. This technique facilitates the study of the load influence on the thermal performance of the HP. Once the HP is filled, it must be separated from the filling system. This separation is performed by closing the valve number 2.

In summary, the procedure of heat pipe filling consists of 5 basic steps: degassing the internal walls; degassing the filling tank; degassing the working fluid; injection of the necessary quantity of fluid into the heat pipe and closing the heat pipe.

5.6 Test cases

We tested mainly three test cases using water and methanol as working fluids, which are described in what follows. Because the lack of time, we were not able to proceed with acetone and ethanol. But aside, we made a pre-design of a HP with an evaporator 100mm long, an adiabatic region 300mm long and a condenser 100mm long. This case, illustrated in figure F.1, is referred to as initial case and is discussed in Appendix F.

5.6.1 Case A

In this test case, see figure 5.12, the evaporator, adiabatic region and condenser lengths are equal to 400mm, 50mm and 50mm, respectively.

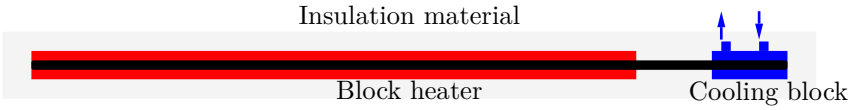

FIGURE 5.12 – Schematic of case A.

5.6.2 Case B

In this test case, see figure 5.13, the evaporator and condenser length are equal to 400mm and 100mm, respectively, without adiabatic region.

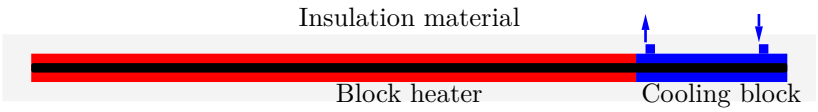

FIGURE 5.13 – Schematic of case B.

5.6.3 Case C

In this test case, see figure 5.14, the evaporator and condenser length are equal to 400mm and 100mm, respectively, without adiabatic region. The condenser is composed of two blocks each one of 50mm.

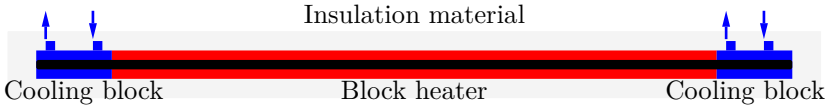

FIGURE 5.14 – Schematic of case C.

5.6.4 HP limits

Using the limits discussed in section 1.7, we found the device working limits that are given in tables 5.3 and 5.4.

Limits	Capillary	Sonic	Viscous	Entrainment
Initial case F.1	19.21	415.16	956.68	256.21
Case A	69.1	415.19	3444.04	256.21
Case B and C	76.83	415.16	3826.7	256.21

TABLE 5.3 – Heat pipe functionality limits for water at 35°C.

Limits	Capillary	Sonic	Viscous	Entrainment
Initial case F.1	15.83	353.9	789.3	189.87
Case A	59	353.9	2842	189.87
Case B and C	65.33	353.9	3157.2	189.87

TABLE 5.4 – Heat pipe functionality limits for methanol at 35°C.

The stronger limit that defines the heat pipe working range is the capillary limit. This limit determines the dry-out limit of the porous medium. As we can see at $T = 35°C$, the initial case F.1 is limited to 15W and 19W for methanol and water, respectively. This is due to the large effective length which is equal to 0.4m. However, for solar applications, we are led to work on the range of 35W heat input. By decreasing the effective length, the capillary limit is increased for case A, B and C. In addition, the mentioned cases come even closer to the HPETSC configuration. Hence, in what follows, we will discuss cases A, B and C only.

5.7 Latin Hypercube Sampling method applied to experimental design

5.7.1 Latin Hypercube Sampling methodology

Over the past several decades, there was a great deal of researches on developing and improving various experimental design methodologies, including random sampling, stratified sampling, orthogonal design and Latin hypercube sampling. The performance of a sampling strategy and the quality of its resulting samples directly controls the efficiency and robustness of any associated sampling-based analysis. Latin Hypercube Sampling (LHS), introduced by McKay *et al.* [178] and its variations such as orthogonal array-based LHS [273], orthogonal LHS [306] and symmetric LHS [140] are among the most commonly used sampling techniques for experiments in a number of applied scientific disciplines including uncertainty analysis [219], parameter calibration [103] and surrogate modeling [77]. The main features of such a methodology are: (1) ease of use compared with random sampling, (2) insurance of one-dimensional projection properties which is one of Latin Hypercube main properties and (3) ease in incorporating other criteria such as orthogonality and symmetry within sampling. One major drawback of traditional LHS and many other sampling strategies is that they generate the entire sample points at once, a process that is referred to as one-stage sampling: their is no way afterward to improve its quality and preserve its properties at the same time.
In this study, the Latin hypercube sampling technique is used for initial population generation, instead of a traditional random method, as it has proven its effectiveness. The method is assessed by one-dimensional projections for every variable (observable) dimension, space-filling criteria and correlation analysis. The LHS random procedure divides the probability distribution into N equiprobable intervals, where N is the number of sampling iterations. Each iteration selects one of the intervals, and a random number is then generated. The same process is repeated for all of the intervals, but each interval should be sampled exactly once. Notice that this method assumes that the variables are independent of each other (which is the case here) and ensures a full coverage of the range of each variable. The variables at hand here are: the heat input power, the condenser temperature and the inclination angle.

Using the above described method eighteen sampling points were generated and which are given in table 5.5 and presented in figure 5.15 (actually, 10 points were generated using LHS and 8 "verties" of the observable domain were added). Then, an interpolation using radial basis functions makes possible retrieving the solution at any desired functioning point. Figure 5.16 shows the interpolation at 41^3 experimental points, each one represented by a circle.

Points n°	1	2	3	4	5	6	7	8	9	10
$\theta°$	9	90	-90	45	-90	90	-90	90	-90	90
T_{cond}(°C)	55	10	10	43	10	10	70	70	70	70
P(W)	47.75	5	5	5	50	50	50	50	5	5

Points n°	11	12	13	14	15	16	17	18
$\theta°$	-45	27	-81	-9	63	-63	81	-27
T_{cond}(°C)	13	19	25	31	37	49	61	67
P(W)	34.25	16.25	11.75	20.75	38.75	29.75	25.25	43.25

TABLE 5.5 – The experimental measurement points.

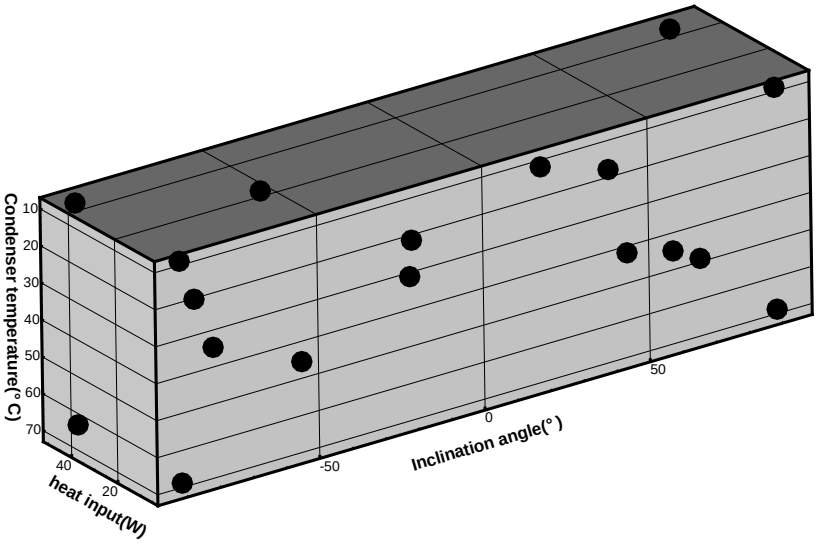

FIGURE 5.15 – The distributions of the 18 points given in table 5.5 and represented by a circle.

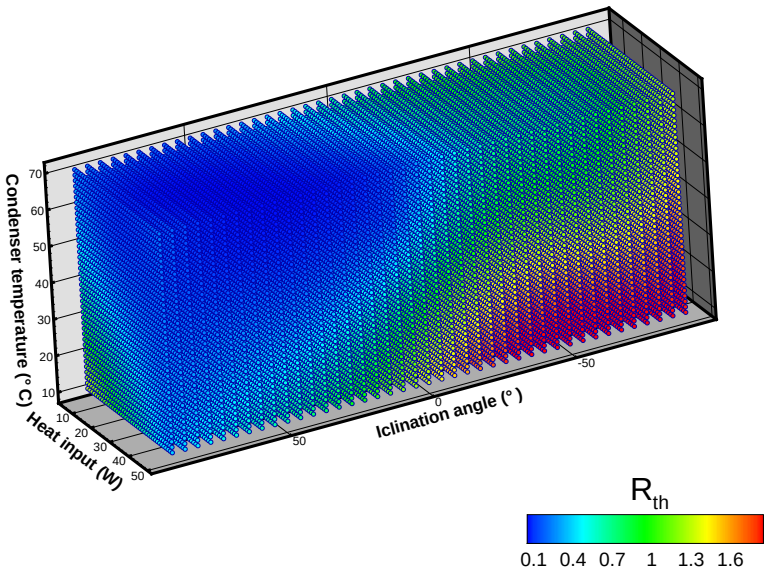

FIGURE 5.16 – Generated points using the LHS for water.

5.7.2 The reliability of the LHS method

In order to assess the accuracy of the LHS method, a comparison between the thermal resistance given directly by the experiments and the interpolation based on the LHS, build from experimental data other then those used for comparison, is carried out. Figure 5.17 shows the variation of the thermal resistance versus the heat input power using LHS method and experimental data under the same working conditions. As we can see, the proposed LHS method provides a fairly good prediction of the thermal resistance in the uncertainty interval of experimental data.

The thermal resistance is the parameter taken as reference to predict the performance of the heat pipe. From this parameter, an error of 5% is assumed to be acceptable.

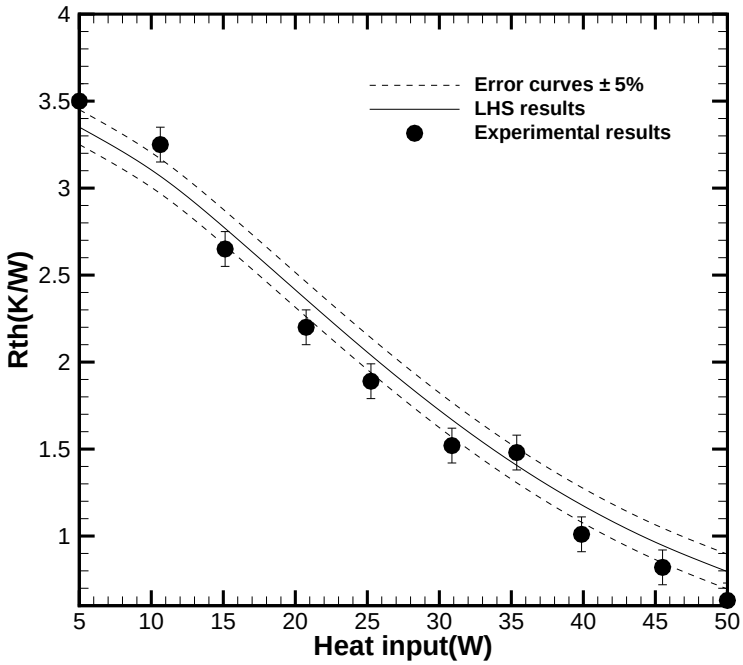

FIGURE 5.17 – Comparison between the LHS and the experimental results.

In what follows, the effect of various parameters on the thermal resistance of the heat pipe is presented and discussed.

5.8 Results and discussions

The performance was evaluated by calculating the corresponding thermal resistance as the ratio of temperature difference between evaporator and condenser to heat input given in equation (4.10). This formula is recalled here:

$$R_{th} = \frac{(\bar{T}_{evap} - \bar{T}_{cond})}{Q} \tag{5.6}$$

where $\bar{T}_{evap}$ is the average evaporator temperature, $\bar{T}_{cond}$ is the average condenser temperature and Q is the heat input.

The determination of the thermal resistance circuit shown in figure 5.18 (the reproduction of figure 5.18) is presented here.

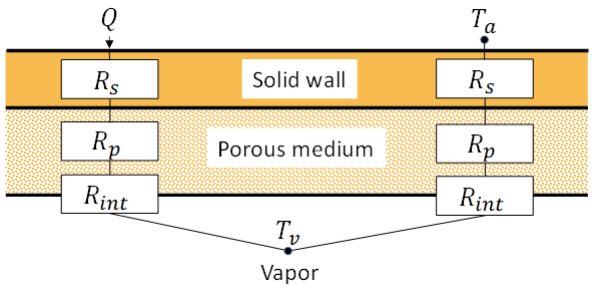

FIGURE 5.18 – Resistance circuit equivalent to the heat pipe.

The resulting total resistance is equal to:

$$R_{th} = R_{s,evap} + R_{p,evap} + R_{int,evap} + R_{int,cond} + R_{p,cond} + R_{s,cond} \tag{5.7}$$

At evaporator section, the total evaporator resistance is equal to:

$$R_{evap} = R_{s,evap} + R_{p,evap} + R_{int,evap} \tag{5.8}$$

At the condenser, the total condenser resistance is equal to:

$$R_{cond} = R_{int,cond} + R_{p,cond} + R_{s,cond} \tag{5.9}$$

where $R_{s,evap}$, $R_{p,evap}$, $R_{int,evap}$, $R_{int,cond}$, $R_{p,cond}$ and $R_{s,cond}$ are given by expressions (4.12) to (4.17).

5.8.1 Case A

Effect of symmetry

Generally, in solar collectors, the received solar radiation falls in two different ways: either symmetric (like HPETSC) or asymmetric (like absorber tube in parabolic concentrator) as shown in figure 5.19.

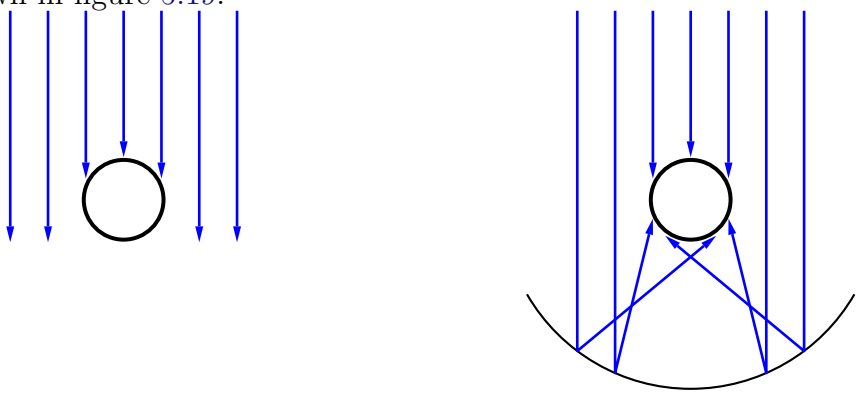

Flat plate type Concentrating type

FIGURE 5.19 – Illustration of solar incident radiation.

Here, we study the effect of the heat flux symmetry on the HP thermal performance. Figure 5.20 presents the two configurations.

Symmetric heating of the evaporator

Asymmetric heating of the evaporator

FIGURE 5.20 – Schematic of the symmetric and asymmetric heating configurations.

Figure 5.21 shows the variation of the thermal resistance versus the heat input. Experimental data are interpolated using radial basis functions and are shown in green and red colors (and there grades). Dotted data are the original experimental data.

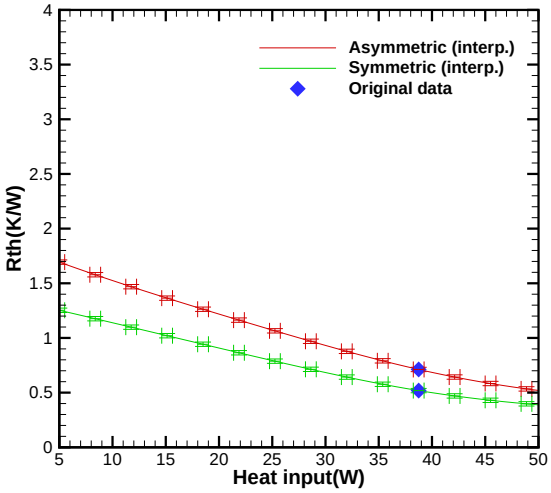

(a) 150% of methanol

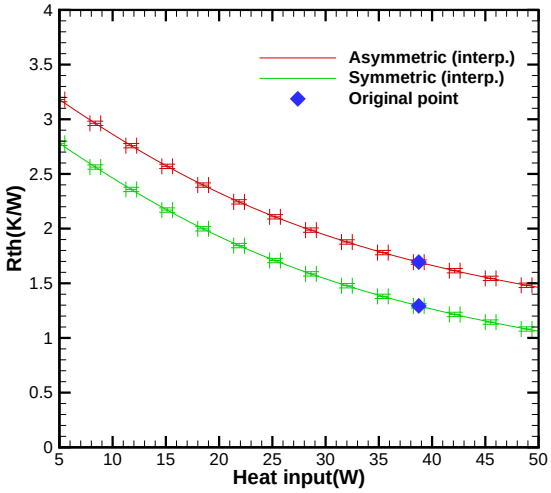

(b) 150% of water

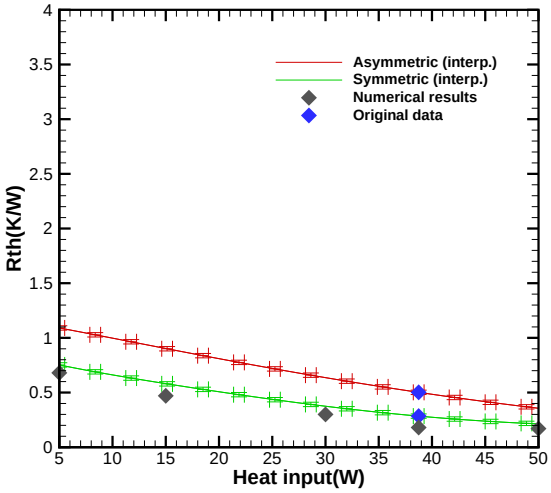

(c) 100% of methanol

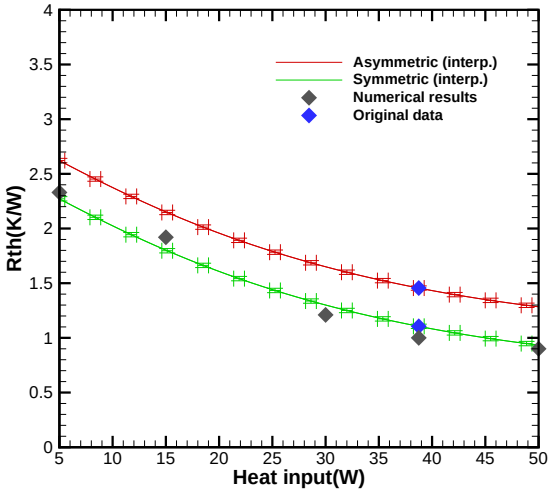

(d) 100% of water

FIGURE 5.21 – Variations of the thermal resistance versus the heat input for different fluids and filling ratios using symmetric and asymmetric configurations under condenser temperature, 37°C, and inclination angle, 63°.

A significant difference does exist between both configurations and it appears that the gap between the symmetry and asymmetry thermal resistance changes slightly with the filling ratio and the nature of the used fluid but chnages are more significant with methanol. Unfortunately, explanation is not straightforward and the axisymmetric numerical model is unable to help more investigations. However, in general, the thermal resistance

seems to be higher for asymmetric configuration for the four curves. This can be explained by the lower heat flux density at the evaporator which contribute to the decrease of the temperature difference in symmetric configuration compared to the asymmetric one. Note that a typical received heat input into the solar collector is about 35W for a cylindrical heat pipe about 1cm diameter and evaporator 40cm long. We can deduce that the symmetric configuration is more interesting. So, we choose to go ahead with discussing only the symmetric configuration.

We also compared these results to numerical results given for water and methanol with 100% filling ratio (as long as different filling ratios are not affordable with the numerical model developed sofar). Good predictions can be observed. However, our model is limited to symmetric configuration using saturated fluids. So, we choose to test its reliability in this range of functionality.

Effect of filling ratio

Experiment was performed to analyze the effect of the filling ratio on the HP performance. Figure 5.22 shows the variations of the thermal resistance versus heat input for water and methanol with two filling ratios. For both fluids, the 100% filling ratio leads to higher thermal performance compared to the 150% filling ratio. In fact, overfilling the heat pipe degrades the heat pipe performance due to liquid film thermal resistance, a consequence of excess liquid. For the considered inclination angle, this excess of liquid increases the evaporator temperature and so the difference of temperature between the condenser and evaporator which leads to increasing the total thermal resistance. However, overfilling extends artificially the capillary limit by preventing earlier dry-out. This due to the thicker layer of liquid compared to liquid saturated mesh.

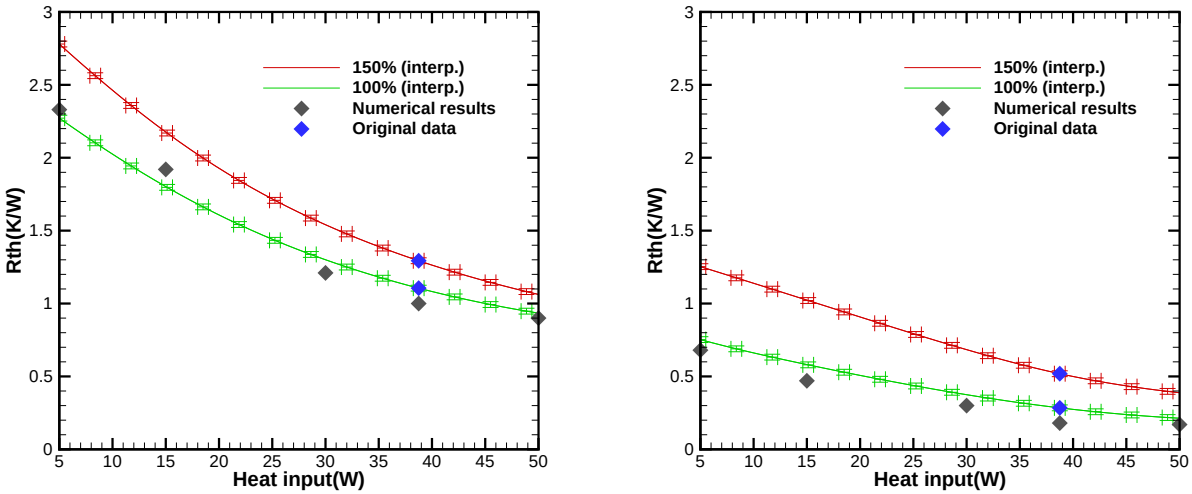

(a) Water

(b) Methanol

FIGURE 5.22 – Variations of the thermal resistance versus the heat input for different filling ratios under condenser temperature, 37°C, and inclination angle, 63°.

Effect of working fluid

Figure 5.23 shows the variations of the thermal resistance versus heat input using water and methanol with two filling ratios. For both filling ratios, methanol leads to higher thermal performance than water as was predicted theoretically. The effects of the working fluid thermophysical properties on the performance of the HP was discussed in section 4.2.1. The working fluids applied in a heat pipe should have the following characteristics: high value of $(dp/dT)_{sat}$, high latent heat of vaporization, high specific heat, high surface tension, and low dynamic viscosity. By referring to Table 4.3, methanol has higher $(dp/dT)_{sat}$ compared to water. In fact, a high value of $(dp/dT)_{sat}$ implies that a small rise in temperature can generate a large pressure difference and accordingly greater driving force necessary for vapor motion.

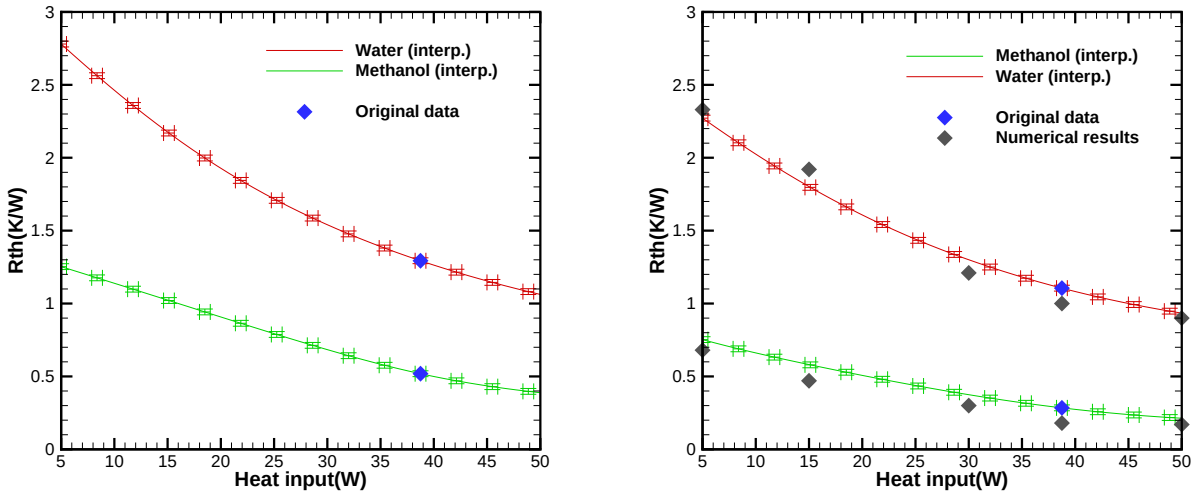

(a) 150% filling ratio

(b) 100% filling ratio

FIGURE 5.23 – Variations of the thermal resistance versus the heat input for different working fluids under condenser temperature, 37°C, and inclination angle, 63°.

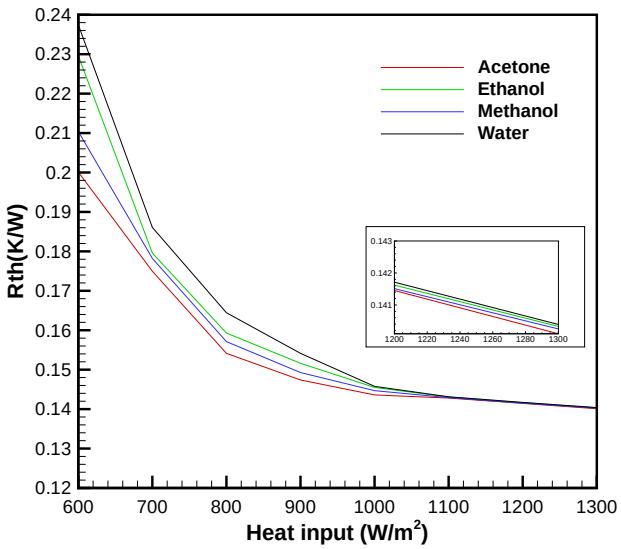

FIGURE 5.24 – Variations of the thermal resistance versus heat input density for different working fluids for a HP with 1.76m of length (1.4m evaporator, 0.06m adiabatic and 0.3 condenser length), $\varepsilon = 0.4$, $K = 1.17 \times 10^{-10} m^{-2}$, convective heat transfer coefficient of $1400 W.m^{-2}.K^{-1}$ and inlet temperature of 22°C.

The same trend is observed in figure 5.24 (reproduction of figure 4.13 showing the nu-

merical results) where methanol shows lower thermal resistance. This suggests the good predictive feature of the developed model. However, the gap between the thermal resistance of the tested working fluids is lower in this numerical tested case. This may due to the difference between the experimental bench test and the HP used configuration in the numerical tested case. In fact, the permeability 10 times higher and the porosity is taken equal to 0.4. Also, we tested a real case of HPETSC dimensions: 1.76m of length (1.4m evaporator, 0.06m adiabatic and 0.3 condenser length). This could explain what was found previously using only the numerical predictions.

Effect of inclination

Experimental tests are carried out to study the effect of the inclination angle, too. Figure 5.26 shows the variations of the thermal resistance versus the inclination angle in the case of gravity-assisted and gravity-opposed orientations.

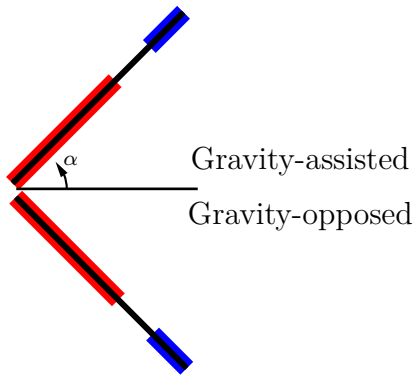

FIGURE 5.25 – Gravity-assisted and gravity-opposed orientations.

The results for the effect of inclination angle on the thermal resistance for gravity-opposed orientations, in the interval of [-45°-0°], is shown in figure 5.26. As the orientation of the heat pipe changes from horizontal to gravity opposed orientation angles, the thermal resistance increases drastically. This occurs because gravity has an adverse effect on the circulation of the liquid within the wick. The large difference in thermal resistance between the horizontal orientation and an inclination of $-45°$ can be attributed to the charging valve being located on the condenser end of the heat pipe. In fact, the condensed liquid accumulates there during gravity-opposed operation and therefore is not able to return to the evaporator. As the inclination angle increases, the resistance to the flow of the liquid along the heat pipe increases and therefore the performance of the heat pipe degrades. Using the gravity-opposed orientation, the HP reaches evaporator dry-out, and

overheating, quickly with at the same time an excess of liquid amount at the condenser region which increases the condenser resistance and consequently the HP resistance.

For gravity-assisted inclination angle cases, the heat pipe clearly performs better. Then, the thermal resistance reaches its minimum for an inclination angle between 60° to 80° . It is obvious that increasing the inclination angle causes the condensed liquid returns easier to the evaporator section by means of favorable gravity and consequently lower thermal resistances is gotten. So the thermal resistance decreases with increasing angle for all working fluids by helping the liquid flowing back to the evaporator, independently of their capillary potential. This observation confirms the results and discussion made previously in section 4.3.5. However, the resulted thermal resistance re-increases for inclination angle between 80° to 90°. This can be explained by the flooding of a part of the evaporator at such large inclinations.

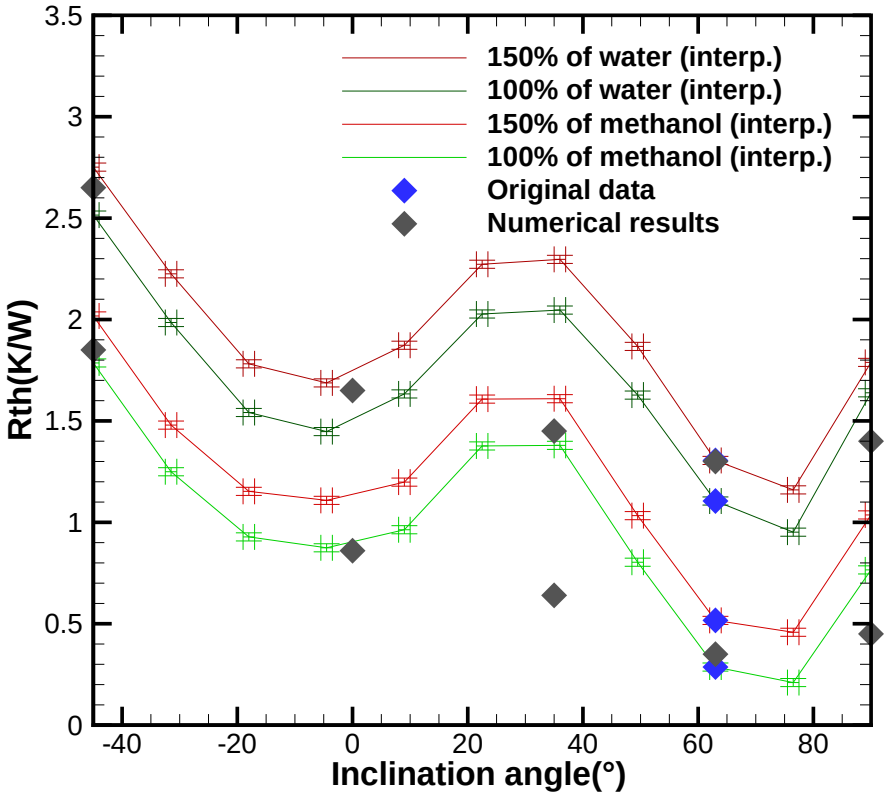

FIGURE 5.26 – Variations of the thermal resistance versus the inclination angle under condenser temperature, 55°C, and heat input, 47.75W.

By comparing the numerical results with experimental data, the error is more important for inclination angle between 20° and 40°. In fact, using the LB model the prediction gives a lower thermal resistance compared to LHS interpolation data. From the developed explanation, the thermal resistance should decreases. However, LHS interpolation results

increases until reaching a constant value then it decreases. This may be related to an interpolation errors. Using the results of the above chapter (see figure 5.27 the reproduction of figure 4.18), we found that the same trend is founded where the thermal resistance decreases.

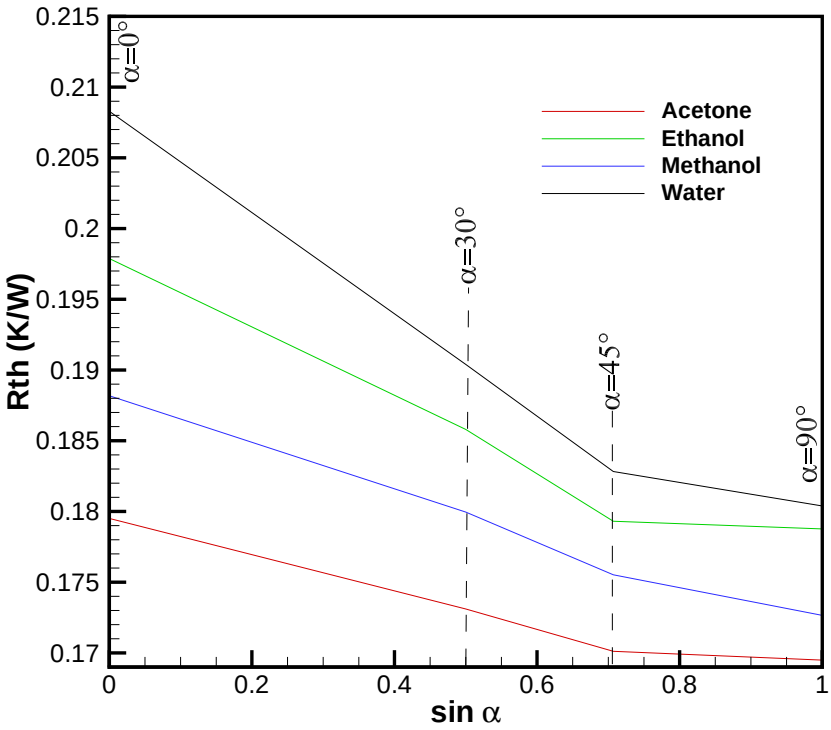

FIGURE 5.27 – Variations of thermal resistance versus the sine of inclination angle for different working fluids for a HP with 1.76m of length (1.4m evaporator, 0.06m adiabatic and 0.3 condenser length), $\varepsilon = 0.4$, $K = 1.17 \times 10^{-10} m^{-2}$, convective heat transfer coefficient of $1400 W.m^{-2}.K^{-1}$ and inlet temperature of 22°C.

Effect of condenser temperature

Experiments data are also used to analyze the impact of condenser temperature on the thermal resistance of the HP.

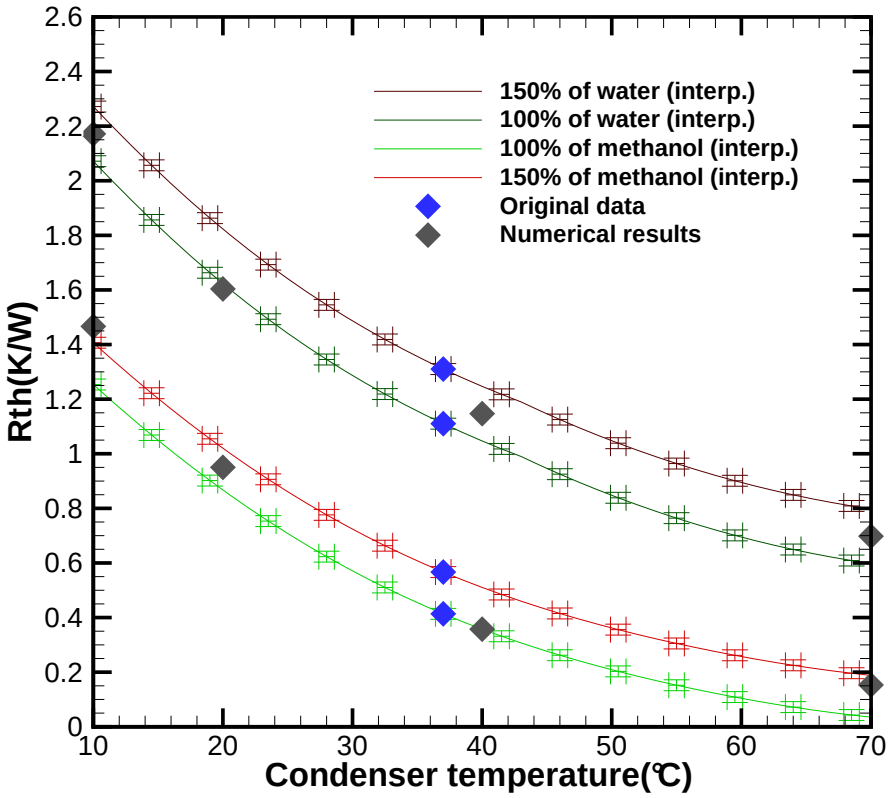

FIGURE 5.28 – Variations of the thermal resistance versus the condenser temperature under inclination angle, 63°, and heat input, 38.75W.

Figure 5.28 presents the variations of thermal resistance versus the heat input power using 100% filling ratio of methanol and water under different condenser temperatures. The curves share the same trends: the thermal resistance decreases with the increase of the condenser temperature. In fact, increasing the condenser temperature increases the liquid temperature which leads to smaller dynamic viscosity and so lower liquid pressure drop. As a consequence, the resulting thermal resistance decreases.

By comparing the numerical results with the experimental prediction, we can see that using saturated water the error is more important.

Comparison between the numerical and experimental results

Because of the complexity of the problem, we assume that the wick is saturated with the working fluid. Hence, in order to make a comparison between the numerical and experimental results, we tested only saturated water and methanol for a classical HPETSC case A. The tested experimental measurement points (1-5) are given in table 5.5.

In order to make a qualitative comparison, points 2 and 3 are taken as an example. The main difference between them is the inclination angle (point 2: gravity-assisted orientation, point 3: gravity-opposed orientation).

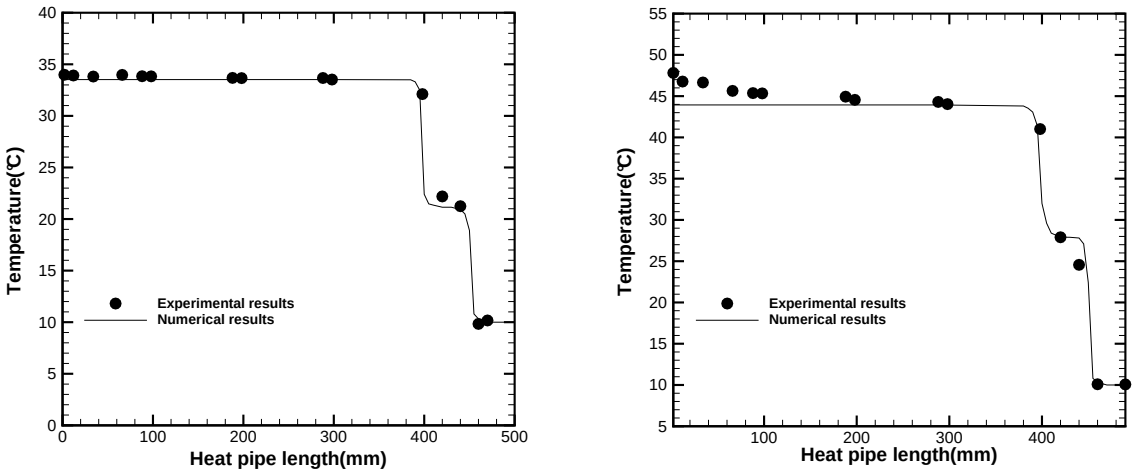

(a) Gravity-assisted (b) Gvarity-opposed

FIGURE 5.29 – Variations of the wall temperature versus the heat pipe length using water as working fluid by referring to experimental and numerical results for gravity-assisted and gravity-opposed orientations under condenser temperature, 10°C, and heat input, 5W.

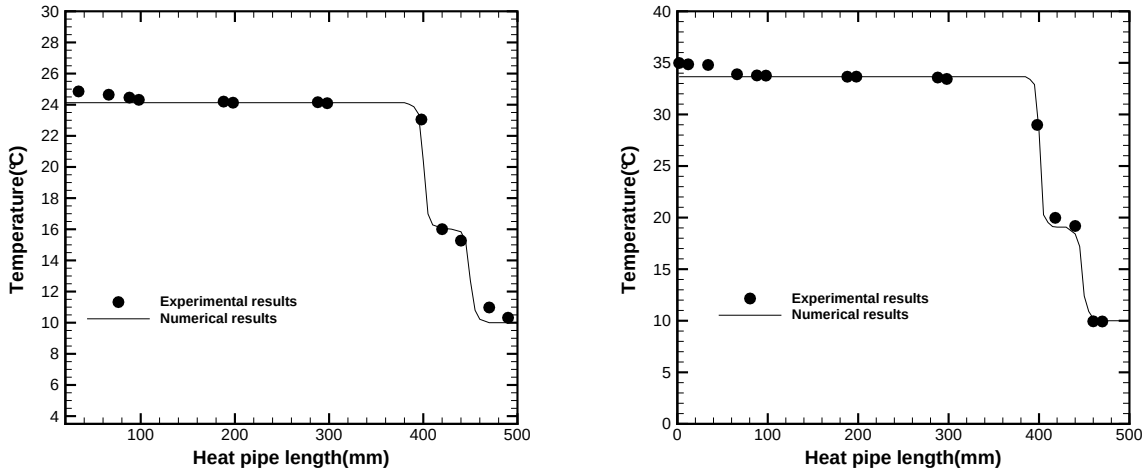

(a) Gravity-assisted (b) Gravity-opposed

FIGURE 5.30 – Variations of the wall temperature versus the heat pipe length using methanol as working fluid by referring to experimental and numerical results for gravity-assisted and gravity-opposed orientations under condenser temperature, 10°C, and heat input, 5W.

The variations of the wall temperature versus the heat pipe length using water and methanol as working fluid is shown in figures 5.29 and 5.30, respectively. In figure 5.29, for the two tested orientations (gravity-assisted and gravity-opposed), the numerical and experimental results are in good agreement. However, for both fluids, we can see that for the evaporator extreme region, the experimental wall temperature is slightly higher than the numerical prediction for gravity-opposed orientation. This is due to the low amount of liquid available in the evaporator region using the unfavorable orientation. In fact using this orientation, the capillary limit is reached more quickly, whereas the condenser is flooded by liquid. It is also found that wall temperature is lower at a favorable orientation. This leads to a lower temperature difference which induces a decrease of the total thermal resistance. Hence, a better performance using favorable orientation is retrieved.

By referring to table 5.1 and equation (1.12), the variations of the maximum power supply versus the operation temperature is given in figure 5.41 for different inclination angles using water and methanol, respectively. We recall the maximum capillary driven pressure given by:

$$\Delta P_{c,max} = \frac{2\sigma}{r_{eff}} \tag{5.10}$$

and the maximum heat flux given by:

$$Q_{c,max} = \frac{\frac{2\sigma}{r_{eff}} + \rho_l sin(\theta) L_{tot}}{\frac{\mu_l L_{eff}}{\rho_l S_p K h_{lv}} + \frac{8\mu_v L_{eff}}{\pi \rho_v R_v^4 h_{lv}}} \tag{5.11}$$

Conventionally, the number of merit, Me, is used as the thermal performance index of

working fluid which was defined as 1.1:

$$Me = \frac{\rho_l h_{lv} \sigma}{\mu_l} \tag{5.12}$$

These curves corroborate the previous observations as at unfavorable inclination HP is closer to reach its theoretical capillary limit. Also, through the calculation of the ratio of Merit number, equal to 10, we can conclude that HP with water has more capacity to go through higher heat capillary limit and so higher heat input capacity although performance is lower when dry-out does not occur.

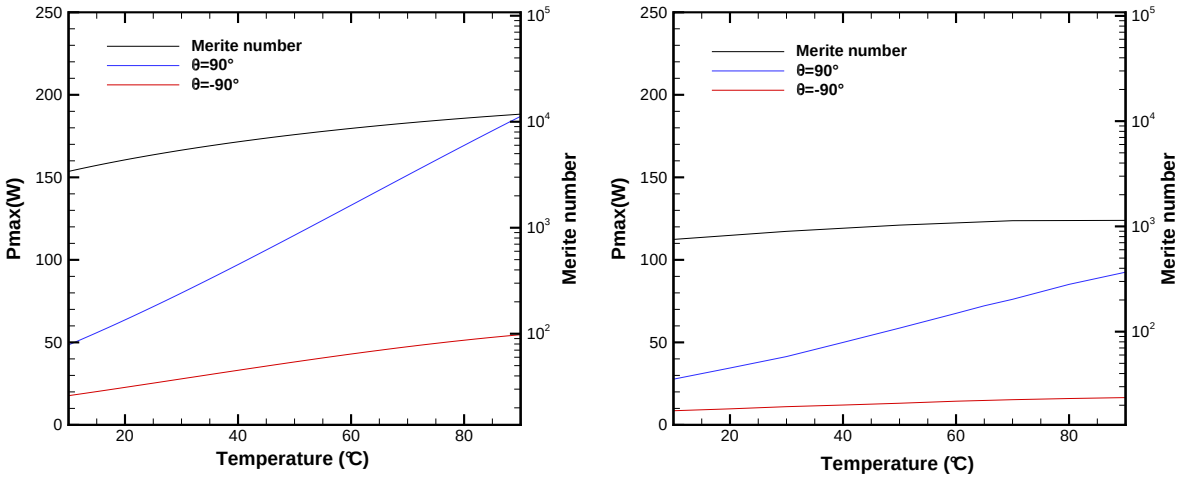

(a) Water

(b) Methanol

FIGURE 5.31 – Variations of the maximum heat input versus the operation temperature for (5.31a) water and (5.31b) methanol.

Figures 5.32 and 5.33 show the 2D temperature variation in solid/liquid-wick region for both fluids. We can see a higher temperature distribution through the wall and liquid region at unfavorable orientation. Also, a higher temperature degradation can be observed. By calculating the heat transfer density through the wall, we found that the heat density crossing the evaporator region is 10 times lower than that of condenser region ($500 W.m^{-2}$ heat density for the evaporator and $5000 W.m^{-2}$ for the condenser). This due to the surface ratio. The heat is evacuated through the condenser region with a 10 times smaller surface. Due to the heat transfer continuity, this amount of heat is transferred through the wall/liquid-wick interface where the heat density through the evaporator region decreases whereas it still the same for the condenser region ($62.5 W.m^{-2}$ heat density for the evaporator and $5000 W.m^{-2}$ for the condenser). This is due to the homogeneity of the condenser temperature through the radial position.

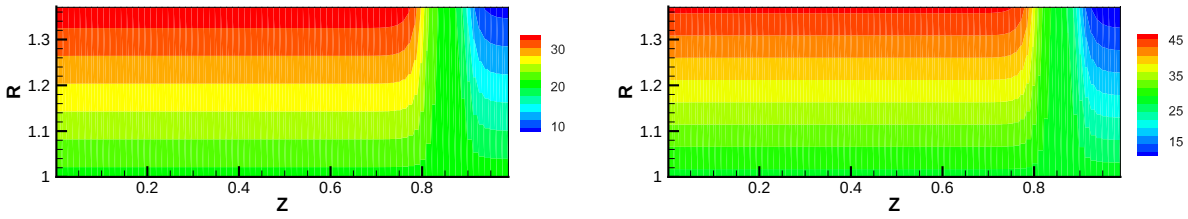

(a) Gravity-assisted (b) Gravity-opposed

FIGURE 5.32 – Temperature iso-contours in °C in the wall/liquid-wick region using water as working fluid by referring to numerical results for gravity-assisted and gravity-opposed orientations under condenser temperature, 10°C, and heat input, 5W.

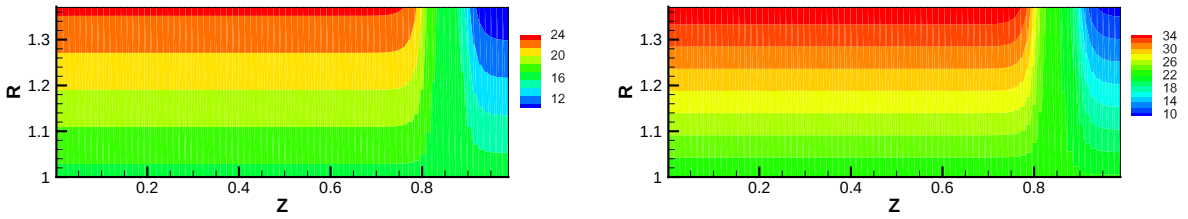

(a) Gravity-assisted (b) Gravity-opposed

FIGURE 5.33 – Temperature iso-contours in °C in the wall/liquid-wick region using methanol as working fluid by referring to numerical results for gravity-assisted and gravity-opposed orientations under condenser temperature, 10°C, and heat input, 5W.

Figures 5.34 and 5.35 show the axial velocity iso-contours in liquid-wick region for both fluids. We can see a higher velocity magnitude at the adiabatic region near the liquid-wick/vapor interface. This is due to the counter-current fluid flow (the vapor circulation

in the vapor region and the liquid return in the liquid/wick region) which generate a high vorticity at the adiabatic region. This can be explained by the fact that the liquid flow is maximum there (all condensed fluid flows through the adiabatic region) and the no-slip condition at the solid-wick interface makes the velocity profil maximum close to the vapor liquid-wick interface.

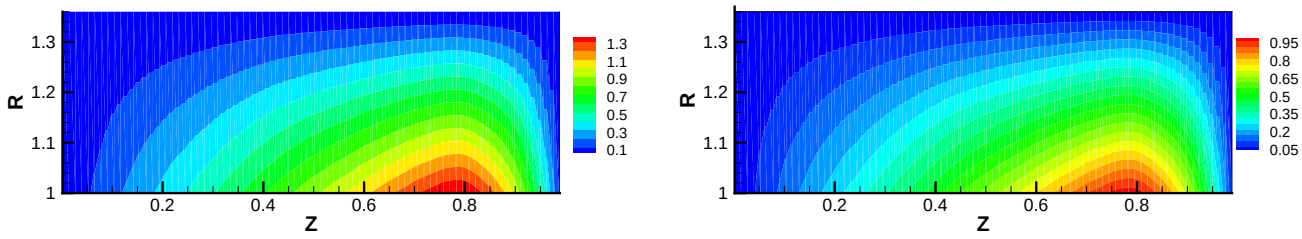

(a) Gravity-assisted

(b) Gravity-opposed

FIGURE 5.34 – Axial liquid-wick velocity iso-contours in $\times 10^{-1}$m/s using water as working fluid by referring to numerical results for gravity-assisted and gravity-opposed orientations under condenser temperature, 10°C, and heat input, 5W.

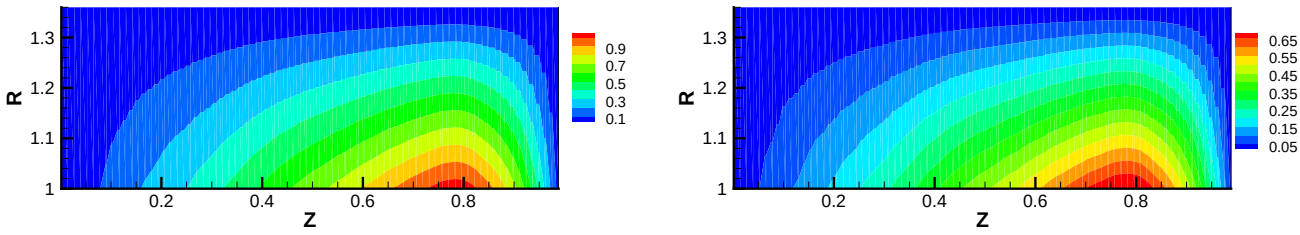

(a) Gravity-assisted (b) Gravity-opposed

FIGURE 5.35 – Axial liquid-wick velocity iso-contours in $\times 10^{-1}$m/s using methanol as working fluid by referring to numerical results for gravity-assisted and gravity-opposed orientations under condenser temperature, 10°C, and heat input, 5W.

Figures 5.36 and 5.37 show the axial iso-contours in vapor region for both fluids. We can see also a higher velocity magnitude in the continuation of the adiabatic region near the liquid-wick/vapor interface. The very same explication as given previously holds.

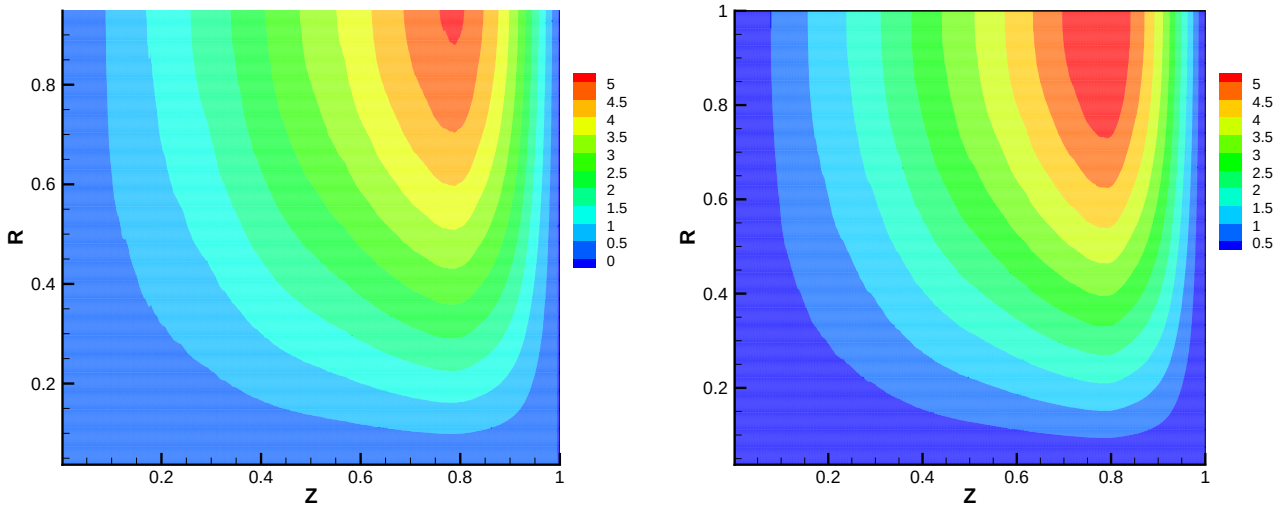

(a) Gravity-assisted (b) Gravity-opposed

FIGURE 5.36 – Axial vapor velocity iso-contours in m/s using water as working fluid by referring to numerical results for gravity-assisted and gravity-opposed orientations under condenser temperature, 10°C, and heat input, 5W.

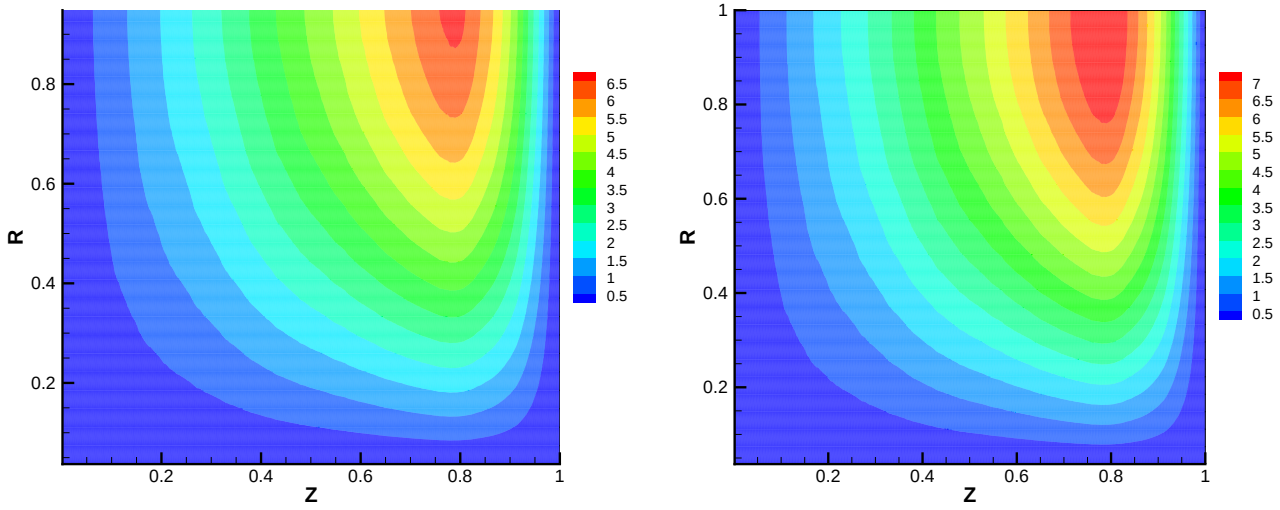

(a) Gravity-assisted (b) Gravity-opposed

FIGURE 5.37 – Axial vapor velocity iso-contours in m/s using methanol as working fluid by referring to numerical results for gravity-assisted and gravity-opposed orientations under condenser temperature, 10°C, and heat input, 5W.

Tables 5.6 and 5.7 show a comparison for points 1 to 5, provided in table 5.5 between:

the numerical and experimental total, evaporator and condenser resistances using water and methanol as working fluids, respectively. The error is calculated as follows:

$$Error(\%) = \frac{Rth_{exp} - Rth_{num}}{Rth_{exp}} \times 100 \tag{5.13}$$

Points	1	2	3	4	5
Rth(num)	0.932	4.49	4.646	4.426	1.77
Rth(exp)	1.02	4.55	4.72	4.678	2.055
Error(%)	10.54	1.31	1.59	5.38	13.86
Revap(num)	0.545	2.37	2.86	1.3	0.9
Revap(exp)	0.57	2.38	2.9	1.27	1.0
Error(%)	5.54	0.58	1.37	-2.34	10
Rcond(num)	0.387	2.11	1.786	3.128	0.97
Rcond(exp)	0.4	2.44	1.9	3.39	1.06
Error(%)	5	0.55	0.22	7.72	3.86

Table 5.6 – Comparison between the numerical and experimental resistances for different experimental tested points using water as working fluid.

Points	1	2	3	4	5
Rth(num)	0.696	2.722	2.69	1.475	1.143
Rth(exp)	0.668	2.738	2.79	1.516	1.312
Error(%)	-4.19	0.5	1.47	2.7	12.88
Rth_{evap}(num)	0.265	1.64	1.15	0.737	0.58
Rth_{evap}(exp)	0.289	1.653	1.2	0.76	0.715
Â£ Error(%)	8.86	0.234	0.91	2.9	17.73
Rth_{cond}(num)	0.43	1.082	1.54	0.738	0.56
Rth_{cond}(exp)	0.38	1.085	1.56	0.735	0.54
Error(%)	-13.05	0.27	0.56	-0.2	-4.85

Table 5.7 – Comparison between the numerical and experimental resistances for different experimental tested points using methanol as working fluid.

From this tables, the error of the total resistance is lower than 14%. However, the error of the evaporator reaches 17.78%. This is due to the limitation of the proposed model which does not take into account the dry-out phenomenon. Hence, globally, this model gives very good prediction but only when the heat pipe is maintained under its normal working conditions.

Figure 5.38 presents histograms of the error of the total, evaporator and condenser resistances as a function of the number of the tested points. As we can see, most of the tested pointed (6 of 10 points) are situated an error below 5% for the three resistances.

Also, we can see that the error of the evaporator resistance is higher than that of the condenser resistance. This may be due to the code weakness in detecting the dry-out phenomenon. In fact, the capillary limit is reached when the pumping effect of the capillary structure cannot overcome the pressure drops for a given working fluid and wick structure. This causes the heat pipe evaporator to dry-out and shuts down heat transfer from at least a part of the evaporator with a rapid evaporator temperature increase. Thus, in order to keep up the operation of such a device, this limit is essential to be taken into account especially for heat pipes with capillary structure.

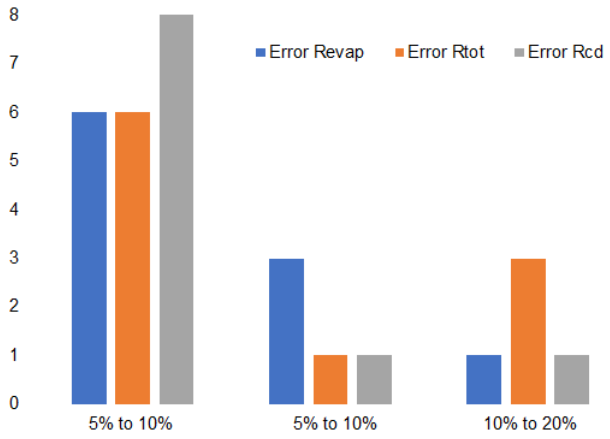

FIGURE 5.38 – A comparison of the error between the experimental and numerical results for the tested points (1 to 5 given in table 5.5) by varying the condenser temperature, the inclination angle and the heat input power.

5.8.2 Cases A and B

The main difference between cases A and B is the condenser length. In case A, the adiabatic region is 50mm long with a condenser 50mm long, too. In case B, in the absence of the adiabatic region, the condenser is 100mm long. Figure 5.39 shows the variations of the thermal resistance versus the heat input for both working fluids with and without adiabatic region. It is observed that the case without adiabatic region gives better performance. In fact, in case B, the exchange surface is multiplied by two. This leads to both a lower heat density at the condenser and a shorter effective length which implies lower total resistance and then better thermal performance. In addition, the main purpose of solar collectors is to collect solar radiation as mush as possible, the evacuation of this received heat takes place in the condenser region. In addition, and conventionally, the role of the adiabatic region is to convey the vapor to the condenser. However, in such application, this region seems to be useless as we intend only to receive and evacuate the recuperated heat with less losses, the location of the condenser being not an issue.

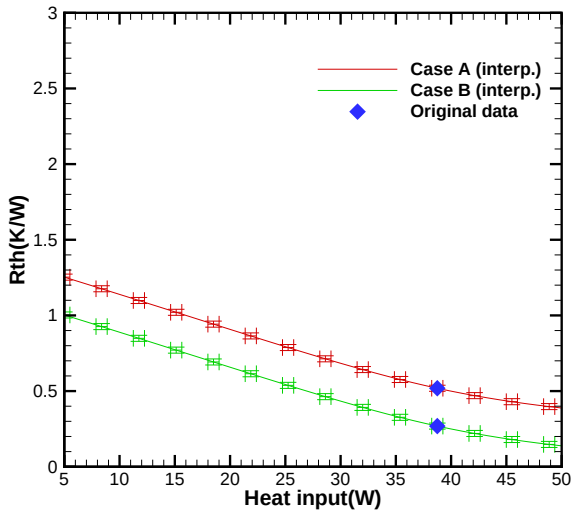

(a) 150% of methanol

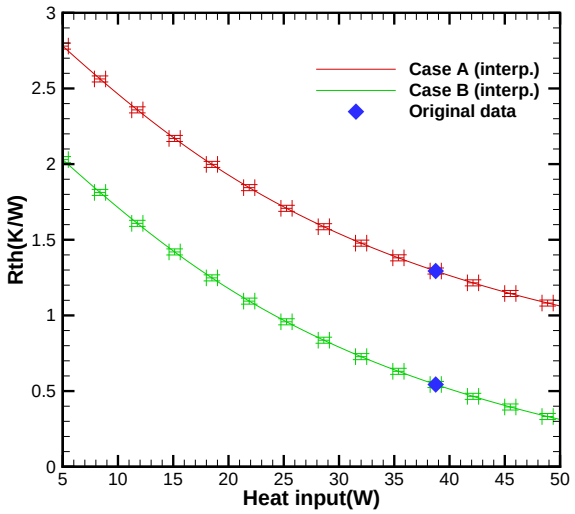

(b) 150% of water

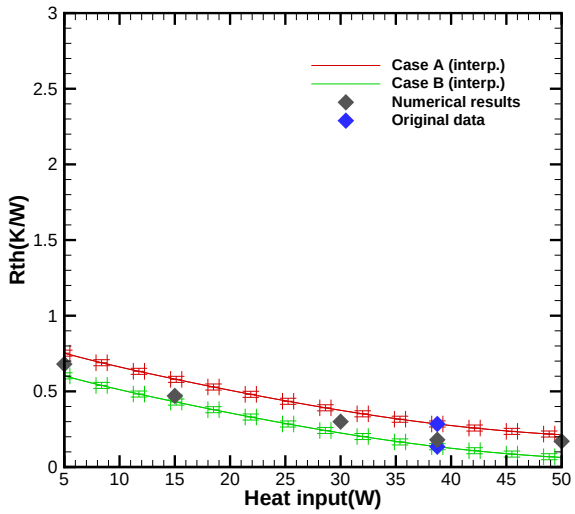

(c) 100% of methanol

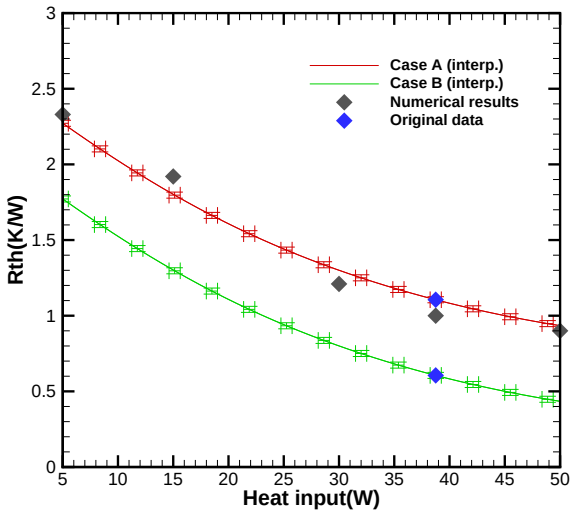

(d) 100% of water

FIGURE 5.39 – Variations of the thermal resistance versus the heat input for different fluids and filling ratios configurations with and without the adiabatic region under condenser temperature, 37°C, and inclination angle, 63°.

5.8.3 Cases A and C

A number of similitude and difference does exist between the cases A, B and C. The main purpose of the design of case C is to see its performance in the case of parabolic solar collector (see 5.19), where the collector represents the evaporator region. By observing this case, one can consider it also as two combined HPs with an evaporator 200mm long and a condenser 50mm long with respect to the central symmetry. This can make it equivalent to case B of two twice shorter HPs. Hence, as discussed before, other things being equal, we observe the same trends like case A where the effect of the adiabatic region is the main difference as discussed in the previously. However, by comparing the three cases together, we observe a response with a lower thermal resistance. We discuss here the effect of symmetry for the three cases.

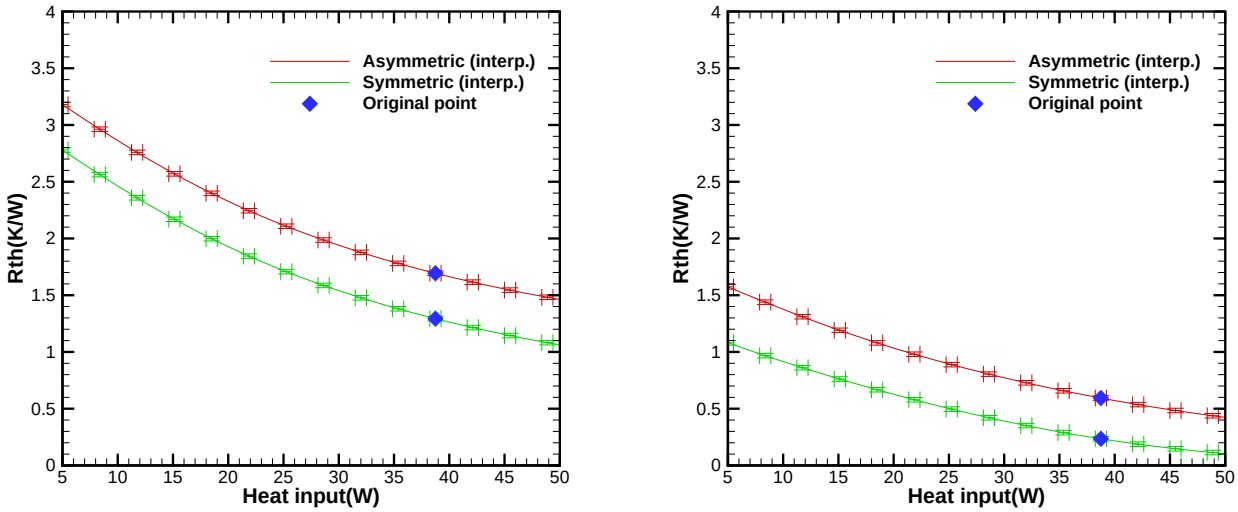

(a) Case A

(b) Case C

FIGURE 5.40 – Variations of the thermal resistance versus the heat input for water with 150% filling ratios using symmetric and asymmetric configurations under condenser temperature, 37°C, and inclination angle, 63°.

From figure 5.40, the symmetry configuration gives higher performance for the two cases. By comparing case C to case A, it appears that the gap between the symmetry and asymmetry thermal resistance is more important. This is may be due to its radial symmetry which could favorite the symmetry HP heating. Also, it is found that the thermal resistance is about two times lower in case C then that of case A. This can be explained by the fact that the heat exchange surface using case C is more important and that liquid pressure drop is approximately twice smaller owing to the shorter effective length. This conduces to a higher heat transfer capacity and then to a lower evaporator temperature. As the condenser is situated on both sides, the generated vapor will migrate

through both directions to reach the condenser part where it gives back the heat latent of vaporization and returns to the evaporator region.

In real application of parabolic solar collectors, the HP is exposed to solar radiation through the bottom and top in order to collect the maximum of it. Using a HP like described in case C could lead to even higher performances.

5.9 The optimum solution in solar collector situations

From the results presented so far, we conclude that the working fluid plays an important role in the HP performance. It was found that using methanol enhances the HP functionality if no dry-out is feared. Furthermore, using fluid amount exactly sufficient to saturate the wick yields higher HP heat transfer capacity. However, oversaturated fluid may extend artificially the capillary limit as an excess of fluid still exists for higher heat input. But, this leads to degrading the performance. An inclination angle between 65° and 77° is recommended for case A. When analyzing the effect of adiabatic length, it seems that case B is more suitable for HPETSC. However, case C could be more interesting for concentrator solar applications even though at higher inclinations angles.

As far as solar applications are concerned, the received flux depends of the location of its installation. The most relevant parameters are the latitude, the inclination angle and the heat losses due to the ambient conditions. Hence, the main question to ask is which inclination should we the HP assume in order to capture and transfer the maximum solar radiation into the condenser ? Through this section, we try to give some details in response to this question.

In order to optimize the heat input, an estimation of the heat losses due to convection and radiation is needed. Using the correlation provided by literature [175], the convective heat losses can be retrieved from the corresponding heat exchange coefficient:

$$h_d = \frac{Nu_d \lambda}{d} \tag{5.14}$$

where

$$Nu_d = 0.53 Ra_d^{1/4} \tag{5.15}$$

$$Ra_d = Ra_L \frac{d^3}{L^3} \tag{5.16}$$

$$Ra_L = \frac{g sin\theta \beta \Delta T L^3}{\alpha \nu} \tag{5.17}$$

and $\Delta T = T - T_{envi}$. Here, T is the evaporator mean temperature and T_{envi} is the ambient temperature. Hence, the convective heat losses can be written as:

$$Q_{cv} = h_d A \Delta T \tag{5.18}$$

where $A = 2\pi r_w L_{tot}$ is the lateral surface. In addition, the radiative heat losses can be approximated by:

$$Q_{rad} = 4\varepsilon\sigma T_{envi}^3 A \Delta T \tag{5.19}$$

Hence, the maximum received heat flux could be calculated as follow:

$$Q_{max} = Qcos(\theta - \alpha) - (Q_{cv} + Q_{rad}) \tag{5.20}$$

where θ is the HP inclination angle and α is the latitude angle. In Poitiers, we will take $\alpha = 45°$.

Figure 5.41 presents the variations of the maximum heat input versus the inclination angle at a location of latitude 45° for different condenser temperature. As we can see, this heat input increases with the increase of the inclination angle until reaching its maximum at an inclination angle of 55°, 56.8° and 57.2° (and not 45°) for a condenser temperature of 20°C, 40°C and 60°C, respectively. Then, the useful heat deceases slowly with the increase of the inclination angle. Worth to note here that the evaporator temperature is influenced by both the inclination angle and the heat losses and vice versa. An iterative method, relying on formula (5.20), is used to determine the ultimate and exact heat poxer received by the HP. This optimum increases slightly with the condenser temperature. This suggests to use a solar collector with different inclination angles for each HP. However, the shadowing effect of each HP should be taken into consideration in that case.

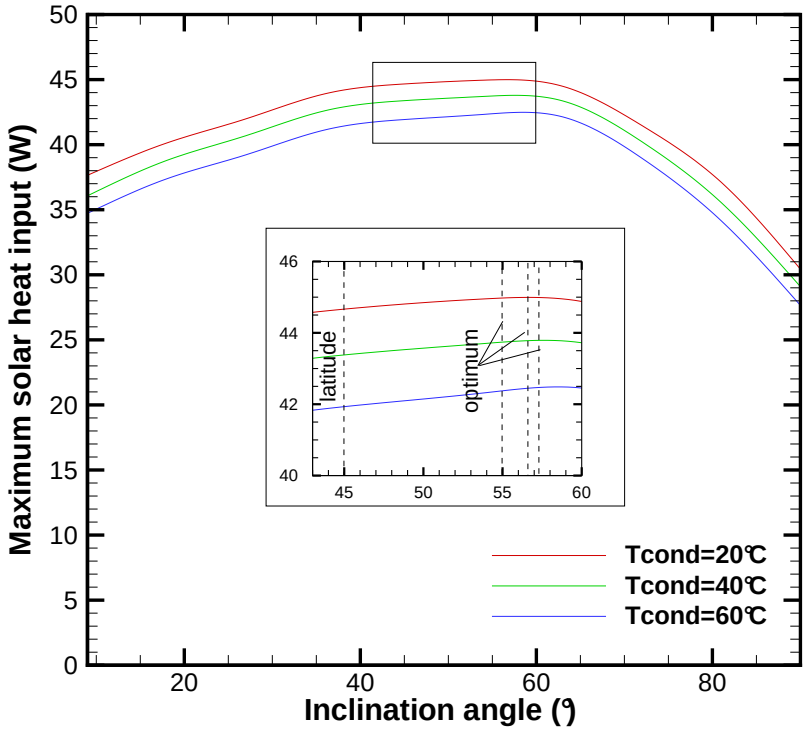

FIGURE 5.41 – The optimum heat input versus the inclination angle.

5.10 Conclusion

In this chapter, in order to grasp the overall performance of a heat pipe, an experimental setup was designed. This bench allowed us on the one hand to estimate the external wall temperature profiles and secondly to evaluate with an acceptable accuracy the thermal transport performance of cylindrical heat pipes. The developed LB model was validated with both the direct and LHS experimental results. A HP configuration was proposed with its optimal working conditions. By focusing on the evaporator zone, the temperature measurements obtained by such a detailed characterization of the HP operation can serve as data to locate in particular the dry-out areas on the evaporator zone in terms of different working parameters as the working fluid, heat input, condenser temperature and inclination angle.

6

Conclusions

6.1 Summary

In the present work, we studied by both numerical and experimental means the performance of heat pipe used in solar collectors for water heating systems. The main purpose was to show the relevance of the lattice Boltzmann method in resolving heat pipe evacuated tube solar collector systems including phase change. For reasons of problem complexity, two-dimensional axisymmetric equations, using saturated wick structure, have been used.

The state of the art pointed out the increasing interest on using heat pipes in solar water heaters. However, most HPs developed so far in HPETSC devices are smooth wickless tubes. In opposite, few surveys have used evacuated tube solar collector with wick structure, desipe their high potential. Owing to this, we focused on analyzing such systems using lattice Boltzmann method, which we developed in the next chapter where we outlined the background theory: different approaches of momentum equation derivation, Boltzmann equation and boundary conditions implementation. The main drawbacks of the methods already developed are the complexity of the source terms involved compared to the original equations and the inconsistency caused by the added forces. In order to overcome these issues, we proposed a new lattice Boltzmann scheme, which inserts the space and time dependent source terms into the evolution equation of the standard lattice Boltzmann method, and makes it recover the mass and momentum equations on cylindrical coordinates system by performing Chapman-Enskog expansion. This new scheme combines the idea proposed by Halliday *et al.* [94] which uses the coordinate transformation method approach with the one introduced by Guo *et al.* [92] to include the effect of porous media on fluid flow into the equilibrium distribution function. Compared with the existing lattice Boltzmann equation models of axisymmetric an isothermal flows through porous media [238–241], the proposed model has the following features: (i) the source terms are simply extra terms in the transformed pseudo-Cartesian equations where the velocity gradient computation is avoided, (ii) the centered scheme is applied to remove the discrete lattice effects leading to a second-order space accuracy, (iii) it is easier to implement when compared to Rong *et al.*'s models [238–241], and the standard calculation of the macroscopic variables is preserved, (iv) it is applied on a uniform rectangular grid in cylindrical coordinates system, which adheres to the inherit property of lattice Boltzmann method, (v) the present approach is suitable for axisymmetric flows involving more physical phenomena. An enhanced derived model wass then proposed. The point is that the compressibility effect in the existing lattice Boltzmann equation models may produce uncontrollable computation error as the fluids are assumed obeying the ideal equation of state; an assumption far to be accurate for liquids. Therefore, most of these models can be used only to simulate compressible flows. That is why this model is considered as an artificial compressible model to solve incompressible mass and momentum equations. Then, we presented the detailed derivation of the new model and tested its accuracy and reability through well-documented cases.

The performance of a capillary driven heat pipe used in solar collectors was then investigated numerically. The analysis includes the wall, the liquid-wick material and the vapor regions. Comparison between the present model results and some numerical results

available in the literature shows very good agreement. The effect of working fluid, wick structure, evaporator length and inclination angle on the system behavior was addressed. Among these results, some suggest the superior performance of acetone heat pipe with sintered copper structure of 7.3 mm of thickness in 45° inclination in typical solar collector applications. Numerical results with these working conditions were presented, which provide guidance for the heat pipe design used in solar collectors. Then, a heat pipe evacuated tube solar collector has been investigated numerically. A detailed theoretical analysis for energy and exergy analysis of the collector was carried out. Based on the numerical results of lattice Boltzmann method, the effect of incident solar radiation intensity and number of tubes was assessed. The results reflect the contribution (and significance) of each of these parameters to the collector overall efficiency. The higher the incident solar radiation, the hotter the water inlet temperature in heat pipe evacuated solar collectors, which leads to decreasing heat transfer rate between the heat pipe's condenser and supplied water. For a cost/performance best ratio, a heat pipe evacuated tube with 15 tubes is preferred with both exergy and energy efficiency. This study can be helpful in designing actual solar collector systems.

An experimental setup has been built in this study, too. The design and construction of the heat pipe, including a detailed description of the setup and the protocol, were presented. Then, the experimental results were analyzed and discussed where different heat pipe configurations, called cases A, B and C, used in solar collectors were compared under different working conditions: applied heat input, inclination angle, condenser temperature, working fluid, filling ratio and symmetric and asymmetric heating. The developed lattice Boltzmann model was validated with both direct and Latin Hypercube Sampling experimental results. From the presented results, we concluded that the working fluid play an important role in the heat pipe performance, owing to its intrinsic thermophysical proprieties which affect the total resistance of the heat pipe and then its thermal performance. It was found that using methanol enhances the heat pipe functionality since it induces higher pressure drop if no dry-out is expected. Furthermore, using fluid amount exactly sufficient to saturate the wick yields higher heat pipe heat transfer capacity. However, oversaturated fluid may extend the capillary limit as an excess of fluid still exists for higher heat input. But, this leads to degrading the performance far from dry-out conditions. An inclination angle between 65° and 77° is recommended for case A. Through comparing the effect of adiabatic length, it seems that case B is more suitable for heat pipe evacuated tube solar collector. However, case C could be more interesting for concentrator solar applications although at higher inclinations angles. As far as solar applications are concerned, the received flux depends of the location of its installation. The relevant parameters are the latitude, the inclination angle and the convective and radiative heat losses into the ambience. Hence, the optimum inclination should be taken in order to capture and transfer the maximum solar radiation into the condenser is equal to 55°, approximately, for Poitiers, France, instead of the angle equal to its latitude, 45°.

6.2 Notable Findings

The originality of the present study can be summarized as follows:

— An extension literature review of the main funding, challenges and future directions was presented for heat pipe evacuated tube solar collectors with a comparative study with flat plate collectors.

— A novel lattice Boltzmann method model was proposed with a second order accuracy.

— A comparison of a typical heat pipe evacuated tube solar collector performances was made under different working conditions. A heat pipe filled with acetone and covered inside by sintered copper abd inclined by 45° gives the higher thermal performance, when no losses occur.

— Both energy and exergy analyses applied to evacuated tube solar collectors with capillary heat pipes were performed. The heat pipe evacuated tube solar collector efficiency reaches 62%.

— A new implementation of heat pipe with moving blocks was designed. This conception makes it possible to easily change the position of different blocks, hence saving time and money.

— A comparison between the numerical and experiment results was presented successfully as far as axisymmetry, saturated wick and no dry-out conditions are regarded.

— An experimental campaign was performed for heat pipe is solar collector conditions. The best heat pipe performance was observed using methanol as working fluid under inclination between between 65° and 77°. Through tests, case C showed good thermal performance. This configuration can be used vitually at any inclination owing to its central symmetry.

6.3 Future Directions

The developed lattice Boltzmann model for multiphase flow together with heat pipe integration into solar applications has opened new research avenues. Among the many applications, experimental, numerical and theoretical studies that can be carried out in this context, we suggest a few directions that can be pursued in the near future:

— With the different boundary conditions developed on moving boundary conditions, we can integrate the study of the effect of liquid/vapor interface on the heat pipe performance. Then, we can compare the results with the experimental one with more realistic boundary conditions where the wick can be either over or under saturated and so be able to predict dry-out. This phenomenon presents a key element of the heat pipe performance limitation.

— A three-dimensional lattice Boltzmann model can be developed by extending the axisymmetric model. This will be helpful to study the effect of a symmetry and validate it with the results made available by the present experimental campaign.

— A bench with a heat pipe evacuated tube solar collector may be tested under

outdoor climate conditions. Then, we can study the problem related to freeze in winter and overheating in summer by testing new working fluids like nanofluids, new surface treatment that may overcome such issues.

— Tests may be carried out on the present bench to compare acetone to other fluids so to reduce heat losses.

Appendices

Appendix A

Derivation of the formula of the velocity field

From equation (3.24), the fluid velocity is given by:

$$\rho \mathbf{u} = \sum_k \mathbf{c}_k f_k + \frac{\Delta t}{2} \rho \mathbf{F}_p \tag{A.1}$$

By substituting the expression of the total body force from equation (3.7) in the above equation, we get:

$$\rho \mathbf{u} = \sum_k \mathbf{c}_k f_k + \frac{\Delta t}{2} \rho \left(-\frac{\varepsilon \upsilon}{K} \mathbf{u} - \frac{\varepsilon F_\varepsilon}{\sqrt{K}} |\mathbf{u}| \mathbf{u} + \varepsilon \mathbf{G} \right) \tag{A.2}$$

which leads to:

$$\rho \left(1 + \frac{\Delta t}{2} \frac{\varepsilon \nu}{K} \right) \mathbf{u} \quad - \quad \rho \frac{\Delta t}{2} \frac{\varepsilon F_\varepsilon}{\sqrt{K}} |\mathbf{u}| \mathbf{u} \quad - \quad \rho \frac{\Delta t}{2} \varepsilon \mathbf{G} \quad - \quad \sum_k \mathbf{c}_k f_k \quad = \quad 0 \tag{A.3}$$

By using the expression of the temporary velocity v, c_o and c_1 introduced in equations (3.26)-(3.28), the above equation can be cast in:

$$2\rho c_0 \mathbf{u} - \rho c_1 |\mathbf{u}| \mathbf{u} - \rho \mathbf{v} = 0 \tag{A.4}$$

Since $\rho \neq 0$, one can write:

$$2c_0 \mathbf{u} - c_1 |\mathbf{u}| \mathbf{u} - \mathbf{v} = 0 \tag{A.5}$$

Thus,

$$\mathbf{u} = \frac{1}{2c_0 - c_1 |\mathbf{u}|} \mathbf{v} \tag{A.6}$$

By taking the norm, the above equation becomes:

$$|\mathbf{u}| = \frac{|\mathbf{v}|}{2c_0 + c_1 |\mathbf{u}|} \tag{A.7}$$

which leads to a quadratic equation of $|\mathbf{u}|$:

$$2c_0|\mathbf{u}| - c_1|\mathbf{u}|^2 - |\mathbf{v}| = 0 \tag{A.8}$$

with two roots:

$$\begin{cases} -\frac{1}{c_1}\left(c_0 + \sqrt{c_0^2 + c_1|\mathbf{v}|}\right) \\ -\frac{1}{c_1}\left(c_0 - \sqrt{c_0^2 + c_1|\mathbf{v}|}\right) \end{cases} \tag{A.9}$$

Since always positive, the second root is the accepted solution. By introducing this solution into equation (A.6), one can find the following expression which is introduced in equation(3.25):

$$\mathbf{u} = \frac{\mathbf{v}}{c_0 + \sqrt{c_0^2 + c_1|\mathbf{v}|}} \tag{A.10}$$

Appendix B

Heat pipe temperature and velocity profiles

In this section, in order to describe more clearly the flow field and temperature field distributions in the heat pipe, we present the profiles in dimensional scales.

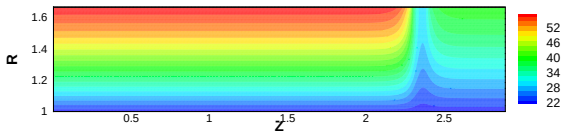

(a) Water

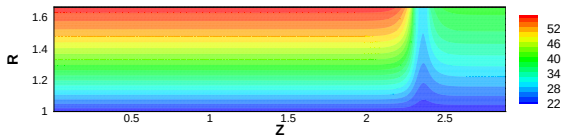

(b) Ethanol

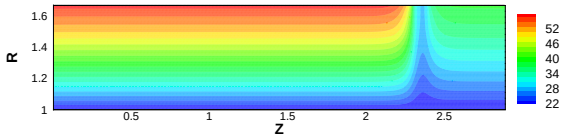

(c) Methanol

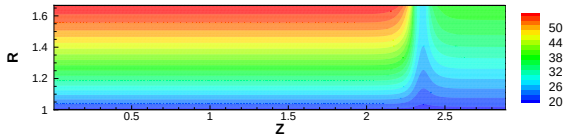

(d) Acetone

FIGURE B.1 – Temperature field in the porous medium expressed in °C for different working fluids using sintered steel (case I).

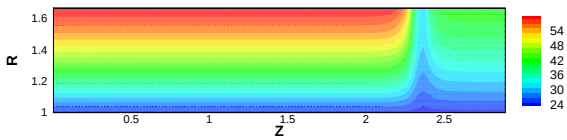

(a) Water

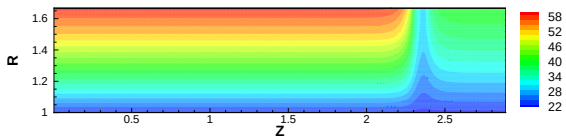

(b) Ethanol

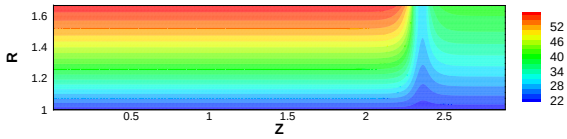

(c) Methanol

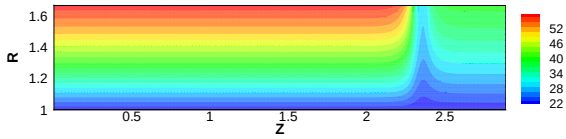

(d) Acetone

FIGURE B.2 – Temperature field in the porous medium expressed in °C for different working fluids using copper screen (case II).

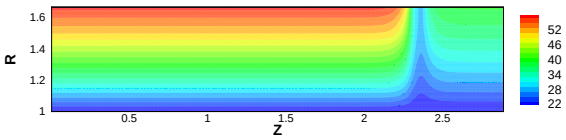

(a) Water

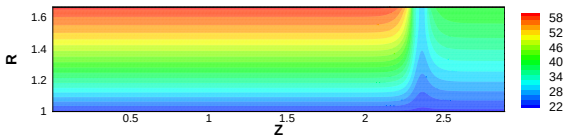

(b) Ethanol

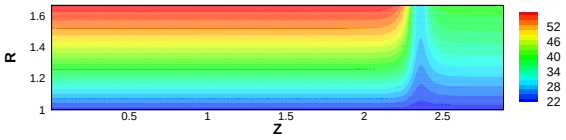

(c) Methanol

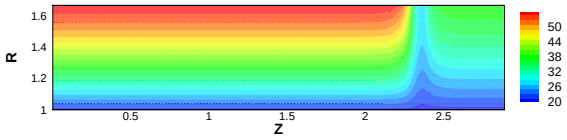

(d) Acetone

FIGURE B.3 – Temperature field in the porous medium expressed in °C for different working fluids using sintered copper (case III).

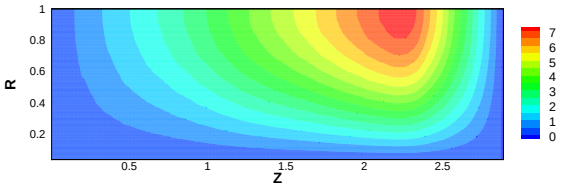

(a) Water

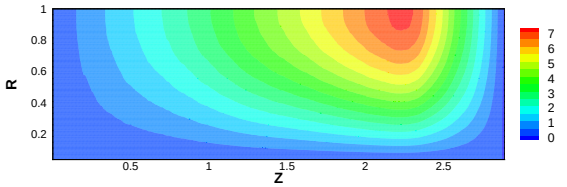

(b) Ethanol

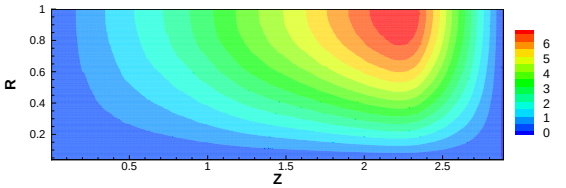

(c) Methanol

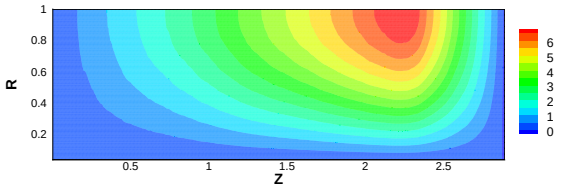

(d) Acetone

FIGURE B.4 – Axial velocity field expressed in the vapor core in m/s for different working fluids using sintered steel in the vapor region (case I).

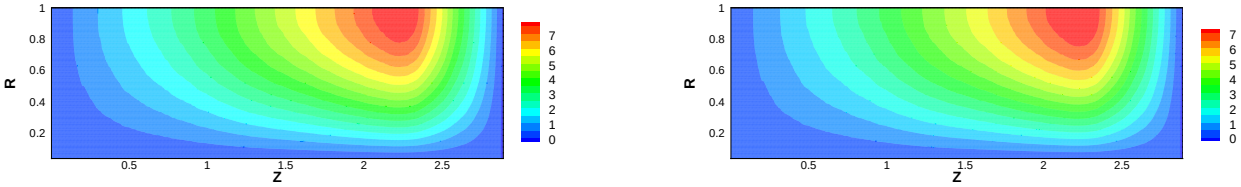

(a) Water (b) Ethanol

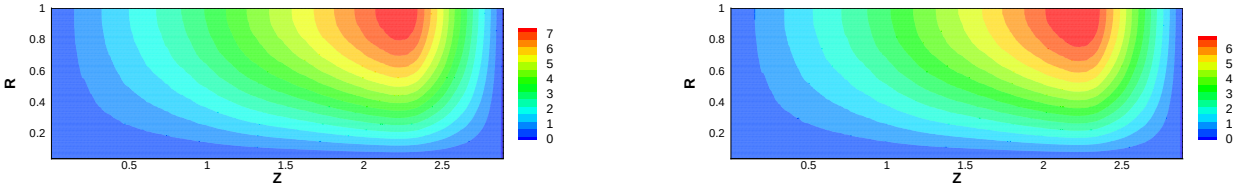

(c) Methanol (d) Acetone

FIGURE B.5 – Axial velocity field expressed in the vapor core in m/s for different working fluids using copper screen in the vapor region (case II).

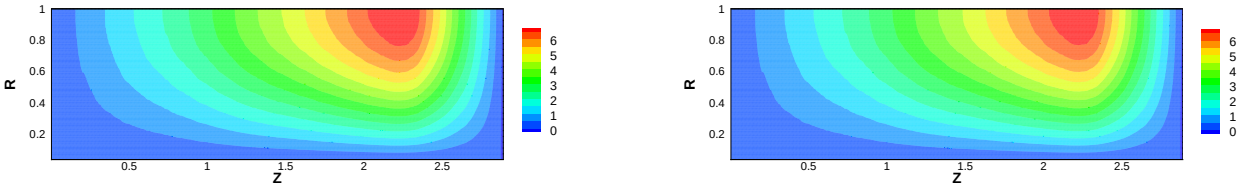

(a) Water (b) Ethanol

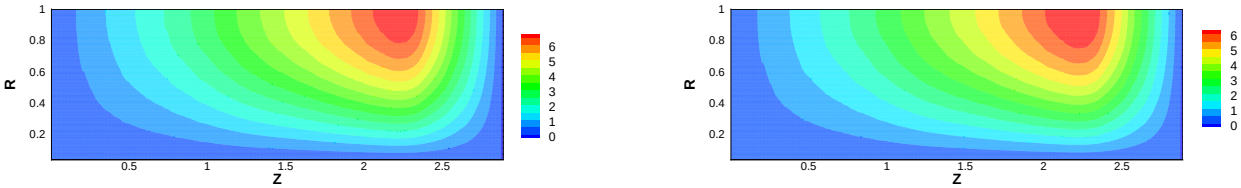

(c) Methanol (d) Acetone

FIGURE B.6 – Axial velocity field expressed in the vapor core in m/s for different working fluids using sintered copper in the vapor region (case III).

Appendix C

Heat pipe plan by Atherm

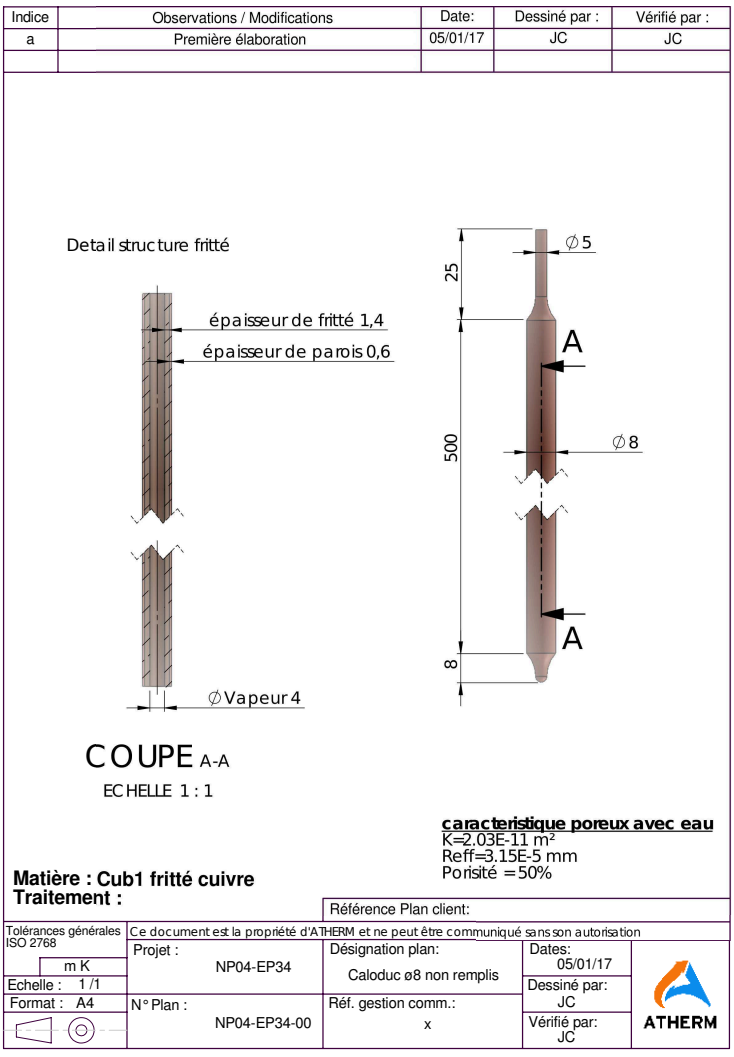

FIGURE C.1 – Heat pipe sizes.

Appendix D

Heat pipe components

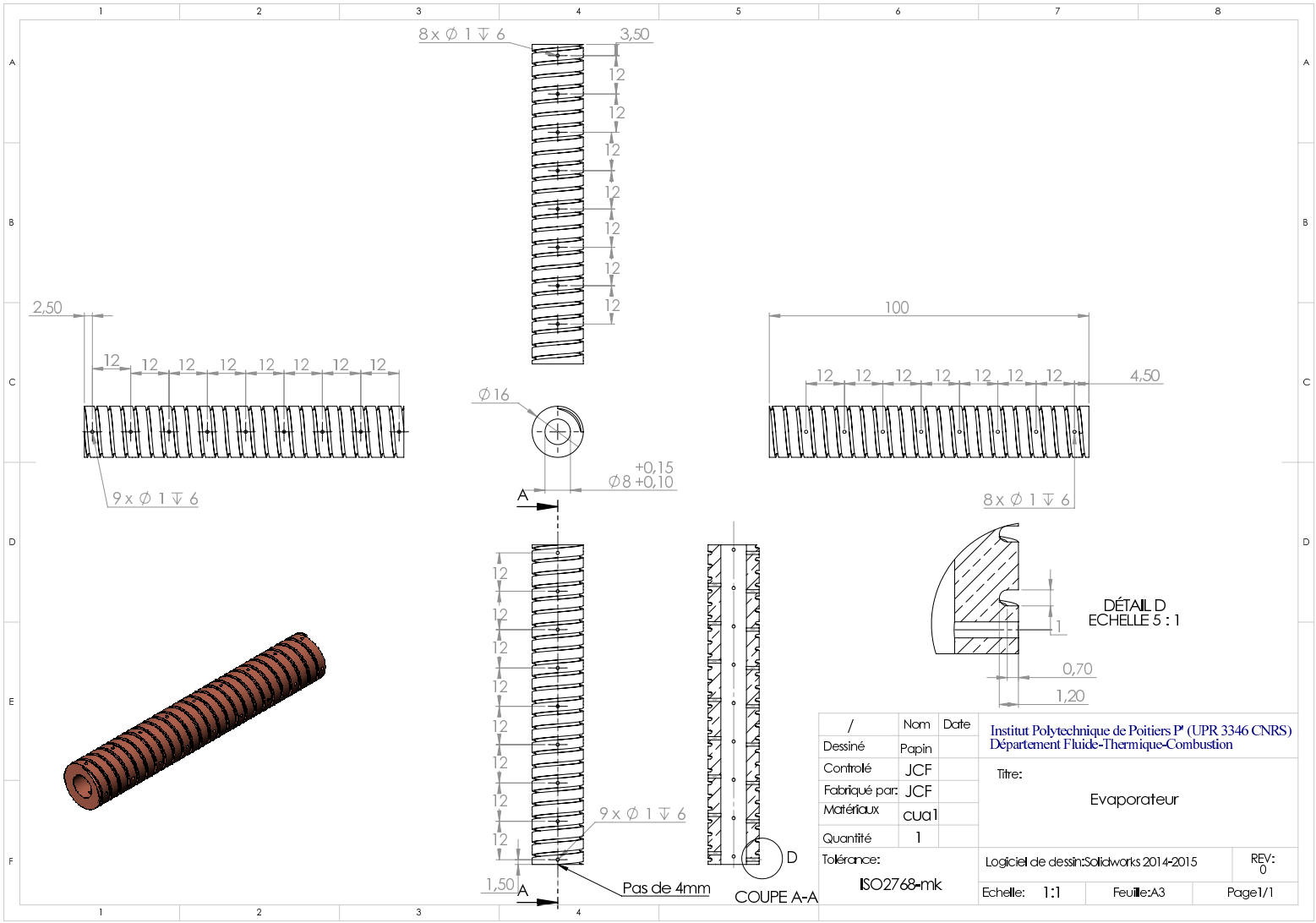

FIGURE D.1 – Evaporator design first version.

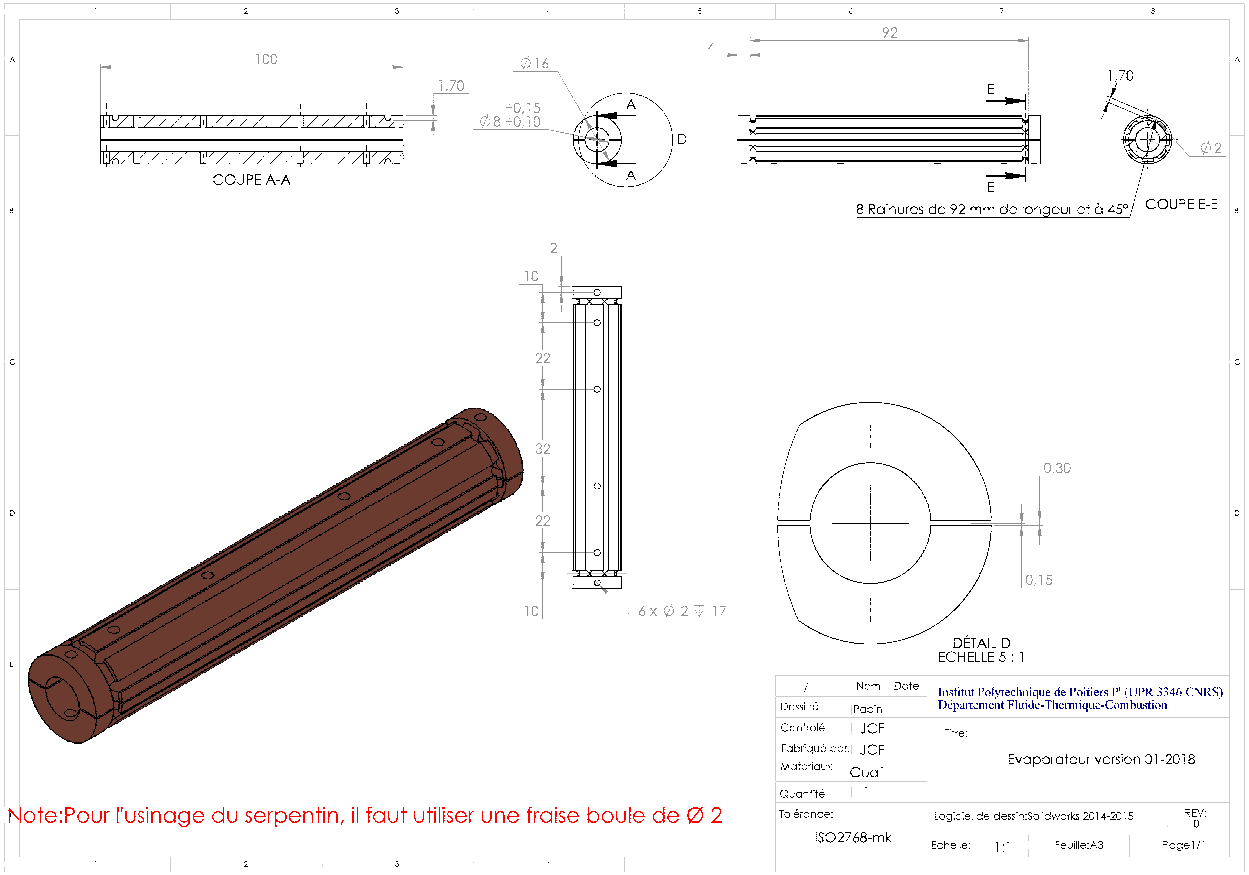

FIGURE D.2 – Evaporator design second version.

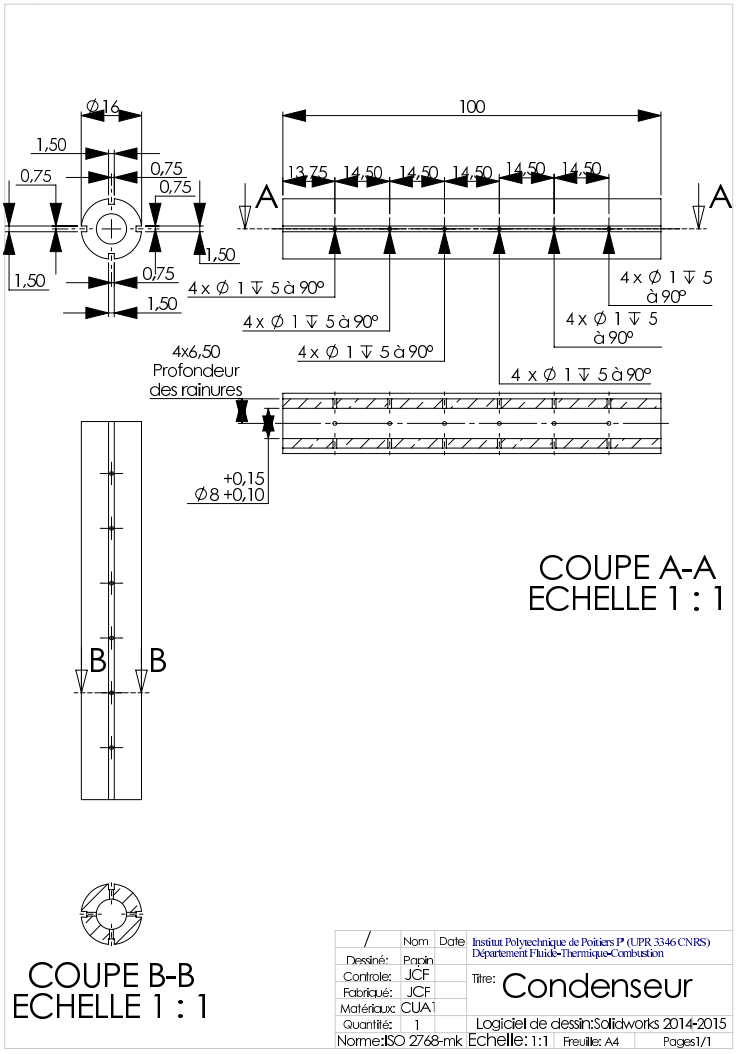

FIGURE D.3 – Condenser design first version.

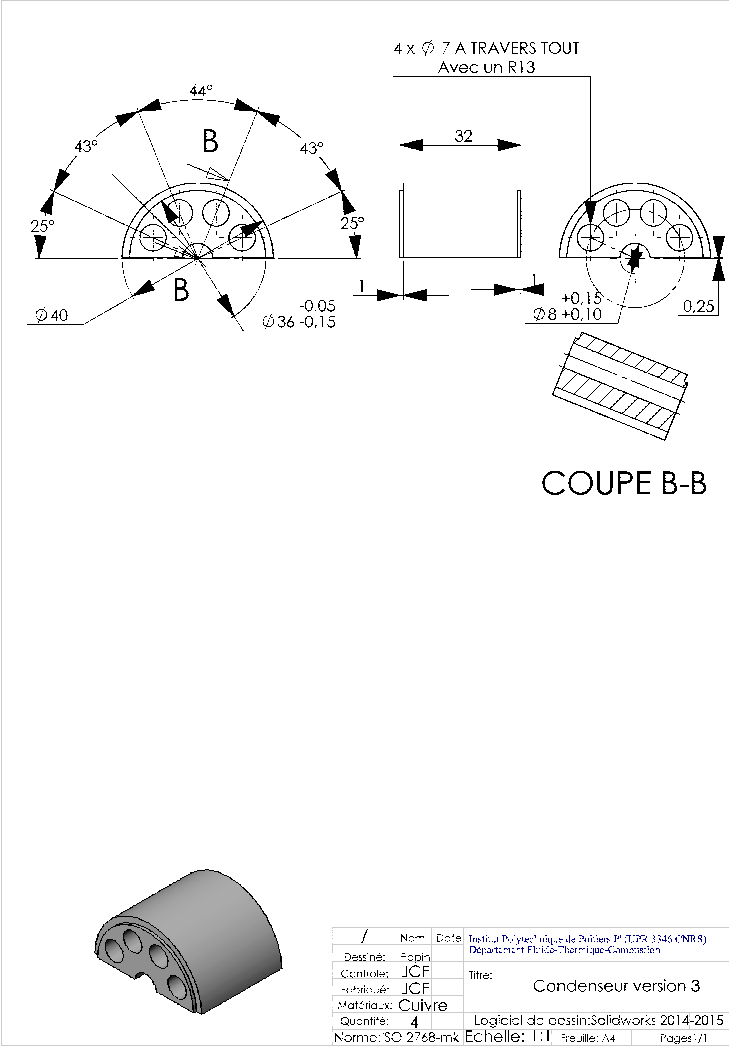

FIGURE D.4 – Condenser design first second version.

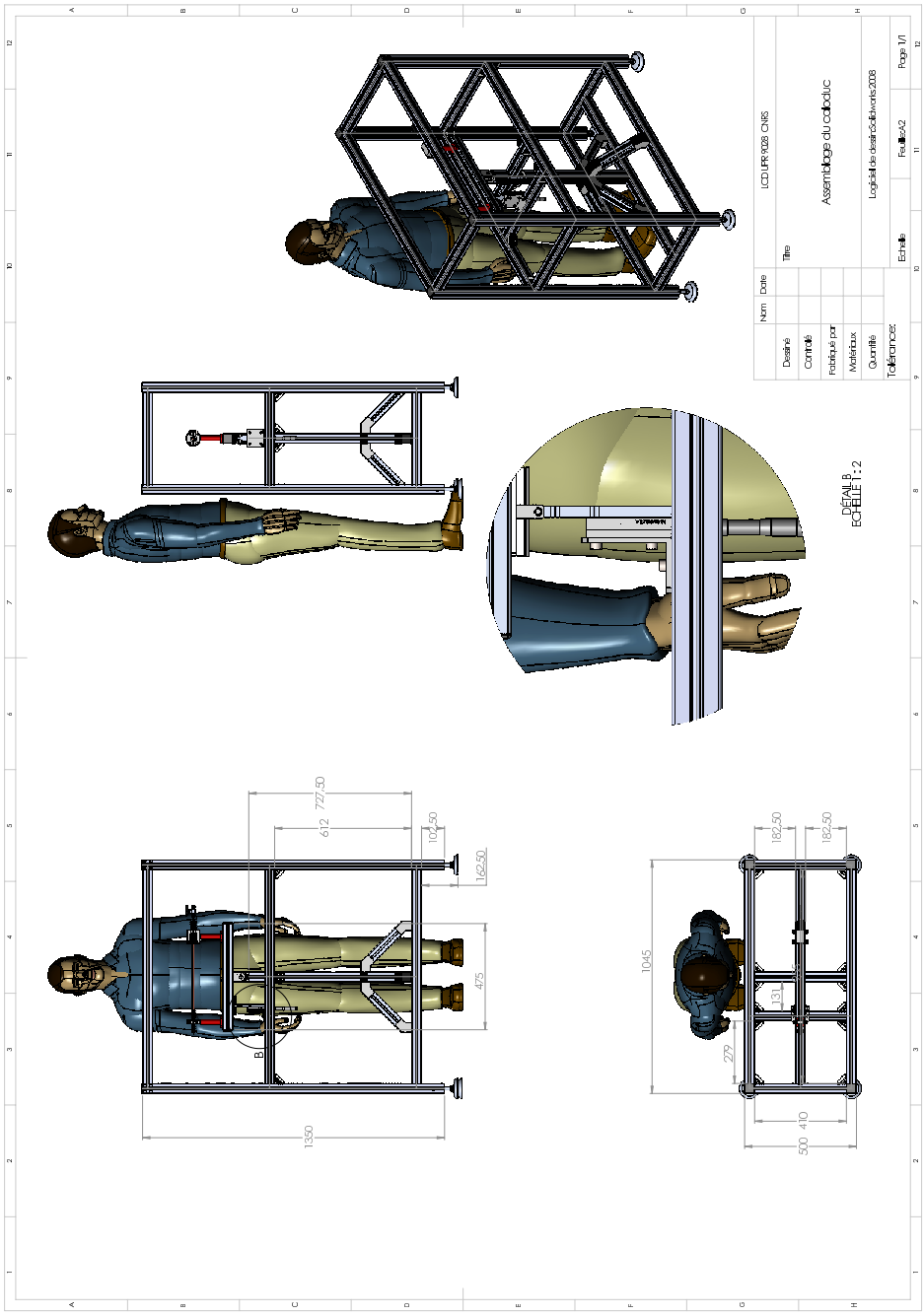

FIGURE D.5 – Bench test.

Appendix E

Uncertainty calculation

The purpose of this appendix is to present the method of calculating measurement uncertainties. Uncertainty calculations are based on the methods recommended by AFNOR. The main concepts to define the uncertainties according to international norms are introduced here.

The quantity y that is measured is called measurand. It is expressed with respect to terms of influence x_i through the function f.

$$y = f(x_1, x_2, x_3, ..., x_n) \tag{E.1}$$

E.1 Calculation of variance and standard uncertainties

E.1.1 Uncertainty type A

It characterizes the dispersion of the measurement results. It is evaluated by a statistical method based on the calculation of arithmetic means, variances and standard deviations. The n measures of the quantity q make it possible to calculate the arithmetic mean:

$$\bar{q} = \frac{1}{n} \sum_{k=1}^{n} q_k \tag{E.2}$$

The dispersion of measures q_k around the mean $\bar{q}$ is estimated by the experimental variance:

$$u^2(q) = \frac{1}{n-1} \sum_{k=1}^{n} (q_k - \bar{q})^2 \tag{E.3}$$

The variance of the mean $u^2(q)$ is expressed as a function of the experimental variance:

$$u^2(q) = \frac{u^2(q_k)}{n} \tag{E.4}$$

The type difference $u(\bar{q})$ is also called standard uncertainty. It corresponds to the square root of the variance.

E.1.2 Uncertainty type B

It is evaluated on the basis of information such as the manufacturer's specifications or the data provided by calibration certificates. The uncertainty is estimated from the data of the limits of the range to which the measured quantity q belongs. If the uncertainty calculation hypothesis is a uniform probability density law over an interval $2a$, centered on the measured value q, the variance of the quantity q is given by the formula:

$$u^2(q) = \frac{a^2}{3} \tag{E.5}$$

Where $u^2(q)$ is the variance of the measured quantity q and $u(q)$ is the standard deviation or uncertainty type of measured quantity q.

For a normal distribution law over the interval $2a$, the variance of the quantity measured q is:

$$u^2(q) = \frac{a^2}{9} \tag{E.6}$$

E.2 Expanded uncertainty

The interval corresponding to a given level of confidence p is called expanded uncertainty. It introduces the enlargement coefficient K_p such that:

$$U_p = K_p u(q) \tag{E.7}$$

with p the probability that: $\bar{q} - U_p \leq q \leq \bar{q} + U_p$

International standards recommend the use of an enlargement coefficient $K_p = 3$, corresponding to a 99% confidence level. This means that for a law of normal probability, an interval of three standard deviations corresponds to a 99% probability that a measure has a value between $q - 3u(q)$ and $q + 3u(q)$.

E.3 Compound uncertainties

The overall uncertainty of a measured quantity depends on the different uncertainties of all influential parameters. This global uncertainty is defined by the compound variance or composite standard uncertainty. The composite variance of the measured quantity can be expressed based on Taylor's first-order expansion of $f(x_1, x_2, x_3, ..., x_n)$

$$u_c^2(y) = \sum_{i=1}^{n} \sum_{j=1}^{n} \frac{\partial f}{\partial x_i} \frac{\partial f}{\partial x_j} u(x_i, x_j) \tag{E.8}$$

where $u(x_i, x_j)$ is the covariance between influential magnitudes x_i and x_j.

By taking into account $u(x_i, x_j) = u^2(x_i)$ and $u(x_i, x_j) = u(x_j, x_i)$, the compound uncertainties can be written as:

$$u_c^2(y) = \sum_{i=1}^{n} \left(\frac{\partial f}{\partial x_i} \right)^2 u^2(x_i) + 2 \sum_{i=1}^{n} \sum_{j=i+1}^{n} \frac{\partial f}{\partial x_i} \frac{\partial f}{\partial x_j} u(x_i, x_j) \tag{E.9}$$

If the parameter x_i is not correlated with the others, we have:

$$u(x_i, x_j) = 0 \tag{E.10}$$

Hence, the expression of the compound uncertainties can be simplified as:

$$u_c^2(y) = \sum_{i=1}^{n} \left(\frac{\partial f}{\partial x_i} \right)^2 u^2(x_i) \tag{E.11}$$

Appendix F

Comparison between the two technical implementations

The initial tests have been conducted using a heat pipe with its three regions: evaporator, adiabatic and condenser. In this case, see figure F.1, the evaporator and condenser length are equal to 100mm while the adiabatic region occupy 300mm of the heat pipe total length. First of all, we compared the two technical implementations (see figure F.1).

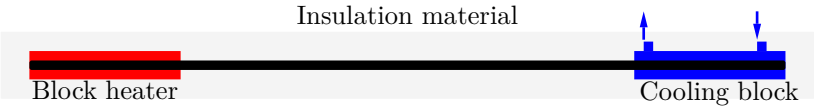

FIGURE F.1 – Schematic of the initial heat pipe experimental system.

Under the same working conditions, we calculated the thermal resistance as a reference parameters. As a result, we found a good prediction for both implementations with an error less than 2% as shown in table F.1 and F.2. This tests validate the reliability of the proposed flexible configuration in terms of accuracy and stability.

Working fluid	Water	Methanol
Filling ratio	100%	100%
Rth initial implementation	0.915	0.807
Rth new implementation	0.922	0.812

TABLE F.1 – Thermal resistance at 30°C under heat input of 5W for case A.

Working fluid	Water	Methanol
Filling ratio	100%	100%
Rth initial implementation	0.924	0.915
Rth new implementation	0.924	0.915

TABLE F.2 – Thermal resistance at 60°C under heat input of 5W for case A.

Bibliography

[1] MS Abd-Elhady, M Nasreldin, and MN Elsheikh. Improving the performance of evacuated tube heat pipe collectors using oil and foamed metals. *Ain Shams Engineering Journal*, 2017. (document), 1.10, 1.8.3, 1.11

[2] Takashi Abe. Derivation of the lattice boltzmann method by means of the discrete ordinate method for the boltzmann equation. *Journal of Computational Physics*, 131(1):241–246, 1997. 2.1, 2.3.3

[3] Mohamed Hany Abokersh, Mohamed El-Morsi, Osama Sharaf, and Wael Abdelrahman. An experimental evaluation of direct flow evacuated tube solar collector integrated with phase change material. *Energy*, 139:1111–1125, 2017. 1.8.3

[4] MA Alghoul, MY Sulaiman, BZ Azmi, and M Abd Wahab. Review of materials for solar thermal collectors. *Anti-Corrosion methods and materials*, 52(4):199–206, 2005. 1.8.1

[5] Mobin Arab and Ali Abbas. Model-based design and analysis of heat pipe working fluid for optimal performance in a concentric evacuated tube solar water heater. *Solar Energy*, 94:162–176, 2013. 1.8.2

[6] Lazarus Godson Asirvatham, Rajesh Nimmagadda, and Somchai Wongwises. Operational limitations of heat pipes with silver-water nanofluids. *Journal of Heat Transfer*, 135(11):111011, 2013. 1.7.2

[7] LM Ayompe and Aidan Duffy. Thermal performance analysis of a solar water heating system with heat pipe evacuated tube collector using data from a field trial. *Solar Energy*, 90:17–28, 2013. 1.8.3

[8] LM Ayompe, Aidan Duffy, M Mc Keever, M Conlon, and SJ McCormack. Comparative field performance study of flat plate and heat pipe evacuated tube collectors (etcs) for domestic water heating systems in a temperate climate. *Energy*, 36(5):3370–3378, 2011. 1.8.1, 1.8.2

[9] LM Ayompe, Aidan Duffy, SJ McCormack, and Michael Conlon. Validated trnsys model for forced circulation solar water heating systems with flat plate and heat pipe evacuated tube collectors. *Applied Thermal Engineering*, 31(8):1536–1542, 2011. 1.8.1, 1.8.2

[10] E Azad. Theoretical and experimental investigation of heat pipe solar collector. *Experimental Thermal and Fluid Science*, 32(8):1666–1672, 2008. 1.8.2

[11] E Azad. Performance analysis of wick-assisted heat pipe solar collector and comparison with experimental results. *Heat and mass transfer*, 45(5):645–649, 2009. 1.8.2

[12] E Azad. Assessment of three types of heat pipe solar collectors. *Renewable and Sustainable Energy Reviews*, 16(5):2833–2838, 2012. 1.8.1, 1.8.2

[13] E Azad. Experimental analysis of thermal performance of solar collectors with different numbers of heat pipes versus a flow-through solar collector. *Renewable and Sustainable Energy Reviews*, 82:4320–4325, 2018. 1.8.2

[14] Raj Kumar Bera, Subodh Gautam Mhaisalkar, Daniel Mandler, and Shlomo Magdassi. Formation and performance of highly absorbing solar thermal coating based on carbon nanotubes and boehmite. *Energy Conversion and Management*, 120:287–293, 2016. 1.8.3

[15] Prabhu Lal Bhatnagar, Eugene P Gross, and Max Krook. A model for collision processes in gases. i. small amplitude processes in charged and neutral one-component systems. *Physical review*, 94(3):511, 1954. 2.4.2

[16] Mita Bhattacharya, Sudharshan Reddy Paramati, Ilhan Ozturk, and Sankar Bhattacharya. The effect of renewable energy consumption on economic growth: Evidence from top 38 countries. *Applied Energy*, 162:733–741, 2016.

[17] M'hamed Bouzidi, Mouaouia Firdaouss, and Pierre Lallemand. Momentum transfer of a boltzmann-lattice fluid with boundaries. *Physics of Fluids (1994-present)*, 13(11):3452–3459, 2001.

[18] Carlos Braga, Jordan Muscatello, Gabriel Lau, Erich A Müller, and George Jackson. Nonequilibrium study of the intrinsic free-energy profile across a liquid-vapour interface. *The Journal of chemical physics*, 144(4):044703, 2016. 1.4.2

[19] Taoufik Brahim, Mohammed Houcine Dhaou, and Abdelmajid Jemni. Theoretical and experimental investigation of plate screen mesh heat pipe solar collector. *Energy conversion and management*, 87:428–438, 2014.

[20] Taoufik Brahim and Abdelmajid Jemni. Effect of the heat pipe adiabatic region. *Journal of heat transfer*, 136(4):042901, 2014. (document), 3.1.2, 4.1.5, 4.6, 4.1

[21] Nicolas Bruot and Frédéric Caupin. Curvature dependence of the liquid-vapor surface tension beyond the tolman approximation. *Physical review letters*, 116(5):056102, 2016. 1.4.2

[22] JM Buick and CA Greated. Gravity in a lattice boltzmann model. *Physical Review E*, 61(5):5307, 2000. 2.4.6, 2.4.6

[23] CA Busse. Theory of the ultimate heat transfer limit of cylindrical heat pipes. *International Journal of Heat and Mass Transfer*, 16(1):169–186, 1973. 1.7.3, 1.7.5

[24] Alfonso Caiazzo. *Asymptotic Analysis of lattice Boltzmann method for Fluid-Structure interaction problems*. PhD thesis, Scuola Normale Superiore PISA, 2007.

[25] Yunus A Cengel and Michael A Boles. Thermodynamics: an engineering approach. *Sea*, 1000:8862, 2002. 4.4.2

[26] Zhenhua Chai, Zhaoli Guo, and Baochang Shi. Lattice boltzmann simulation of mixed convection in a driven cavity packed with porous medium. In *International Conference on Computational Science*, pages 802–809. Springer, 2007. 3.1.1

[27] Zhenhua Chai and TS Zhao. Lattice boltzmann model for the convection-diffusion equation. *Physical Review E*, 87(6):063309, 2013. 3.2.2

[28] Miqdam T Chaichan and Hussein A Kazem. Water solar distiller pro-

ductivity enhancement using concentrating solar water heater and phase change material (pcm). *Case studies in thermal engineering*, 5:151–159, 2015. 1.8.3

[29] CW Chan, E Siqueiros, J Ling-Chin, M Royapoor, and AP Roskilly. Heat utilisation technologies: A critical review of heat pipes. *Renewable and Sustainable Energy Reviews*, 50:615–627, 2015.

[30] Sydney Chapman and Thomas George Cowling. *The mathematical theory of non-uniform gases: an account of the kinetic theory of viscosity, thermal conduction and diffusion in gases*. Cambridge university press, 1970. 2.3, 2.3.2

[31] Hassam Nasarullah Chaudhry, Ben Richard Hughes, and Saud Abdul Ghani. A review of heat pipe systems for heat recovery and renewable energy applications. *Renewable and Sustainable Energy Reviews*, 16(4):2249–2259, 2012. 1.5.1

[32] Hudong Chen, Steven A Orszag, and Ilya Staroselsky. Macroscopic description of arbitrary knudsen number flow using boltzmann–bgk kinetic theory. *Journal of Fluid Mechanics*, 574:495–505, 2007.

[33] Lin Chen and Xin-Rong Zhang. Experimental analysis on a novel solar collector system achieved by supercritical co 2 natural convection. *Energy Conversion and Management*, 77:173–182, 2014. 1.8.1

[34] S-W Chen, F-C Liu, T-Y Wang, W-K Lin, J-R Wang, H-T Lin, J-D Lee, J-J Peir, and C-K Shih. Modeling and analyses of boiling and capillary limitations for micro channel wick structures. *Journal of Mechanics*, 32(3):357–368, 2016. 1.7.2

[35] Sheng Chen, Jonas Tölke, Sebastian Geller, and Manfred Krafczyk. Lattice boltzmann model for incompressible axisymmetric flows. *Physical Review E*, 78(4):046703, 2008. 3.1.1

[36] Shiyi Chen and Gary D Doolen. Lattice boltzmann method for fluid flows. *Annual review of fluid mechanics*, 30(1):329–364, 1998.

[37] Shiyi Chen, Daniel Martinez, and Renwei Mei. On boundary conditions in lattice boltzmann methods. *Physics of fluids*, 8(9):2527–2536, 1996. 2.5.2

[38] Xi Chen and Peng Han. A note on the solution of conjugate heat transfer problems using simple-like algorithms. *International Journal of Heat and Fluid Flow*, 21(4):463–467, 2000. 4.1.4

[39] SW Chi. Heat pipe theory and practice. *Washington, DC, Hemisphere Publishing Corp.; New York, McGraw-Hill Book Co., 1976. 256 p.*, 1976.

[40] L-H Chien and Y-C Shih. An experimental study of mesh type flat heat pipes. *Journal of Mechanics*, 27(02):167–176, 2011.

[41] SS Chikatamarla, SKIV Ansumali, and IV Karlin. Grad's approximation for missing data in lattice boltzmann simulations. *EPL (Europhysics Letters)*, 74(2):215, 2006.

[42] B Chopard, JL Falcone, and J Latt. The lattice boltzmann advection-diffusion model revisited. *The European Physical Journal Special Topics*, 171(1):245–249, 2009. 3.2.2

[43] Tin-Tai Chow, Zhaoting Dong, Lok-Shun Chan, Kwong-Fai Fong, and Yu Bai. Performance evaluation of evacuated tube solar domestic hot water systems in hong kong.

Energy and Buildings, 43(12):3467–3474, 2011. 1.8.2

[44] Wongee Chun, Yong Heack Kang, Hee Youl Kwak, and Young Soo Lee. An experimental study of the utilization of heat pipes for solar water heaters. *Applied Thermal Engineering*, 19(8):807–817, 1999. 1.8.2

[45] Michel Cloitre and Roger T Bonnecaze. A review on wall slip in high solid dispersions. *Rheologica Acta*, 56(3):283–305, 2017. 1.4.2

[46] Carlos Colosqui, Hudong Chen, Xiaowen Shan, I Staroselsky, and Victor Yakhot. Propagating high-frequency shear waves in simple fluids. *Physics of Fluids*, 21(1):013105, 2009.

[47] Carlos E Colosqui. High-order hydrodynamics via lattice boltzmann methods. *Physical Review E*, 81(2):026702, 2010.

[48] TP Cotter. Theory of heat pipes. Technical report, DTIC Document, 1965. 1.1, 1.7

[49] TP Cotter. Principles and prospects for micro heat pipes. Technical report, Los Alamos National Lab., NM (USA), 1984.

[50] TP Cotter. Principles and prospects of micro heat pipes. In *Proceedings of the 5th International Heat Pipe Conference, Tsukuba, Japan*, volume 1, pages 328–335, 1984. 1.6.5

[51] Roonak Daghigh and Abdellah Shafieian. Theoretical and experimental analysis of thermal performance of a solar water heating system with evacuated tube heat pipe collector. *Applied Thermal Engineering*, 103:1219–1227, 2016. 1.8.2

[52] Orla Dardis and John McCloskey. Lattice boltzmann scheme with real numbered solid density for the simulation of flow in porous media. *Physical Review E*, 57(4):4834, 1998. 3.1.1

[53] Daxiang Deng, Dejie Liang, Yong Tang, Jiemin Peng, Xiaodong Han, and Minqiang Pan. Evaluation of capillary performance of sintered porous wicks for loop heat pipe. *Experimental Thermal and Fluid Science*, 50:1–9, 2013. 1.3.3

[54] Kyu Hyung Do, Hyo Jun Ha, and Seok Pil Jang. Thermal resistance of screen mesh wick heat pipes using the water-based al2o3 nanofluids. *International Journal of Heat and Mass Transfer*, 53(25):5888–5894, 2010. 1.3.2

[55] Eyup Dogan and Fahri Seker. Determinants of co2 emissions in the european union: The role of renewable and non-renewable energy. *Renewable Energy*, 94:429–439, 2016.

[56] Eyup Dogan, Fahri Seker, and Serap Bulbul. Investigating the impacts of energy consumption, real gdp, tourism and trade on co2 emissions by accounting for cross-sectional dependence: A panel study of oecd countries. *Current Issues in Tourism*, 20(16):1701–1719, 2017.

[57] Bin Du, Eric Hu, and Mohan Kolhe. An experimental platform for heat pipe solar collector testing. *Renewable and Sustainable Energy Reviews*, 17:119–125, 2013.

[58] Peter Dunn and David Reay. *Heat pipes*. Elsevier, 2016.

[59] Mostafa A Abd El-Baky and Mousa M Mohamed. Heat pipe heat exchanger for heat recovery in air conditioning. *Applied Thermal Engineering*, 27(4):795–801, 2007. 1.5.1

[60] MS Elmosbahi, AW Dahmouni, C Kerkeni, AA Guizani, and S Ben Nasrallah. An experimental investigation on the gravity assisted solar heat pipe under the climatic conditions of tunisia. *Energy Conversion and Management*, 64:594–605, 2012. 1.8.2

[61] Sabri Ergun. Fluid flow through packed columns. *Chem. Eng. Prog.*, 48:89–94, 1952. 3.1.2

[62] Mustafa Ali Ersöz. Effects of different working fluid use on the energy and exergy performance for evacuated tube solar collector with thermosyphon heat pipe. *Renewable Energy*, 96:244–256, 2016. 1.8.2

[63] Mehmet Esen and Hikmet Esen. Experimental investigation of a two-phase closed thermosyphon solar water heater. *Solar Energy*, 79(5):459–468, 2005. 1.8.2

[64] Amir Faghri. *Heat pipe science and technology*. Global Digital Press, 1995. 4.1.4

[65] Amir Faghri. Review and advances in heat pipe science and technology. *Journal of Heat Transfer*, 134(12):123001, 2012.

[66] Amir Faghri and S Thomas. Performance characteristics of a concentric annular heat pipe: Part i- experimental prediction and analysis of the capillary limit. *Journal of heat transfer*, 111(4):844–850, 1989. 1.7.2, 1.7.6

[67] O Filippova and D Hänel. Boundary-fitting and local grid refinement for lattice-bgk models. *International Journal of Modern Physics C*, 9(08):1271–1279, 1998.

[68] Olga Filippova and Dieter Hänel. Grid refinement for lattice-bgk models. *Journal of computational Physics*, 147(1):219–228, 1998.

[69] GL Fleischman and BD Marcus. Steady state and transient performance of hot reservoir gas controlled heat pipes. Technical report, TRW Systems Group, Redondo Beach, Calif.(USA), 1970. 1.1

[70] Uriel Frisch, Dominique d'Humiéres, Brosl Hasslacher, Pierre Lallemand, Yves Pomeau, Jean-Pierre Rivet, et al. Lattice gas hydrodynamics in two and three dimensions. *Complex systems*, 1(4):649–707, 1987.

[71] Uriel Frisch, Brosl Hasslacher, and Yves Pomeau. Lattice-gas automata for the navier-stokes equation. *Physical review letters*, 56(14):1505, 1986. 2.1, 2.6.1

[72] Pei Gang, Li Guiqiang, Zhou Xi, Ji Jie, and Su Yuehong. Experimental study and exergetic analysis of a cpc-type solar water heater system using higher-temperature circulation in winter. *Solar Energy*, 86(5):1280–1286, 2012. 1.8.1

[73] Dongyan Gao, Zhenqian Chen, and Linghai Chen. A thermal lattice boltzmann model for natural convection in porous media under local thermal non-equilibrium conditions. *International Journal of Heat and Mass Transfer*, 70:979–989, 2014. 3.1.1

[74] RS Gaugler. Heat transfer device, us patent no. 2350348, applied december 21, 1942. *Published June*, 6, 1994. 1.1

[75] Javad Ghaderian, Nor Azwadi Che Sidik, Alibakhsh Kasaeian, Sepideh Ghaderian, Amir Okhovat, Amirabbas Pakzadeh, Syahrullail Samion, and Wira Jazair Yahya. Performance of copper oxide/distilled water nanofluid in evacuated tube solar collector (etsc) water heater with internal coil under thermosyphon system circula-

tions. *Applied Thermal Engineering*, 121:520–536, 2017.

[76] Morteza Ghanbarpourgeravi. *Investigation of Thermal Performance of Cylindrical Heatpipes Operated with Nanofluids*. PhD thesis, KTH Royal Institute of Technology, 2017. 1.7.4

[77] Nikhilesh Ghanta and Arvind Pattamatta. A numerical and optimization study of compressible phase-change heat transfer in a part-unit-cell model of a pulsating heat pipe (php). In *ASME 2016 International Mechanical Engineering Congress and Exposition*, pages V008T10A046–V008T10A046. American Society of Mechanical Engineers, 2016. 5.7.1

[78] Irina Ginzburg and Dominique d'Humiéres. Multireflection boundary conditions for lattice boltzmann models. *Physical Review E*, 68(6):066614, 2003.

[79] Mounir Gourdache. *Etude du fonctionnement d'un caloduc soumis á des forces externes*. PhD thesis, Poitiers, 1994. 1.7.2

[80] Harold Grad. Note on n-dimensional hermite polynomials. *Communications on Pure and Applied Mathematics*, 2(4):325–330, 1949. 2.3, 2.3.1

[81] Harold Grad. On the kinetic theory of rarefied gases. *Communications on pure and applied mathematics*, 2(4):331–407, 1949. 2.3, 2.3.1, 2.3.3

[82] Harold Grad. Statistical mechanics, thermodynamics, and fluid dynamics of systems with an arbitrary number of integrals. *Communications on Pure and Applied Mathematics*, 5(4):455–494, 1952.

[83] Harold Grad. On boltzmann's h-theorem. *Journal of the Society for Industrial and Applied Mathematics*, 13(1):259–277, 1965. 2.4.4

[84] Kods Grissa, Raoudha Chaabane, Zied Lataoui, Adel Benselama, Yves Bertin, and Abdelmajid Jemni. Lattice boltzmann model for incompressible axisymmetric thermal flows through porous media. *Physical Review E*, 94(4):043306, 2016. 3.2.1, 3.6.1

[85] George M Grover. Evaporation-condensation heat transfer device, January 18 1966. US Patent 3,229,759. 1.1

[86] GM Grover, JE Km, and ES Keddy. Advances in heat pipe technology. In *Second International Conference on Thermionic Electrical Power Generation*, pages 477–490, 1968. 1.1

[87] Simon Gruener, Dirk Wallacher, Stefanie Greulich, Mark Busch, and Patrick Huber. Hydraulic transport across hydrophilic and hydrophobic nanopores: Flow experiments with water and n-hexane. *Physical Review E*, 93(1):013102, 2016.

[88] Xiao Guangming, Du Yanxia, Gui Yewei, Liu Lei, Yang Xiaofeng, and Wei Dong. Heat transfer characteristics and limitations analysis of heat-pipe-cooled thermal protection structure. *Applied Thermal Engineering*, 70(1):655–664, 2014. 1.7.2

[89] Zhaoli Guo, Haifeng Han, Baochang Shi, and Chuguang Zheng. Theory of the lattice boltzmann equation: lattice boltzmann model for axisymmetric flows. *Physical Review E*, 79(4):046708, 2009. 3.1.1, 3.3

[90] Zhaoli Guo, Baochang Shi, and Nengchao Wang. Lattice bgk model for incompressible navier–stokes equation. *Journal of Computational Physics*, 165(1):288–306, 2000. 3.6.1

[91] Zhaoli Guo and TS Zhao. A lattice boltzmann model for convection heat transfer in porous media. *Numerical Heat Transfer, Part B*, 47(2):157–177, 2005. 3.1.1, 3.1.2, 3.2.1, 3.2.2

[92] Zhaoli Guo, Chuguang Zheng, and Baochang Shi. Discrete lattice effects on the forcing term in the lattice boltzmann method. *Physical Review E*, 65(4):046308, 2002. 2.4.6, 3.1.1, 3.2, 3.2.1, 3.4.1, 3.6.3, 6.1

[93] Zhaoli Guo, Chuguang Zheng, and Baochang Shi. An extrapolation method for boundary conditions in lattice boltzmann method. *Physics of Fluids (1994-present)*, 14(6):2007–2010, 2002.

[94] I Halliday, LA Hammond, CM Care, K Good, and A Stevens. Lattice boltzmann equation hydrodynamics. *Physical review E*, 64(1):011208, 2001. 3.1.1, 3.2, 6.1

[95] Stewart Harris. *An introduction to the theory of the Boltzmann equation*. Courier Corporation, 2004. 2.4.2

[96] Michel Hayek, Johnny Assaf, and William Lteif. Experimental investigation of the performance of evacuated-tube solar collectors under eastern mediterranean climatic conditions. *Energy Procedia*, 6:618–626, 2011. 1.8.2

[97] Majdi Hazami, Nabiha Naili, Issam Attar, and Abdelhamid Farhat. Solar water heating systems feasibility for domestic requests in tunisia: thermal potential and economic analysis. *Energy conversion and management*, 76:599–608, 2013. 1.8.2

[98] Xiaoyi He and Li-Shi Luo. Lattice boltzmann model for the incompressible navier–stokes equation. *Journal of statistical Physics*, 88(3):927–944, 1997. 2.4.5, 3.6.1

[99] Xiaoyi He and Li-Shi Luo. A priori derivation of the lattice boltzmann equation. *Physical Review E*, 55(6):R6333, 1997.

[100] Xiaoyi He and Li-Shi Luo. Theory of the lattice boltzmann method: From the boltzmann equation to the lattice boltzmann equation. *Physical Review E*, 56(6):6811, 1997. 2.1, 2.3.3

[101] Hassan Heidari, Salih Turan Katircioğlu, and Lesyan Saeidpour. Economic growth, co2 emissions, and energy consumption in the five asean countries. *International Journal of Electrical Power & Energy Systems*, 64:785–791, 2015.

[102] Daniel Heubes. Lattice boltzmann method in theory and in application to coupled problems. 2010. 2.4.4

[103] Dave Higdon, Jim Gattiker, Earl Lawrence, Charles Jackson, Michael Tobis, Matt Pratola, Salman Habib, Katrin Heitmann, and Steve Price. Computer model calibration using the ensemble kalman filter. *Technometrics*, 55(4):488–500, 2013. 5.7.1

[104] FJ Higuera and J Jimenez. Boltzmann approach to lattice gas simulations. *EPL (Europhysics Letters)*, 9(7):663, 1989.

[105] Hoyte Hottel and Austin Whillier. Evaluation of flat-plate solar collector performance. In *Trans. Conf. Use of Solar Energy;()*, volume 3, 1955. 4.4.2

[106] Yang Hu, Decai Li, Shi Shu, and Xiaodong Niu. Finite-volume method with lattice boltzmann flux scheme for incompressible porous media flow at the representative-elementary-volume scale. *Physical Review E*, 93(2):023308, 2016.

[107] Haibo Huang, TS Lee, and C Shu. Hybrid lattice boltzmann finite-

difference simulation of axisymmetric swirling and rotating flows. *International journal for numerical methods in fluids*, 53(11):1707–1726, 2007. 3.1.1

[108] Lianmin Huang and Mohamed S El-Genk. Experimental investigation of transient operation of a water heat pipe. In *AIP Conference Proceedings*, volume 271, pages 365–374. AIP, 1993.

[109] Xiao Huang and George Franchi. Design and fabrication of hybrid bimodal wick structure for heat pipe application. *Journal of Porous Materials*, 15(6):635–642, 2008.

[110] Yonghua Huang and Qiang Chen. A numerical model for transient simulation of porous wicked heat pipes by lattice boltzmann method. *International Journal of Heat and Mass Transfer*, 105:270–278, 2017. 1.4.1

[111] Ahmed Kadhim Hussein, Dong Li, Lioua Kolsi, Sanatana Kata, and Brundaban Sahoo. A review of nano fluid role to improve the performance of the heat pipe solar collectors. *Energy Procedia*, 109:417–424, 2017. 1.8.3

[112] HMS Hussein. Transient investigation of a two phase closed thermosyphon flat plate solar water heater. *Energy Conversion and Management*, 43(18):2479–2492, 2002. 1.8.2

[113] HMS Hussein. Optimization of a natural circulation two phase closed thermosyphon flat plate solar water heater. *Energy Conversion and Management*, 44(14):2341–2352, 2003. 1.8.2

[114] HMS Hussein. Theoretical and experimental investigation of wickless heat pipes flat plate solar collector with cross flow heat exchanger. *Energy Conversion and Management*, 48(4):1266–1272, 2007. 1.8.2

[115] HMS Hussein, HH El-Ghetany, and SA Nada. Performance of wickless heat pipe flat plate solar collectors having different pipes cross sections geometries and filling ratios. *Energy conversion and management*, 47(11):1539–1549, 2006. 1.8.2

[116] GS Hwang, M Kaviany, WG Anderson, and J Zuo. Modulated wick heat pipe. *International Journal of Heat and Mass Transfer*, 50(7):1420–1434, 2007.

[117] Roula Inglesi-Lotz. The impact of renewable energy consumption to economic growth: A panel data application. *Energy Economics*, 53:58–63, 2016.

[118] Soudeh Iranmanesh, Ong Hwai Chyuan, Bee Chin Ang, Emad Sadeghinezhad, Alireza Esmaeilzadeh, and Mohammad Mehrali. Thermal performance enhancement of an evacuated tube solar collector using graphene nanoplatelets nanofluid. *Journal of Cleaner Production*, 2017. 1.8.3

[119] M Raisul Islam, K Sumathy, and Samee Ullah Khan. Solar water heating systems and their market trends. *Renewable and Sustainable Energy Reviews*, 17:1–25, 2013.

[120] Davoud Jafari, Hamidereza Shamsi, Sauro Filippeschi, Paolo Di Marco, and Alessandro Franco. An experimental investigation and optimization of screen mesh heat pipes for low-mid temperature applications. *Experimental Thermal and Fluid Science*, 84:120–133, 2017.

[121] Farzad Jafarkazemi and Hossein Abdi. Evacuated tube solar heat pipe

collector model and associated tests. *Journal of Renewable and Sustainable Energy*, 4(2):023101, 2012. 1.8.2

[122] Farzad Jafarkazemi, Emad Ahmadifard, and Hossein Abdi. Energy and exergy efficiency of heat pipe evacuated tube solar collectors. *Thermal Science*, 20(1):327–335, 2016. 1.8.2

[123] A Jahanbakhsh, HR Haghgou, and S Alizadeh. Experimental analysis of a heat pipe operated solar collector using water–ethanol solution as the working fluid. *Solar Energy*, 118:267–275, 2015. 1.8.2

[124] S Jaisankar, J Ananth, S Thulasi, ST Jayasuthakar, and KN Sheeba. A comprehensive review on solar water heaters. *Renewable and Sustainable Energy Reviews*, 15(6):3045–3050, 2011. 1.8.1

[125] Chunyu Jin, Paul A Langston, Galina E Pavlovskaya, Mattew R Hall, and Sean P Rigby. Statistics of highly heterogeneous flow fields confined to three-dimensional random porous media. *Physical Review E*, 93(1):013122, 2016.

[126] Khalid A Joudi and AM Witwit. Improvements of gravity assisted wickless heat pipes. *Energy conversion and management*, 41(18):2041–2061, 2000. 1.8.2

[127] JF Judge. Rca test thermal energy pipe. *Missile Rockets*, 18:36–38, 1966. 1.1

[128] Jan Julin, Paul M Winkler, Neil M Donahue, Paul E Wagner, and Ilona Riipinen. Near-unity mass accommodation coefficient of organic molecules of varying structure. *Environmental science & technology*, 48(20):12083–12089, 2014. 4.1.4

[129] Li Junfeng and Hu Runqing. Solar thermal in china: Overview and perspectives of the chinese solar thermal market. *Refocus*, 6(5):25–27, 2005. 1.8.2

[130] Michael Junk and Zhaoxia Yang. One-point boundary condition for the lattice boltzmann method. *Physical Review E*, 72(6):066701, 2005.

[131] Soteris A Kalogirou. Solar thermal collectors and applications. *Progress in energy and combustion science*, 30(3):231–295, 2004. 1.8.1

[132] Soteris A Kalogirou. *Solar energy engineering: processes and systems*. Academic Press, 2013. 1.8.1, 1.8.2

[133] Qinjun Kang, Peter C Lichtner, and Dongxiao Zhang. An improved lattice boltzmann model for multicomponent reactive transport in porous media at the pore scale. *Water Resources Research*, 43(12), 2007. 3.1.1

[134] Qinjun Kang, Dongxiao Zhang, and Shiyi Chen. Unified lattice boltzmann method for flow in multiscale porous media. *Physical Review E*, 66(5):056307, 2002. 3.1.1

[135] Nadarajah Kannan and Divagar Vakeesan. Solar energy for future world:-a review. *Renewable and Sustainable Energy Reviews*, 62:1092–1105, 2016. 1.8.2

[136] H Kargarsharifabad, S Jahangiri Mamouri, MB Shafii, and M Taeibi Rahni. Experimental investigation of the effect of using closed-loop pulsating heat pipe on the performance of a flat plate solar collector. *Journal of Renewable and Sustainable Energy*, 5(1):013106, 2013.

[137] Adnan Kasman and Yavuz Selman Duman. Co2 emissions, economic growth, energy consumption, trade

and urbanization in new eu member and candidate countries: a panel data analysis. *Economic Modelling*, 44:97–103, 2015.

[138] R Kempers, D Ewing, and CY Ching. Effect of number of mesh layers and fluid loading on the performance of screen mesh wicked heat pipes. *Applied thermal engineering*, 26(5):589–595, 2006.

[139] Cheryl E Kennedy. Review of mid-to high-temperature solar selective absorber materials. Technical report, National Renewable Energy Lab., Golden, CO.(US), 2002. 1.8.3

[140] Q Ye Kenny, William Li, and Agus Sudjianto. Algorithmic construction of optimal symmetric latin hypercube designs. *Journal of statistical planning and inference*, 90(1):145–159, 2000. 5.7.1

[141] M Khalili and MB Shafii. Experimental and numerical investigation of the thermal performance of a novel sintered-wick heat pipe. *Applied Thermal Engineering*, 94:59–75, 2016.

[142] Hyung Dae Kim, Jeongbae Kim, and Moo Hwan Kim. Experimental studies on chf characteristics of nanofluids at pool boiling. *International journal of multiphase flow*, 33(7):691–706, 2007. 1.3.2

[143] Kyung Mo Kim and In Cheol Bang. Effects of graphene oxide nanofluids on heat pipe performance and capillary limits. *International Journal of Thermal Sciences*, 100:346–356, 2016. 1.7.2

[144] Kyung Mo Kim and In Cheol Bang. Heat transfer characteristics and operation limit of pressurized hybrid heat pipe for small modular reactors. *Applied Thermal Engineering*, 112:560–571, 2017. 1.7.6

[145] N Kladias and V Prasad. Experimental verification of darcy-brinkman-forchheimer flow model for natural convection in porous media. *Journal of thermophysics and heat transfer*, 5(4):560–576, 1991. 3.5.2

[146] PME Koffi, HY Andoh, P Gbaha, S Toure, and G Ado. Theoretical and experimental study of solar water heater with internal exchanger using thermosiphon system. *Energy Conversion and Management*, 49(8):2279–2290, 2008. 1.8.2

[147] Amine Kouta, Fahad A Al-Sulaiman, and Maimoon Atif. Energy analysis of a solar driven cogeneration system using supercritical co2 power cycle and mee-tvc desalination system. *Energy*, 119:996–1009, 2017. 1.8.1

[148] S Siva Kumar, K Mohan Kumar, and SR Sanjeev Kumar. Design of evacuated tube solar collector with heat pipe. *Materials Today: Proceedings*, 4(14):12641–12646, 2017. 1.8.2

[149] Pierre Lallemand and Li-Shi Luo. Lattice boltzmann method for moving boundaries. *Journal of Computational Physics*, 184(2):406–421, 2003.

[150] Jonas Latt. *Hydrodynamic limit of lattice Boltzmann equations*. PhD thesis, University of Geneva, 2007. 2.3.2, 2.6.1, 2.8.2

[151] TS Lee, Haibo Huang, and C Shu. An axisymmetric incompressible lattice boltzmann model for pipe flow. *International Journal of Modern Physics C*, 17(05):645–661, 2006. 3.1, 3.1.1, 3.6.1

[152] MINISTÈRE DE L'ENVIRONNEMENT. Chiffres clés de l'énergie: édition 2016, 2017. (document), 1, 2, 3, 4, 5

[153] Chen Li, GP Peterson, and Yaxiong Wang. Evaporation/boiling in thin capillary wicks wick thickness effects. *Journal of Heat Transfer*, 128(12):1312–1319, 2006. 4.3.3

[154] Guiqiang Li, Jie Ji, Gan Zhang, Wei He, Xiao Chen, and Hongbing Chen. Performance analysis on a novel micro-channel heat pipe evacuated tube solar collector-incorporated thermoelectric generation. *International Journal of Energy Research*, 40(15):2117–2127, 2016. 1.8.2, 1.8.3, 4.4.1

[155] Q Li, YL He, GH Tang, and WQ Tao. Lattice boltzmann model for axisymmetric thermal flows. *Physical Review E*, 80(3):037702, 2009. 3.1.1

[156] Tianyu Li, Zongchang Zhao, Xiaodong Zhang, and Xican Sun. Molecular dynamics studies on liquid/vapor interface properties and structures of 1-ethyl-3-methylimidazolium dimethylphosphate-water. *The Journal of Physical Chemistry B*, 121(14):3087–3098, 2017. 1.4.2

[157] Yong Li, Heng-fei He, and Zhi-xin Zeng. Evaporation and condensation heat transfer in a heat pipe with a sintered-grooved composite wick. *Applied Thermal Engineering*, 50(1):342–351, 2013.

[158] Ruobing Liang, Liangdong Ma, Jili Zhang, and Dan Zhao. Theoretical and experimental investigation of the filled-type evacuated tube solar collector with u tube. *Solar Energy*, 85(9):1735–1744, 2011. 1.8.3

[159] Jean-Michel Tournier Lianmin Huang, Mohamed S El-Genk. Transient performance of an inclined water heat pipe with a screen wick. *ASME National Heat Transfer Conference*, 236(5):87, 1993. (document), 4.1.5, 4.7

[160] Boqiang Lin and Mohamed Moubarak. Renewable energy consumption–economic growth nexus for china. *Renewable and Sustainable Energy Reviews*, 40:111–117, 2014.

[161] Zhifang Lin, Haiping Fang, and Ruibao Tao. Improved lattice boltzmann model for incompressible two-dimensional steady flows. *Physical Review E*, 54(6):6323, 1996.

[162] Zhen-Hua Liu and Yuan-Yang Li. A new frontier of nanofluid research–application of nanofluids in heat pipes. *International Journal of Heat and Mass Transfer*, 55(23):6786–6797, 2012.

[163] CK Loh, Enisa Harris, and DJ Chou. Comparative study of heat pipes performances in different orientations. In *Semiconductor Thermal Measurement and Management Symposium, 2005 IEEE Twenty First Annual IEEE*, pages 191–195. IEEE, 2005.

[164] Lin Lu, Zhen-Hua Liu, and Hong-Sheng Xiao. Thermal performance of an open thermosyphon using nanofluids for high-temperature evacuated tubular solar collectors: Part 1: Indoor experiment. *Solar energy*, 85(2):379–387, 2011. 1.8.3

[165] Li-Shi Luo. Lattice-gas automata and lattice boltzmann equations for two-dimensional hydrodynamics. 1993. 2.4.6

[166] IM Mahbubul, Mohammed Mumtaz A Khan, Nasiru I Ibrahim, Hafiz Muhammad Ali, Fahad A Al-Sulaiman, and R Saidur. Carbon nanotube nanofluid in enhancing the efficiency of evacuated tube solar collector. *Renewable Energy*, 2018. 1.8.3

[167] Yu F Maidanik, Yu G Fershtater, and KA Goncharov. Capillary-pump loop for the systems of thermal regulation of spacecraft. In *In ESA, 4th European Symposium on Space Environmental Control Systems, Volume 1 p 87-92 (SEE N92-25828 16-18)*, 1991. 1.6.3, 1.6.4

[168] Robert S Maier, DM Kroll, YE Kutsovsky, HT Davis, and Robert S Bernard. Simulation of flow through bead packs using the lattice boltzmann method. *Physics of Fluids*, 10(1):60–74, 1998. 2.6.1

[169] Sina Jahangiri Mamouri and André Bénard. New design approach and implementation of solar water heaters: A case study in michigan. *Solar Energy*, 162:165–177, 2018. 1.8.4

[170] Daniele Mangini, Mauro Mameli, Anastasios Georgoulas, Luciano Araneo, Sauro Filippeschi, and Marco Marengo. A pulsating heat pipe for space applications: ground and microgravity experiments. *International Journal of Thermal Sciences*, 95:53–63, 2015. 1.5.2

[171] R Marek and J Straub. Analysis of the evaporation coefficient and the condensation coefficient of water. *International Journal of Heat and Mass Transfer*, 44(1):39–53, 2001. 4.1.4

[172] Danial O Martinez, William H Matthaeus, Shiyi Chen, and DC Montgomery. Comparison of spectral method and lattice boltzmann simulations of two-dimensional hydrodynamics. *Physics of Fluids*, 6(3):1285–1298, 1994.

[173] Francisco Javier Rey Martinez, Mario Antonio Álvarez-Guerra Plasencia, Eloy Velasco Gómez, Fernando Varela Diez, and Ruth Herrero Martin. Design and experimental study of a mixed energy recovery system, heat pipes and indirect evaporative equipment for air conditioning. *Energy and Buildings*, 35(10):1021–1030, 2003. 1.5.1

[174] Patricia M Martinez, Vladimir A Pozdin, Alexios Papadimitratos, William Holmes, Fatemeh Hassanipour, and Anvar A Zakhidov. Dual use of carbon nanotube selective coatings in evacuated tube solar collectors. *Carbon*, 119:133–141, 2017. 1.8.3

[175] Ph Marty. Transferts thermiques convectifs. *Cours IUP GSI, INPG*, 2001. 5.9

[176] Emmanouil Mathioulakis and Vassilis Belessiotis. A new heat-pipe type solar domestic hot water system. *Solar Energy*, 72(1):13–20, 2002.

[177] Keijo Mattila, Jari Hyväluoma, Jussi Timonen, and Tuomo Rossi. Comparison of implementations of the lattice-boltzmann method. *Computers & Mathematics with Applications*, 55(7):1514–1524, 2008. 2.7.2

[178] Michael D McKay, Richard J Beckman, and William J Conover. Comparison of three methods for selecting values of input variables in the analysis of output from a computer code. *Technometrics*, 21(2):239–245, 1979. 5.7.1

[179] Renwei Mei, Li-Shi Luo, Pierre Lallemand, and Dominique d'Humiéres. Consistent initial conditions for lattice boltzmann simulations. *Computers & Fluids*, 35(8):855–862, 2006. 2.5.1

[180] Renwei Mei, Li-Shi Luo, and Wei Shyy. An accurate curved boundary treatment in the lattice boltzmann method. *Journal of computational physics*, 155(2):307–330, 1999.

[181] A Meyer and RTRT Dobson. A heat pipe heat recovery heat exchanger for a mini-drier. *Journal of Energy in Southern Africa*, 17(1):50–57, 2017. 1.5.1

[182] Siamak Mirmasoumi and Mohammad Pourgol-Mohammad. A review on experimental and numerical investigations on using nanofluid in volumetric solar energy collectors. In *ASME 2014 International Mechanical Engineering Congress and Exposition*, pages V08BT10A048–V08BT10A048. American Society of Mechanical Engineers, 2014. 1.8.2

[183] Masataka Mochizuki, Thang Nguyen, Koichi Mashiko, Yuji Saito, Tien Nguyen, and Vijit Wuttijumnong. A review of heat pipe application including new opportunities. *Front. Heat Pipes*, 2(1):1–15, 2011. 1.5.1

[184] AA Mohamad and A Kuzmin. A critical evaluation of force term in lattice boltzmann method, natural convection problem. *International Journal of Heat and Mass Transfer*, 53(5):990–996, 2010. 2.4.6

[185] AA Mohamad, QW Tao, YL He, and S Bawazeer. Treatment of transport at the interface between multilayers via the lattice boltzmann method. *Numerical Heat Transfer, Part B: Fundamentals*, 67(2):124–134, 2015. 4.1.4

[186] Abdulmajeed A Mohamad. *Lattice Boltzmann method: fundamentals and engineering applications with computer codes*. Springer Science & Business Media, 2011. (document), 2.2, 2.6

[187] A Montessori, P Prestininzi, M La Rocca, and S Succi. Lattice boltzmann approach for complex nonequilibrium flows. *Physical Review E*, 92(4):043308, 2015.

[188] Mahmud Jamil Muhammad, Isa Adamu Muhammad, Nor Azwadi Che Sidik, and Muhammad Noor Afiq Witri Muhammad Yazid. Thermal performance enhancement of flat-plate and evacuated tube solar collectors using nanofluid: a review. *International Communications in Heat and Mass Transfer*, 76:6–15, 2016. 1.8.3

[189] Shiladitya Mukherjee and John Abraham. Investigations of drop impact on dry walls with a lattice-boltzmann model. *Journal of colloid and interface science*, 312(2):341–354, 2007. 3.1

[190] Shiladitya Mukherjee and John Abraham. Lattice boltzmann simulations of two-phase flow with high density ratio in axially symmetric geometry. *Physical Review E*, 75(2):026701, 2007. 3.1.1

[191] Misheck G Mwaba, Xiao Huang, Junjie Gu, et al. Influence of wick characteristics on heat pipe performance. *International journal of energy research*, 30(7):489–500, 2006.

[192] MS Naghavi, KS Ong, IA Badruddin, M Mehrali, M Silakhori, and HSC Metselaar. Theoretical model of an evacuated tube heat pipe solar collector integrated with phase change material. *Energy*, 91:911–924, 2015. (document), 1.8.3, 1.12

[193] MS Naghavi, KS Ong, IA Badruddin, Mohammad Mehrali, and HSC Metselaar. Thermal performance of a compact design heat pipe solar collector with latent heat storage in charging/discharging modes. *Energy*, 127:101–115, 2017. (document), 1.8.3, 1.14

[194] Youngsuk Nam, Stephen Sharratt, Chan Byon, Sung Jin Kim, and

Y Sungtaek Ju. Fabrication and characterization of the capillary performance of superhydrophilic cu micropost arrays. *Journal of Microelectromechanical Systems*, 19(3):581–588, 2010.

[195] Youngsuk Nam, Stephen Sharratt, Gilhwan Cha, and Y Sungtaek Ju. Characterization and modeling of the heat transfer performance of nanostructured cu micropost wicks. *Journal of Heat Transfer*, 133(10):101502, 2011.

[196] Rupert W Nash, Hywel B Carver, Miguel O Bernabeu, James Hetherington, Derek Groen, Timm Krüger, and Peter V Coveney. Choice of boundary condition for lattice-boltzmann simulation of moderate-reynolds-number flow in complex domains. *Physical Review E*, 89(2):023303, 2014. 2.5.2

[197] Patrik Nemec, Alexander Čaja, and Milan Malcho. Mathematical model for heat transfer limitations of heat pipe. *Mathematical and Computer Modelling*, 57(1):126–136, 2013.

[198] KC Ng, C Yap, and TH Khor. Outdoor testing of evacuated-tube heat-pipe solar collectors. *Proceedings of the Institution of Mechanical Engineers, Part E: Journal of Process Mechanical Engineering*, 214(1):23–30, 2000.

[199] XD Niu, C Shu, and YT Chew. A lattice boltzmann bgk model for simulation of micro flows. *EPL (Europhysics Letters)*, 67(4):600, 2004. 2.6.3

[200] Dan Nchelatebe Nkwetta and Mervyn Smyth. Performance analysis and comparison of concentrated evacuated tube heat pipe solar collectors. *Applied energy*, 98:22–32, 2012.

[201] Dan Nchelatebe Nkwetta, Mervyn Smyth, Aggelos Zacharopoulos, and Trevor Hyde. Experimental performance analysis and optimisation of medium temperature solar thermal collectors with silicon oil as a heat transfer fluid. *International Journal of Energy Research*, 37(6):570–581, 2013. 1.8.2

[202] Seyed Hossein Noie-Baghban and GR Majideian. Waste heat recovery using heat pipe heat exchanger (hphe) for surgery rooms in hospitals. *Applied thermal engineering*, 20(14):1271–1282, 2000. 1.5.1

[203] Steven A Orszag and Victor Yakhot. Reynolds number scaling of cellular-automaton hydrodynamics. *Physical review letters*, 56(16):1691, 1986.

[204] Anggie Rincon Ortega and Mauricio Carmona. Exergy analysis of a flat plate solar collector with latent heat storage by phase change material for water heating applications at low temperature. *Journal of Contemporary Urban Affairs*, 1(3):43–48, 2017. 1.8.3

[205] Ahmet Ozsoy and Vahit Corumlu. Thermal performance of a thermosyphon heat pipe evacuated tube solar collector using silver-water nanofluid for commercial applications. *Renewable Energy*, 122:26–34, 2018. 1.8.3

[206] J Paetzold, S Cochard, DF Fletcher, and A Vassallo. Wind engineering analysis of parabolic trough collectors to optimise wind loads and heat loss. *Energy Procedia*, 69:168–177, 2015. 1.8.3

[207] Krishna Murari Pandey and Rajesh Chaurasiya. A review on analysis and development of solar flat plate collector. *Renewable and Sustainable Energy Reviews*, 67:641–650, 2017. 1.8.3

[208] Alexios Papadimitratos, Sarvenaz Sobhansarbandi, Vladimir Pozdin,

Anvar Zakhidov, and Fatemeh Hassanipour. Evacuated tube solar collectors integrated with phase change materials. *Solar Energy*, 129:10–19, 2016. (document), 1.8.3, 1.13

[209] G Paul, M Chopkar, I Manna, and PK Das. Techniques for measuring the thermal conductivity of nanofluids: a review. *Renewable and Sustainable Energy Reviews*, 14(7):1913–1924, 2010. 1.8.3

[210] Gang Pei, Guiqiang Li, Xi Zhou, Jie Ji, and Yuehong Su. Comparative experimental analysis of the thermal performance of evacuated tube solar water heater systems with and without a mini-compound parabolic concentrating (cpc) reflector (c< 1). *Energies*, 5(4):911–924, 2012. 1.8.1

[211] Chen Peng. The lattice boltzmann method for fluid dynamics: theory and applications. *M. Math, Department of Mathematics, Ecole Polytechnique Federale de Lausanne*, 2011. 2.4.2, 2.4.4

[212] Y Peng, C Shu, and YT Chew. A 3d incompressible thermal lattice boltzmann model and its application to simulate natural convection in a cubic cavity. *Journal of Computational Physics*, 193(1):260–274, 2004. 2.6.4

[213] Y Peng, C Shu, YT Chew, and J Qiu. Numerical investigation of flows in czochralski crystal growth by an axisymmetric lattice boltzmann method. *Journal of Computational Physics*, 186(1):295–307, 2003. 3.1.1

[214] J Perkins. Uk patent no. 7059. 1836. 1.1

[215] R Petela. Exergy of heat radiation. *ASME J. Heat Transfer*, 86(2):187–192, 1964. 4.4.2

[216] Paulo C Philippi, Luiz A Hegele Jr, Luís OE Dos Santos, and Rodrigo Surmas. From the continuous to the lattice boltzmann equation: the discretization problem and thermal models. *Physical Review E*, 73(5):056702, 2006. 2.3.3

[217] Benjamin Piaud, Stéphane Blanco, Richard Fournier, and Michael J Clifton. Energy-conserving lattice boltzmann thermal model in two dimensions. *Journal of statistical physics*, 121(1-2):119–131, 2005. 2.1

[218] Carlos Javier Porras-Prieto, Fernando R Mazarrón, Victoria de los Mozos, and José Luis García. Influence of required tank water temperature on the energy performance and water withdrawal potential of a solar water heating system equipped with a heat pipe evacuated tube collector. *Solar Energy*, 110:365–377, 2014. 1.8.2

[219] Derek J Posselt, Bruce Fryxell, Andrea Molod, and Brian Williams. Quantitative sensitivity analysis of physical parameterizations for cases of deep convection in the nasa geos-5. *Journal of Climate*, 29(2):455–479, 2016. 5.7.1

[220] Kannan N Premnath and John Abraham. Lattice boltzmann model for axisymmetric multiphase flows. *Physical Review E*, 71(5):056706, 2005. 3.1.1

[221] F Coyne Prenger and JE Kemme. Performance limits of gravity-assist heat pipes with simple wick structures. In *Advances in Heat Pipe Technology*, pages 137–146. Elsevier, 1982. 1.7.6

[222] Jefferson G Pruyne, Ming-Tao Lee, Csaba Fabri, Amaia Beloqui Redondo, Armin Kleibert, Markus Am-

mann, Matthew A Brown, and Maria J Krisch. Liquid–vapor interface of formic acid solutions in salt water: a comparison of macroscopic surface tension and microscopic in situ x-ray photoelectron spectroscopy measurements. *The Journal of Physical Chemistry C*, 118(50):29350–29360, 2014. 1.4.2

[223] Nandy Putra and Wayan Nata Septiadi. Improvement of heat pipe performance through integration of a coral biomaterial wick structure into the heat pipe of a cpu cooling system. *Heat and Mass Transfer*, pages 1–12, 2016.

[224] Nandy Putra, Wayan Nata Septiadi, and Ridho Irwansyah. Effect of concentration and loading fluid of nanofluids on the thermal resistance of sintered powder wick heat pipe. In *Advanced Materials Research*, volume 651, pages 728–735. Trans Tech Publ, 2013.

[225] Nandy Putra, Wayan Nata Septiadi, Haolia Rahman, and Ridho Irwansyah. Thermal performance of screen mesh wick heat pipes with nanofluids. *Experimental thermal and fluid science*, 40:10–17, 2012.

[226] Nandy Putra, Wayan Nata Septiadi, Rosari Saleh, Rardi Artono Koestoer, and Suhendro Purbo Prakoso. The effect of cuo-water nanofluid and biomaterial wick on loop heat pipe performance. In *Advanced Materials Research*, volume 875, pages 356–361. Trans Tech Publ, 2014.

[227] Ram Ranjan, Jayathi Y Murthy, Suresh V Garimella, and Unnikrishnan Vadakkan. A numerical model for transport in flat heat pipes considering wick microstructure effects. *International Journal of Heat and Mass Transfer*, 54(1):153–168, 2011.

[228] Boris Rassamakin, Sergii Khairnasov, Vladilen Zaripov, Andrii Rassamakin, and Olga Alforova. Aluminum heat pipes applied in solar collectors. *Solar Energy*, 94:145–154, 2013. (document), 1.8.3, 1.16

[229] David Reay, Ryan McGlen, and Peter Kew. *Heat pipes: theory, design and applications*. Butterworth-Heinemann, 2013. (document), 1.1, 1.3.2, 1.1, 1.3.2, 1.3, 1.5, 1.6, 1.7, 4.2.1

[230] David AG Redpath. Thermosyphon heat-pipe evacuated tube solar water heaters for northern maritime climates. *Solar energy*, 86(2):705–715, 2012. 1.8.2

[231] Timothy Reis and Timothy Nigel Phillips. Modified lattice boltzmann model for axisymmetric flows. *Physical Review E*, 75(5):056703, 2007. 3.1.1

[232] Timothy Reis and Timothy Nigel Phillips. Numerical validation of a consistent axisymmetric lattice boltzmann model. *Physical Review E*, 77(2):026703, 2008. 3.1.1, 3.3

[233] Roger R Riehl. Characteristics of an open loop pulsating heat pipe. Technical report, SAE Technical Paper, 2004.

[234] SB Riffat, X Zhao, and PS Doherty. Developing a theoretical model to investigate thermal performance of a thin membrane heat-pipe solar collector. *Applied Thermal Engineering*, 25(5):899–915, 2005. 1.8.1, 1.8.2

[235] SB Riffat, X Zhao, PS Doherty, and Song Lin. Development of a simplified heat pipe numerical model and case study/experimental validation using

a long 'wicked'heat pipe. *International journal of energy research*, 28(14):1293–1311, 2004. 1.4.1

[236] Brian S Robinson and M Keith Sharp. Heating season performance improvements for a solar heat pipe system. *Solar Energy*, 110:39–49, 2014.

[237] Cyril Romestant. *Etudes théoriques et expérimentales de caloducs et de thermosiphons soumis á de fortes accélérations*. PhD thesis, Université de Poitiers, 2000. (document), 1.3, 1.7.2, 1.7.2, 1.7.3, 1.7.4, 1.7.5

[238] Fumei Rong, Zhaoli Guo, Zhenhua Chai, and Baochang Shi. A lattice boltzmann model for axisymmetric thermal flows through porous media. *International Journal of Heat and Mass Transfer*, 53(23):5519–5527, 2010. (document), 3.1.1, 3.2, 3.5.2, 3.5, 3.5.3, 3.8, 6.1

[239] Fumei Rong and Baochang Shi. Incompressible lattice boltzmann model for axisymmetric flows through porous media. *International Journal of Modern Physics C*, 26(04):1550036, 2015. 3.1.1, 3.2, 3.5.2, 3.6.1, 6.1

[240] Fumei Rong, Baochang Shi, and Xilin Cui. Lattice boltzmann simulation of heat and fluid flow in 3d cylindrical heat exchanger with porous blocks. *Applied Mathematics and Computation*, 276:367–378, 2016. 3.1.1, 3.2, 6.1

[241] Fumei Rong, Wenhuan Zhang, Baochang Shi, and Zhaoli Guo. Numerical study of heat transfer enhancement in a pipe filled with porous media by axisymmetric tlb model based on gpu. *International Journal of Heat and Mass Transfer*, 70:1040–1049, 2014. (document), 3.1.1, 3.2, 3.5.4, 3.5.4, 3.10, 6.1

[242] Radim Rybár and Martin Beer. The comparative field performance study of heat pipe evacuated tube collectors with standard design manifold header and parallel flow manifold header based on the metal foam structural element. *Solar Energy*, 122:359–367, 2015. (document), 1.8.3, 1.17

[243] Radim Rybár, Martin Beer, and Michal Cehlár. Thermal power measurement of the novel evacuated tube solar collector and conventional solar collector during simultaneous operation. *Measurement*, 88:153–164, 2016. 1.8.2

[244] Kais Saidi and Sami Hammami. The impact of co 2 emissions and economic growth on energy consumption in 58 countries. *Energy Reports*, 1:62–70, 2015.

[245] Rosari Saleh, Nandy Putra, Suhendro Purbo Prakoso, and Wayan Nata Septiadi. Experimental investigation of thermal conductivity and heat pipe thermal performance of zno nanofluids. *International Journal of Thermal Sciences*, 63:125–132, 2013.

[246] Robert W Scharge. A theoretical study of interface mass transfer, 1953. 4.1.4

[247] N Selvakumar and Harish C Barshilia. Review of physical vapor deposited (pvd) spectrally selective coatings for mid-and high-temperature solar thermal applications. *Solar Energy Materials and Solar Cells*, 98:1–23, 2012. 1.8.3

[248] R Senthilkumar, S Vaidyanathan, and B Sivaraman. Experimental analysis of cylindrical heat pipe using copper nanofluid with an aqueous solution of n-hexanol. *Frontiers in Heat Pipes (FHP)*, 2(3), 2012. 4.2.1

[249] Joseph Seo, In-Cheol Bang, and Jae-Young Lee. Length effect on entrainment limit of large-l/d vertical heat

pipe. *International Journal of Heat and Mass Transfer*, 97:751–759, 2016. 1.7.6

[250] Takeshi Seta, Eishun Takegoshi, and Kenichi Okui. Lattice boltzmann simulation of natural convection in porous media. *Mathematics and Computers in Simulation*, 72(2):195–200, 2006. 3.1.1

[251] Xiaowen Shan and Hudong Chen. Simulation of nonideal gases and liquid-gas phase transitions by the lattice boltzmann equation. *Physical Review E*, 49(4):2941, 1994. 2.4.6

[252] Xiaowen Shan and Xiaoyi He. Discretization of the velocity space in the solution of the boltzmann equation. *Physical Review Letters*, 80(1):65, 1998. 2.1, 2.3, 2.3.3

[253] Xiaowen Shan, Xue-Feng Yuan, and Hudong Chen. Kinetic theory representation of hydrodynamics: a way beyond the navier-stokes equation. *Journal of Fluid Mechanics*, 550(1):413, 2006. 2.3.3

[254] Yuli Shan, Heran Zheng, Dabo Guan, Chongmao Li, Zhifu Mi, Jing Meng, Heike Schroeder, Jibo Ma, and Zhuguo Ma. Energy consumption and co2 emissions in tibet and its cities in 2014. *Earth's Future*, 2017.

[255] Atul Sharma, V Veer Tyagi, CR Chen, and Dharam Buddhi. Review on thermal energy storage with phase change materials and applications. *Renewable and Sustainable energy reviews*, 13(2):318–345, 2009. 1.8.3

[256] Neeraj Sharma and Gerardo Diaz. Performance model of a novel evacuated-tube solar collector based on minichannels. *Solar Energy*, 85(5):881–890, 2011. 1.8.1

[257] Suping Shen, Wenjian Cai, Xinli Wang, Qiong Wu, and Haoren Yon. Investigation of liquid desiccant regenerator with heat recovery heat pipe system. *Energy and Buildings*, 146:353–363, 2017. 1.5.1

[258] Mahmood RS Shirazy, Sonia Blais, and Luc G Fréchette. Mechanism of wettability transition in copper metal foams: From superhydrophilic to hydrophobic. *Applied Surface Science*, 258(17):6416–6424, 2012. 1.3.3

[259] H Shokouhmand, F Jam, and MR Salimpour. Simulation of laminar flow and convective heat transfer in conduits filled with porous media using lattice boltzmann method. *International Communications in Heat and Mass Transfer*, 36(4):378–384, 2009. 3.1.1

[260] Ruchi Shukla, K Sumathy, Phillip Erickson, and Jiawei Gong. Recent advances in the solar water heating systems: A review. *Renewable and Sustainable Energy Reviews*, 19:173–190, 2013. 1.8.1

[261] K Sivakumar, N Krishna Mohan, and B Sivaraman. Performance analysis of elliptical heat pipe solar collector. *Indian Journal of Science and Technology*, 4(1):4–7, 2011. 1.8.2

[262] R Sivanesapillai, H Steeb, and A Hartmaier. Transition of effective hydraulic properties from low to high reynolds number flow in porous media. *Geophysical Research Letters*, 41(14):4920–4928, 2014. 3.5.2

[263] B Sivaraman and N Krishna Mohan. Analysis of heat pipe solar collector using artificial neural network. 2007.

[264] B Sivaraman and N Krishna Mohan. Analysis of heat pipe solar collector with different heat pipe parameters.

International Energy Journal, 8(2), 2007.

[265] PA Skordos. Initial and boundary conditions for the lattice boltzmann method. *Physical Review E*, 48(6):4823, 1993. 2.5.1

[266] Alexander D Smith, Daniel W Field, Armen Askijian, and James Grossman. Satellite radiator panels with combined stiffener/heat pipe, 2015. US Patent 20160288926A1. 1.5.2

[267] Sarvenaz Sobhansarbandi, Patricia M Martinez, Alexios Papadimitratos, Anvar Zakhidov, and Fatemeh Hassanipour. Evacuated tube solar collector with multifunctional absorber layers. *Solar Energy*, 146:342–350, 2017. 1.8.3

[268] A Brusly Solomon, K Ramachandran, and BC Pillai. Thermal performance of a heat pipe with nanoparticles coated wick. *Applied Thermal Engineering*, 36:106–112, 2012.

[269] Dhanabal Somasundaram, Annamalai Mani, and Muthusamy Kamaraj. Experimental investigation of thermal performance of metal foam wicked flat heat pipe. *Experimental Thermal and Fluid Science*, 82:482–492, 2017.

[270] Francis J Stenger. Experimental feasibility study of water-filled capillary-pumped heat-transfer loops. 1966. 1.6.4

[271] S Succi, P Santangelo, and R Benzi. High-resolution lattice-gas simulation of two-dimensional turbulence. *Physical review letters*, 60(26):2738, 1988.

[272] R Sureshkumar, S Tharves Mohideen, and N Nethaji. Heat transfer characteristics of nanofluids in heat pipes: a review. *Renewable and Sustainable Energy Reviews*, 20:397–410, 2013. 1.3.2, 1.8.3

[273] Boxin Tang. Orthogonal array-based latin hypercubes. *Journal of the American statistical association*, 88(424):1392–1397, 1993. 5.7.1

[274] GH Tang, WQ Tao, and YL He. Gas slippage effect on microscale porous flow using the lattice boltzmann method. *Physical Review E*, 72(5):056301, 2005. 3.1.1

[275] Runsheng Tang, Zhimin Li, Hao Zhong, and Qing Lan. Assessment of uncertainty in mean heat loss coefficient of all glass evacuated solar collector tube testing. *Energy conversion and management*, 47(1):60–67, 2006. 1.8.1

[276] Brahim Taoufik, Mhiri Foued, and Jemni Abdelmajid. Parametric study of a flat plate wick assisted heat pipe solar collector. *Journal of Solar Energy Engineering*, 135(3):031016, 2013.

[277] A Tarokh, AA Mohamad, and L Jiang. Simulation of conjugate heat transfer using the lattice boltzmann method. *Numerical Heat Transfer, Part A: Applications*, 63(3):159–178, 2013. 4.1.4

[278] HM Teamah, MF Lightstone, and JS Cotton. An alternative approach for assessing the benefit of phase change materials in solar domestic hot water systems. *Solar Energy*, 158:875–888, 2017. 1.8.3

[279] Yuan Tian and Chang-Ying Zhao. A review of solar collectors and thermal energy storage in solar thermal applications. *Applied Energy*, 104:538–553, 2013. 1.8.3

[280] Yijie Tong and Honghyun Cho. Comparative study on the thermal performance of evacuated solar collectors with u-tubes and heat pipes. *International Journal of Air-Conditioning*

and Refrigeration, 23(03):1550019, 2015. 1.8.2

[281] Mohsen Torabi, Kaili Zhang, Guangcheng Yang, Jun Wang, and Peng Wu. Heat transfer and entropy generation analyses in a channel partially filled with porous media using local thermal non-equilibrium model. *Energy*, 82:922–938, 2015.

[282] Kambiz Vafai. *Handbook of porous media*. Crc Press, 2015.

[283] Pieter Van Leemput, Martin Rheinländer, and Michael Junk. Smooth initialization of lattice boltzmann schemes. *Computers & Mathematics with Applications*, 58(5):867–882, 2009. 2.5.1

[284] Joris CG Verschaeve and Bernhard Müller. A curved no-slip boundary condition for the lattice boltzmann method. *Journal of Computational Physics*, 229(19):6781–6803, 2010.

[285] Jinku Wang, Moran Wang, and Zhixin Li. A lattice boltzmann algorithm for fluid solid conjugate heat transfer. *International journal of thermal sciences*, 46(3):228–234, 2007. 4.1.4

[286] Keyong Wang, Fatemeh Tavakkoli, and Kambiz Vafai. Analysis of gaseous slip flow in a porous micro-annulus under local thermal non-equilibrium condition–an exact solution. *International Journal of Heat and Mass Transfer*, 89:1331–1341, 2015. 4.1.4

[287] Lingquan Wang, Zhong Zeng, Liangqi Zhang, Haiqiong Xie, Gongyou Liang, and Yiyu Lu. A lattice boltzmann model for thermal flows through porous media. *Applied Thermal Engineering*, 108:66–75, 2016. 3.1.1

[288] Moran Wang, Jihuan He, Jianyong Yu, and Ning Pan. Lattice boltzmann modeling of the effective thermal conductivity for fibrous materials. *International Journal of Thermal Sciences*, 46(9):848–855, 2007. 4.1.4

[289] Xun Wang, Tong Han, Lei Wang, Xin Xin Mao, and Cheng Si Yang. Experimental study on start-up characteristics of pulsating heat pipe. In *Advanced Materials Research*, volume 354, pages 87–91. Trans Tech Publ, 2012.

[290] Y Wang, C Shu, and CJ Teo. A fractional step axisymmetric lattice boltzmann flux solver for incompressible swirling and rotating flows. *Computers & Fluids*, 96:204–214, 2014. 3.1.1

[291] Y Wang and K Vafai. An experimental investigation of the transient characteristics on a flat-plate heat pipe during startup and shutdown operations. *TRANSACTIONS-AMERICAN SOCIETY OF MECHANICAL ENGINEERS JOURNAL OF HEAT TRANSFER*, 122(3):525–535, 2000.

[292] Y Wang and K Vafai. Transient characterization of flat plate heat pipes during startup and shutdown operations. *International Journal of Heat and Mass Transfer*, 43(15):2641–2655, 2000.

[293] Justin A Weibel and Suresh V Garimella. Visualization of vapor formation regimes during capillary-fed boiling in sintered-powder heat pipe wicks. *International Journal of Heat and Mass Transfer*, 55(13):3498–3510, 2012.

[294] Leonard M Weinstein. Open loop heat pipe radiator having a free-piston for wiping condensed working fluid, 2015. US Patent 9,091,490. 1.5.2

[295] Adam P Willard and David Chandler. The molecular structure of the interface between water and a hydrophobic substrate is liquid-vapor like. *The Journal of chemical physics*, 141(18):18C519, 2014. 1.4.2

[296] C Wilson, B Borgmeyer, RA Winholtz, HB Ma, D Jacobson, and D Hussey. Thermal and visual observation of water and acetone oscillating heat pipes. *Journal of Heat Transfer*, 133(6):061502, 2011.

[297] Dieter A Wolf-Gladrow. *Lattice-gas cellular automata and lattice Boltzmann models: an introduction*. Springer, 2004. 2.1, 2.6.1

[298] Shwin-Chung Wong and Yi-Huan Kao. Visualization and performance measurement of operating mesh-wicked heat pipes. *International Journal of Heat and Mass Transfer*, 51(17):4249–4259, 2008.

[299] Shwin-Chung Wong and Yu-Chung Lin. Effect of copper surface wettability on the evaporation performance: Tests in a flat-plate heat pipe with visualization. *International journal of heat and mass transfer*, 54(17):3921–3926, 2011.

[300] Shwin-Chung Wong, Hsin-Ho Tseng, and Shih-Heng Chen. Visualization experiments on the condensation process in heat pipe wicks. *International Journal of Heat and Mass Transfer*, 68:625–632, 2014.

[301] Gordon Wu. Heat pipe and radiator system with thermoelectric cooler, 2017. US Patent 9714777B1. 1.5.2

[302] Haiqiong Xie, Zhong Zeng, Liangqi Zhang, Yuui Yokota, Yoshiyuki Kawazoe, and Akira Yoshikawa. Simulation on thermocapillary-driven drop coalescence by hybrid lattice boltzmann method. *Microgravity Science and Technology*, 28(1):67–77, 2016.

[303] H Sheng Xue. Experimental investigation of a domestic solar water heater with solar collector coupled phase-change energy storage. *Renewable energy*, 86:257–261, 2016. 1.8.3

[304] Xue Fei Yang, Zhen-Hua Liu, and Jie Zhao. Heat transfer performance of a horizontal micro-grooved heat pipe using cuo nanofluid. *Journal of Micromechanics and Microengineering*, 18(3):035038, 2008. 1.3.2

[305] YH Yau and M Ahmadzadehtalatapeh. A review on the application of horizontal heat pipe heat exchangers in air conditioning systems in the tropics. *Applied Thermal Engineering*, 30(2):77–84, 2010. 1.5.1

[306] Kenny Q Ye. Orthogonal column latin hypercubes and their application in computer experiments. *Journal of the American Statistical Association*, 93(444):1430–1439, 1998. 5.7.1

[307] T Yousefi, SA Mousavi, B Farahbakhsh, and MZ Saghir. Experimental investigation on the performance of cpu coolers: Effect of heat pipe inclination angle and the use of nanofluids. *Microelectronics Reliability*, 53(12):1954–1961, 2013.

[308] Dazhi Yu, Renwei Mei, and Wei Shyy. A unified boundary treatment in lattice boltzmann method. In *41st Aerospace Sciences Meeting and Exhibit*, page 953, 2003.

[309] Raoyang Zhang, Xiaowen Shan, and Hudong Chen. Efficient kinetic method for fluid simulation beyond the navier-stokes equation. *Physical Review E*, 74(4):046703, 2006.

[310] Ting Zhang, Baochang Shi, Zhenhua Chai, and Fumei Rong. Lat-

tice bgk model for incompressible axisymmetric flows. *Communications in Computational Physics*, 11:1569–1590, 2012. 3.3, 3.6.1, 3.6.2

[311] Ting Zhang, Baochang Shi, Zhaoli Guo, Zhenhua Chai, and Jianhua Lu. General bounce-back scheme for concentration boundary condition in the lattice-boltzmann method. *Physical Review E*, 85(1):016701, 2012. 2.5.2

[312] Xinyu Zhang, Shijun You, Hongchuan Ge, Yan Gao, Wei Xu, Min Wang, Tao He, and Xuejing Zheng. Thermal performance of direct-flow coaxial evacuated-tube solar collectors with and without a heat shield. *Energy Conversion and Management*, 84:80–87, 2014.

[313] Xinyu Zhang, Shijun You, Wei Xu, Min Wang, Tao He, and Xuejing Zheng. Experimental investigation of the higher coefficient of thermal performance for water-in-glass evacuated tube solar water heaters in china. *Energy Conversion and Management*, 78:386–392, 2014. 1.8.1

[314] Hongfei Zheng, Jianying Xiong, Yuehong Su, and Haiyin Zhang. Influence of the receiver's back surface radiative characteristics on the performance of a heat-pipe evacuated-tube solar collector. *Applied Energy*, 116:159–166, 2014. 1.8.3

[315] Lin Zheng, Baochang Shi, Zhaoli Guo, and Chuguang Zheng. Lattice boltzmann equation for axisymmetric thermal flows. *Computers & Fluids*, 39(6):945–952, 2010. 3.1.1

[316] Jian Guo Zhou. *Lattice Boltzmann methods for shallow water flows*, volume 4. Springer, 2004. 3.2.1, 3.4.1, 3.6.3

[317] Jian Guo Zhou. Axisymmetric lattice boltzmann method. *Physical Review E*, 78(3):036701, 2008. 3.1.1, 3.3

[318] Jian Guo Zhou. Axisymmetric lattice boltzmann method revised. *Physical Review E*, 84(3):036704, 2011. 3.1.1, 3.3

[319] N Zhu and K Vafai. Analysis of cylindrical heat pipes incorporating the effects of liquid–vapor coupling and non-darcian transport a closed form solution. *International Journal of Heat and Mass Transfer*, 42(18):3405–3418, 1999. (document), 1.4.1, 4.1.5, 4.2, 4.1.5, 4.7

[320] Ting-Ting Zhu, Yan-Hua Diao, Yao-Hua Zhao, and Feng-Fei Li. Thermal performance of a new cpc solar air collector with flat micro-heat pipe arrays. *Applied Thermal Engineering*, 98:1201–1213, 2016. 1.8.1

[321] Ting-ting Zhu, Yao-hua Zhao, Yan-hua Diao, Feng-Fei Li, and Zhen-hua Quan. Experimental investigation and performance evaluation of a vacuum tube solar air collector based on micro heat pipe arrays. *Journal of cleaner production*, 142:3517–3526, 2017. 1.8.3

[322] Qisu Zou and Xiaoyi He. On pressure and velocity boundary conditions for the lattice boltzmann bgk model. *Physics of fluids*, 9(6):1591–1598, 1997. 2.5.2, 2.5.2

[323] Qisu Zou, Shuling Hou, Shiyi Chen, and Gary D Doolen. A improved incompressible lattice boltzmann model for time-independent flows. *Journal of Statistical Physics*, 81(1):35–48, 1995.

ETUDE NUMERIQUE ET EXPERIMENTALE DES CALODUCS UTILISES DANS DES APPLICATIONS SOLAIRES

Résumé :
En raison de la tendance positives pour le développement durable, les systèmes solaires (capteurs solaires, concentrateur solaire, etc.) Intègrent (et demandent d'intégrer encore plus) intensivement les résidences et les industries. Dans ce contexte, les systèmes diphasiques comme le caloduc semblent être très efficaces en raison de leurs capacités élevées de transport de chaleur et de leur fonctionnement passif appliqués aux capteurs. Compte-tenu de la complexité des caloducs à structure poreuse dans ce type d'application, la plupart des systèmes existants sur le marché utilisent des thermosiphons. Ainsi, le besoin croissant de solutions de contrôle thermique fiables et plus efficaces croit rapidement pour de tels systèmes.
Ce travail de thèse porte sur la caractérisation des performances des caloducs à structure poreuse utilisés dans les applications solaires. Une étude numérique a été réalisée pour modéliser et simuler le comportement d'un caloduc typique à l'aide de la méthode lattice Boltzmann. Une étude expérimentale a également été réalisée pour caractériser les performances de trois prototypes testes dans différentes conditions (température du condenseur, puissance introduite et angle d'inclinaison). Les effets induits par plusieurs paramètres incluant le taux de remplissage, le fluide de travail et la symétrie de la puissance appliquée sur les performances de ces dispositifs ont également été étudiés. En particulier, l'asymétrie du chauffage induit un assèchement plus précoce, toutes choses étant égales par ailleurs. L'inclinaison optimale est également déterminée là où est équilibrée la chaleur solaire maximale disponible et reçue par le caloduc et l'écoulement de liquide assisté par gravité à l'intérieur de ce dispositif.

Mots clés : développement durable, énergie solaire, caloducs, transfert de chaleur, matériaux poreux, méthode de lattice Boltzmann, applications solaires.

NUMERICAL AND EXPERIMENTAL STUDY OF HEAT PIPES USED IN SOLAR APPLICATIONS

Abstract:

Owing to the trend to development sustainability, solar systems (solar collector, solar concentrator, etc.) Are integrating (and asked to integrate even more) intensively residences and industries. In this context, two-phase systems like heat pipe seem highly effective because of their high heat transport capabilities and their passive operation in collectors' technology. In view of the complexity of the heat pipes with a porous structure in this kind of application, most of the existing systems on the market use thermosyphons. Thus, the growing need of reliable and more efficient thermal control solutions is increasing for such systems.

This thesis work focuses on the performance characterization of heat pipes with porous structure used in solar applications. A numerical study has been performed to model and simulate the behavior of a typical heat pipe using the lattice Boltzmann method. An experimental study has also been done to characterize the performance of three prototypes tested under different conditions (condenser temperature, heat input and inclination angle). The effects induced by several parameters including the filling rate, working fluid and symmetry of the applied heat on the performance of these devices has also been investigated. In particular, heating asymmetry is found to induce dry-out earlier, all other things being equal. Optimal inclination is also determined where is balanced the maximum solar heat available and received by the heat pipe and the gravity-assisted liquid flow inside that device.

Keywords: sustainable development, solar energy, heat pipes, heat transmission, porous media, lattice Boltzmann method, solar applications.